JAERI-Conf
2000-007

PROCEEDINGS OF THE FIFTH AUSTRALIA-JAPAN WORKSHOP ON PLASMA DIAGNOSTICS DECEMBER 15-17, 1999, NAKA, JAPAN

March 2000

Department of Fusion Plasma Research

日本原子力研究所
Japan Atomic Energy Research Institute

本レポートは、日本原子力研究所が不定期に公刊している研究報告書です。
入手の問合わせは、日本原子力研究所研究情報部研究情報課（〒319-1195　茨城県那珂郡東海村）あて、お申し越し下さい。なお、このほかに財団法人原子力弘済会資料センター（〒319-1195　茨城県那珂郡東海村日本原子力研究所内）で複写による実費頒布を行っております。

This report is issued irregularly.
Inquiries about availability of the reports should be addressed to Research Information Division, Department of Intellectual Resources, Japan Atomic Energy Research Institute, Tokai-mura, Naka-gun, Ibaraki-ken 〒319-1195, Japan.

編集兼発行　日本原子力研究所

JAERI－Conf 2000－007

Proceedings of the Fifth Australia- Japan Workshop on Plasma Diagnostics December 15 – 17, 1999, Naka, Japan

Department of Fusion Plasma Research

Naka Fusion Research Establishment
Japan Atomic Energy Research Institute
Naka-machi, Naka-gun, Ibaraki-ken

(Received March 6, 2000)

The fifth Australia-Japan Workshop on Plasma Diagnostics was held at Japan Atomic Energy Research Institute (JAERI), Naka, Japan, from December 15 to 17 in 1999. The first workshop was held at JAERI, Naka in 1989, and the workshops have been held almost every two years in Australia and Japan under the Agreement between the Government of Japan and the Government of Australia on cooperation in the field of Science and Technology. In the workshops, latest research works for plasma diagnostics and plasma experiment have been presented and discussed. The research works of both countries have been developed, and the mutual understanding became deeper through the workshops.

In the fifth workshop, the statuses of JT-60U (JAERI), LHD (National Institute for Fusion Science) and H-1NF (Australian National University) were introduced, and the latest research works for plasma diagnostics were also presented. The active and deeper discussions were performed.

This report contains twenty-eight papers presented at the workshop.

Keywords: Australia- Japan Workshop, Plasma Diagnostics, Spectroscopy, Interferometer, Reflectometer, Neutron, Laser Scattering, FIR-laser, Gyrotron, Fusion

JAERI－Conf 2000－007

第５回　プラズマ診断に関する日豪ワークショップ
（1999 年 12 月 15 日～17 日，日本原子力研究所 那珂研究所）
論文集

日本原子力研究所那珂研究所
炉心プラズマ研究部

（２０００年３月６日受理）

プラズマ診断に関する日豪ワークショップは、日豪科学技術協力協定のもとで、両国におけるプラズマ診断、及び実験に関する最新の研究結果について情報交換を行い両国の研究開発を促進するとともに、相互の理解と交流を深めることを目的として 1989 年に原研で第１回が開催され、その後、日豪交互にほぼ２年毎に開催されている。

第５回プラズマ診断に関する日豪ワークショップは 1999 年 12 月 15 日から 17 日の３日間、日本原子力研究所那珂研究所で開催され、計 37 名の参加者があった。

このワークショップでは、JT-60U（原研）、LHD（核融合科学研究所）、H-1NF（オーストラリア国立大学）における研究の現状、並びに最新のプラズマ診断技術の進展と研究成果等に係わる、計 28 件の発表があり、活発な議論が行われた。本報告書は、このワークショップでの発表論文をまとめたものである。

那珂研究所：〒311-0193 茨城県那珂郡那珂町向山 801-1

Contents

Second Day Session

This is a blank page.

1-1 H-1NF program and diagnostic systems

John Howard on behalf of H-1NF team
Plasma Research Laboratory, Australian National University.
Canberra ACT 0200

The H-1NF heliac has undergone major upgrades during 1999. These include the commissioning of a new magnet power supply to produce fields up to 1T for 1s, the installation of an additional 500kW of rf heating power and the near completion of the 28GHz ECH heating system. The latter will be operated at 0.5 T in year 2000.

New diagnostic systems include the 4-channel 2mm microwave scattering system, the swept frequency 2mm interferometer, a multiplicity of visible spectroscopy systems, including correlation spectroscopy, a new set of magnetic pick-up coils and various probe diagnostic enhancements. The MDS data system software has been upgraded to MDSPlus. We are now routinely using this platform and have developed a simple IDL-based point-and-click interface for easy access to the diagnostic signals.

This paper reports some recent H-1NF results, gives an overview of the program planned for H-1 in 2000 and describes briefly the important diagnostic systems that will be used during the next campaign.

1-2 Initial plasma experiments and plasma diagnostics on LHD

Kazuo Kawahata and LHD experimental group
National Institute for Fusion Science.
Tokishi 509-5952, Japan
S. Okajima
Faculty of Engineering, Chubu University
Kasugai 487, Japan

In National Institute for fusion Science, the Large Helical Device (R = 3.9 m, ap = 0.65 m, B = 1.5-3.0 T) has been construted in Toki City, and its first plasma experiments started at the end of March in 1998. Almost of the main diagnostics such as the Thomson scattering system, FIR laser interferometer and others have been installed in the summer of 1998 just before the 2nd experimental campaign of the LHD, and routinely provide us plasma profile information such as Te(r,t), Ne(r,t) and so on. In this workshop we will report about initial plasma experiments and major diagnostics, especially IR/MM wave diagnostics, on the LHD.

1 Introduction

The Large Helical Device(LHD) experiments has successfully started[1] after the eight-years of construction period(1990-1997). The magnetic field up to 3 T is generated by a pair of superconducting helical winding of pitch parameters of m/l = 2/10 and three sets of superconducting poloidal coils. The plasma is genarated by ECRH of 84 and 82.6 GHz, and heated up by NBI (negative ion sources, ~4.5 MW) and ICRH (38MHz, ~1.5MW).The plasma parameters obtained in the 3rd experimental campaign are: the electron /ion temperatures of 1.0-5.0 keV, the line-averaged electron density of 2-12 x 10^{19} m^{-3} and the maximum stored energy of ~870 kJ. There are no mechanical disturbance caused by the change of the magnetic field in the laser diagnostics which usually need the exact spatial alignment. Among various activities of the LHD plasma giagnostics, the characteristic major diagnostics are described below.

2 FIR Laser Interferometer System

A multi-channel FIR laser interferometer system [2] has been developed for the measurement of the spatial and temporal behaviors of the electron density on the LHD. Among several candidates of the high power laser sources a 119-μm CH_3OH laser was adapted as a probing light. The optical configuration is of the Michelson

interferometer type with 13 channels.

Figure 1 shows a schematic drawing of the interferometer system installed in the LHD experimental room. The FIR lasers are installed in the laser room 30 m apart from the LHD, and propagate about 40 m through a couple of the dielectric waveguides to reach the optical housing of the interferometer. The optical housing, where 150 optical components are installed, is mounted on a massive frame. The frame encircles the plasma vacuum vessel and floats on three pneumatic vibration isolation mounts in order to minimise the transmission of vibrations from the machine. This isolation stand is 18.4 meters tall and weights about 30 tons. The diameter of the three main supports is 712 mm. The upper shelf of the stand supports thirteen corner cube reflectors, while the interferometer housing(3900 x 1500 x 4500 mm3) is supported by the lower shelf which is located below the floor of the Large Helical Device. The optical housing is air tight and filled with dry air in order to reduce absorption of the CH3OH laser radiation by atmospheric water vapor. Figure 2 shows the time behavior of the line integrated electron density profile measured by the FIR laser interferometer. In this experiment the plasma was produced by the second harmonic ECH with the power level of 100-200 kW and auxiliary heated with NBI of 2 MW. The observed mechanical vibration level is about 1/100 fringes for the high frequency components and 1/50 fringes for f 1 Hz. At the present experimental condition, the resolution of fringe counters is 1/100 fringes, and it corresponds to a line averaged density of 5.6 x $10^{16}m^{-3}$ at the central chord.

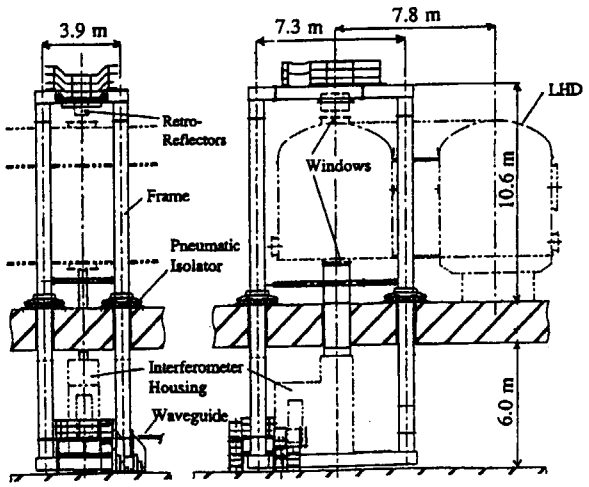

Fig.1 Schematic of the interferometer system installed in the pnumatic vibration isolation stand.

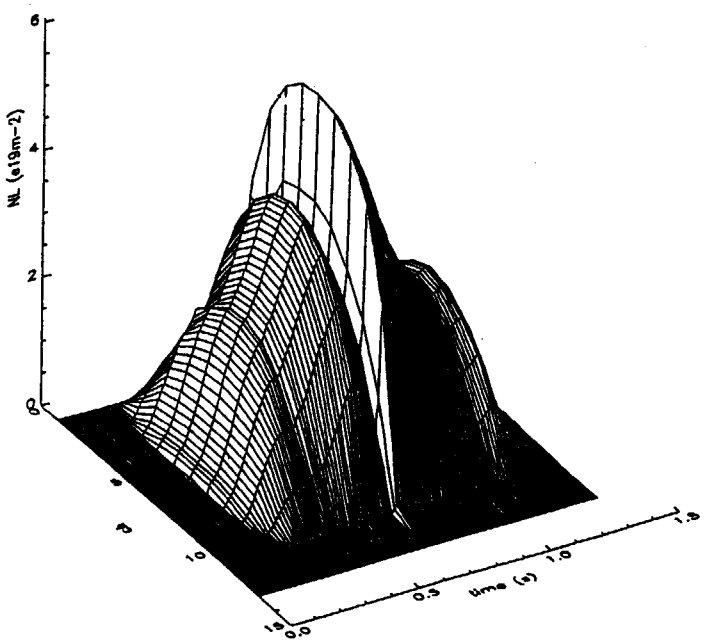

Fig. 2 Output of the 13-channel interferometer as a function on time.
A hydrogen ice pellet is injected at 0.6 s.

3 Thomson Scattering System

After comparing various Thomson scattering systems under operation, and taking into account the limited access to the plasma confined in the helical magnetic field, an obliquely back-scattered YAG Thomson scattering system[3] was chosen as is shown in Fig.3.This configuration enables us to measure electron temperature and density profiles from the outer edge to the inner edge of the plasma in one laser shot. A bundle of 6 Nd:YAG laser beams, guided by mirror relay system, are injected along the major radius, and the nearly back scattered light are collected through the same port as that used for injection by a spherical mirror(1.5m x 1.8m) and focused onto the end of arrayed optical fibers 2 mm in diameter and 45m in length. Each YAG laser operates with a maximum repetition rate of 50 Hz. They are planed to achieve a shortest time interval of 10 us for studying high temporal profile evolution. The scattered lights at ~130 different spatial points are analyzed by the polychromators which have 5 color channels. The spatial resolutions are estimated to be 15 - 40 mm. Figure 4 shows the typical electron temperature profile obtained in the NBI plasma.

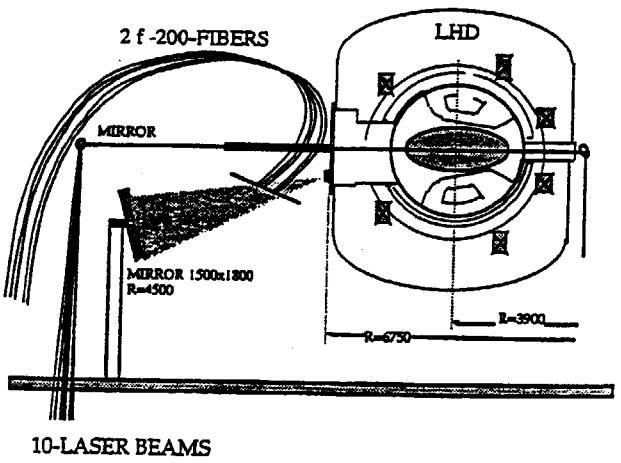

Fig.3 The schematic drawing of the LHD Thomson Scattering.

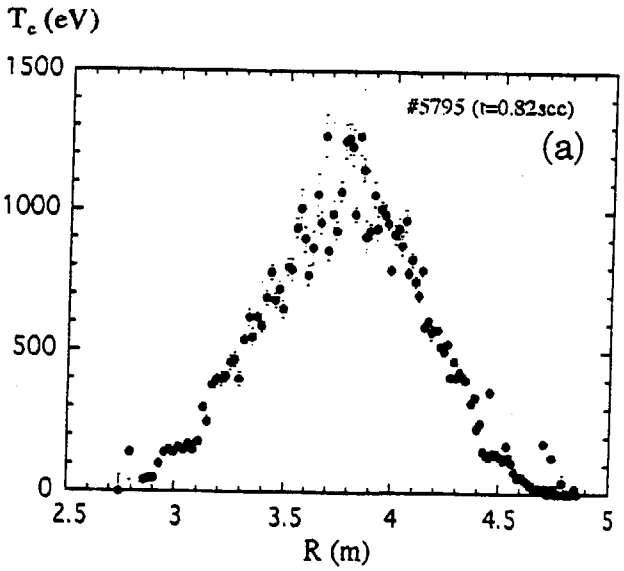

Fig.4 The radial profile of electron temperature, Te(r).

References

1) A. Iiyoshi, K. Komori, A. Ejiri, M. Emoto, et al., Proc. of the 17th IAEA Fusion Energy Conference, Yokohama, Japan, 1998(IAEA, Vienna), IAEA-CN-69/OV1/4.
2) K.Kawahata, K. Tanaka, Y. Ito, E. Ejiri, S. Okajima, Y. Naitou , far infrared laser interferometer on the LHD, Rev. Sci. Instrum. 70 (1999) 707.
3) K.Narihara, K. Yamauchi, I. Yamada and T. Minami, et al. Fusion Engineering and Design 34-35 (1997) 57.

1-3 Recent results on steady state and confinement improvement research on JT-60U

S. Ide and the JT-60 team

Naka Fusion Research Establishment, Japan Atomic Energy Research Institute
Naka-machi, Naka-gun, Ibaraki, 311-0193 Japan

Abstract : On the JT-60U tokamak, fusion plasma research for realization of a steady state tokamak reactor has been pursued. Towards that goal, confinement improved plasmas such as H-mode, high β_p, reversed magnetic shear (RS) and latter two combined with H-mode edge pedestal have been developed and investigated intensively. A key issue to achieve non-inductive current drive relevant to a steady state fusion reactor is to increase the fraction of the bootstrap current and match the spatial profile to the optimum. In 1999, as the result of the optimization, the equivalent deuterium-tritium (D-T) fusion gain (Q_{DT}^{eq}) of 0.5 was sustained for 0.8 s, which is roughly equal to the energy confinement time, in a RS plasma. In order to achieve a RS plasma in steady state two approach have been explored. One is to use external current driver such as lower hybrid current drive (LHCD), and by optimizing LHCD a quasi-steady RS discharge was obtained. The other approach is to utilize bootstrap current as much as possible, and with highly increased fraction of the bootstrap current, a confinement enhancement factor of 3.6 was maintained for 2.7 s in a RS plasma with H-mode edge. A heating and current drive system in the electron cyclotron range of frequency for localized heating and current drive has been installed on JT-60U, and in initial experiments a clear increase of the central electron temperature in a RS high density central region was confirmed only with injected power of 0.75 MW.

1 Introduction

The JT-60U tokamak is a single null divertor tokamak device, the plasma major radius (R_p) 3 – 3.5 m, the plasma minor radius (a_p) 0.6 – 1.1 m and the maximum toroidal magnetic field (B_t) <4 T at R = 3.32 m. The main objectives of the JT-60U project are studies on confinement, stability, steady state, heat and particle handling by a divertor configuration and understanding of underlaying physics in order to establish physics basis for the international thermonuclear experimental reactor (ITER) and steady state reactor such as SSTR [1]. For this purpose high performance plasmas, such as H-mode, high β_p [2], reversed magnetic shear (RS) plasmas [3] and the latter two combined with an H-mode edge [4,5], have been developed. What is essential to keep improved confinement in those plasmas is to maintain the internal and/or the edge transport barriers (ITB [3,6] and/or ETB). A variety of heating and current drive method such as neutral beam injection (NBI; both positive and negative ion based), lower hybrid waves (LHW), ion cyclotron range of frequency (ICRF) and newly installed electron cyclotron range of frequency (ECRF) systems has been utilized to optimize heating, pressure, rotation and current profiles for maximizing the confinement characteristics and the β limit. Plasma shaping control is also a key issue to improve the β limit. To date, the equivalent deuterium-tritium (D-T) fusion gain (Q_{DT}^{eq}) of 0.5 was succeeded to be maintained for 0.8 s in a RS plasma with L-mode edge. A RS plasma of the confinement improvement factor relative to the ITER 89 power law (H^{89p}) $\sim$ 1.4 and the normalized beta (β_N) $\sim$ 1 was succeeded to be sustained fully non-inductively by LHCD with almost fixed current profile. With the ELMy H-mode edge, a RS plasma of H^{89p} = 3.6 and $\beta_N \sim 2$ has been maintained for 2.7 s with bootstrap current fraction of about 80%. A high β_p H-mode plasma has been demonstrated to be maintained for long ($> 5\tau_E$) with high β_N of 2.5 – 2.7 even at low safety factor regime by optimizing pressure profile and plasma shaping. It should be noted that by using various heating method situations in which T_e is close to or even higher than

T_i (as high as twice) have been obtained. ECRF system of 110 GHz has been installed on JT-60U and started operation since February 1999 for local heating and current drive. The latest progress of the JT-60U experiments in steady state fusion plasma research is highlighted in this paper.

2 High performance RS plasmas in JT-60U

A RS plasma has a region of negative magnetic shear ($s = r/qdq/dr$, q being the safety factor and r being the minor radius) region, as its name indicates. Usually, negative shear is

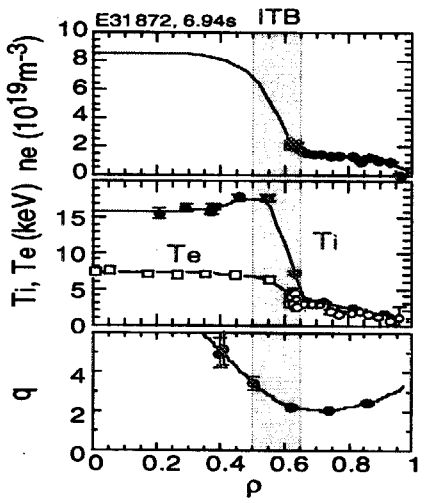

Figure 1: Spatial profiles of n_e, T_e, T_i and q in a plasma in which $Q_{DT}^{eq} = 1.25$ was achieved (I_p = 2.6 MA, B_t = 4.4 T and $P_{NB}^{abs} = 12\ MW$).

produced in a plasma by injecting heating power (usually neutral beam power, in some cases RF powers) during fast I_p ramp up phase to raise T_e and retard current penetration. In many tokamaks it is found that a plasma with a RS configuration can achieve high confinement [3, 7, 8]. The improvement is established by formation of ITBs. In the case of JT-60U, ITBs are formed in both the electron and ion temperatures and in the electron density [3]. Thanks to the improved confinement due to formation of ITBs, Q_{DT}^{eq} of 1.25 was achieved in a RS plasma with an L-mode edge of I_p = 2.6 MA at B_t = 4.4 T with P_{NB}^{abs} = 12 MW. [5]. In Fig. 1, spatial profiles of n_e, T_e, T_i and q in the discharge at when Q_{DT}^{eq} reached 1.25 are shown. As shown in the figure, ITBs in all the profiles are found to be formed and to locate at near q became minimum.

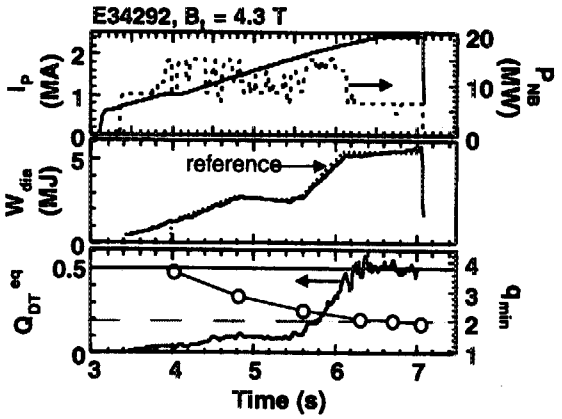

Figure 2: Wave forms of a discharge in which $Q_{DT}^{eq} = 0.5$ was maintained for 0.8 s, I_p, P_{NB}, feedbacked W_{dia} (reference and measured), Q_{DT}^{eq} and q_{min}.

In these high Q_{DT}^{eq} discharges, input NB power was feedback (FB) controlled by monitoring the neutron yield (S_n) in order to avoid a β collapse to reach best performance. However, a discharge was terminated by a β collapse when the minimum value of q (q_{min}) reached about two. Since then FB control based on the stored energy (W_{dia}) measurement was developed and applied in order to extend sustainable period of modest Q_{DT}^{eq}. As the results, Q_{DT}^{eq} of 0.5 was succeeded to be maintained for 0.8 s, which is roughly equal to energy confinement time, in a RS plasma, as shown in Fig. 2. However even in this discharge q_{min} continued to decrease as shown in the bottom box, and the plasma ended up with a β collapse when q_{min} reached about two. The results indicate that towards steady state sustainment of high confinement RS discharge control of q_{min} or the current profile is necessary.

3 Approach towards steady state sustainment of RS plasmas

As shown in the last section, current profile control is indispensable toward realization of a steady state RS plasma. In order to control or maintain the current profile, two approaches have been tried in JT-60U, one is external non-inductive current drive and the other is to utilize the bootstrap current.

3.1 Sustainment of a RS plasma by LHCD

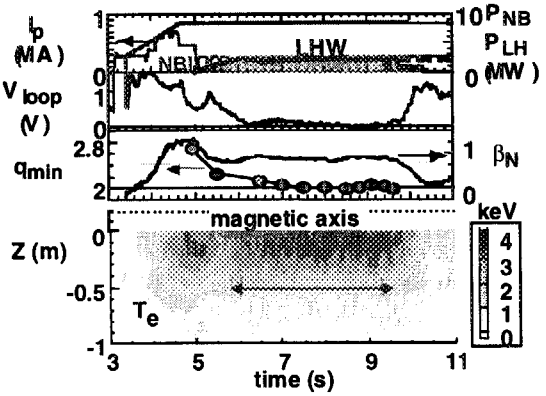

Figure 3: Sustainment of a RS plasma by means of LHCD. I_p, LHCD and NB powers, surface loop voltage, β_N, q_{min} and contour plot of T_e.

On the former approach, lower hybrid current drive (LHCD) has been used and a RS plasma accompanied by ITBs was successfully sustained in quai-steady state with β_N of about unity [9]. Wave forms of the discharge are shown in Fig. 3. Nearly zero surface loop voltage indicates that the current is sustained almost non-inductively, and q_{min} stays around two since the current profile is fixed by the external LHCD. As shown in the bottom box, T_e profile is also fixed.

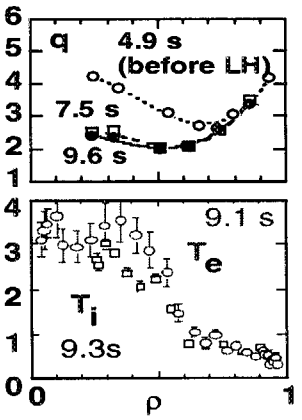

Figure 4: Spatial profiles of q before and during LHCD (top box), and T_e and T_i profiles at the later phase of LHCD.

In Fig. 4 shown are spatial profiles of q at different times and T_e and T_i just before LHCD was turned off. As shown in the figure, the q profile is almost fixed after LHCD was switched on. And even just before the end of LHCD pulse, a steep gradient, in other words ITB, in both the T_e and T_i profiles ITBs are found to be maintained. From the motional Stark effect (MSE) measurement and the code calculation, LHCD driven current fraction was evaluated as 77% of the total current and the rest 23% was driven by the bootstrap current.

3.2 A high bootstrap fraction RS plasma

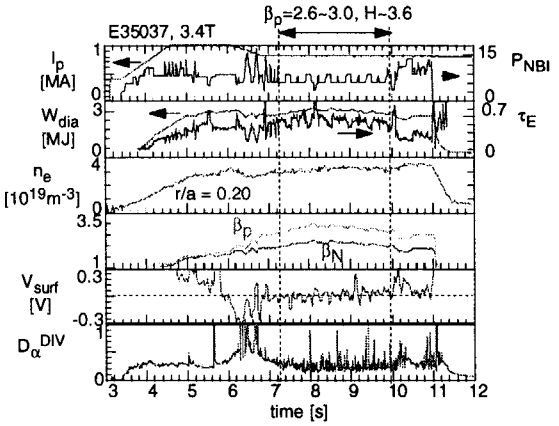

Figure 5: Wave forms of a high bootstrap current fraction RS discharge; I_p, P_{NB}, W_{dia}, τ_e, n_e at $r/a = 0.2$, β_N, β_p, V_{surf} and D_α.

Along with the latter approach, a plasma with high bootstrap current fraction was established and maintained for 2.7 s. In Fig. 5, wave forms of the discharge, at B_t =3.4 T, q at 95% flux (q_{95}) = 8.4 and the triangularity (δ) = 0.37, are shown. In this discharge, only NB heating power was used. As shown in the figure, $W_{dia} \sim 3$ MJ, high β_p of 2.6 - 3.0, $\beta_N \sim 2$ and H-factor of about 3.6 were maintained for 2.7 s by 6 - 7 MW of P_{NB}. As the deuterium α line intensity (D_α) shows the plasma edge stayed in ELMy H-mode. The profiles of T_e and n_e at 8.5 s and the T_i profiles at 7.45, 8.5 and 9.9 s are shown in Fig. 6. The profiles had a steep gradient at $\rho \sim 0.5 - 0.7$ indicating the existence of the ITB and did not change for 2.7 s. The surface loop voltage (V_{surf}) was kept nearly zero indicating that a large fraction of I_p should be sustained non-inductively. From the MSE measurement it could be evaluated that about 80% of I_p could be driven by the bootstrap current and the rest 20% was driven by tangential NBs. Further optimization to raise I_p will be tried.

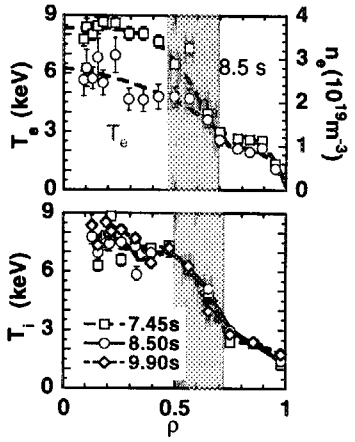

Figure 6: The spatial profiles in the discharge shown in Fig. 5; T_e and n_e at 8.5 s and the T_i at 7.45, 8.5 and 9.9 s.

4 JT-60U ECRF system

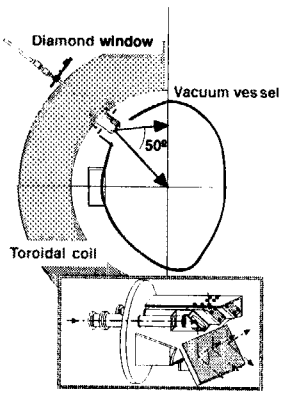

Figure 7: Schematic view of ECRF injection system. The antenna is shown in a bottom box.

A heating and current drive system in the electron cyclotron range of frequency (ECRF), for localized heating and current drive (ECH and ECCD) has been installed on JT-60U and started operation since February 1999 [10]. Major objectives of the ECRF experiments in JT-60U are, suppression of the neo-classical tearing mode (NTM), verification of ECCD application in a fusion plasma, pure electron heating, transport studies such as heat pulse propagation, and so forth. Among them, suppression of NTM is of a great interest, since it limits sustainable β_N in a high performance discharges. Also in the ITER, it is expected that NTM may limit β_N. The power source is a gyrotron of 110 GHz with 1 MW output. Key technological advantages of the gyrotron are the collector potential depression (CPD) technique [11] and a diamond window. The transmission line is about 60 m long and transmission efficiency from the gyrotron to the torus is about 75%. To date, the output power of 1 MW was generated for 2 s and 0.3 MW for 5 s and injected into plasmas (as mentioned above, injected power was 75% of the output

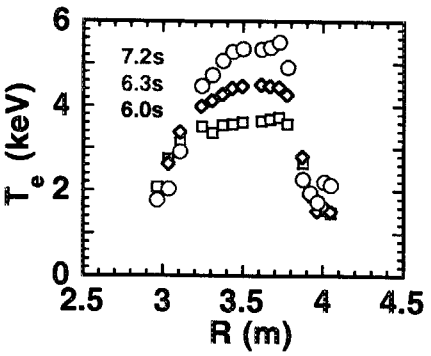

Figure 8: Changes of the T_e profile by fundamental O-mode central ECH in a RS plasma; I_p = 1.2 MA, P_{NB} = 5 MW, R_{axi} = 3.41 m, a_p = 0.83 m, $n_{e0} \sim 3 \times 10^{19}$m^{-3} and $T_{i0} \sim 7$ keV at 6.0 s. ECRF was injected from 6.0 s.

power). One steerable mirror and three antennas are installed in a port located about 45° above the equatorial plane; currently only one out of three has been used. Schematic view of the ECRF injection system and the antenna are shown in Fig. 7. In Fig 8, a change in T_e profile in a RS plasma with fundamental O-mode central heating is shown. Although the central n_e is rather high ($\sim 3 \times 10^{19}$m^{-3}), a clear increase in T_e is found. From the Spring of the year 2000 on, other two gyrotrons will start operation and about 2.3 MW of injected power will be available. Further studies on NTM suppression, ECCD and so on will intensively carried out.

5 Summaries

Recent results in JT-60U experiments towards steady state and confinement improvement are briefly reviewed in this paper. On high performance RS discharges, Q_{DT}^{eq} of 0.5 was succeeded to be maintained for 0.8 s with L-mode edge by utilizing W_{dia} feedback. On steady state RS studies, a RS plasma of $H^{89p} \sim 1.4$ and $\beta_N \sim 1$ was succeeded to be sustained fully non-inductively by LHCD with almost fixed current profile and with the ELMy H-mode edge, a RS plasma of

$H^{89p} = 3.6$ and $\beta_N \sim 2$ has been maintained for 2.7 s with bootstrap current fraction of about 80%. ECRF system of 110 GHz has been installed on JT-60U and started operation since February 1999 for local heating and current drive. Clear increase of T_e in a RS plasma high density central region was demonstrated.

References

[1] M. Kikuchi, Nucl. Fusion **30**, 265 (1990).

[2] S. Ishida, Y. Koide, T. Ozeki *et al.*, Phys. Rev. Lett. **68**, 1531 (1992).

[3] T. Fujita, S. Ide, H. Shirai *et al.*, Phys. Rev. Lett. **78**, 2377 (1997).

[4] Y. Koide, S. Ishida, M. Kikuchi *et al.*, in *Proceedings of the 15th International Conference on Plasma Physics and Controlled Nuclear Fusion Research*, Seville, 1994 (International Atomic Energy Agency, Vienna, 1995), Vol. 1, p. 199.

[5] T. Fujita, Y. Kamada, S. Ishida *et al.*, Nucl. Fusion **39**, 1627 (1999).

[6] Y. Koide, M. Kikuchi, M. Mori *et al.*, Phys. Rev. Lett. **72**, 3662 (1994).

[7] F. M. Levinton, M. C. Zarnstorff, S. H. Batha *et al.*, Phys. Rev. Lett. **75**, 4417 (1995).

[8] E. J. Strait, L. L. Lao, M. E. Mauel *et al.*, Phys. Rev. Lett. **75**, 4421 (1995).

[9] S. Ide, O. Naito, T. Oikawa, T. Fujita, T. Kondoh, M. Seki, K. Ushigusa and the JT-60 team, "LHCD Current Profile Control Experiments towards Steady State Improved Confinement on JT-60U", accepted for publication, Nucl. Fusion.

[10] Y. Ikeda, A. Kasugai, K. Takahashi *et al.*, "Initial results of ECRF operation and experiments in JT-60U", submitted to Fusion Eng. Design.

[11] K. Sakamoto, M. Tsuneoka, A. Kasugai, T. Imai, T. Kariya, K. Hayashi and Y. Mitsunaka, Phys. Rev. Lett. **73**, 3532 (1994).

1-4 Optical Coherence Techniques for Plasma Doppler Spectroscopy

J. Howard, C. Michael, F. Glass and A. D. Cheetham
Plasma Research Laboratory,
Australian National University. Canberra ACT 0200
http://rsphysse.anu.edu.au/prl/MOSS.html

Abstract

A new electro-optically Modulated Optical Solid-State (MOSS) interferometer has been constructed for measurement of the low order spectral moments of line emission from optically thin radiant media. The instrument, which is based on the principle of the Fourier transform spectrometer, has high etendue and is rugged, compact and inexpensive. By employing electro-optical path-length modulation techniques, the spectral information is transferred to the temporal frequency domain and can be obtained using a single photodetector. Specifically, the zeroth moment (brightness) is given by the average signal level, the first moment (shift) by the modulation phase and the second moment (line width) by the modulation amplitude.

1 Introduction

This paper describes an electro-optically modulated solid state (MOSS) spectrometer for general purpose optical plasma spectroscopy [3, 4]. The spectrometer monitors the temporal coherence of an isolated spectral line using polarization interferometric techniques. It is essentially a Fourier transform spectrometer modulated about a fixed delay. The amplitude of the interference fringes produced by the modulation is related to the light temporal coherence while the phase conveys the line centre frequency.

When the line-centre frequency changes (e.g. Doppler drift), the interferogram phase varies (much like an accordion), leaving the envelope unchanged. On the other hand, when the lineshape (e.g. Doppler width) changes, only the coherence envelope is affected, the carrier phase remaining undisturbed. As shown below, this decoupling of first and higher-order spectral moments is one of the more important fundamental advantages offered by time-domain spectroscopic methods applied to spectroscopy of plasmas.

In this paper we discuss a number of experiments based on MOSS technology that are presently installed on the H-1 heliac at the ANU. These include the MOSS spectroscopic camera (see also Michael and Howard - these proceedings), the ToMOSS (Tomographic MOSS) spectroscopy system, the SOFT (Spread-spectrum Optical Fourier Transform) spectrometer and various polarization spectroscopy systems.

2 MOSS spectrometer

The spectrometer is shown in Fig. 1. A narrowband interference filter isolates the spectral line of interest. The first polarizing cube transmits the horizontally polarized component of the filtered plasma light before traversing a birefringent crystal (typically $LiNbO_3$, $L = 25$ mm thick, birefringence $B = 0.1$) whose fast axis is at 45° to the plane of polarization. For light of centre frequency $\nu_0 = c/\lambda_0$, this introduces a phase delay $\phi_0 = 2\pi\nu_0 BL/c = 2\pi\nu_0\tau_0$ between the orthogonal characteristic waves. An additional small delay modulation $\tilde{\phi}_1 = 2\pi\nu_0\tilde{\tau}_1 = \phi_1 \sin(\Omega t)$ of amplitude $\phi_1 = \pi/2$ is imposed by applying an oscillating voltage (typically at tens of kilohertz) along the crystal z-axis. Finally, the light is once more polarized using a beamsplitter cube to allow the independent components to interfere at photomultiplier tubes intercepting the transmitted and reflected beams.

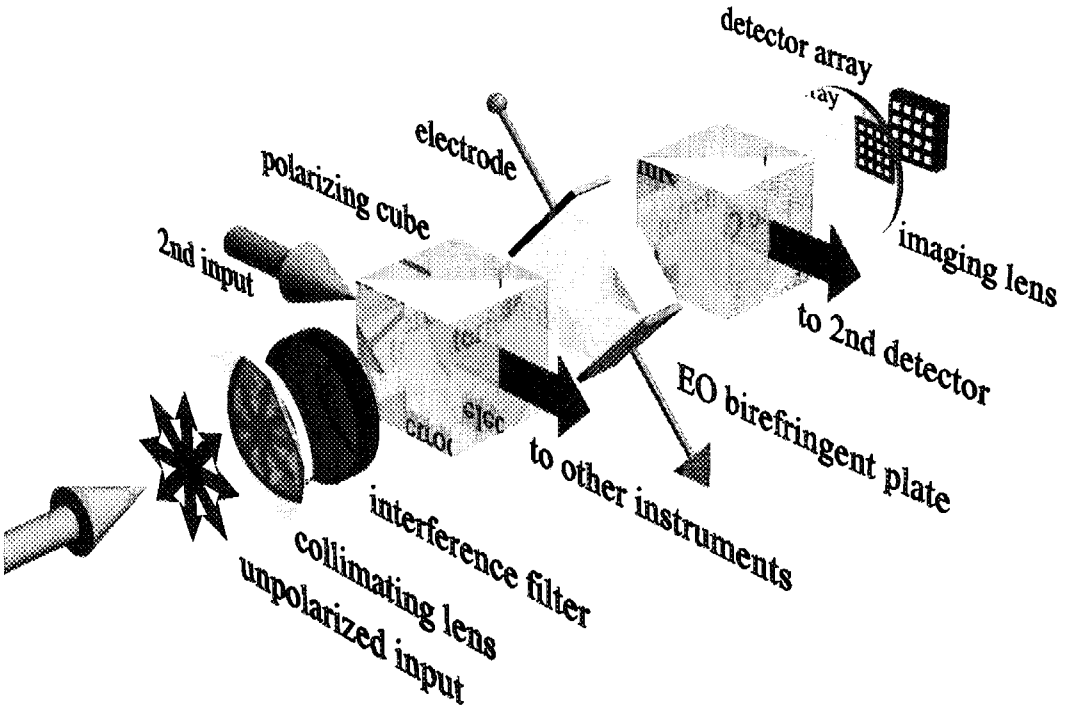

Figure 1: Optical layout for the modulated solid state spectrometer.

The operating principle of the instrument is illustrated in Fig. 2. When the species temperature increases (decreases), the light coherence decreases (increases). This is monitored by dithering the instrument phase electrooptically by $\pm\pi/2$ about the fixed delay (phase) offset. When the centre frequency changes,

the intereferogram expands or contracts and the offset phase changes. This is registered as a change in the ratio of the power in the odd and even harmonics of the applied modulation. Because of the large fixed delay τ_0, even small changes in wavelength can give significant shifts in the interferogram phase.

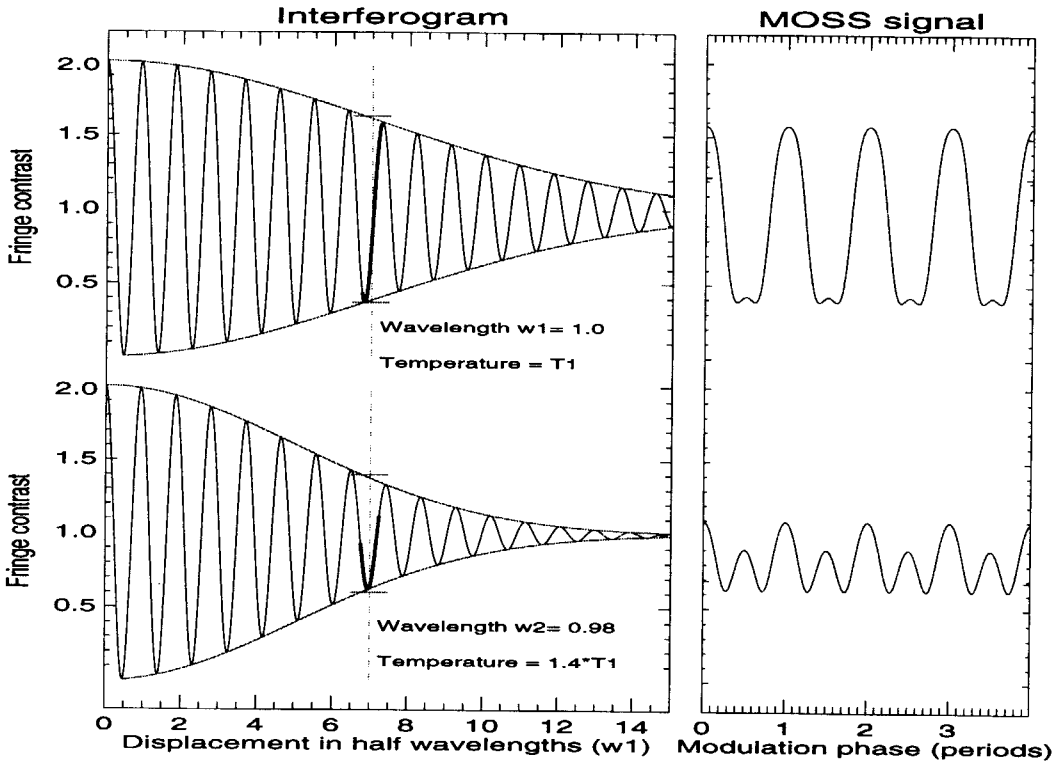

Figure 2: Simulated interferograms showing the effect on the interferogram phase of a change in line centre frequency (exaggerated for clarity). The dashed vertical line corresponds to the delay introduced by the birefringent crystal while the bold section is the portion of the interferogram swept by the electrooptic modulation. The fringe contrast also varies with changes in the temperature of the emitting species.

The intensity at the output port is proportional to

$$S_{\pm} = \int_0^{\infty} I(\nu, \hat{\boldsymbol{l}})[1 \pm \cos(\phi\nu/\nu_0)]\, \mathrm{d}\nu/\nu_0 \qquad (1)$$

where $\phi = \phi_0 + \tilde{\phi}_1$ is the total phase delay introduced by the birefringent crystal and $I(\nu, \hat{\boldsymbol{l}})$ is the line integrated intensity at impact parameter p on the plasma and in the direction $\hat{\boldsymbol{l}}$.

The high voltage modulation of the electrooptic plate(s) is achieved using a function generator, a standard audio-amplifier and step-up transformer (100:1).

This system has been optimized using a detailed circuit model (Cheetham, Michael and Howard - these proceedings) and is capable of operating over a range of frequencies from 0.5 kHz to 100kHz.

The low level signal to the modulator is provided by a PC card (PCI-MIO-16E-4) controlled using a LabVIEW virtual instrument. The card/software also acquires the MOSS signals, processes, displays and archives the data from up to 8 channels in real-time. Other instrumental issues such as sensitivity and resolution are discussed at length elsewhere [2].

3 Doppler Tomography

The most basic optical spectroscopy measures the Doppler shift and broadening of emission from excited plasma atoms and ions. Usually these measurements are line integrated. Though charge exchange recombination spectrosopy achieves a degree of localization, colder edge emission often masks the charge exchange light. Multi-channel measurements and tomographic techniques must then be employed. However, because of the summation of Doppler spectra of varying width and shift along the line-of-sight, spectral-domain (i.e. grating based) systems are not well suited for the inverse procedure.

We consider an inhomogeneous drifting isotropic velocity distribution function $f(\boldsymbol{r}, \boldsymbol{\beta} - \boldsymbol{\beta}_D)$ where $\boldsymbol{\beta}_D(\boldsymbol{r}) = \boldsymbol{v}_D/c$ is the normalized local drift velocity. The integrated measurement along some line L viewing the plasma in direction $\hat{\boldsymbol{l}}$ is given by

$$I(\xi; \hat{\boldsymbol{l}}) = \int_L I_0(\boldsymbol{r})\, g(\boldsymbol{r}, \xi; \hat{\boldsymbol{l}})\, \mathrm{d}l \tag{2}$$

where $\xi = (\nu - \nu_0)/\nu_0$ is a normalized optical frequency coordinate, $I_0(\boldsymbol{r})$ is the local emission spectrum and

$$g(\boldsymbol{r}, \xi; \hat{\boldsymbol{l}}) = \int f(\boldsymbol{r}, \boldsymbol{\beta} - \boldsymbol{\beta}_D)\, \delta(\xi - \boldsymbol{\beta}.\hat{\boldsymbol{l}})\, \mathrm{d}\boldsymbol{\beta}. \tag{3}$$

The delta function selects the part of the velocity distribution f that contributes via the Doppler effect to the optical intensity at normalized frequency ξ.

Taking the Fourier transform of Eq. (3) delivers a remarkable simplification – the contributions from the drift and the body of the distribution separate:

$$G(\boldsymbol{r}, \phi\hat{\boldsymbol{l}}) \equiv \mathcal{F}[g(\boldsymbol{r}, \xi; \hat{\boldsymbol{l}})] = \exp\left(\mathrm{i}\phi\boldsymbol{\beta}_D.\hat{\boldsymbol{l}}\right)\hat{G}(\boldsymbol{r}, \phi\hat{\boldsymbol{l}}). \tag{4}$$

$\hat{G}(\boldsymbol{r}, \phi\hat{\boldsymbol{l}})$ is a central slice of the Fourier transform of $f(\boldsymbol{r}, \boldsymbol{\beta})$ in the direction $\hat{\boldsymbol{l}}$.

As noted above, this Fourier transform can be achieved optically using interferometric techniques. The MOSS spectrometer (interferometer) measures the complex coherence whose modulus (envelope) is independent of the spatially varying drift $\boldsymbol{\beta}_D$:

$$|\gamma(\phi; \hat{\boldsymbol{l}})| = \int_L I_0(\boldsymbol{r})\, \hat{G}(\boldsymbol{r}, \phi\hat{\boldsymbol{l}})\, \mathrm{d}l. \tag{5}$$

The inversion of Eq. (5) gives the isotropic but inhomogeneous distribution function $f(\boldsymbol{r}, \xi)$[4]. For a locally Maxwellian velocity distribution, this becomes:

$$|\gamma(\phi; \hat{\boldsymbol{l}})| = \int_L I_0(\boldsymbol{r}) \exp[-T_S(\boldsymbol{r})/T_C] \mathrm{d}l \tag{6}$$

where $T_S(\boldsymbol{r})$ is the species temperature distribution and T_C is a "characteristic temperature" set by the interferometer phase delay ϕ_0 and species mass m_S:

$$kT_C = \frac{1}{2} m_S v_C^2 \qquad v_C = \frac{2c}{\phi_0}. \tag{7}$$

Tomographic inversion of Eq. (6) gives $T_S(\boldsymbol{r})$.

The imaginary part (phase) of the interferogram is given (to first order in small quantities) by

$$\Im\left[\gamma(\phi; \hat{\boldsymbol{l}})\right] = \phi_0 \int_L I_0(\boldsymbol{r})\, \hat{G}(\boldsymbol{r}, \phi\hat{\boldsymbol{l}})\, \boldsymbol{\beta}_D . \mathrm{d}\boldsymbol{l} \tag{8}$$

where $\boldsymbol{l} = \hat{\boldsymbol{l}}\mathrm{d}l$. Observe that the small Doppler shift component is amplified by the fixed phase delay ϕ_0. Equation (8) is a vector field line integral whose inversion gives the vorticity of the field $I_0 \hat{G} \boldsymbol{\beta}_D$. Under conditions of LTE, we write $\hat{G} \equiv \zeta_S = \exp[-T_S(\boldsymbol{r})/T_C]$. Under some conditions, it is possible to reconstruct the component of the flow-field vector potential that is normal to the measurement plane [1].

4 MOSS Doppler measurements in H-1NF

If we ignore the spatial integration and assume LTE, Eq. (1) gives the signal at the spectrometer ports as

$$S_\pm = I_0 \pm I_0 \zeta \cos[\phi_0(1 + \beta_D) + \phi_1 \sin(\Omega t)] \tag{9}$$

where the total fringe visibility (coherence envelope) $\zeta = \zeta_I \zeta_S$ includes an instrumental component analogous to the familiar slit function for grating spectrometers. The instrumental fringe contrast ζ_I is determined by the collected light solid angle and optical imperfections, and can be represented by the factor $\zeta_I = \exp(-T_I/T_C)$, where T_I is the instrument "temperature". It is apparent that the source temperature T_S can be obtained from the measured fringe contrast via a simple subtraction of exponents proportional to the measured and instrumental temperatures rather than requiring the usual deconvolution correction for the instrument function.

Uncertainty in the instrumental phase offset ϕ_0 is equivalent to a wavelength calibration error for grating instruments. Generally, it is difficult to absolutely determine the phase shift ϕ_0 corresponding to a given wavelength ν_0. Estimates

of the Doppler drift β_D are usually obtained with respect to the measured phase ϕ_0 at the commencement of the discharge.

The unknown quantities I_0, β_D and T_S can be recovered numerically from $S_\pm$ synchronously sampled at times $t = 0, T/4, T/2, 3T/4, \ldots$ where $T = 2\pi/\Omega$ is the modulation period. The instrument is "optimum" in the sense that all available photons are used simultaneously to determine only the three unknown quantities I_0, β_D and T_S.

To demonstrate the instrument performance, we show temperature and flow data for an rf heated (7MHz, 80kW max) argon discharge in a low-shear magnetic configuration close to the 3/2 resonance. ArII light at 488nm is collected from a cylindrical plasma volume of diameter $\sim$ 30 mm with axis parallel to the major axis of the bean-shaped plasma cross-section. The viewing chord can be translated across the plasma poloidal cross-section on a shot-to-shot basis. The system has been used for study of ion dynamics during confinement transitions and during power modulation experiments.

The observed ion temperatures are in the range 10-100 eV and match well the dynamic range for a $LiNbO_3$ crystal of thickness 25mm (T_C = 70 eV). The instrument temperature, measured using an expanded argon ion laser beam at 488nm is $\sim 20 - 25$ eV and arises from mainly imperfections in the birefringent plate. The estimated component due to beam divergence is less than a few eV.

By virtue of its high light throughput (in our case, $\sim$ 40 times greater than for an equivalent-resolution grating instrument) and direct sensitivity to low order spectral moments, the MOSS spectrometer is especially well suited to measurements that require high time resolution such as for the observation of fluctuations and coherent modes.

Figure 3 shows the temporal evolution of various diagnostic signals for a discharge which exhibits a spontaneous transition from low to high confinement at t = 13 ms. The first two traces are the plasma line-density and stored energy. The MOSS quadrature sampled signal for a chord at position 20 mm outside the magnetic axis is the third signal (four independent traces are shown). The following three traces are the inferred zeroth moment $\langle I_0 \rangle$, ion temperature $\langle T_s \rangle$ and flow velocity $\langle v_D \rangle$, where angle brackets denote line-averaged quantities. Since the absolute phase for the unshifted spectral line is not calibrated, the absolute flow velocity is not significant. However, note that the change in flow velocity throughout the transition is small ($<$ 500 m/s). This is also true at other measurement positions. The final trace is ArI atomic emission intensity showing a slight decrease at the time of the transition. The ion temperature has not been corrected for the instrument temperature, while the observed noise levels for the ion temperature and flow are consistent with estimates based on the light signal to noise ratio.

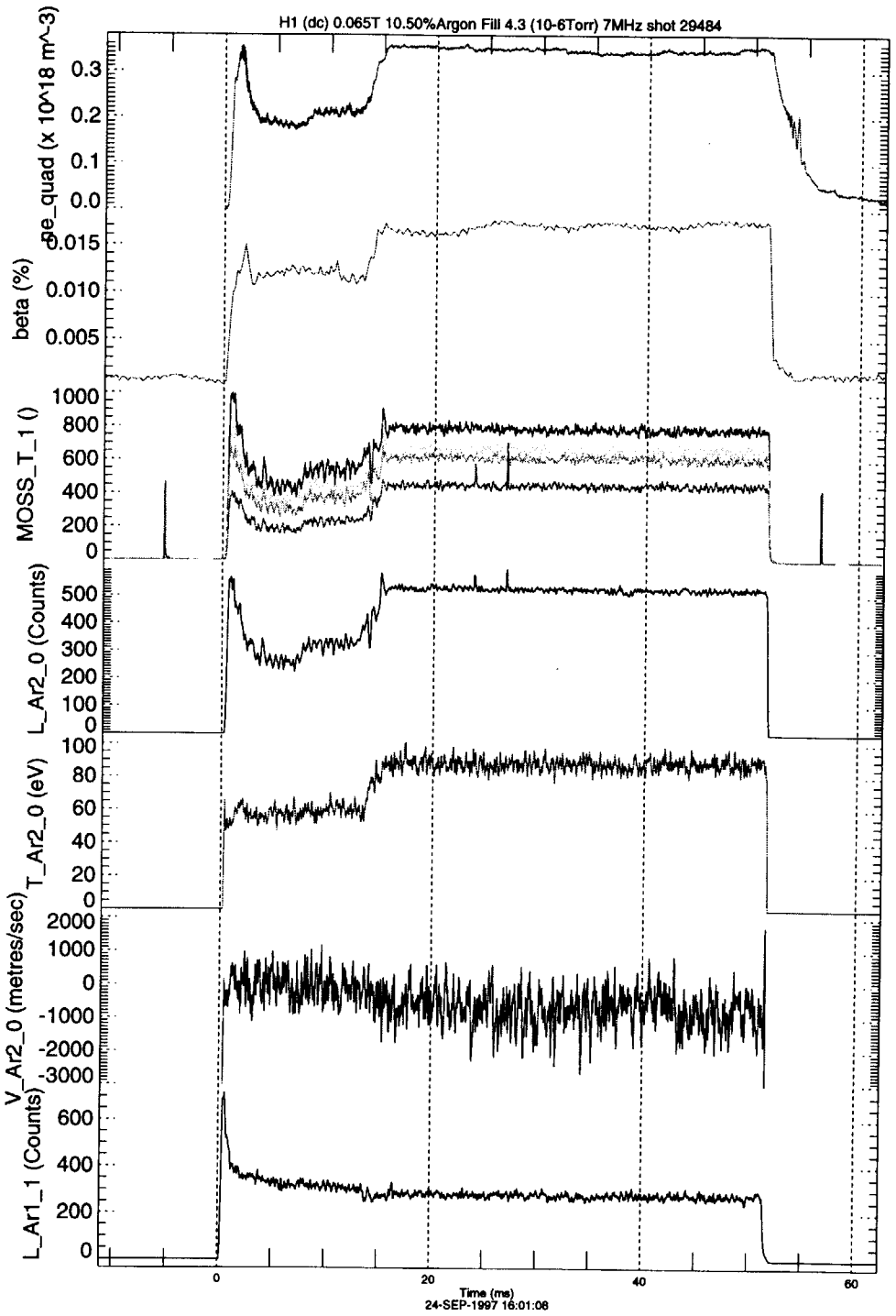

Figure 3: Plot showing temporal evolution of plasma parameters during spontaneous transition from low to high confinement at $t = 13$ ms. From top to bottom: Line averaged density, plasma stored energy, quadrature sampled MOSS light signal at impact parameter -20 mm , inferred light intensity, ion temperature, flow velocity and ArI atom light emission intensity.

4.1 Spectroscopic Camera

It is natural to extend the MOSS spectrometer to allow for multiple spatial channels. Because the information is contained in the temporal frequency domain, it is possible to use the camera for truly two-dimensional plasma spectral imaging with high time-resolution. Each spatial channel requires its own detector, and the associated signals must be separately acquired. Commercially available multi-anode photomultiplier detectors (MAD) are well suited for this application. We are constructing two cameras. One views the plasma directly using a 16 element linear detector array (Michael and Howard - these proceedings). The second camera utilizes an 8×8 MAD array to process light input from an array of 55 lens-coupled optical fibres as described below. Issues such as instrument contrast and field-of-view are discussed in the companion paper by Michael and Howard.

4.2 ToMOSS

The Tomographic MOSS (ToMOSS) spectroscopy experiment is designed to obtain detailed tomographic reconstructions of edge flow fields and temperature distributions in the H-1 heliac. A large diameter ($\sim$ 800mm) rotatable stainless steel ring that encircles the plasma in a poloidal cross-section, is used for mounting 5 independent modules each containing 11 lens coupled optical fibres for collecting plasma light emission along parallel chords separated by $\sim$ 20mm. Fig. 4 shows the mounting ring, supporting frame and the five sets of viewing chords superimposed on the plasma cross-section. A photograph of one of the optical modules showing the collecting lenses is given in Fig 5.

The optical fibres drape around the edge of the wheel and are shielded from the plasma. The lenses can be rotated away from the plasma region when not in use. An array of narrow (4mm) fluorescent tubes are located in the viewing cross-section (above the plasma region) for calibrating the relative channel sensitivities. The fibres exit the H-1 vacuum chamber via rubber O-ring seals and terminate at a patch panel. The rotatble ring, which has been recently installed, is driven by a stepper motor outside the vacuum vessel under CAMAC control. Light from the 55 channels will be fibre coupled to an imaging MOSS camera and the parallel signals acquired via CAMAC.

4.3 Spread-spectrum methods - the SOFT spectrometer

A generalization of the MOSS spectrometer that utilizes a number of birefringent electrooptic plates mutually aligned at 45° and placed between crossed or parallel polarizers has been constructed and tested. The Spread-spectrum Optical Fourier Transform (SOFT) Spectrometer allows simultaneous measurements of the coherence enevlope of a narrowband spectral feature at a multiplicity of

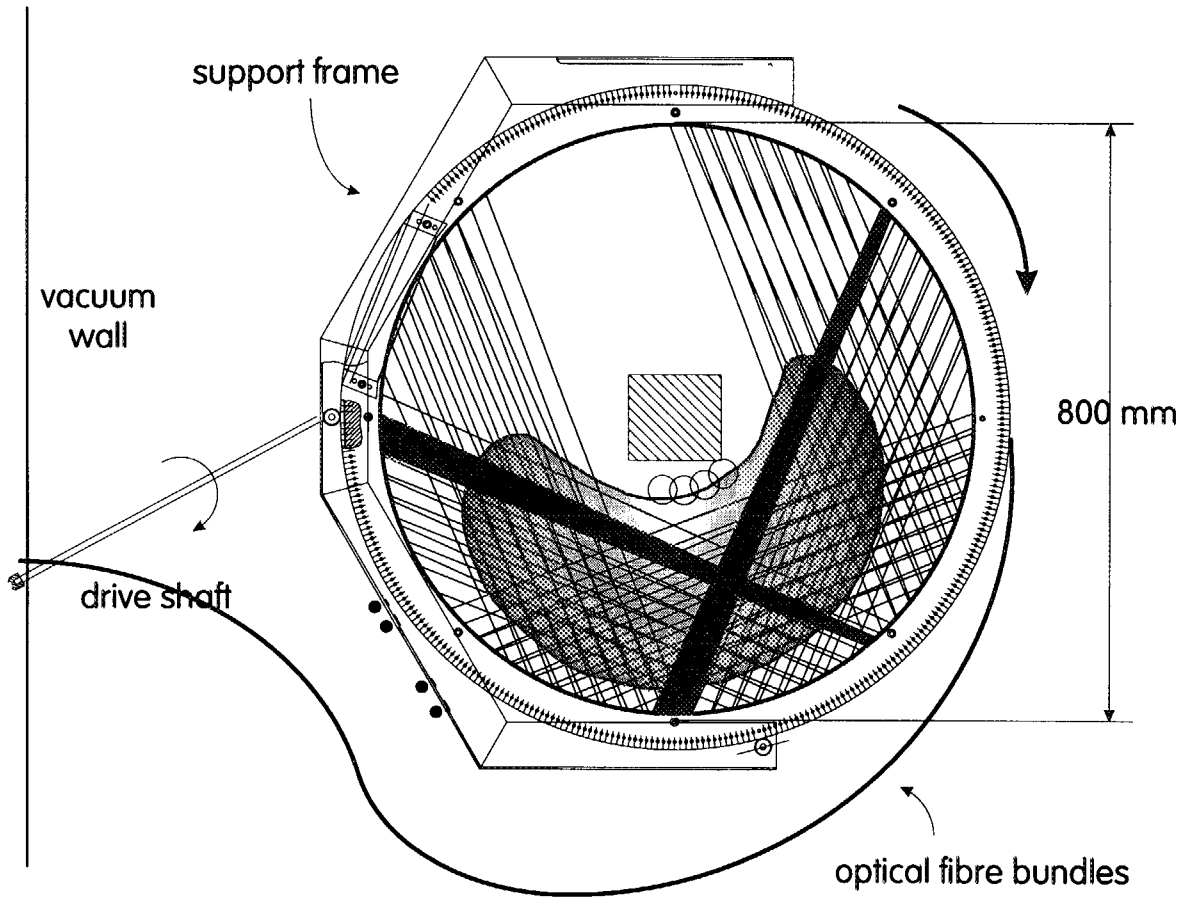

Figure 4: Schematic drawing of ToMOSS optical ring and support structure showing plasma region and viewing chords. Two chords have been shaded for clarity.

delays. As its name suggests, the information is now encoded across a series of harmonics of the common sinusoidal drive voltage applied to the electrooptic crystals.

A representative 3-crystal layout for the SOFT spectrometer is shown in Fig. 6. The three crystals give rise to six independent fixed delay modulated interferometers. Because the modulation indices ϕ_{1i} are in the same ratio as the delays ϕ_{0i}, the larger the delay, the greater is the modulation depth and the higher in frequency are the generated harmonic carriers.

The interferogram can be processed numerically using a series of bandpass filters centred on the respective carriers and having a bandwidth determined by

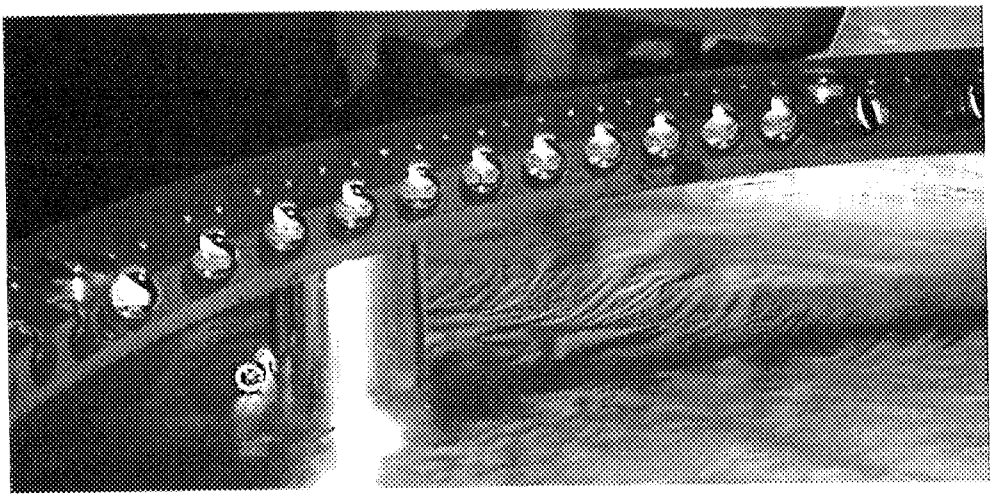

Figure 5: Photograph of lens-coupled fibre module. The lenses are 5mm in diameter. Five such modules are mounted on the carrier ring at intervals of 45°.

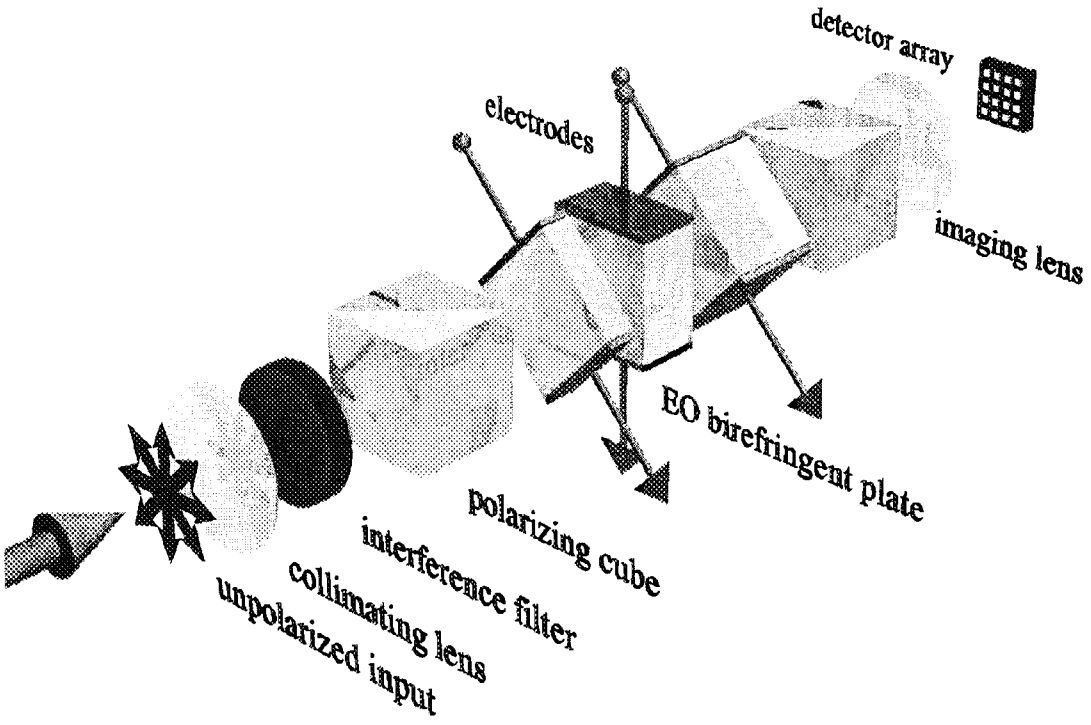

Figure 6: Diagram showing the relative orientation of the polarizers and birefringent crystals for a 3-crystal SOFT spectrometer.

the plasma properties and the modulation frequency. Inverse FFT recovers a set of time vectors which can be unwrapped to extract 12 independent pieces of information pertaining to the spectral line shape. The drive voltage should be sufficient to produce a modulation amplitude of at least $\pi/2$ radians for the interferometer having the least phase delay offset to ensure data inversion with good condition number. The SOFT spectrometer is ideal for the study of non-thermal or complex spectra or for effectively extending the dynamic range of the MOSS spectrometer.

Acknowledgements

It is a pleasure to acknowledge technical assistance provided by Mr J. Wach, Mr M. Blacksell and Mr. Rob Davies.

References

[1] J. HOWARD. Vector tomography applications in plasma diagnostics. *Plasma Phys. Control Fusion*, 38:489–503, 1996.

[2] J. HOWARD. Electro-optically modulated solid state spectrometer for plasma flow and temperature diagnostics. *Rev. Sci. Instrum.*, page In Preparation, 1999.

[3] J. HOWARD. Modulated optical solid-state spectrometer applications in plasma diagnostics. *Rev. Sci. Instrum.*, 70:368–371, 1999.

[4] J. HOWARD. Doppler spectroscopy of extended radiating media. *J. Opt. Soc. Am. A*, 1999 (submitted).

1-5 MOSS spectroscopic camera for imaging time resolved plasma species temperature and flow speed.

Clive Michael and John Howard

Plasma Research Laboratory,
Research School of Physical Sciences and Engineering,
Australian National University,
Canberra, A.C.T. 0200
Australia

1. Introduction

The MOSS (Modulated Optical Solid-State) spectroscopic camera has been developed for temporal and spatial measurements of the temperature T_s and flow speed V_s of plasma ions and neutrals from the Doppler broadening of transition radiation. It is a modulated, fixed delay Fourier transform spectrometer [1,2], which measures the three lowest spectral moments of a given spectral line (quantities related to the light intensity, centre frequency, and line width). It is able to resolve the relative direction of flows and can provide information about the poloidal plasma rotation. In addition, it can spatially resolve the average temperature along its viewing chords, which, subject to the assumption that flux surfaces are isotherms, can be tomographically unfolded to yield the temperature profile $T(\rho)$, where ρ is the flux surface label.

As opposed to a single channel MOSS spectrometer, the camera images light from spatially distinct regions within a plasma, through a single instrument, onto an array of light detectors. It can be used for 2-D imaging of the plasma temperature and flow profile. As compared to grating spectrometers, the MOSS Camera has a light-collecting ability (etendue), orders of magnitude higher because it uses large aperture optics instead of a thin slit. Gathering more light means that it has improved signal-to-noise ratio and much better time resolution. In fact, in most cases, the limiting factor of the etendue is not the spectrometer but the light collection optics. However, there are limits on the spectrometer's etendue, and understanding these limits defines certain design considerations.

A MOSS camera has been installed on the H-1NF Heliac in Canberra, Australia. It is to be used, in conjunction with other diagnostics, for measuring the ion thermal diffusivity by modulating the plasma heating source and measuring the spatial profile of corresponding modulations in ion temperature.

A camera can be used to obtain spatial resolution in other spectroscopic applications, such as Zeeman effect and motional Stark effect measurements of the orientation and magnitude of a magnetic field, and the SOFT system [1,2] for measuring non-thermal distribution functions.

2. MOSS spectroscopy

The MOSS spectrometer is a modulated fixed delay polarisation interferometer, shown in figure 1. A polariser first selects a plane polarisation state from the incident light. A birefringent, electro-optic Lithium Niobate ($LiNBO_3$) crystal, whose fast axis is oriented at 45° to first polariser resolves this polarisation state into two components, and introduces a fixed mutual delay of N wave periods.

$$N = \frac{LB}{\lambda} \tag{1}$$

where L is the length of the crystal, B is its birefringence and λ is the wavelength of the atomic transition.

This delay defines the spectral resolution, which defines the measurable range of temperature and flow speed. A final polarising beam splitter, whose polarisation axis is the same as the first polariser is used to mix these two wave components together. It then sends conjugate signals out -

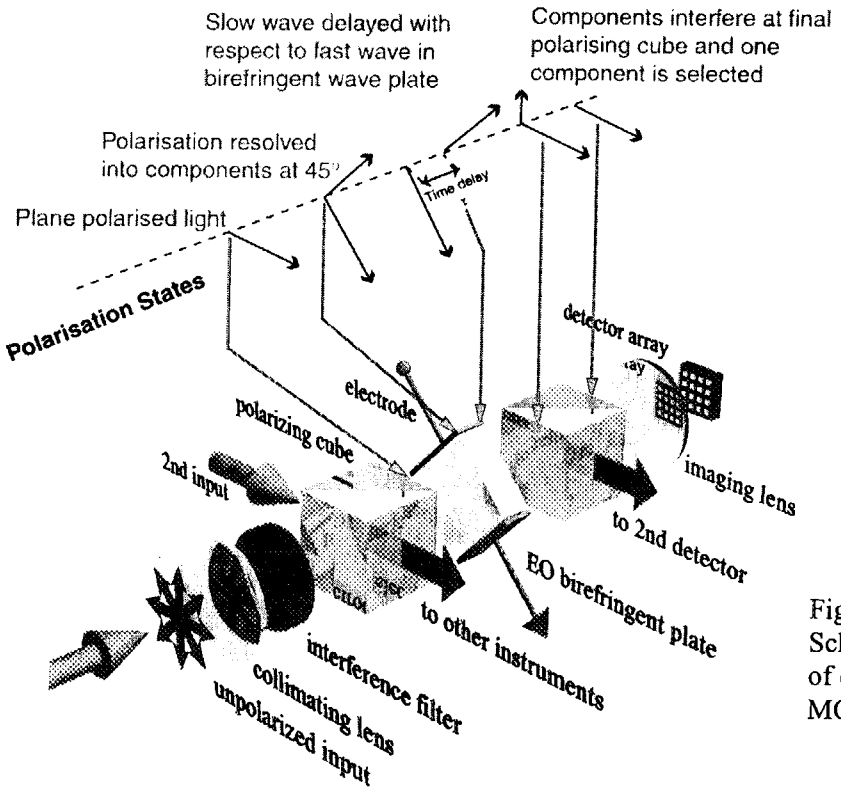

Figure 1: Schematic layout of optics of MOSS Camera.

the transmit and reject ports respectively. In addition, a narrow band (~1nm) interference filter is used to select the spectral line corresponding to the atomic transition of interest.

The electro-optic crystal has the property that the birefringence can be modified by applying a electric field across it, so that $B = B_0 + C\,E$. E is the applied electric field strength, B_0 is the birefringence with no electric field, and C is a constant specific to the crystal and the orientation of its axes. In this way, the delay N is modulated in time by applying a sinusoidal AC voltage to electrodes across the fast axis of the crystal.

$$N=N_0+N_1\sin(\Omega t)$$

where typically, $N_0 \sim$ 1000-5000, and N_1 is ¼.

For many spectral lines in a high temperature plasma, Doppler broadening dominates the fine structure, and so the centre frequency shift ν_D and broadening σ are related to the species flow velocity V_s and temperature T_s, if the distribution function is Maxwellian (line shape is Gaussian):

$$\frac{\nu_D}{\nu_0}=\frac{V_s}{c}$$
$$\frac{\sigma}{\nu_0}=\sqrt{\frac{k_B T_s}{m_s c^2}} \qquad (2)$$

where ν_0 is the frequency of the atomic transition.

The intensity at the output port is an interferogram characterised by the quantites I_0 (the light intensity), fringe contrast, ζ, and fringe phase ϕ.

$$I=\frac{I_0}{2}(1+\zeta\cos\phi)$$

The variation in phase is related to the species flow velocity V_s, through the Doppler frequency shift. Similarly, the measured contrast ζ is related to the plasma temperature T_s through Doppler broadening.

$$\zeta = \zeta_{inst} e^{-\frac{T_s}{T_{crystal}}} \text{ and}$$

$$\phi = 2\pi(1 + \frac{V_s}{c})N_0$$

The fringe contrast ζ and phase ϕ, which are sufficient to determine T_s and V_s, are measured from I(t). They are determined from the relative amplitude of the zeroth, first and second harmonics of Ω [1,2].

The instrument function, which is built in through the quantities $T_{crystal}$, ζ_{inst} and N is analogous to that of a grating spectrometer. $T_{crystal}$, which defines the measurable temperature range, depends on N_0 (which depends on crystal thickness): $T_{crystal} = \frac{mc^2}{kN_0^2}$ and is analogous to the number of lines per mm of the grating. The range of path lengths for rays entering the MOSS (ΔN_0) is responsible for a false measurement of line broadening, which reduces the fringe contrast, by multiplying it by ζ_{inst}. N_0 is the phase calibration, analogous the frequency calibration of grating spectrometers. Although this is determined from known parameters, the length of the crystal, its birefringence, and the wavelength of the line being examined, these quantities are not known accurately enough to determine N. In particular, the birefringence is a sensitive function of temperature, and can vary over the timescale of minutes, so N_0 it must be measured

3. The MOSS camera

The MOSS Spectrometer can be easily extended to imaging applications, because only a single light detector per spatial channel is required; time-resolved spectral information is carried at harmonics of the modulation frequency Ω.

A schematic diagram of the imaging optics of the MOSS camera is shown in figure 2. It images light from the object plane (the plasma) to the image plane (a detector array) through a MOSS spectrometer with two lenses, a collimating lens and an imaging lens. The collimating lens collimates rays from the object plane, so that they are quasi-parallel as they pass through the MOSS optics. The imaging lens then focuses these rays down onto the detector array. Each detector on the detector array is of finite spatial extent; which determines the spatial resolution in the plasma, the amount of light gathered per detector, and the angles of the off-axis rays. The larger each detector element, the larger the range of angles between the axis and each ray, as the rays pass through the electro-optic crystal, as shown in figure 3.

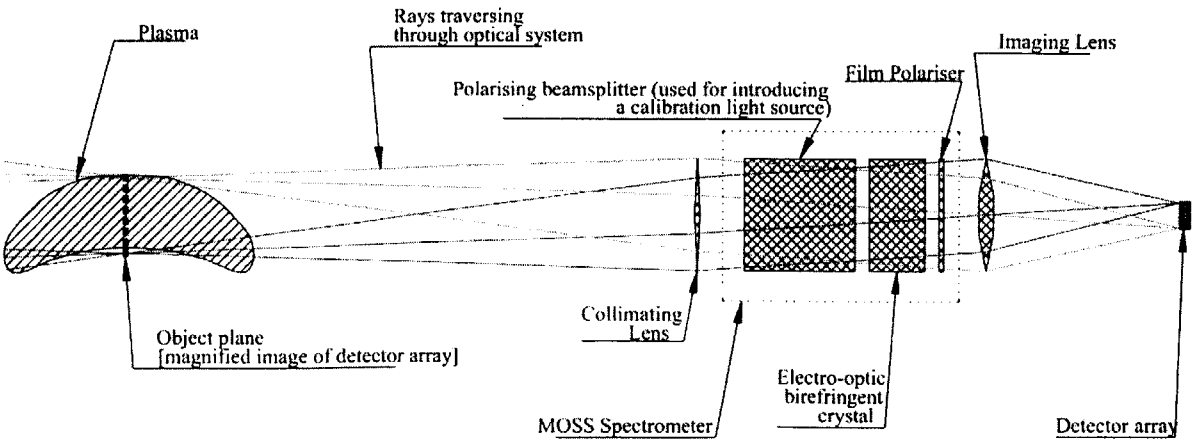

Figure 2: Ray diagrams and imaging optics of MOSS camera [plasma is not to scale]

4. Design considerations for imaging optics

In order to maximise the signal-to-noise ratio, the amount of light gathered per detector must be maximised, and ζ_{inst}, which determines the fraction of light contributing to spectral information, must be close to unity.

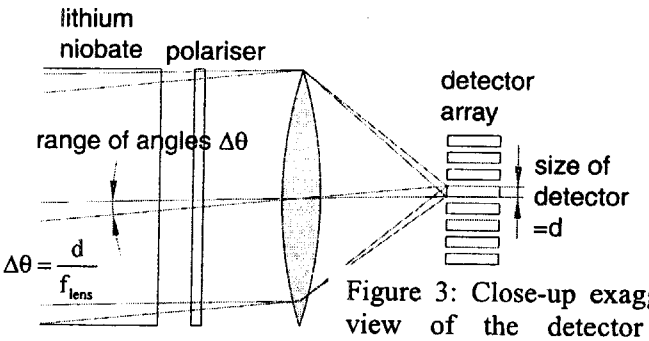

Figure 3: Close-up exaggerated view of the detector array showing that rays arriving at a detector element are not parallel through the crystal; they have a finite range of angles.

ζ_{inst} depends on the spatial and angular variation of N_0 for each ray, and can be calculated by equation 3.

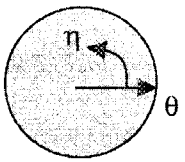

$$\zeta_{inst} = \frac{\left| \iint_{P\,A} e^{i2\pi N_0(x,y,\theta,\eta)} dx\, dy\, \theta d\theta\, d\eta \right|}{\iint_{P\,A} dx\, dy\, \theta d\theta\, d\eta} \qquad (3)$$

where ray's position is (x,y), and angles are (θ,η). θ is the angle of each ray through the electro-optic crystal subtended between the ray and the central axis, and η is the azimuth with respect to the fast axis (shown by arrows in the above picture). The integration region P is the entire surface of the lithium niobate crystal, and A is the region in angular space of rays arriving at a detector. A simple calculation of the instrument contrast as a function of the range of path lengths (ΔN_0) is shown in figure 4.

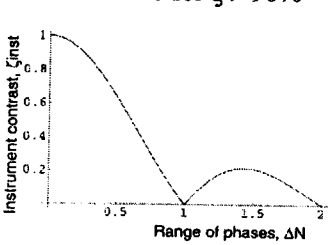

Figure 4: Instrument contrast variation with range of phases

The instrument contrast can be separated out as $\zeta_{inst} = \zeta_{crystal}\,\zeta_{det}$, where $\zeta_{crystal}$ is the contrast due to spatial variations of N_0, and ζ_{det} is due to the range of angles collected at each detector element.

$$N_0(\vec{r}) = N_0 + N_{spatial}(x,y) + N_{angle}(\theta_x,\theta_y)$$
$$\zeta_{inst} = \zeta_{crystal}\,\zeta_{det}$$

In order for $\zeta_{crystal}$ to be close to unity, $\Delta N_0 << 1$. Therefore the Lithium Niobate must be made to very stringent specifications of spatial homogeneity of B_0, the surface roughness and degree of parallelism between faces. In practice, the best crystals obtainable have $\zeta_{crystal} = 0.9$ (for N_0=5000, 25mm thickness at 488nm), and 0.98 (for N_0=1000, 5mm thickness at 488nm).

For $\zeta_{det} \to 1$, the range of angles of each ray collected by each detector element must be small, $\Delta\theta \to 0$, $\Delta\eta \to 0$; this is why the rays are collimated through the MOSS optics. However, due to the finite spatial extent of each detector element, the rays collected have a non-zero range of angles, which degrades ζ_{det}.

The variation of N_0 with angles θ,η is

$$N_0 = \frac{LB}{\underset{N_e}{\lambda}}\left(1 + \frac{\sin^2\theta}{2n_o}\left(\frac{\cos^2\eta}{n_e} - \frac{\sin^2\eta}{n_o}\right)\right) \qquad (4)$$

where n_e and n_o are the two refractive indices.

This function has a saddle point at the origin. Along the axis η=0, the delay increases, along η=90° it decreases and along $\eta = \pm\tan^{-1}(\sqrt{\frac{n_e}{n_o}}) \approx 45°$ (since $n_e/n_o \sim 1$), there is no variation. The interference pattern corresponding to this phase variation is a contour plot of N_0. A photograph of

Figure 5: Photograph of interference pattern

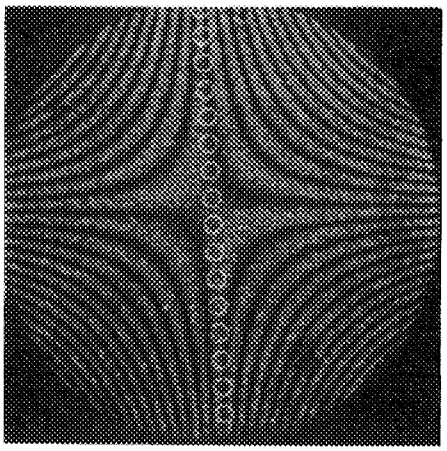

this pattern as it appears at the focus of the imaging lens is shown in figure 5. The circles indicated in the diagram represent the placement of a line of circular detector elements.

The following approximate calculation illustrates the factors contributing the degradation of ζ_{det}. The range of angles gathered by a single detector element is : $\Delta\omega_{detect} = \frac{d_{detect}}{f_{imaging\ lens}}$

and the characteristic angular distance $\Delta\omega$ (not necessarily directed towards the centre) for ΔN_0=1 is approximately: $\Delta\omega_{fringe} \approx \frac{1}{N_c n_0 n_e \sin\theta}$. Therefore,

$$\Delta N_0 = \frac{\Delta\omega_{detect}}{\Delta\omega_{fringe}} \approx \frac{d_{detect} N_c n_0 n_e \sin\theta}{f_{imaging\ lens}} \qquad (5)$$

This shows that the contrast degrades (ΔN_0 increases) by increasing $\Delta\omega_{detect}$ ($d_{detect}/f_{imaging\ lens}$), the spectral resolution N_0 and θ, the angle off axis at which the detector is located. This trend can be understood from figure 6. The decrease with angle is due to the fringes becoming closer together towards the edge, and defines a circular boundary in which detectors can be placed. This is defined as a maximum angle θ_{view} : $\zeta_{det}(\theta_{view}) = 50\%$.

The angle spanned by each detector determines what fraction of a fringe (ΔN) is gathered. It also scales with N_0; higher resolution results in less detectors possible.

ζ_{det} varies very little with η, even though the phase varies dramatically. This is because the width of the fringes remains the same; only the direction of phase variation changes (according to the fringes' hyperbolic shape). This change in direction does not matter for a circular detector as it has no preferred directionality.

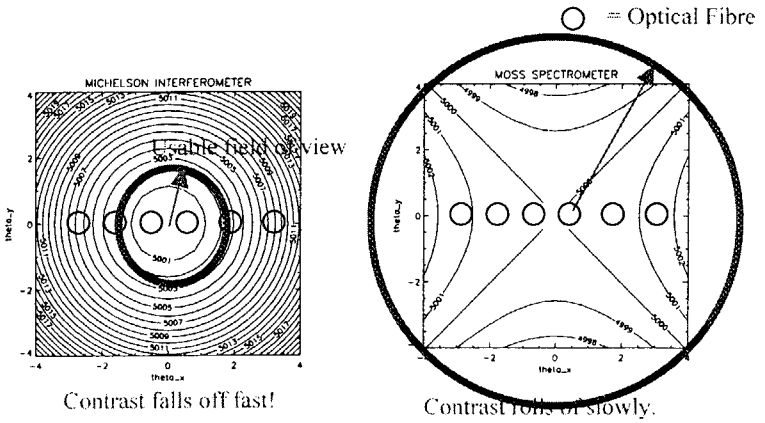

Figure 6: Interference fringe patterns for Michelson interferometer and MOSS spectrometer.

The interference pattern differs from that of a Michelson interferometer, which has circular fringes. The variation with η is because of the birefringence variation. This is an advantage, because detectors can be aligned along the axis with no phase variation. $\Delta\omega_{fringe}$ is larger, because rays bend towards the normal in the crystal, which means that the field of view θ_{view} is approximately 2 times bigger because the refractive index is very high (n_e=2.2 and n_o=2.3).

Field Widening

In some instances, θ_{view} is not sufficient to image the entire plasma region. Instead of decreasing ω_{fringe} (by decreasing the focal length of the imaging lens, for example), which would decrease the amount of light gathered, it is possible widen θ_{view} by using two lithium niobate crystals and a ½ wave plate [3].

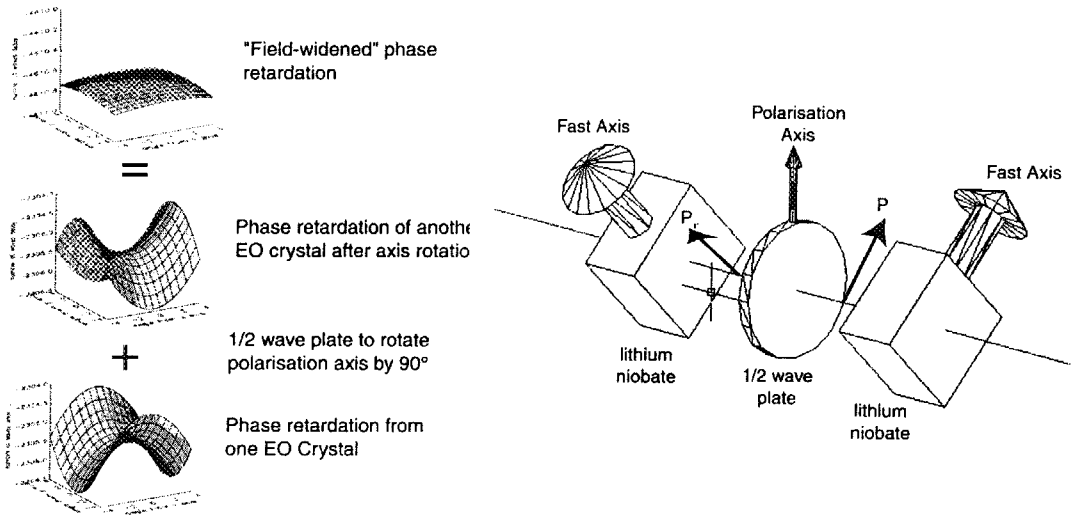

The set up is shown in the above figure. Two crystals of identical size are placed in line with their fast axes perpendicular to each other. A ½ wave plate is placed in between with its polarisation axis at 45° to each crystal's fast axis. This rotates the polarisation state of the light from the first crystal by 90° as it enters the second crystal. The resultant phase delay N_{wide} is given in equation 6

$$N_{wide}(\theta,\eta) = N(\theta,\eta) + N(\theta,\eta+90°) = N_c\left(2 + \frac{\sin^2\theta}{2n_0}\left[\frac{1}{n_0} - \frac{1}{n_e}\right]\right) \qquad (6)$$

This has a much weaker variation than for one crystal only; this is because the two phase delay profiles (with angle), which are saddle shapes, almost cancel each other out. The axis along which the phase was increasing for the first crystal now becomes the axis along which it decreases for the second crystal. The resultant phase variation is only due to the difference between n_0 and n_e. This is pictorially explained in the above figure.

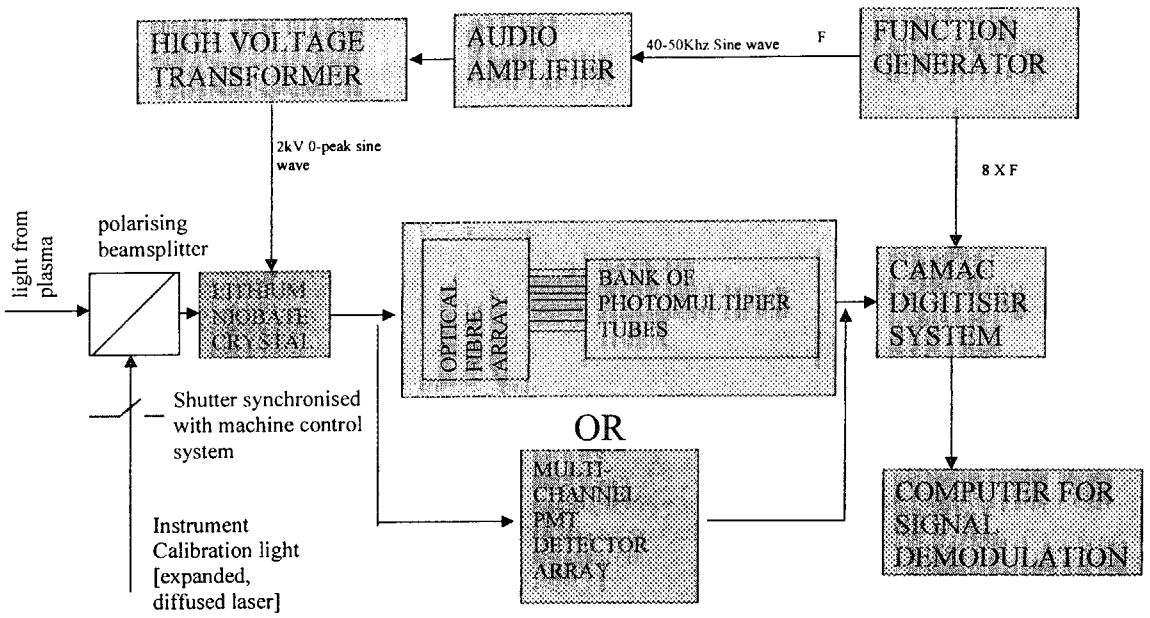

5. MOSS Camera on H-1NF

The MOSS camera installed on H-1NF has been designed to optimise the etendue and still maintain a low instrument temperature. It images a transverse cross-section of the plasma, along its long axis, for symmetry reasons (see figure on next page). Although 2-D imaging is possible with the camera, access through the toroidal field coils permits only a 1-D view of the plasma. The vacuum vessel of H-1NF encompasses the field coils and many other diagnostic systems. In order to place the camera as close as possible to the plasma, and hence maximise the collection solid angle, it is placed just outside the vacuum vessel. Mirrors in the vacuum vessel direct the line of sight along the long axis of the plasma, and a viewing dump is located behind so that no stray light is gathered. All optical elements in the camera have 40-50mm apertures.

The instrument temperature, or contrast, relative phase and intensity calibration for each channel is achieved by introducing a narrow-band light source into the 2nd input port of the first polarising beam splitter. This is simply an expanded, diffused laser beam, and is brought in by an optical fibre.

The instrument calibration is carried out before or after each plasma shot by using a shutter which is synchronised to the machine control system. This is necessary as the phase and contrast can vary over time scales of minutes due to temperature variations.

The detector array consists of a line of optical fibres, which transmit the light to a bank of photo-multiplier tubes. However, another solution is to use a multi-channel photo-multiplier tube [5], saving cost and instrumentation overhead, as only one high voltage bias is required for many output channels, and the cost is comparable to a single photo-multiplier tube.

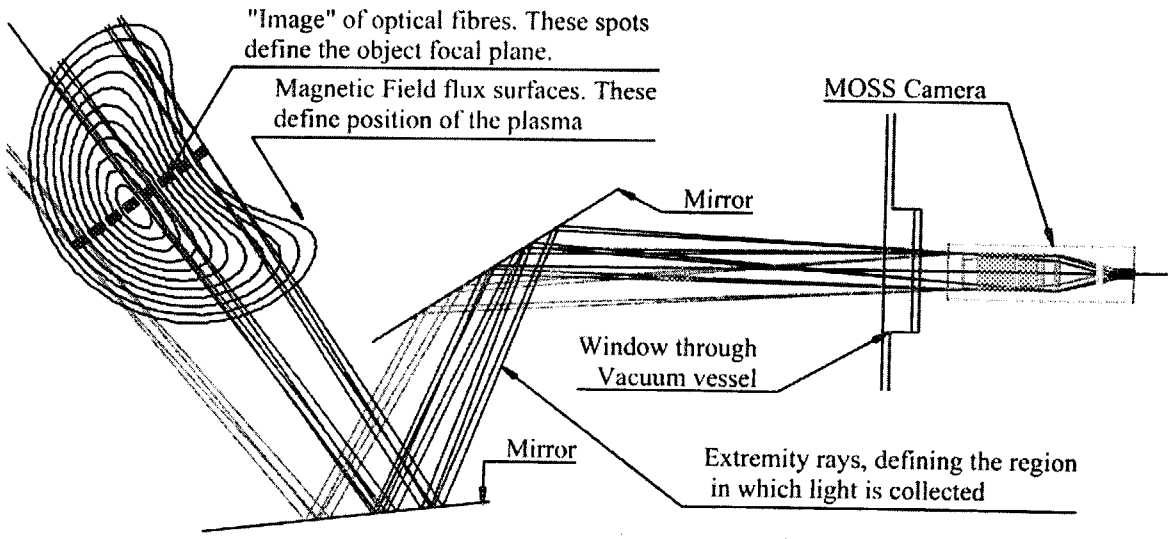

The signals are acquired with a set of digitisers and are stored and processed on a computer, using a Fourier-transform based demodulation algorithm.

The high voltage drive signal for modulating the crystal is achieved with a transformer and audio amplifier [4]. The modulation frequency is 40-50kHz, which is sufficient for a minimum of 20μs time resolution; however, the attainable time resolution (for a reasonable signal-to-noise ratio) depends on the brightness and is imposed by convoluting the time-resolved signals with a windowing function.

References

[1] Howard, J., Glass, F., Michael, C. *MOSS Spectrometer applications in plasma diagnostics,* 5th Australia-Japan Diagnostics workshop, 1999

[2] Howard, J., Glass, F., Michael, C. *MOSS Spectrometer applications in plasma diagnostics,* Submitted to Physics of Plasmas,1999

[3] Steele, *Interferometers*

[4] Cheetam, A., *drive circuitry for MOSS Spectrometer,* Australia-Japan Diagnostics workshop, 1999

[5] Hamamatsu Corporation, *A5958 photo-multiplier tube*

1-6 TIME- AND SPATIALLY-RESOLVED STUDIES OF A DIELECTRIC BARRIER DISCHARGE

W. Payne, B.W. James, I.S. Falconer and J. Khachan
School of Physics, A28, University of Sydney, NSW 2006, Australia

Abstract

We have recorded time- and spatially-resolved images of the light emission from a dielectric barrier discharge. The discharge is a scaled-up version of the type used in plasma display panels (PDPs). These results can be used for comparison with a modelling that has been done for such discharges.

Introduction

A dielectric barrier discharge (DBD), or silent discharge, is a discharge formed in a gas-filled gap between two electrodes, with a dielectric either on or between the electrodes. When a voltage is applied between the electrodes the gas breaks down and a current flows in the ionised gas. Charge builds up on the dielectric to reduce voltage across the cell, and terminate the current pulse. Dielectric barrier discharges (DBDs) were first produced in 1857 by W. Siemens [1]. Until recently their main use has been for the production of ozone.

An AC plasma display panel consists of an array of DBD cells between to sheets of glass, where a DBD cell is formed by the overlap between a vertical electrode on one sheet and a horizontal electrode on the other. The cell is separated from its neighbours by barrier ribs, the electrodes are coated with a dielectric and there is usually a phosphor, to produce colour, on the walls of the cell. Normally the filling gas is a mixture of an inert gas and xenon, which produces UV to excite the phosphors. More recent designs use coplanar electrodes, where the cell has the two discharge electrodes on one sheet, and the other sheet has an address electrode [2,3].

In the past few years research into and production of large screen, light-weight, flat-panel, low production cost displays has greatly increased because of the introduction of high-definition television (HDTV). The plasma display panel is competing for this market, or a share of this market, along with display technologies such as liquid crystal displays (LCDs), field emission displays (FEDs), and projection-type displays.

The important attributes for a display are production and running costs, lifetime, luminous efficiency, brightness, and size. In most areas the plasma display panel achieves these aims, except efficiency. It is expected that efficiency can be improved by optimising gas mixtures, cell structure, and the driving voltage waveform.

We have taken time and spatially resolved measurements of a dielectric barrier discharge for comparison with the results of 2-dimemsional modelling.

Experimental Setup

The gas filling pressure, normally 50 mBar, is lower than in a standard plasma display panel by an order of magnitude, because the dimensions of our discharge are scaled up by an order of magnitude: thus pressure x distance is the same in both cases. A diagram of the discharge cell is shown in figure 1. The opposing electrode cell has

two parallel 2mm wide, 21.4mm long silver electrodes, covered with glass microscope cover slips (100μm), separated by a 2mm gap filled with a gas, or gas mixture. The width of the discharge cavity is 6mm. Figure1 is a diagram of the cell. The cell is driven by a voltage of 320 volts which is switched alternately to each electrode at 50 kHz. There is a driving circuit which switches a dc voltage alternately to the electrodes, using the signal from a function generator.

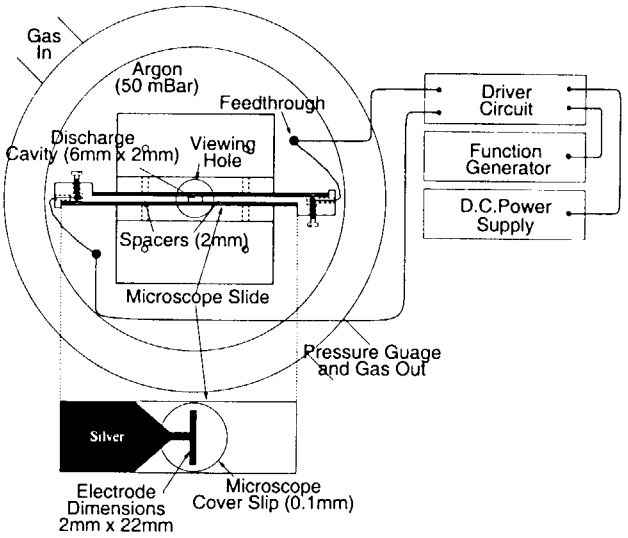

Figure 1: The DBD cell

Images were obtained using an image intensified CCD, with a telecentric optical system. The telecentric optical system is comprised of a lens and a small aperture placed at the focal plane of the lens. The aperture passes only rays which are parallel (or very nearly, depending on the aperture diameter) to the optical axis on the object side of the lens. The means that each line along the length of the discharge parallel to the electrodes falls only on a small region of the image intensifier. Hence the 3-dimensional cell is viewed as a 2-dimensional image, without the ends of the discharge being out of focus. This is required for comparison with 2-dimensional models. The image intensifier is gated a by a pulser which is triggered from the function generator signal. The gate width was 0.01 μs. A diagram of the experimental equipment used to obtain images is shown in figure 2.

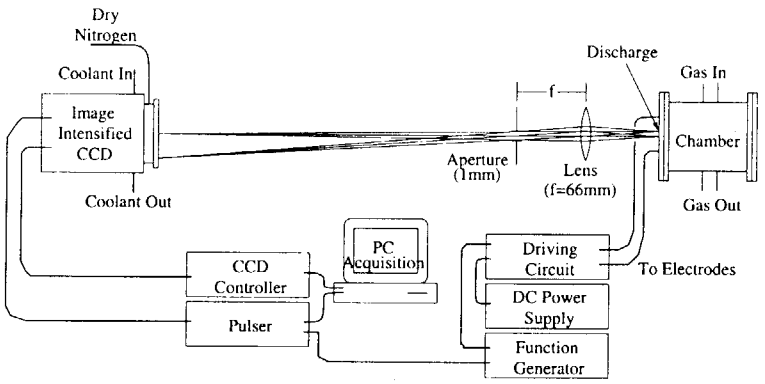

Experimental Set-up

Figure 2: Diagram of Experiment

Results

Figure 3 shows the voltage waveform, the current pulse and the light emission pulse. Figure 4 shows some images from an argon discharge at various times after the voltage is applied to the cathode.

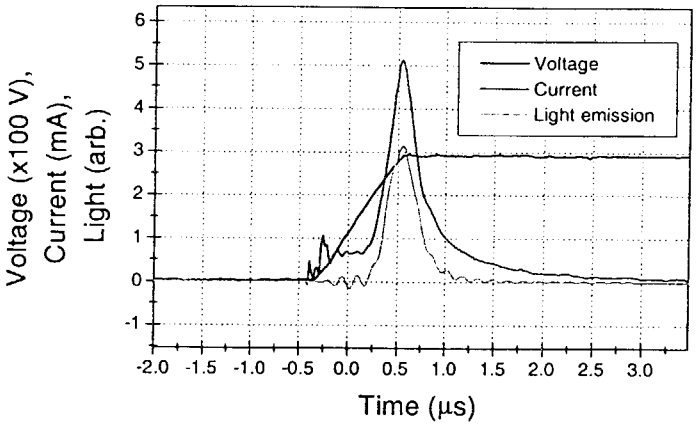

Figure 3: Voltage waveform with current and light emission pulse

For the period of interest, before, after and during the current pulse, a series of images as in figure 4 were obtained every 20 ns. For each of these a line from the top to the bottom of the middle of the electrode was plotted as a function of time to obtain contour plots as shown in figure 5.

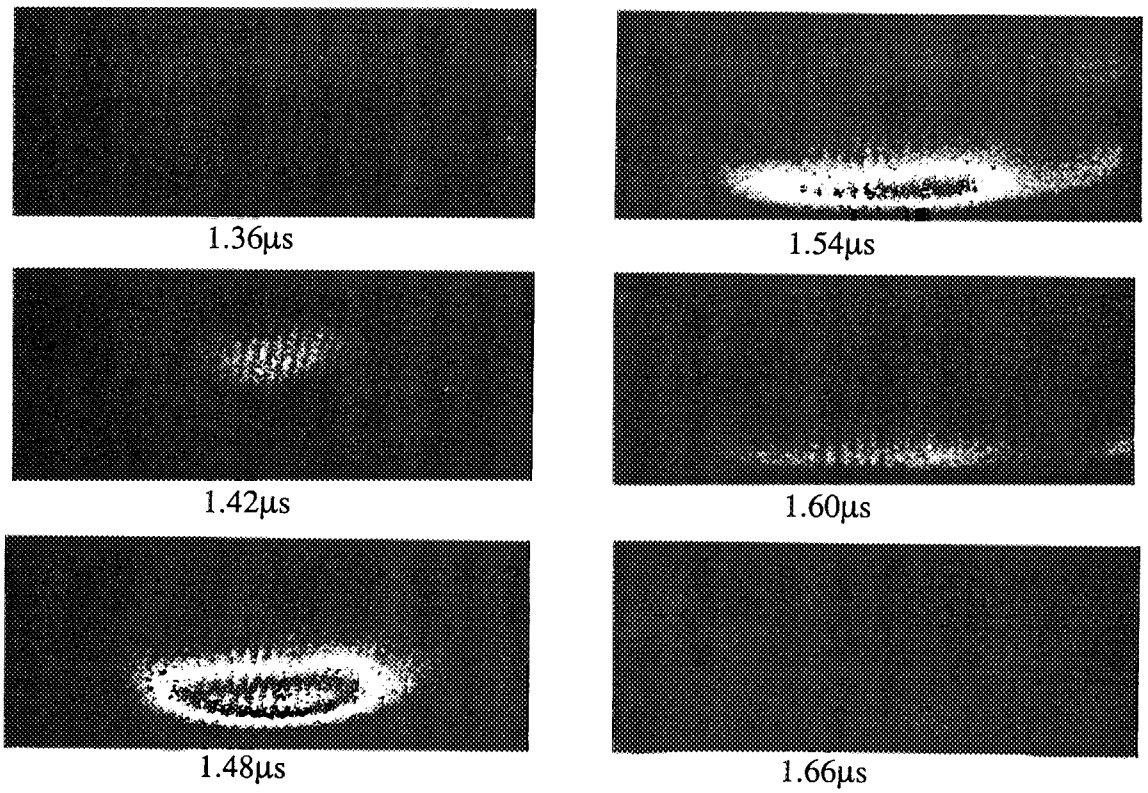

Figure 4: Time-resolved images of Ne discharge at 38 torr.

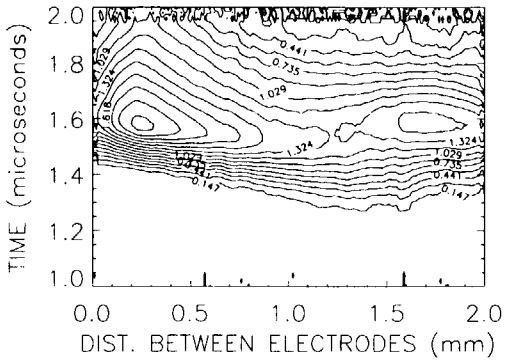

(i) Argon, 38 torr

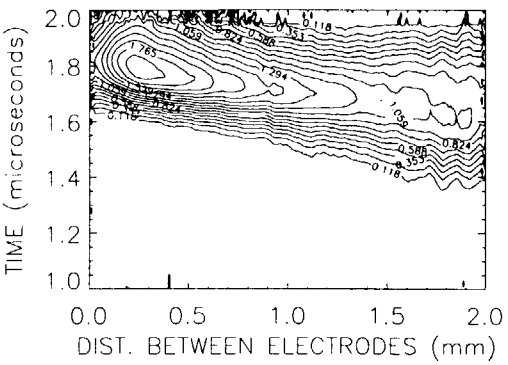

(ii) Argon, 4s→4p′ transition, 38 torr

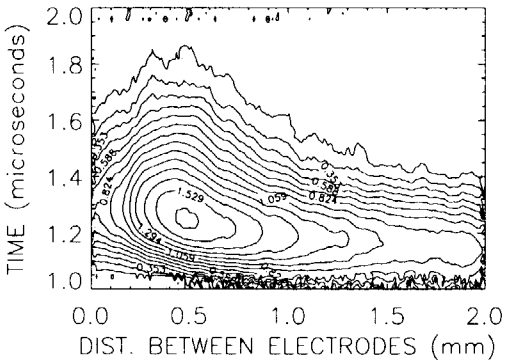

(iii) Argon, 7.6 torr

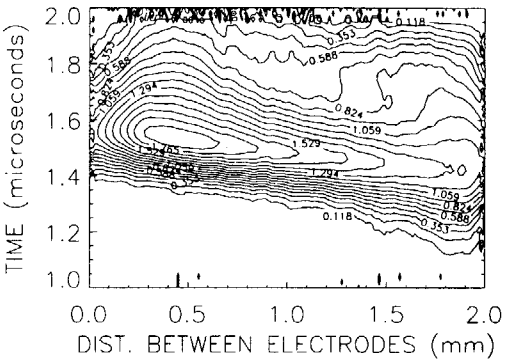

(iv) Neon, 38 torr

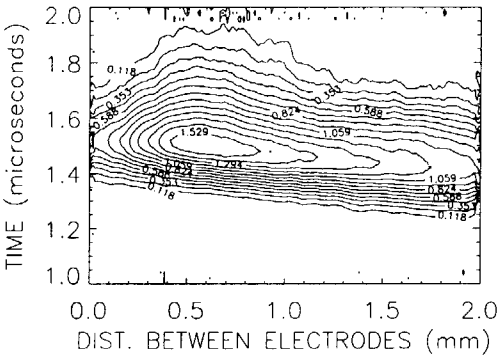

(v) Helium, 38 torr

Figure 5: Log contour plots of emission for centre vertical line, for various conditions, the cathode is at 0mm, the anode at 2mm.

The 4s→4p′ transition of argon in figure 5(ii) gives an approximate indication of relative electron density[4]. The electron density plot shows a lower relative intensity at the anode than the total light emission plot. The rise in electron density starts at the anode, while the rise in total light intensity begins closer to the middle of the gap.

The pressure in the discharge has a strong influence on the light emission both spatially and temporally (figure 5 (iii)). For a lower pressure the discharge pulse occurs at an earlier time, and it is shorter in duration. The light emission from the

plasma at 7.6 torr is significantly lower than for 38 torr. At the anode it is less intense, with respect to the cathode, than for 38 torr.

The various gases, Ar, Ne, He, all show similar characteristics for 38 torr. The light emission pulse begins at the same time. The helium discharge is far less intense than the argon and neon. The decay at the anode is faster for helium than for argon and neon discharges. Helium and neon have a faster decay at the cathode than the argon discharge. The intense region of the discharge is nearest the cathode for argon, further away for neon and helium.

Conclusion

The images taken showed that during the rise of the current pulse the discharge moves from the anode to the cathode. During the fall of the current pulse the discharge stays at the cathode and decreases in intensity. The total light emission pulse follows the current pulse very closely.

The pressure and gas have a significant effect on the spatial, and temporal characteristics of the plasma. This is important for plasma display panels, where it is desirable to get maximum excitation of phosphors by UV emission from xenon, because excitation will depend upon the spatial characteristics of the discharge as well as the structure of the cell and location of the phosphors.

References

[1] Eliasson B., Kogelschatz U., *IEEE Transactions on Plasma Science*, **19** (2), 1991.

[2] Eliasson B., Kogelschatz U., Egli W., *International Conference on Phenomena in Ionized Gases (ICPIG XXIII)*, 1997.

[3] Sobel A., *IEEE Transactions on Plasma Science*, **19** (6), 1991.

[4] Grift, Marc van de, PhD thesis, Technische Universiteit Eindhoven, 1997.

1-7 Development of frequency tunable gyrotrons for plasma diagnostics

T.Idehara, S.Mitsudo, S.Sabchevski, M.Glyavin, I.Ogawa[A], M.Sato[B], K.Kawahata[B] and G.F.Brand[C]

Research Center for Development of Far-Infrared Region, Fukui University
[A] *Faculty of Engineering, Fukui University*
[B] *National Institute for Fusion Science*
[C] *School of Physics, University of Sydney*

Development of two types of frequency tunable gyrotrons are described. One is frequency step-tunable gyrotrons (Gyrotron FU Series) which cover wide range from millimeter to submillimeter wavelegth region. The other is a quasi-optical gyrotron operating in 90 and 180 GHz bands. Both are applicable for plasma diagnostics as power sources.

1. Introduction

The development of gyrotrons is proceeding in two directions. One is the development of high power, millimeter wave gyrotrons as the power sources for electron cyclotron heating of plasmas and electron cyclotron current drive of tokamaks and for industrial technologies, for example, ceramic sintering. The second direction is the development of high frequency, medium power gyrotrons as millimeter to submillimeter wave sources for plasma scattering measurements, ESR experiments and so on.

Gyrotrons developed in Fukui University, under cooperation with University of Sydney and National Institute for Fusion Science belong to the second group. High frequency, medium power gyrotrons covering a broad frequency band in millimeter and submillimeter wavelength regions have been developed. 'Gyrotron FU series' consisting of 8 gyrotrons has many achievements including frequency tunability from 38 GHz to 889 GHz, high harmonic operations up to the fourth harmonics, studies of mode competition and mode cooperation, high purity mode operation, frequency and amplitude modulations, frequency step switching, complete cw operation for a long time ($\geqq$15 hours), high stabilization of the amplitude by feed back control of anode voltage of electron gun and so on.

A quasi optical gyrotron for plasma diagnostics is being developed in National Institute for Fusion Science in cooperation with Fukui University. The frequency tunabilities in two bands near 92 GHz (fundamental operation) and 184 GHz (second harmonic operations) will be achieved.

This paper summarizes achievements of 'Gyrotron FU series' and present status of the quasi-optical gyrotron development.

2. Gyrotron FU Series

Gyrotrons included in Gyrotron FU series are frequency step-tunable sources covering a wide wavelength range from millimeter to submillimeter wave region. The output powers are not so high, that is, from several hundreds watt to several tens kilowatt for fundamental operation and from several tens watt to several kilowatt for second

harmonic operation. The main results are summarized as following.

(a) Frequency tunability in broad band from 38 GHz to 889 GHz[1-3]

All frequencies achieved up to now by 5 gyrotrons included in Gyrotron FU series are summarized as functions of field intensity B_0 in Fig. 1. Solid lines represent the fundamental ($f=f_c$), the second and the third harmonic ($f=2f_c$, $3f_c$) resonances. Frequency step-tunability from 38 to 889 GHz is achieved by the fundamental, second and third harmonic operations. Gyrotron FU IVA has achieved the highest frequency of 889 GHz for single mode operation on the $TE_{8,6,1}$ cavity mode at the second harmonic ($f=2f_c$). The corresponding wavelength is 337 μm.

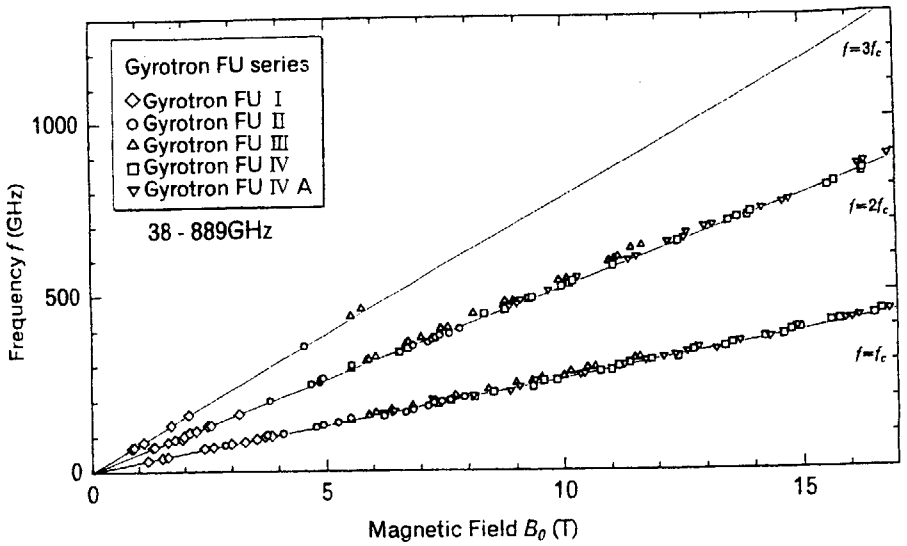

Fig.1 All frequencies achieved up to now by Gyrotron FU series as functions of field intensity B_0. Solid curves show the fundamental, the second harmonic and the third harmonic resonances.

(b) Amplitude modulation[4,5]

Gyrotrons FU III and IV have achieved amplitude modulation of their outputs. A modulation of the anode voltage V_a will modulate the velocity distribution function of beam electrons, which, in its turn, will modulate the gyrotron output. Fig. 2 shows a typical result of amplitude modulation in the submillimeter wave gyrotron (Gyrotron FU III) with the ratio $\Delta V_a/V_a$ as a parameter. This ratio represents the modulation level of the anode voltage V_a. The gyrotron, in this instance, is operating on the second harmonics of the cyclotron frequency. The cavity mode is $TE_{1,6,1}$, the frequency is 444 GHz, and the output power is about 300 W. The modulating frequency is 5 kHz and modulation mode is sinusoidal wave. The upper traces show the high voltage pulse applied to the anode. The small sinusoidal wave modulation signal is visible on the traces. The lower traces show the output power of the gyrotron. The modulation rate $\Delta P_{out}/P_{out}$ of gyrotron output increases with the modulation rate $\Delta V_a/V_a$ of the anode voltage. The 100 percent modulation of the output ($\Delta P_{out}/P_{out}$=1.0) is attained, when $\Delta V_a/V_a$ is only several percent ($\Delta V_a/V_a$~0.055). The modulation rate $\Delta P_{out}/P_{out}$ of output power is almost linearly proportional to $\Delta V_a/V_a$. This means the sinusoidal modulation of output power is possible by the sinusoidal modulation of anode voltage. Sinusoidal modulation of P_{out} at the modulation frequency up to 600 kHz has been achieved with the low $\Delta V_a/V_a$ value of $1.1 \cdot 10^{-3}$.

In Fig.3, the amplitude modulation efficiency $(\Delta P_{out}/P_{out})/(\Delta V_a/V_a)$ is plotted as a function of the beam current I_b. The theoretical prediction for the efficiency is derived from the energy transfer function between electrons and electromagnetic wave, as follows,

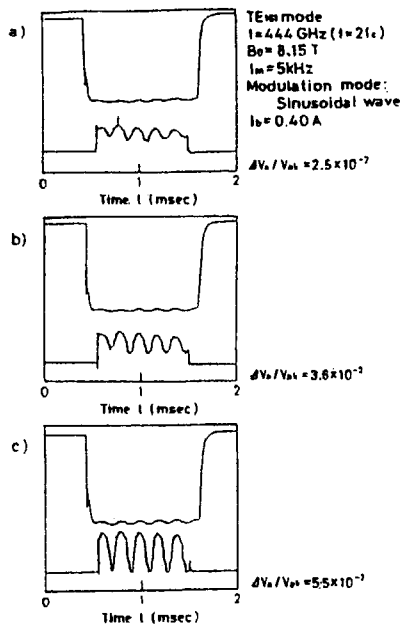

Fig. 2 Amplitude modulation result for Gyrotron FU III. Upper traces are high voltage pulses applied to the anode and lower traces output powers of gyrotron. Operation conditions are shown beside the figure. Unmodulated beam voltage V_b=40 kV.

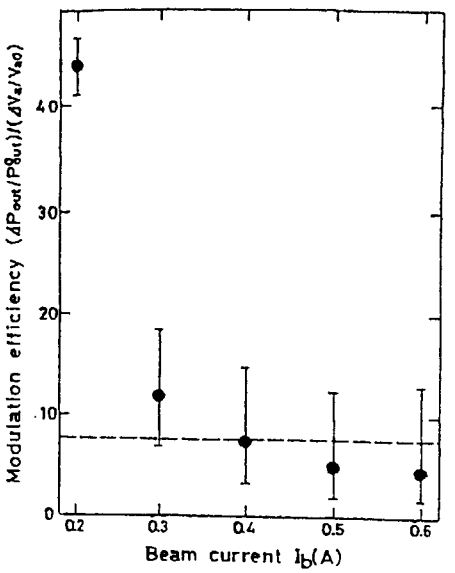

Fig. 3 Amplitude modulation efficiency of $(\Delta P_{out}/P_{out})/\Delta V_a/V_a)$ as a function of the beam current I_b.

$(\Delta P_{out}/P_{out})/(\Delta V_a/V_a) = (1 + P_{ohm}/P_{out})(3\alpha^2 + 4)$,

where P_{ohm} is the ohmic power loss in a cavity and α the pitch angle of beam electrons. The broken line in Fig.3 shows the efficiency when P_{ohm}/P_{out} is neglected. In the figure, experimentally obtained efficiency becomes close to the theoretical prediction (the broken line), when I_b is so high that P_{out} is high enough.

(c) Frequency modulation[6]

Gyrotron FU IV has achieved the frequency modulation within the limit of resonance frequency width of a cavity mode. The mechanism is as follows. The energy of beam electrons is modulated by variation in the body potential. The body includes the cavity and is separated electrically from the beam collector by a ceramic insulator. Therefore, the electron cyclotron frequency is modulated by the changing of electron mass and, as the results, a frequency modulation takes place.

The output power is transmitted by circular waveguides and emitted to a horn antenna. The frequencies measured by a heterodyne detection system consisting of a sweep oscillator, a frequency counter, a harmonic mixer and a modulation domain analyzer. The detected signal (f) is mixed with a high harmonic of the local oscillator and converted to the low frequency signal (f_{IF}). The time and frequency resolutions of the detection system are 10 μsec and 10 kHz, respectively.

A typical result of the frequency modulation experiment is demonstrated in Fig. 4. A trace in the left hand side shows the sinusoidal modulation of body potential V_b. The amplitude of the modulation is around 120 V. Corresponding frequency modulation is demonstrated in the f_{IF} trace in the right hand side. It is also close to sinusoidal modulation and the amplitude is around 30 MHz. The modulation frequency f_m is 10 kHz in this instance.

The frequency modulation amplitude Δf versus the body potential modulation amplitude ΔV_b is plotted in Fig. 5 for several values of the modulation frequency f_m. There is an almost linear dependence between Δf and ΔV_b for all values of f_m. The efficiency of frequency

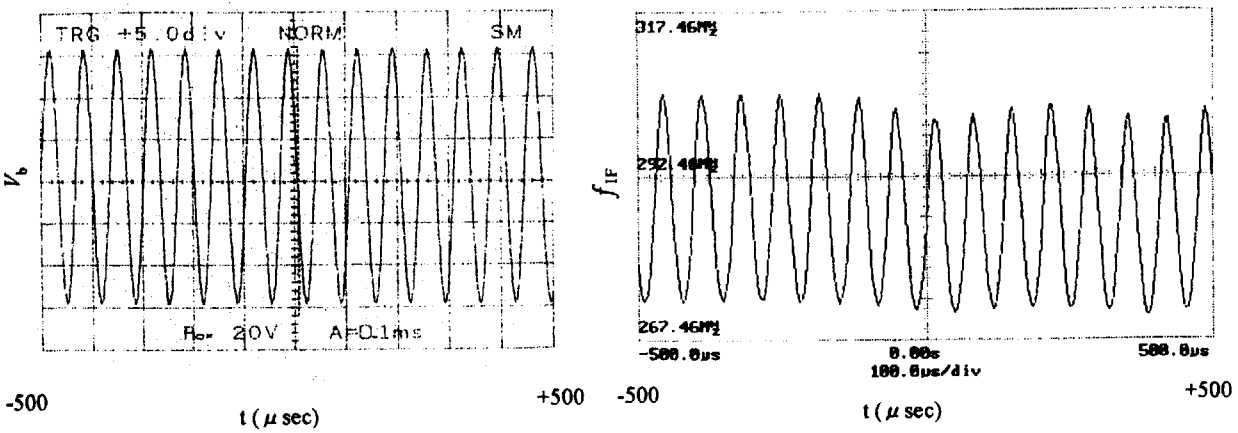

Fig. 4 Typical xperimental results of frequency modulation. The traces show the modulation of V_b (in the left hand side) and the modulation of the output frequency which is demonstrated by the modulation of f_{IF} (in the right hand side) f_m=15 kHz, ΔV_b=120 V and Δf=31.1 MHz.

modulation $\Delta f/\Delta V_b$=0.247 MHz/V. The simulation results are also indicated by solid circles in the figure. The estimated efficiency is distributed close to the experimentally obtained values. The submillimeter wave gyrotron is used as a radiation source for plasma scattering measurement and ESR experiment in our laboratory. The advantages of frequency and amplitude modulations will be useful in these applications.

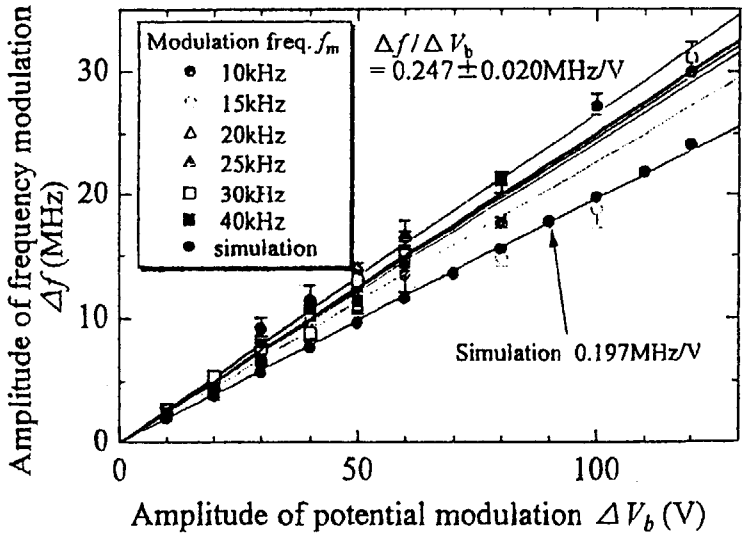

Fig. 5 Experimental and simulation results for frequency modulation amplitude Δf versus the amplitude of body potential modulation ΔV_b for f_m=10, 15, 20, 25, 30 and 40 kHz. Observed frequency modulation efficiency $\Delta f/\Delta V_b$=0.247 MHz/V. Output power P=20 W.

(d) Complete cw operation with high stabilities of amplitude and frequency

One of the advantages of complete cw operation is stabilization of the frequency and the amplitude of the gyrotron output. The longest period of the operation which our gyrotron series has achieved was 15 hours. This means 'complete cw'. We employ a current-stabilized high voltage power supply in our experiment to ensure stable operation. A variation in the output frequency was measured by a time-resolved frequency measurement system which is the same as the one used for measurement of frequency

modulation. The measured frequency variations δf during 100 msec are several MHz and $\delta f/f$ are of the order of 10^{-5} for several cavity modes. The output power variations measured by Schottky diode during ten minutes are several percent. These variations come from the variations of anode and cathode voltages of electron gun. We are planning first to stabilize both voltages, and then, we will try feed back control of them to achieve further high quality stabilization.

Fig.6 shows a preliminary result for amplitude stabilization by the feed-back control of the anode voltage of electron gun. It is seen in the upper trace, that the fluctuation level of the amplitude is decreased lower than 0.1 percent.

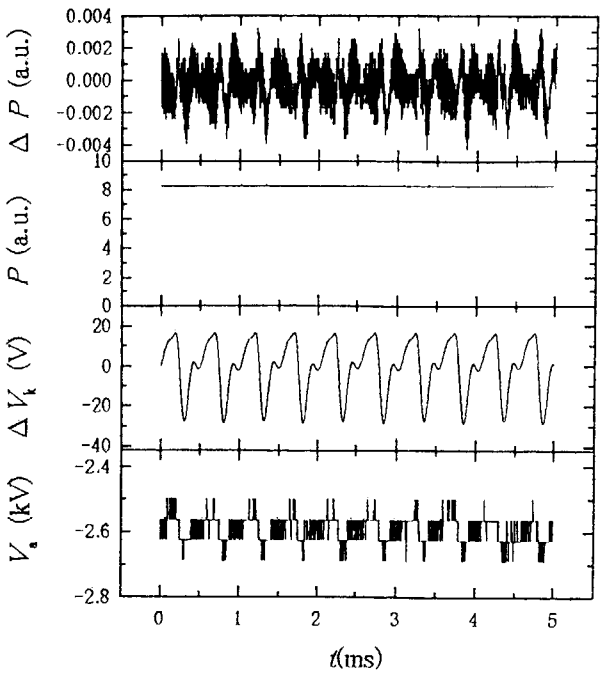

Fig. 6 A typical result of amplitude stabilization experiment by feed-back control of anode voltage V_a.

3. Quasi optical gyrotron

Fig. 7 shows a schematic drawing of a quasi optical gyrotron which is being developed by the collaboration between National Institute for Fusion Science and Fukui University. In the gyrotron, Fabry-Perot resonator is installed. It enables frequency tuning in wide ranges near 90 GHz and 180 GHz. The operation parameters of the gyrotron are listed inTable 1. The output powers obtained by computer simulations are around 100 kW for fundamental operations and 50 kW for second harmonic ones.

Table 1 The operation parameters of the quasi optical gyrotron

Frequency ranges	80~100 GHz (fundamental operations)
	160~200 GHz (second harmonic operations)
Output power	~100 kW (fundamental operations)
	~50 kW (second harmonic operations)
Efficiencies	20~30 % (fundamental operations)
	10~20 % (second harmonic operations)
Maximum field	4.5 T
Electron beam parameter	70 kV, 10 A, 1msec (first stage)
	80 kV, 20 A, 10 msec (final stage)

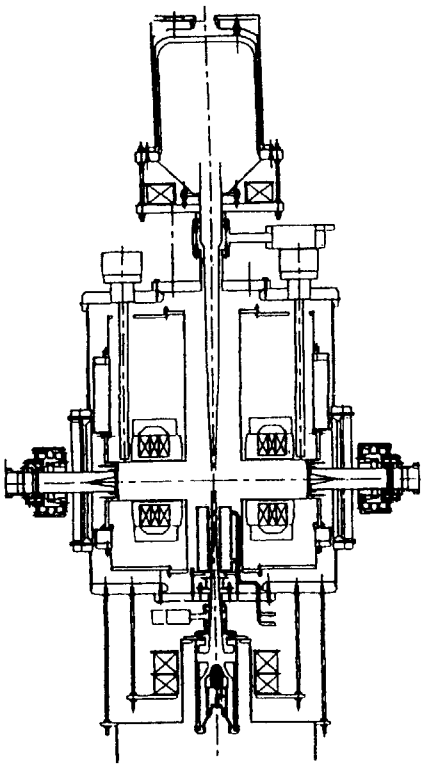

Fig. 7 A schematic drawing of the quasi optical gyrotron

Frequency tunability of such a high power gyrotron will be useful for application to plasma diagnostics and high power spectroscopies in wide fields.

4. Conclusion

We have developed frequency tunable, submillimeter wave gyrotrons (Gyrotron FU series) with medium power and a quasi optical millimeter wave gyrotron with high power for plasma diagnostics and millimeter to submillimeter wave spectroscopy. The former gyrotrons have achieved frequency and amplitude modulations and high stability of the output power.

The fluctuation level of output powers is now lower than 0.1 percent. These advantages of the gyrotron series enable us to apply them to high power, millimeter to submillimeter wave spectroscopies in wide fields. The gyrotrons are used for measurement of LHD in National Institute for Fusion Science in near future.

References

1) T.Idehara, N.Nishida, K.Yoshida, I.Ogawa, T.Tatsukawa, D.Wagner, G.Gantenbein, W.Kasparek and M.Thumm, Int. J. Infrared and Millimeter Waves, **19**, 919 (1998).

2) T.Idehara, Y.Shimizu, K.Ichikawa, S.Makino, K.Shibutani, T.Tatsukawa, I.Ogawa, Y.Okazaki and T.Okamoto, Phys. Plasmas, **2**, 3246 (1995).

3) Y.Shimizu, S.Makino, K.Ichikawa, T.Kanemaki, I.Ogawa, T.Tatsukawa, T.Idehara, Phys. Plasmas, **2**, 2110 (1995).

4) T.Idehara, Y.Shimizu, S.Makino, K.Ichikawa, T.Tatsukawa, I.Ogawa and G.F.Brand, Phys. Plasma **1**, 461 (1994).

5) T.Idehara, Y.Shimizu, S.Makino, K.Ichikawa, T.Tatsukawa, I.Ogawa and G.F.Brand, Int. J. Infrared and Millimeter Waves, **18**, 391 (1997).

6) T.Idehara, M.Pereyaslavets, N.Nishida, K.Yoshida and I.Ogawa, Phys. Rev. Lett. **81**, 1973 (1998).

1-8 Design of a system for conversion of gyrotron output into a gaussian beam

I.Ogawa, T.Idehara[A], S.Sabchevski[A], M.Glyavin[A], S.Mitsudo[A], M.Sato[B], K.Kawahata[B] and G.F.Brand[C]
Faculty of Engineering, Fukui University
[A]Research Center for Development of Far-Infrared Region, Fukui University
[B]National Institute for Fusion Science
[C]School of Physics, University of Sydney

Abstract

A quasi-optical system consisting of a quasi-optical antenna, two ellipsoidal mirrors and a filter to block sidelobes can convert four TE_{1n} mode outputs of the Gyrotron FU IVA into gaussian-like beams with waist size of 16.3 mm. This system can convert three TE_{0n} mode outputs into bigaussian-like beams with waist size of 23.5 mm in width and 16.4 mm in length.

1. Introduction

High frequency gyrotrons are characterized by their capacity to deliver high powers in submillimeter wavelength range and frequency step-tunability due to the alternation of an operating mode. Considering that some applications like plasma scattering measurements need more intense waves, they are the most promising candidates as power sources in this wavelength range.

The gyrotron output should be converted into a gaussian-like beam because the gyrotron delivers the TE_{mn} waveguide mode output, which is far from what is usually required as radiation power source.

In an earlier paper, we presented a quasi-optical system to convert the gyrotron output (TE_{15} mode, 354 GHz) into a gaussian-like beam. In this system, a quasi-optical antenna converts the gyrotron output into a linearly-polarized beam. Its far field consists of a main beam with a circular cross-section and sidelobes. Quality of the beam produced is improved only by focusing the main beam using an ellipsoidal mirror.

If we apply the system to other TE_{1n} modes, the positions and sizes of beam waist undergo changes. For most purposes, the gaussian beam with waist whose position and size are constant is required.

Although the size of main beam of the far-field depends on gyrotron output mode, it is expressed by the gaussian beam with constant size waist located at the antenna[8]. Therefore, the objective beam is obtained by focusing main beam of the far-field using two ellipsoidal mirrors.

As an example of this approach, we will design the system compatible with four TE_{1n} mode outputs of the Gyrotron FU IV A. This system will also be examined with respect to its compatibility with three TE_{0n} mode outputs.

2. Calculation of radiation patterns

If the electromagnetic fields produced by a quasi-optical antenna are known, then those at any subsequent point can be obtained by solving the Helmholtz equation together with the boundary conditions on each mirror. Solving the Helmholtz equation is equivalent in calculating the Huygens equation.

The quasi-optical antenna (Fig. 1) consists of a circular waveguide (internal radius a_w=10 mm) with a step-cut and a parabolic cylinder reflector (focal length f_p=15.5 mm). This antenna converts the TE_{1n} output of Gyrotron FU IVA into a linearly-polarized beam. The electric and magnetic fields are parallel to the x- and y-directions, respectively.

Radiation reflected from the parabolic cylinder reflector of the quasi-optical antenna is treated as if it came from a plane image source lying behind the parabolic cylinder with emission angle α (=8.63 °). This emission angle is independent on the mode, if the radiation is excited in a gyrotroncavity operating at the cut-off. The fields over this image source are calculated using geometrical optics.

The incident electromagnetic fields at the first mirror are calculated using the Huygens equation. The electromagnetic fields reflected from the mirror are given by the boundary conditions. The electromagnetic fields on subsequent mirrors are obtained by repeated use of the Huygens equation and the boundary conditions together with the previously calculated results as the source fields.

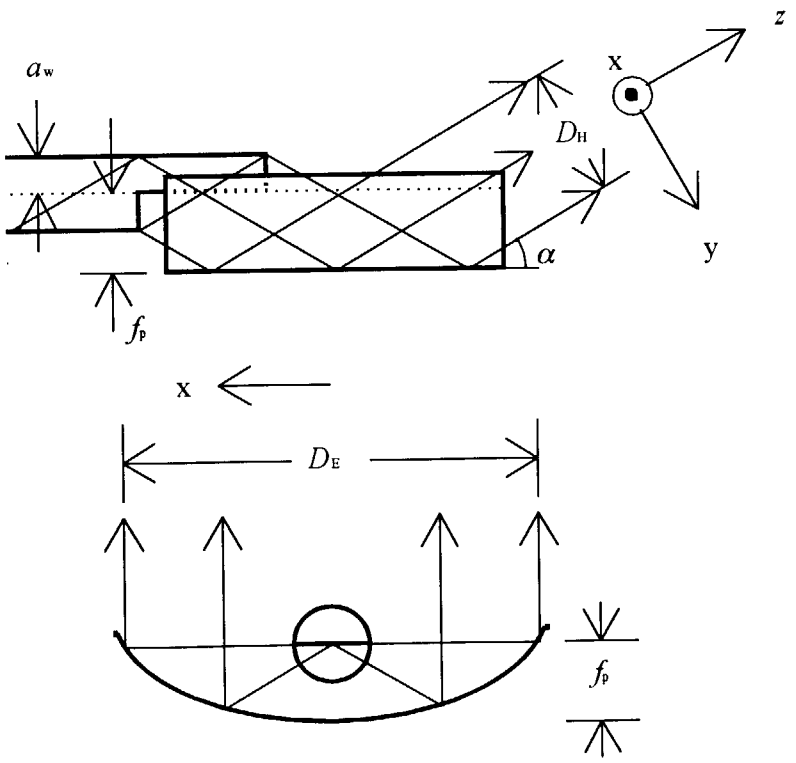

Fig. 1 Quasi-optical antenna.

3. Design of the system using gaussian optics

In order to investigate how the beams spread, their intensity profiles have been calculated for a plane at a distance from the image source. The image source is located so that the beam with

polarization in the x-direction propagates along the z-direction (Fig. 2). The intensity profiles TE_{1n} modes are shown in Fig. 3.

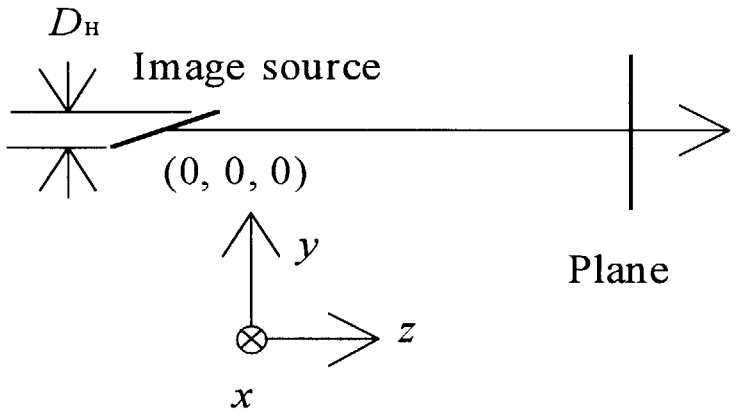

Fig. 2 Plane image source used in the calculation of the subsequent radiation patterns of the quasi-optical antenna with a single parabolic reflector. The beam propagates along the *z*-axis.

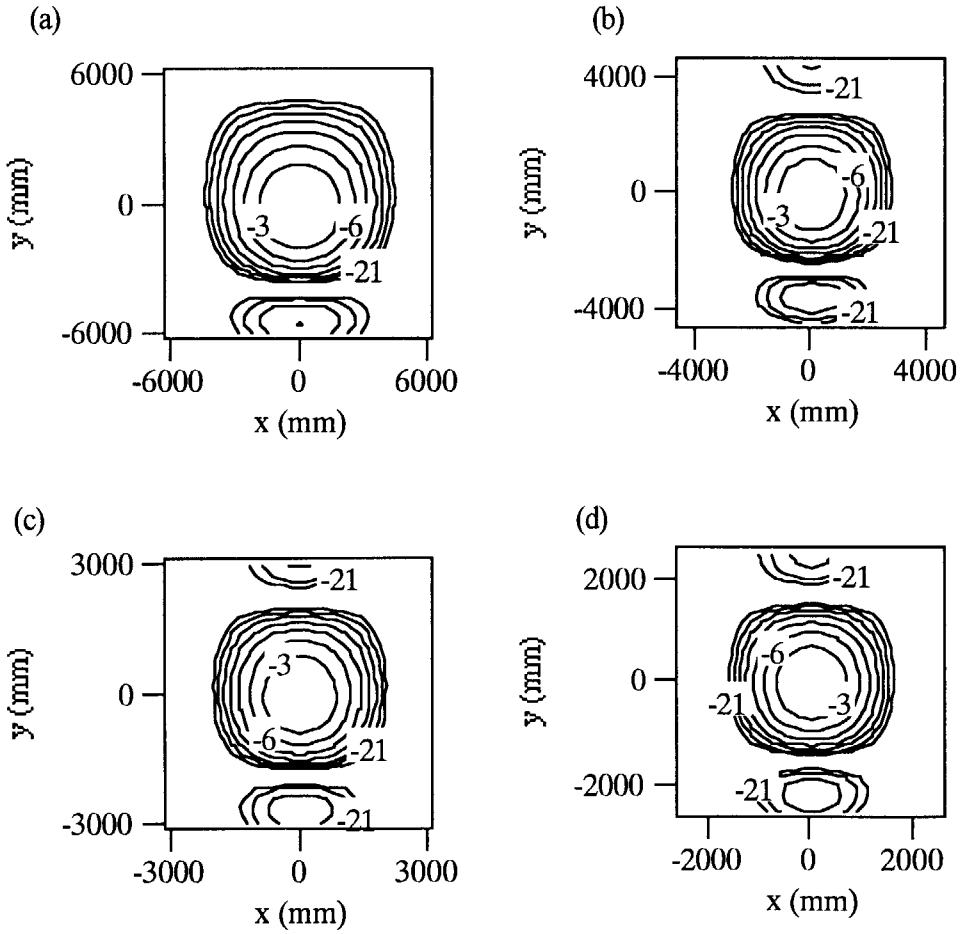

Fig.3 Calculated intensity contours in the far-field region (Distance 100000 mm). (a); TE_{12} mode (170 GHz), (b); TE_{13} mode (271 GHz), (c); TE_{14} mode (372 GHz), (d); TE_{15} mode (472 GHz)

Each far-field consists of a main beam and additional sidelobes. The main beams for TE_{1n} modes are circular and their spot sizes are given by assuming a gaussian beam whose waist (waist size w_0=18.1 mm) is located at the center of the image source.

Propagation and focusing of a bigaussian beam is most conveniently treated by the use of the complex beam parameters.

In the system (Fig. 4), the focal length f_1 of the mirror m1 coincides with the distance d_1, namely, $f_1=d_1$ (=1500 mm). For this special arrangement, the far-field of the image source appears in the y=1241 plane.

If we treat the main beam as a bigaussian beam having a waist at the position of the image source, the beam waist size $w_{0'}$ at the y=1241 plane as

$$w_{0'} = \frac{f_1 \lambda}{\pi w_0} \qquad (1)$$

The equations show that since one waist is at the image source, the beam will come to a waist at the y=1241 plane. Because the mirror m2 has also the special arrangement ($f_2=d_2$=1241 mm), the beam will come to a waist at the z=1241 plane. The final waist size $w_{0''}$ at the z=1241 plane as

$$w_{0''} = \frac{f_2}{f_1} w_0 \qquad (2)$$

This result generally holds for a confocal system consisting of two mirrors. Note that this result does not depend on frequency.

The focal lengths f_1 and f_2 are determined as 1500 mm and 1241 mm so that this system produces a gaussian beam with the waist size $w_{0''}$=15.0 mm for TE_{1n} mode.

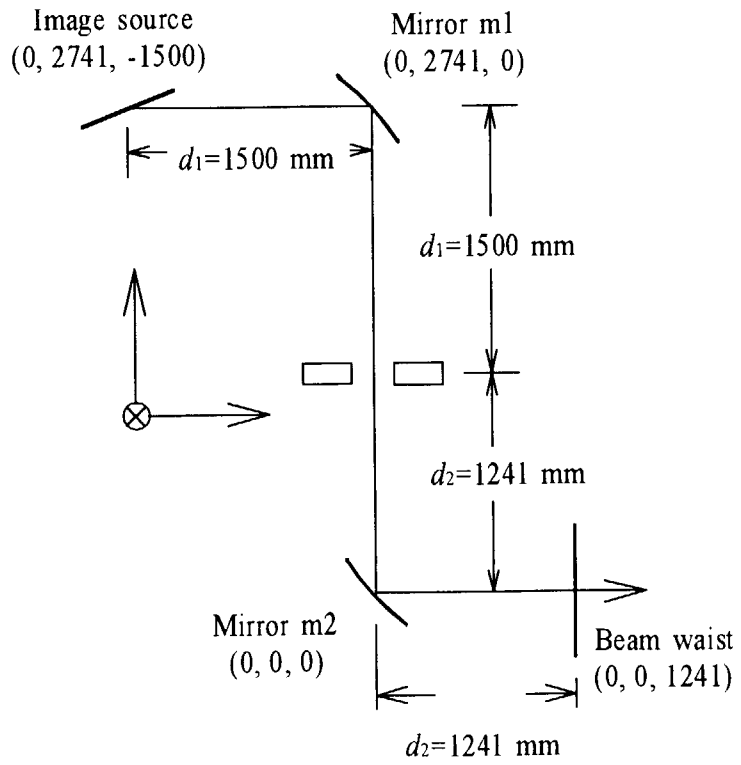

Fig. 4 Quasi-optical system.

4. Calculation results using the Huygens equation

The mirrors m1 and m2 are wide enough (m1; 160 mm in width and 590 mm in length, m2; 170 mm in width and 240 mm in length) to avoid any diffraction loss due to beam truncation. The shape of the mirror m1 is defined by an ellipse with focal points (0, 2741, -10000) and (0, 976, 0) resulting in a focal length of f_1=1500 mm. The shape of the mirror m2 is also defined by an ellipse with focal points (0, 10000, 0) and (0, 0, 1417) resulting in a focal length of f_2=1241 mm.

In order to improve the quality of the beams produced, it is necessary to remove the sidelobes from the far-field of the image source. This is experimentally done by inserting a spatial filter to block the sidelobes in the y=1241 plane.

In principle, loss-less methods exist to transform any field distribution to gaussian beams, but these techniques are not broad band. Therefore, a small power loss is taken into account.

At first, the incident electromagnetic fields at the y=1241 plane are calculated. The electromagnetic fields on the subsequent mirror m2 are obtained by repeatedly using the Huygens equation with the previous calculated results as the sources.

The intensity profiles at the z=1241 plane with spatial filtering for TE_{0n} modes are shown in Fig. 5 and those for TE_{1n} modes are shown in Fig. 6. One can see, that this system converts four TE_{1n} mode outputs of the Gyrotron FU IVA into gaussian-like beams with waist size of $w_{x'}$=$w_{y'}$=16.3 mm and converts three TE_{0n} mode outputs into bigaussian-like beams with waist size of $w_{x'}$=23.5 mm and $w_{y0'}$=16.4 mm. The spot sizes $w_{x'}$ and $w_{y'}$ agree well with the waist sizes $w_{x0'}$ and $w_{y0'}$ given by equation (2).

Most (85 % for TE_{0n} mode and 90 % for TE_{1n} mode) of power from the image source still arrives at the beam waist in spite of the truncation of the sidelobes at the y=1241 plane.

5. Conclusion

A system consisting of a quasi-optical antenna, two focusing mirrors and a spatial filter to block the sidelobes can convert four TE_{1n} mode outputs of the Gyrotron FU IVA into gaussian like beams with waist size of $w_{x'}$=$w_{y'}$=16.3 mm and can convert three TE_{0n} mode outputs into bigaussian-like beams with waist size of $w_{x'}$=23.5 mm and $w_{y0'}$=16.4 mm. The system has the advantage of being applicable to frequency tunable gyrotrons as the Gyrotron FU IVA.

In this system, the beam quality is improved by truncating the sidelobes of the far-field. In spite of the beam truncation, most (85 % for TE_{0n} mode and 90 % for TE_{1n} mode) of the image source power is transferred to the waist. This enables us to produce an intense beam in submillimeter wavelength range.

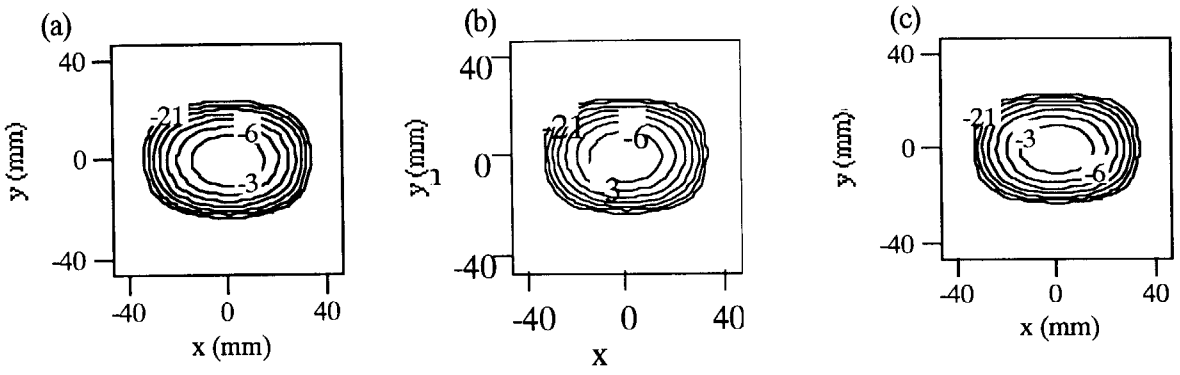

Fig. 5 Calculated intensity contours. (a); TE_{02} mode (223 GHz), (b); TE_{03} mode (323 GHz), (c); TE_{04} mode (423 GHz)

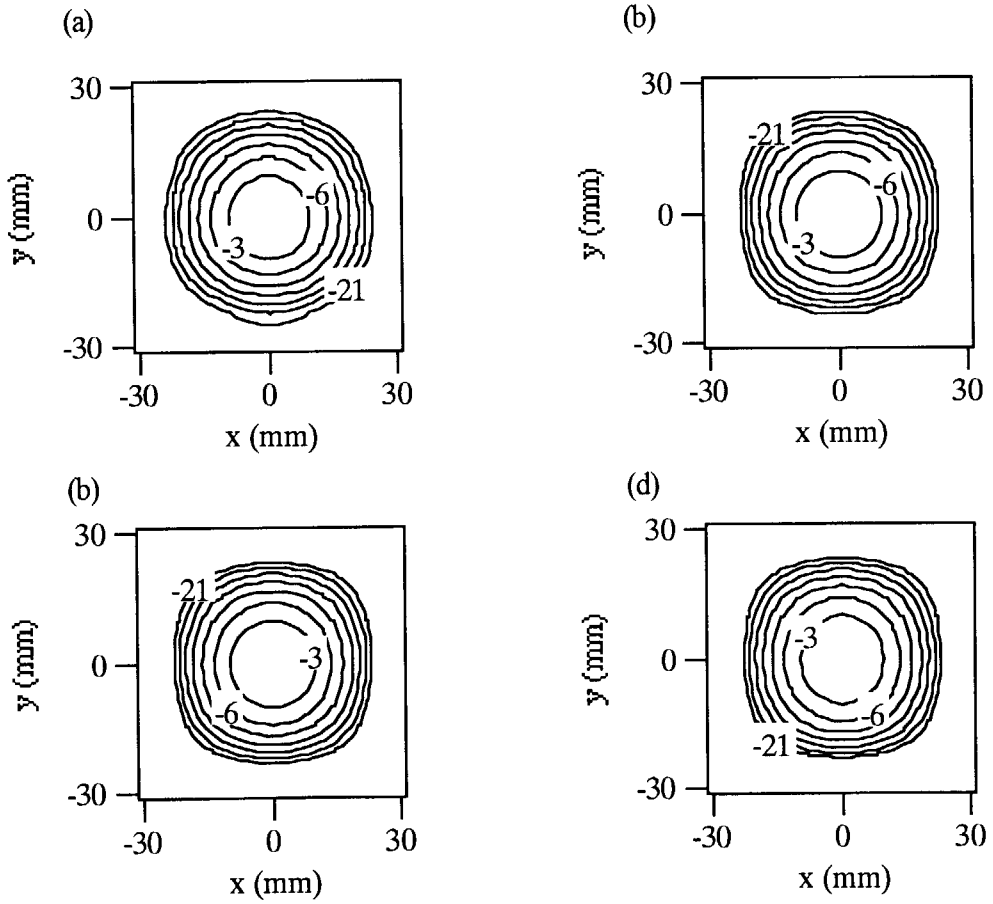

Fig. 6 Calculated intensity contours. (a); TE_{12} mode (170 GHz), (b); TE_{13} mode (271 GHz), (c); TE_{14} mode (372 GHz), (d); TE_{15} mode (472 GHz)

1-9 Development of Short-Wavelength Far-Infrared Laser for Future Plasma Diagnostics

S.Okajima, K.Nakayama and H.Tazawa
College of Engineering, Chubu University
Kasugai, Aichi 487-8501,Japan

K.Kawahata, K.Tanaka, T.Tokuzawa and Y.Itoh
National Institute for Fusion Science
Toki, Gifu 509-5292,Japan

1.Introduction

Powerful and stable FIR (Far-Infrared) lasers of 25 μm to 1 mm in wavelength are useful for optical sources of plasma diagnostics, molecular- and solid state-spectroscopy, research of astronomy and metrology. Recently, the development of short wavelength FIR lasers are required for several applications.

2.Stable and powerful 119-μm CH_3OH laser

We have constructed powerful and stable 119-μm CH_3OH laser to measure the electron density profile of LHD-plasmas in National Institute for Fusion Science (NIFS) by using the results of R&D for CO_2 laser pumped FIR laser in Chubu University[1] . This laser is composed by a pump CO_2 laser and a twin FIR laser. On 119-μm CH_3OH laser, we have obtained maximum power of 0.62W for 99W pumping. For a precise phase measurement, the high beat frequency stability of the two FIR lasers is necessary in addition to amplitude stability. In order to achieve the stable laser operation with high power, we have applied active feedback control system in addition to passive stabilization as in Fig.1. The frequency of 9P(36) pump CO_2 laser is stabilized by using external CH_3OH Stark cell modulation. The output power of CH_3OH laser of probe beam is stabilized at a point on the slope of the de-tuning curve by using a stepping motor. The frequency of CH_3OH laser of reference beam is locked at the frequency shifted with respect to that of the probe beam laser by 1 MHz. As the result, we have achieved less than 0.5% of the long term drifts of the laser output power and beat frequency for times longer than 15 h. The

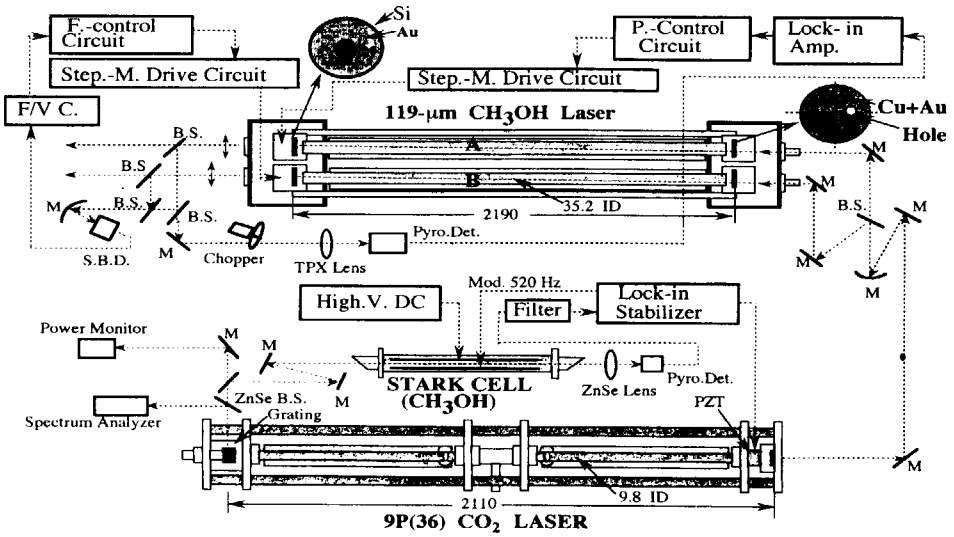

Fig.1 Schmatic drawing of 119-μm CH_3OH laser system for LHD diagnostics

short term fluctuations of the beat frequency are limited at ±5 kHz of the control boundary. This laser system has been equipped for a 13-channel interferometer system, and is using for everyday experiments of LHD[2].

3.Construction of data-base of short-wavelength FIR lasers

For the higher density operations of LHD and for future large plasma machine, FIR lasers of from 40 to 100 μm in wavelength may be useful rather than the long wavelength FIR lasers mentioned above and 10-μm CO_2 laser from the view points of refraction and vibration effects and fringe shifts in the interferometer.

On this wavelength region of FIR laser spectrum, lasers from CH_3OH and the isotopes have a dominant role. However, the details on available lasing line, the power level and the pressure dependence have not been so well known. In order to establish new optical sources for plasma diagnostics, we have constructed new R&D laser system in Chubu University as shown in Fig.2.

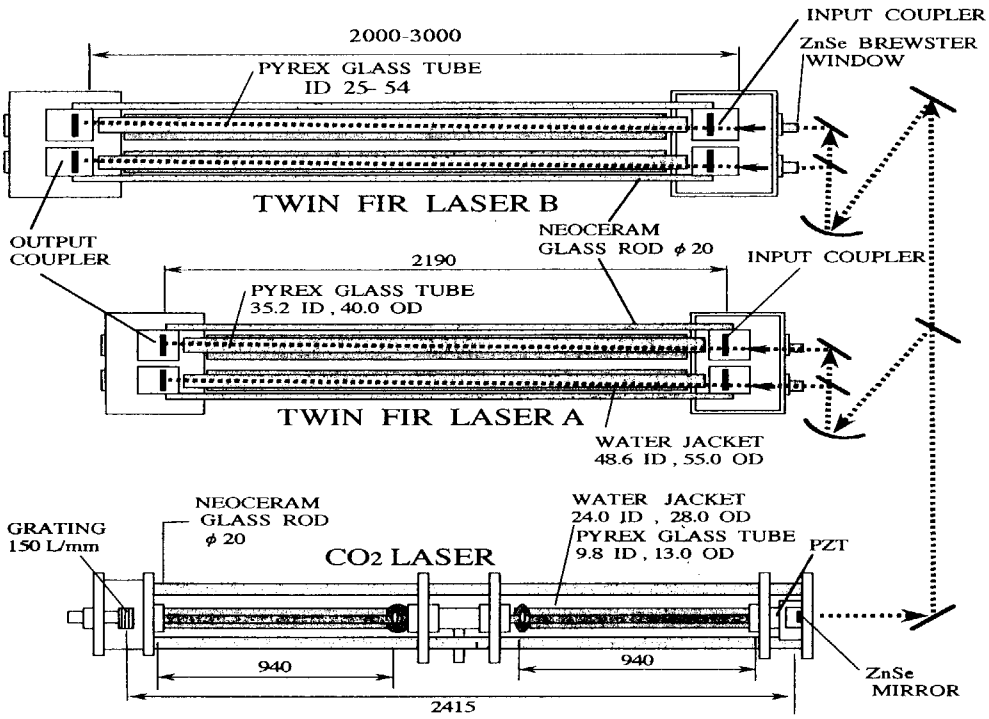

Fig.2 CO_2 laser pumped FIR laser system to constract the data-base

This FIR laser sysem is the twin type and can instal the laser tube of 25 to 54 mm in diameter and 2 to 3 m in length. Using the laser sytem, we are constructing now the data base for

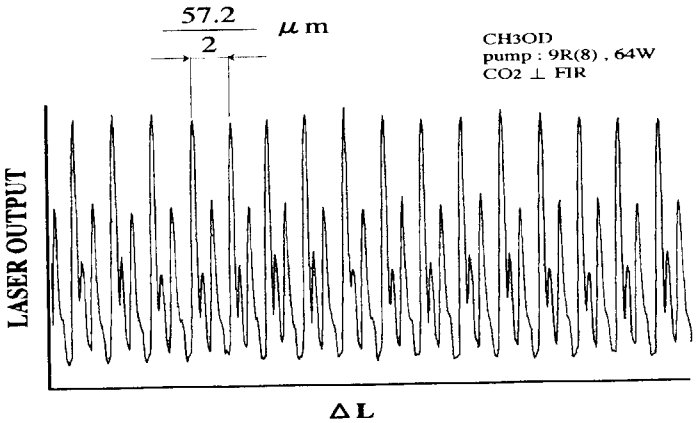

Fig.3 Detunning curve of 57.2-μm CH_3OD laser pumped by 9R(8) cw CO_2 laser

Table1 CO_2 laser pumped FIR lasers

CO_2 laser		FIR laser						
line	power (W)	molecule	wavelength (μm)	pol.	pressure (torr)	power (mW)	tube diameter(mm)	output mirror type
9R(26)	87	CH3OH	151	∥	0.78	3	25	Si hybrid coupler
9R(18)		CH3OH	61	⊥			25	Si hybrid coupler
		CH3OH	186	∥			25	Si hybrid coupler
9R(10)	80	CH3OH	96.5	∥	0.7	[68]	25	Si hybrid coupler
9R(8)	65	CH3OH	77.3	∥		[1.5]	25	Si hybrid coupler
9P(24)	96	CH3OH	133.1	∥	0.34	14	34	Si hybrid coupler
9P(34)	75	CH3OH	70.5	⊥	0.2	65	34	Si hybrid coupler
9P(36)	99	CH3OH	118.8	⊥	0.37	620	34	Si hybrid coupler
9P(38)		CH3OH	193	⊥	0.16	3.3	25	Si hybrid coupler
		CH3OH	198	⊥	0.14	4.4	25	Si hybrid coupler
		CH3OH	292	∥			25	Si hybrid coupler
10R(38)	64	CH3OH	163.0	∥	0.33		25	Si hybrid coupler
		CH3OH	251	∥	0.34		25	Si hybrid coupler
10R(16)	90	CH3OH	63.0	∥	0.28		34	Si hybrid coupler
9R(34)	63	CD3OH	52.9	⊥	0.35	10	34	Si hybrid coupler
9R(28)	81	CD3OH	55.6	⊥	0.3	4	34	Si hybrid coupler
	78	CD3OH	42.6	∥	0.25	4	34	Si hybrid coupler
9P(40)	42	CD3OH	198.6	∥	0.33		34	Si hybrid coupler
10R(36)	85	CD3OH	253.7	⊥	0.35	28	34	Si hybrid coupler
	57	CD3OH	418.7	∥	0.27	2	34	Si hybrid coupler
10R(34)	71	CD3OH	128.0	⊥	0.3	9	34	Si hybrid coupler
	76	CD3OH	168.1	⊥	0.17	3	34	Si hybrid coupler
10R(18)	89	CD3OH	41.4	⊥	0.18	13	34	Si hybrid coupler
	107	CD3OH	43.7	∥	0.3	6	34	Si hybrid coupler
10R(16)	98	CD3OH	81.6	∥	0.30	5	34	Si hybrid coupler
	99	CD3OH	86.4	⊥	0.3		34	Si hybrid coupler
10P(24)	83	CD3OH	286.7	∥	0.26		34	Si hybrid coupler
10P(42)	79	CD3OH	188.4	∥	0.2	3	25	Si hybrid coupler
9P(10)	96	CH3OD	133	∥	0.27	3	34	Si hybrid coupler
9P(26)	85	CH3OD	117.2	∥	0.3	26	34	Si hybrid coupler
9P(30)	84	CH3OD	103.1	⊥	0.32	23	34	Si hybrid coupler
◎ 9R(8)	60	CH3OD	57.2	⊥	0.31	85	25	Si hybrid coupler
	60	CH3OD	47.8	∥			25	Si hybrid coupler
10R(24)		CD3OD	184.7	⊥	0.24		34	Si hybrid coupler
10R(10)		CD3OD	227.7	⊥	0.22		34	Si hybrid coupler
9P(10)	65	CH2DOH	183.6	∥	0.19	10	25	Si hybrid coupler
9P(12)	56	CH2DOH	108.8	∥	0.31	16	25	Si hybrid coupler
	56	CH2DOH	112.5	∥	0.31	38	25	Si hybrid coupler
9P(14)	85	CH2DOH	206.7	∥	0.17	19	25	Si hybrid coupler
9P(16)	82	CH2DOH	102.0	⊥	0.29	15	25	Si hybrid coupler
9P(30)	95	CH2DOH	44	∥	0.13	6	25	Si hybrid coupler
10R(34)	74	CH2DOH	150.8	∥	0.26	22	25	Si hybrid coupler
	74	CH2DOH	156	⊥	0.09	7	25	Si hybrid coupler
10P(26)	110	CH2DOH	150.6	⊥	0.23	24	25	Si hybrid coupler
10P(34)	91	CH2DOH	124.4	∥	0.43	63	25	Si hybrid coupler
10P(46)	43	CH2DOH	49.1*	⊥	0.2	17	25	Si hybrid coupler
10R(20)	82	CHD2OH	260	∥	0.29	4	25	Si hybrid coupler
10R(16)	96	CHD2OH	179	∥	0.20		25	Si hybrid coupler
9R(30)	54	NH3	67	∥	0.23	43	25	Si hybrid coupler
9R(32)	81	CH2F2	184.3	⊥	0.19	298	34	Si hybrid coupler
	81	CH2F2	195.8	⊥	0.19	146	34	Si hybrid coupler
	81	CH2F2	235.6	∥			34	Si hybrid coupler
9R(20)	81	CH2F2	117.7	⊥	0.50	62	25	Si hybrid coupler
9P(10)	50	CH2F2	158.5	∥			34	Si hybrid coupler
9P(16)	79	CH2F2	105.5	∥			34	Si hybrid coupler
10P(18)	97	CH3I	447	∥	0.20	3	25	Si hybrid coupler
9R(32)	69	CD3I	444	⊥	0.26	1	25	Si hybrid coupler
9R(12)	45	CD3I	460	⊥	0.20		25	Si hybrid coupler
9R(22)	68	HCOOH	418	∥			34	Si hybrid coupler
9R(20)		HCOOH	432.4	∥	0.23	5	25	Si hybrid coupler
9R(18)	90	HCOOH	393.2	∥	0.32	21	25	Si hybrid coupler
9R(16)	107	CH3CN	453	⊥	0.14	0.4	25	Si hybrid coupler
9R(12)	87	CH3CN	388	∥	0.13	5	25	Si hybrid coupler
9P(6)	30	CH3CN	494	⊥	0.16	0.15	25	Si hybrid coupler
10P(20)	112	CH3CN	374	∥	0.17	1	25	Si hybrid coupler
9P(8)	75	CD3CN	455	⊥	0.16	0.5	25	Si hybrid coupler

* new line

characteristics of FIR lasers at from 40 to 500 μm in wavelength. Presently, we have obtained 66 laser lines with useful power level from 13 lasing species as shown in Table 1. From the results, 70.5-μm CH_3OH laser, 67-μm NH_3 laser, 57.2- μm CH_3OD laser are powerful and useful as short-wavelength FIR optical sources. In Fig.3, we showed the detunning curve of 57.2-μm CH_3OD laser. For these lasers, the output power (85 mW for 57-μm CH_3OD laser) is not so high because the FIR laser cavity is not optimized for the wavelength yet. The improvement of the laser cavity is proceeding now.

4.Detection of short-wavelength FIR laser light

We could detect the 57-μm (5.2 THz) laser light by using a GaAS Schottky barrier diode (SBD) detector with corner reflector as shown in FIg.4. The improvement of the detector are proceeding now, too.

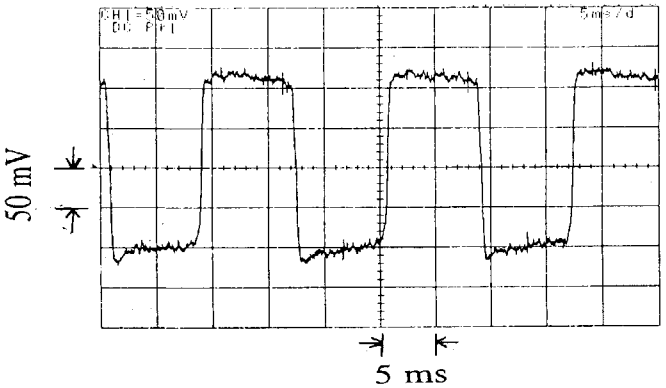

Fig.4 Video signal of 57-μm CH_3OD laser output detected by GaAs Schottky barrier diode .

5. Conclusion

We have developed powerful and stable 119-μm CH_3OH laser to measure the electron density profile of LHD-plasmas in NIFS by using the results of R&D for CO_2 laser pumped FIR laser in Chubu University.

For the higher density operations of LHD and for future large plasma machine, we are developing now short wavelength FIR lasers of from 40 to 100 μm in wavelength in Chubu University. We have detected the 57-μm (5.2 THz) laser light by using a GaAS SBD detector with corner reflector.

The improvement of the detector for short wavelength FIR are proceeding now.

References

[1] K.Kawahata et.al., Design and construction of a far infrared laser interferometer for the LHD, Fusion Engineering and Design, **34-35**, (1999) 34-35.

[2] K.Kawahata et.al., Far-infrared laser interferometer system on the Large Helical Device, Review of Scientific Instruments, **70**,(1999) 707-709.

1-10 THE PROGRESS OF FAR INFRARED TANGENTIAL INTERFEROMETRY/POLARIMETRY SYSTEM ON NSTX

H. K. PARK

Princeton Plasma Physics Laboratory, P.O. Box 451, Princeton, New Jersey 08543

B.H. DENG, C. W. DOMIER, M. JOHNSON and N. C. LUHMANN, JR.

Department of Applied Science, University of California at Davis, California 95616

It is essential to measure the core $B_T(r,t)$ value in NSTX, since effects of paramagnetism and diamagnetism in NSTX are expected to be considerably greater than that in higher aspect ratio tokamaks. The multi-chord Tangential Far Infrared Interferometer/Polarimeter (FIReTIP) system[1] currently under development for NSTX will provide temporally and radially resolved toroidal field profile $[B_T(r,t)]$ and 2-D electron density profile $[n_e(r,t)]$ data.

1. Introduction

The toroidal magnetic field (B_T) is modified very little in the presence of plasmas in conventional toroidal devices such as stellarator and conventional tokamaks. Important plasma parameters such as safety factor (q), local β and magnetic shear are consequently estimated based on the use of the vacuum magnetic field strength without independent measurement. However, the vacuum magnetic field in spherical tokamaks, is expected to be altered significantly in the presence of plasmas. Without independent measurement of B_T, it would be difficult to obtain q-profile from the measured pitch angle unless the MSE system has an intricate configuration of beam and sight lines to address B_p and B_T independently[2]. The technique based on Faraday rotation effect also has evolved and has been applied routinely in machines where accessibility is not a problem. This paper will describe a far infrared tangential interferometer/polarimeter (FIReTIP) system using the source wavelength of 119 μm that is the optimum wavelength for NSTX parameters to measure the toroidal magnetic field. The FIReTIP system design will be based on a triple FIR laser system[3] including

Stark-tuned laser to avoid the effect of machine vibration for Faraday rotation measurement. The primary goal of this system is the measurement of the toroidal magnetic field, thus answering one of the perceived needs for NSTX diagnostics. Simultaneoùsly, temporally resolved 2-D density profile information will be available as well.

2. Optical Arrangement and Measuremental Technique

The FIReTIP system will have a fan beam arrangement composed of seven laser beams which enter the three different entrance windows located at Bay K as shown in Fig. 1. Each beam traverses a different chord along the horizontal mid-plane of the device, reflects from a corner cube retro-reflector, and traverses back through the plasma to return to a common point for detection. Four retro-reflectors (#1, #2, #5, #7) will be located outside of the vessel whereas three of them (#3, #4 and #6) will be installed inside the vessel. The tangencies of each chord are R(1) = 33.3 cm, R(2) = 57.9 cm, R(3) = 78 cm, R(4) = 102.8 cm, R(5) = 123 cm, R(6) = 137.2 cm, and R(7) = 149.9 cm. Here, the O-mode polarized radiation undergoes a phase shift given by

$$\phi(x) = 2.8\times10^{-15}\lambda\int_{o}^{x} n(x')dx'$$

In the presence of a parallel magnetic field component, B_T, the polarization of the wave is Faraday rotated through an angle

$$\Psi(x) = 2.6\times10^{-13}\lambda^2\int_{o}^{x} n(x')B_T(x')dx'$$

With seven chords spanning the plasma with a properly arranged spacing, FIR interferometry data can be inverted to yield the temporally and radially resolved plasma density $n_e(r,t)$. FIR polarimetry data can be subsequently inverted to yield the time dependent parallel magnetic field $B_T(r,t)$.

The FIReTIP system geometry is similar to the fan beam densitometer concept introduced by Howard[4] and Jobes[5]. In the densitometer concept, however, only the Faraday rotation signal from

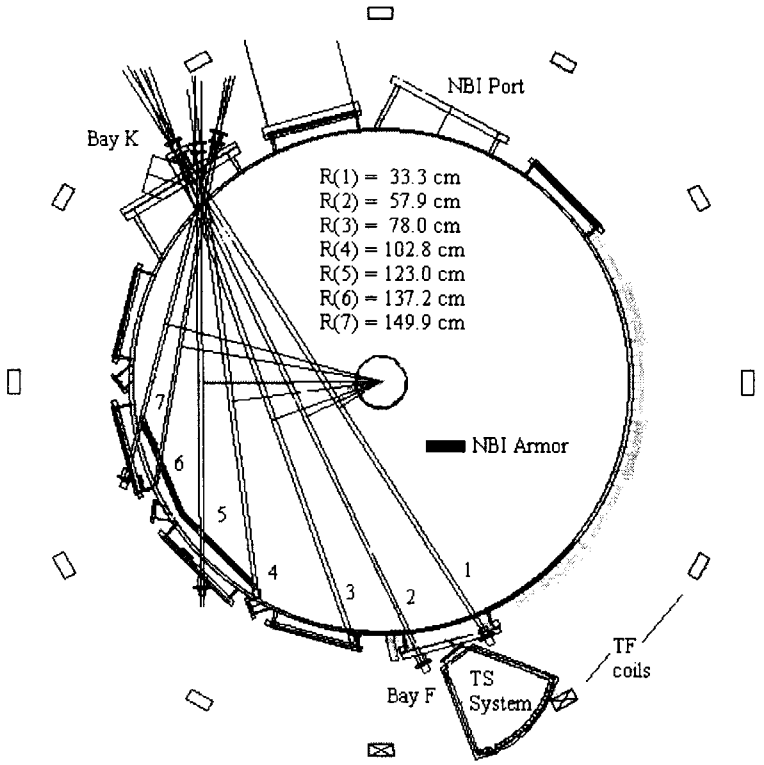

Fig. 1. Schematic illustration of top view of beam arrangement for the FIReTIP system on NSTX. Seven beam lines are shown together with retro-reflectors and windows. NBI beam armor and penetration holes are indicated in this figure.

each chord is utilized to provide density information and the interferometer phase signal is basically ignored. The assumption of a constant and known toroidal magnetic field, while essentially correct in the case of tokamaks and stellarators, is not valid for the case of spherical torus devices such as the spherical tokamak and the spheromak. Hence, the FIReTIP system utilizes both the interferometer phase and the Faraday rotation angles to extract both density profile and toroidal magnetic field profile information. Simulation results for nominal NSTX parameters shown in Fig. 2, demonstrate a large signals (~10 interferometer fringes and ~10° of Faraday rotation) with good signal-to-noise ratios (minimum detectable signal for interferometer and Faraday rotation are 1/32 fringe and 0.02°, respectively), while the refraction of the beam is insignificant (< 0.5 mm).

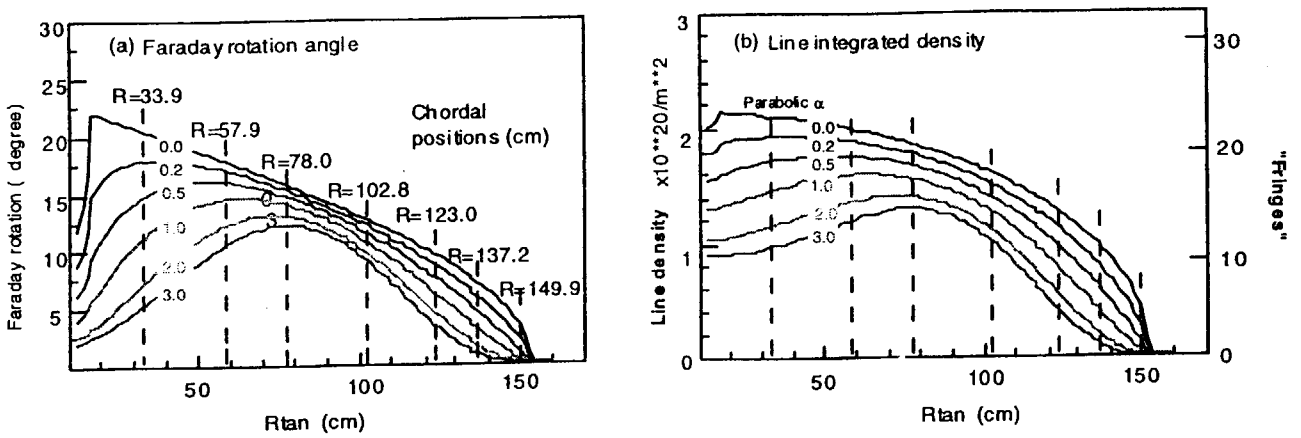

Fig. 2. The choice of 119 μm is ideal for NSTX parameters: Simulation results for NSTX parameter (R_{inside} = 17 cm, $R_{outside}$ = 153 cm, R_{axis} = 98.6 cm, Shafranov shift = 20 cm, B = 0.3 T) show (a) Faraday rotation angle and (b) line integrated density as a function of tangential position. The central electron density is assumed to be 7.5 x 10^{13}/cm^3 with various profile shape factors (α) for $n_e(\rho)=n_e(0)[1-(r/a)^2]^{\alpha}$.

Measurement of the Faraday rotation signal will be performed via a variation of the rotating elliptically polarized wave technique that was successfully implemented first by Rice[6,7] on the MTX tokamak. A major limitation of the rotating half-wave plate is the limited modulation rate (< 10 kHz) that can be created by the mechanically rotating plate. This limitation can be removed by replacing the rotating plate by an additional FIR laser. In this approach pioneered by Rommers and Howard on RTP[3], the rotating elliptically polarized wave is formed by injecting two co-aligned counter-rotating circularly polarized laser beams into the plasma. This scheme is illustrated in Fig. 3. The beams, generated by separate FIR lasers with frequencies ω_2 and ω_1, are offset to allow the use of heterodyne detection methods.

A polarizing grid or polarizer is placed in front of each mixer, forming three IF signals corresponding to the difference frequencies $\omega_2-\omega_1$, $\omega_1-\omega_{LO}$, and $\omega_2-\omega_{LO}$. The interferometer phase ϕ can be obtained from the average of the phase changes registered by the two probe-LO signals with the difference between the two phase angles being equal to twice the Faraday rotation angle ϕ_m. Alternatively, the Faraday rotation angle may be determined directly by

the mixing product between the two probing waves. The Faraday rotation measured by these two techniques is equivalent, although signal-to-noise concerns may favor one over the other.

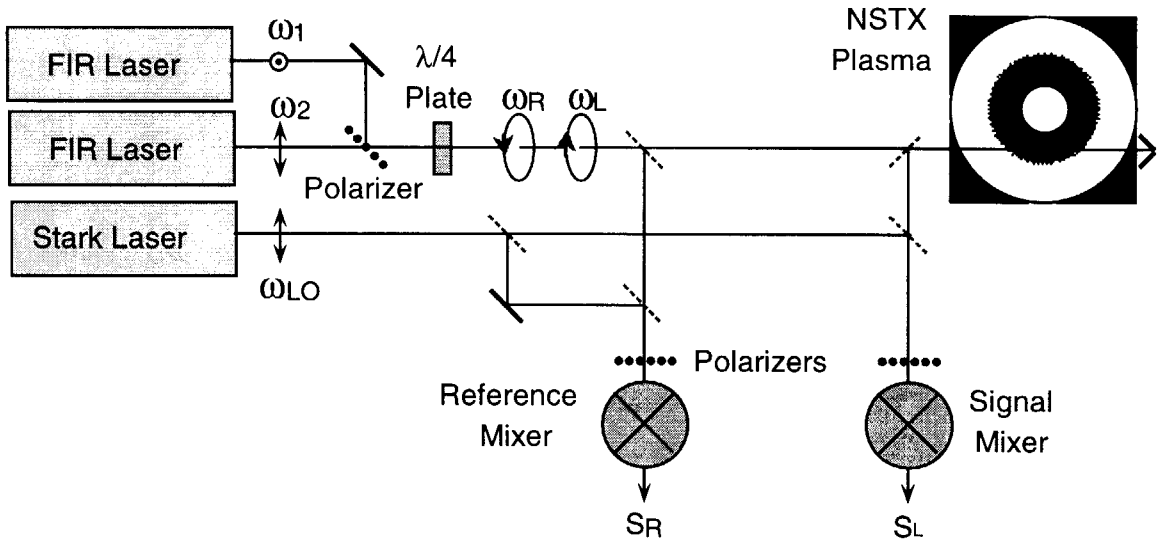

Fig. 3 Schematic illustration of the triple laser approach to be implemented on NSTX

Since the FIReTIP system utilizes three lasers, there are practical problems to be considered in order to maintain the required IF frequency. Two FIR lasers will run at 119 μm with a difference frequency of 2 MHz and the difference frequency will be maintained by mechanical cavity tuning. The third laser, LO source, will be a Stark-tuned laser operating at offset frequency of 5 MHz which will be controlled by a combination of applied electric field and mechanical tuning. Therefore the three IF frequencies will be $\omega_1-\omega_{LO} = 4\pm0.75$ MHz, $\omega_2-\omega_{LO} = 6\pm0.75$ MHz and $\omega_1-\omega_2 = 2\pm0.5$ MHz, respectively. Note that only a single detector is required for each chord in the tangential interferometer system, but that a total of three digitizers would be required for simultaneous interferometer (1 per chord) and polarimeter measurements (2 per chord). A phase-locked quadrature phase comparator system will be used to detect both density and Faraday rotation signals with high temporal resolution[8]. In this approach, the ~2 MHz raw polarimeter signals can be transformed into quadrature Faraday rotation signals with a significantly fast temporal resolution.

3. Optical System Design and Future plan

The preliminary analysis results[1] have pointed out that the most well suited wavelength for this measurement technique is 119 μm, based on optimizing the signal to noise ratio and minimizing problems associated with the beam refraction for NSTX plasma parameters. Therefore the experimental design is largely based on utilizing existing hardware custom designed for the TFTR MIRI system. For instance, the windows fabricated for FIReTIP system are based on etalon cut crystal quartz window material from TFTR MIRI system. FIR laser system optimized for 119 μm operation will be combined with a modern CO_2 laser developed by the UCD group. In addition, there are numerous optical parts and control systems that can be used for the FIReTIP system.

The three laser system will be located in the test cell basement and optical arrangements for the initial installation (phase1) are shown in Fig. 4. Here, the laser system and optical tables are

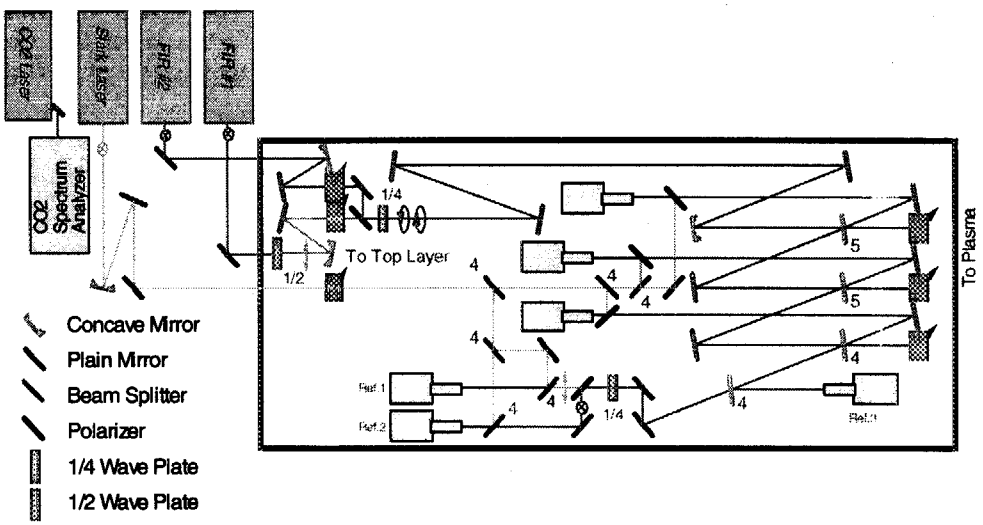

Fig. 4. Top view of the phase 1 optical arrangement for FIReTIP system. The laser system is located in the test cell and beams are separated using wire-mesh beam splitters [4 and 5 stand for 400 and 500 lpi, respectively].

positioned on the NSTX test cell level. It is important to minimize a distortion of the circular polarization required for this measurement. The wire-meshes[9] (400 and 500 lpi) at a small angle (~10°) will be used to split the beams. In this arrangement, the FIR laser beams are transported to and from the NSTX vacuum vessel via an enclosed fiber glass structure. In early year 2000, laser system will be installed to operate three channel (#1, #2, and #3) interferometry system. At the same time, the polarimeter system will be tested. The seven channel system will be completed in year 2002 and the optical arrangement will be quite similar to this initial system.

Since this system will entirely rely upon the retro-reflectors mounted on the wall of vacuum vessel, the research must be concerned with the identification of a possible vibration compensation, even though the fringe shift is expected to be large (up to ~30 fringes). If the initial operation (three channels) could not serve as a reliable density measurement tool, it will provide the scope of the visible compensation laser system needed for the system but it is not a necessary condition. **Here, if one is only interested in the Faraday rotation signal, there is no need for a two color (i.e. two wavelength) system to separate out the effect of mechanical vibrations. This is because the Faraday rotation signal is derived from the phase difference of two co-propagating circularly-polarized (left and right) signals which experience the phase change due to mechanical vibration. Such is not the case for the interferometer signals themselves. For the interferometer signals, the use of co-propagating visible light interferometer system may prove necessary. We plan to install first a single channel polarimeter system to study this problem, and design and incorporate a co-propagating visible light laser interferometer system based on the test results obtained in the early operation stages.**

4. Summary

This paper presents a multi-purpose Far Infrared Tangential Interferometer/ Polarimeter (FIReTIP) system to measure $B_T(r,t)$ and $n_e(r,t)$, simultaneously on NSTX. It is essential to

make a measurement of time dependent toroidal field variation in NSTX, since paramagnetism and diamagnetism will alter the vacuum magnetic field significantly in the presence of plasmas in spherical torus.

Acknowledgment

This work is supported by the U.S. Department of Energy under contract Nos. DE-AC02-76-CHO-3073 and DE-FG03-95ER54295.

References

1. H. Park, C. Domier, W.R. Geck and N.C. Luhmann, Jr., "Far Infrared tangential interferometer/polarimeter on National Spherical Tokamak Experiment", *Review of Scientific Instruments* 70, pp 710—713 (1999).
2. F.M. Levinton, "The motional Stark Effect: Overview and Future Development", *Review of Scientific Instruments* 70, pp. 810-820 (1999).
3. J.H. Rommers, A.J.H. Donné, F.A. Karelse and J. Howard, "The Multichannel Triple-Laser Interferometer/Polarimeter System at RTP," *Review of Scientific Instruments* 68, pp. 1217-1226 (1997).
4. H.J. Gardner and J. Howard, "Faraday Rotation as a Density Diagnostic for Helical Axis Stellerators," *Plasma Physics and Controlled Fusion* 36, pp. 245-258 (1994).
5. F.C. Jobes, "Midplane Faraday Rotation: A Tokamak Densitometer," *Review of Scientific Instruments* 66, pp. 386-388 (1995).
6. B.W. Rice, "Fifteen Chord FIR Polarimeter System on MTX," *Review of Scientific Instruments* 63, pp. 5002-5004 (1992).
7. B.W. Rice, "Poloidal Field Measurements on MTX Using Far-Infrared Polarimetry," *Proceedings of the U.S.-Japan Workshop on Millimeter and Submillimeter Wave Plasma Diagnostics*, (Los Angeles, CA December 9-11, 1992).

8. C.W. Domier, W.A. Peebles, and N.C. Luhmann, Jr., "Millimeter-Wave Interferometer for Measuring Plasma Electron Density," *Review of Scientific Instruments* 59, pp. 1588-1590 (1988).

9. Y.S. Hwang and H.K. Park, "Polarization Characteristics of Wire Mesh at 119 μm," *Applied Optics* 28, pp. 4999-5001 (1989).

1-11 New Applications of Microwave

A.Ejiri, K.Tanaka[A], K.Kawahata[A], Y.Ito[A] and T.Tokuzawa[A]
Graduate School of Frontier Sciences, Univ. Tokyo, Tokyo 113-0033, Japan
[A]National Institute for Fusion Science, Toki 509-5292, Japan

Abstract

Interferometry and reflectometry measure phase of the transparent or the reflected wave to derive the information on plasma density. Homodyne reflectometry for an interlock and transmissiometry for sheet plasma measurements could be another class of microwave diagnostics which does not measure the phase.

1. Homodyne reflectometry for an interlock

In helical system, neutral beam is usually injected to a target plasma produced by other methods. If the neutral beam is injected to a very low density plasma most of the injected particles go to the wall directly, so that they cause damage to the vacuum vessel wall. Thus, we need some kind of interlock of NBI. Since the possibility of particles to hit the wall depends on density, a method to determine whether the plasma has the density high enough to avoid such problems is appropriate. In contrast to tokamaks, plasma current or stored energy can not be used as an indicator of target plasma in helical systems. Interferometry is a standard diagnostic to measure density, but it requires appropriate signal or data processing to provide real time density information. In addition, one must be careful to fix integer fringe ambiguity, and it could be impossible to do it in some cases (e.g. after pellet injection). Homodyne reflectometry has been proposed as a density interlock for NBI in LHD. It has the possibility to satisfy the requirements as an interlock.

A reflectometer launches microwave to a plasma and measures returned wave which is reflected at a cutoff in the plasma. In the case of ordinary mode (O-mode) the cutoff condition depends on the density. For a given microwave frequency, the reflection occurs if the maximum density exceeds the critical density for the frequency. This idea has been test with a homodyne reflectometer in Compact Helical System (CHS). The frequencies 26.5, 32.5, 40 GHz were launched to the plasma from the midplane along the major radius. The polarization is matched to have pure O-mode around the plasma edge. In addition the same antenna is used to launch and receive the wave. When the maximum density is below the critical density for the launched wave frequency, the system measures the wave of interferometry path, in which the wave penetrates the plasma and reflected at the inner wall of the vacuum vessel. At the initial phase of a discharge, the density is very low, and the homodyne signal

show a large amplitude sinusoidal oscillation (Fig.1(a),(c)). This corresponds to the phase change of the interferometry path. With the increase of density the amplitude decreases and the sinusoidal oscillation disappears quickly. With the father increase of density fluctuating signals with much higher frequencies grows. This signal arises from the wave reflected at the cutoff. This picture was confirmed by comparing the signal behavior with the position (and/or appearance) of cutoff (Fig.1(b)), which is calculated from the density profile obtained by a multi chord HCN laser interferometer. In order to distinguish the slow oscillation due to inteferometry from the high frequency fluctuations due to reflectometry a numerical frequency filter is applied to the signal. The frequency band is adjusted to get clear contrast in the final signal before and after the appearance of cutoff (Fig.1(d)). Qualitatively similar behavior are obtained in the other frequencies.

A homodyne reflectometer with the frequency 34.9 GHz has been installed into LHD. Figure 2 shows a case where the reflectometer provided an interlock signal, by which NBI was terminated. The system provides rms amplitude of the homodyne signal (Fig.2(b)). At the highest density, the radiation power increased abruptly and the plasma collapsed. Then the density and the rms amplitude decreased. When the rms amplitude became below a threshold level, the digital signal, which indicates the existence of the cutoff, turned off. Then NBI was stopped.

2. Transmissiometry for sheet plasma measurement

Measurement of transmitted wave can be another class of microwave diagnostics in which phase is not measured. When microwave propagate to a cutoff, the wave is reflected and it cannot pass through the cutoff, because the region beyond the cutoff is an evanescent region where the wave is exponentially damped. If the evanescent region is not too thick, the wave with a damped amplitude appears from the opposite surface of the cutoff, and can propagate forward. In the following, we propose microwave transmissiometry, in which microwave is injected perpendicularly to a sheet plasma, and the transmissivity is measured to obtain density information.

The transmissivity can be represented by the Gamov's penetration factor, which is a function of density profile for O-mode propagation. Let us consider a sheet plasma, and microwave is injected perpendicularly. When the microwave frequency is well above the maximum plasma frequency the microwave pass through the plasma. As the frequency decreases from the maximum plasma frequency the transmissivity decreases quickly, and the reflectivity becomes almost 100%. The behavior of the transmissivity can be represented by Gamov's penetration factor except the frequency around the maximum plasma frequency. This is because the WKB approximation fails in this region. Figure 3 shows the transmissivity as a function of probing frequency for parabolic density profile with three

different widths. One dimensional wave equation is solved to calculate transmissivity and plotted in the same figure. These show good agreement. For parabolic profiles the transmissivity becomes a straight line in the semi-logarithm scale. As the width increases the slope of the line becomes steep. Figure 3 shows the principle of transmissiometer. When we measure the transmissivity with a frequency swept source, we will obtain a curve similar to Fig3. The maximum density is obtained from the frequency where the exponential curve and the flat line intersect. The information on the profile will be obtained from the slope.

While a parabolic profile shows a line in the semi-logarithm scale, the curvature changes its sign as the index of the profile passes the value 2 (Fig.4). Although this feather yields the possibility of getting the profile shape, the determination of profile may be a complicated procedure.

In the following, several points which degrade the performance of transmissionmetry are listed. When a plasma is thick, the slope in the exponential region becomes very steep. In this case the accurate measurement will be difficult because of the accuracy in the frequency and because of the finite dynamic range in transmissivity measurement. For given dynamic range and relative frequency accuracy, the measurable width decreases with the frequency. Multi reflection causes another difficulty in the measurement. If there exists significant level of multi reflection at the launching side, both waves interfere, and the effective amplitude of the incident wave changes. The same effect could happen in the transmitted region. These lead to an error in the measurement. Tilting the beam from perpendicular direction to the plasma is one of the method to reduce the effect. However, it destroys the one-dimensional configuration, and refraction causes new error in the measurement. Thus, the multi reflection should be avoided by appropriate isolators. If inhomogeneity in the density and width exists, the transmitted wave experiences different phase shift within the cross section of the beam, so that refraction of the beam occurs. The refraction causes the wave to escape from the receiving antenna, and it results in an error of the measurement. Semi-analytic study shows that mild homogeneity in the width and density of the sheet is required to avoid the effect of refraction.

3. Summary

Homodyne reflectometry for an interlock and transmissiometry for sheet plasma measurement could be another class of microwave diagnostics in which phase is not measured. They are characterized by their simplicity. The former has been tested in CHS and applied to NBI interlock in LHD. It is operated routinely. The feasibility of latter has been studied. And it is shown the target sheet plasma should be thin, and it should have mild homogeneity along the sheet. Transmissiometry may be applied to diverter plasmas and process plasmas.

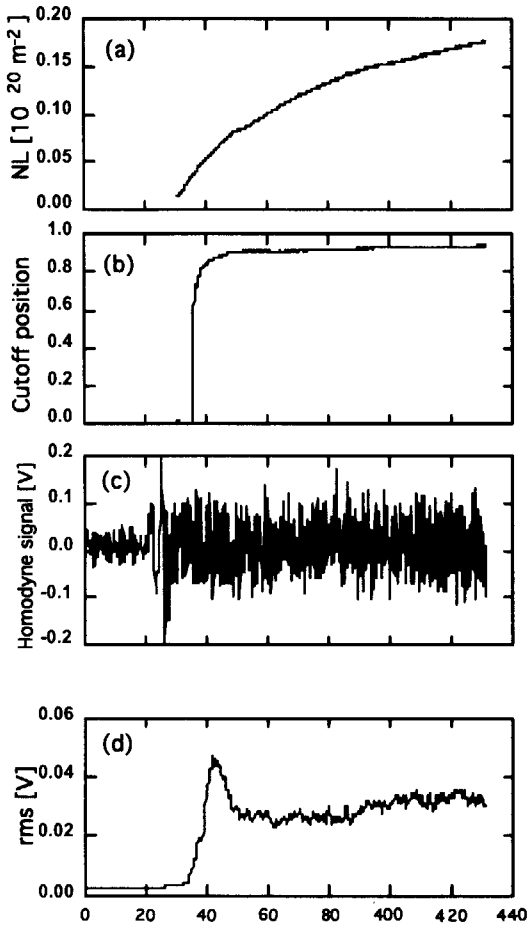

Fig.1 Time behavior of line integrated density (a), normalized radius of the cutoff position (b), homodyne signal (c), rms amplitude (d).

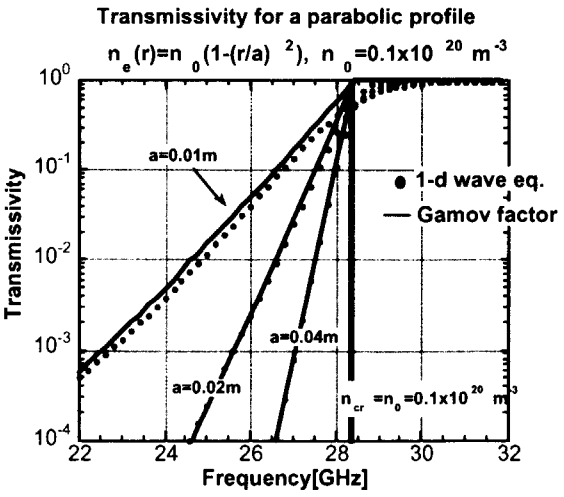

Fig.3 Transmissivity as a function of frequency for parabolic density profiles with different widths.

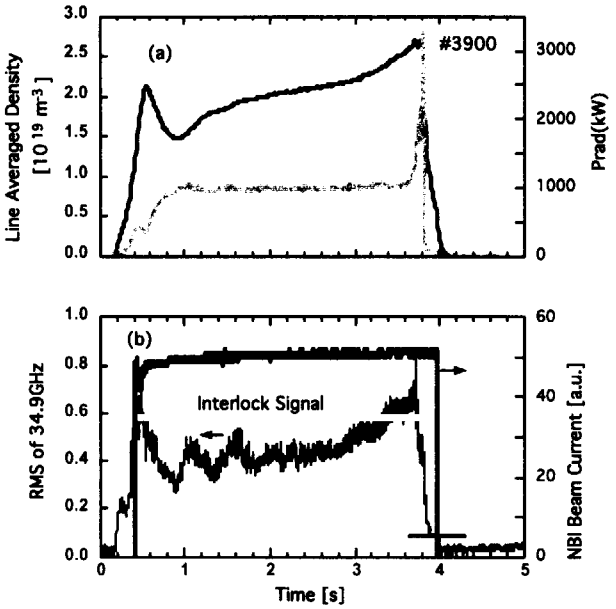

Fig.2 Time behavior of line integrated density and radiation power (a), rms amplitude, interlock signal and NBI (b).

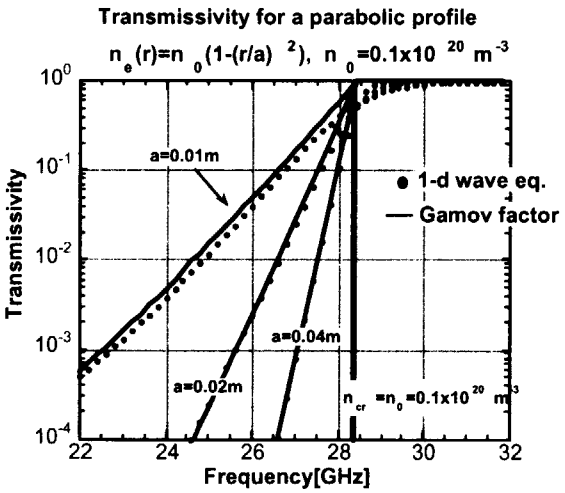

Fig.4 Transmissivity as a function of frequency for various density profiles with same FWHM.

2-1 Millimeter-Wave Imaging on GAMMA 10 and LHD

A. Mase [a], H. Negishi [b], N. Oyama [c], K. Watabe [d], K. Mizuno [e], Y. Nagayama [f], K. Kawahata [f], H. Matsuura [g], K. Uchida [g], A. Miura [g], Tamano [b], K. Yatsu [b]

[a] *Advanced Science and Technology Center for Cooperative Research, Kyushu University, Kasuga 816-8580, Japan*
[b] *Plasma Research Center, University of Tsukuba, Tsukuba 305-8577, Japan*
[c] *Japan Atomic Energy Research Institute, Naka 311-0193, Japan*
[d] *Communications Research Laboratory, Koganei 184-8795, Japan*
[e] *Research Institute of Electrical Communication, Tohoku Univ., Sendai 980-8577, Japan*
[f] *National Institute for Fusion Science, Toki 509-5292, Japan*
[g] *Department 1, Teratec Co., Musashino 180-0006, Japan*

Millimeter-wave imaging system in the frequency range of 70-140 GHz was developed for diagnostics of magnetically confined plasmas. It successfully measures time evolutions of three-dimensional (radial and axial) profiles of line density and electron cyclotron emission (ECE) in the plug cell of the GAMMA 10 tandem mirror. It is also being installed in Large Helical Device (LHD). In order to cover the frequency range of the second harmonic ECE on LHD, a novel detector using monolithic microwave integrated circuit (MMIC) technology is designed and fabricated. The optical system consisting of an ellipsoidal and a flat mirrors is constructed and evaluated experimentally at 140 GHz.

1. INTRODUCTION

Millimeter-wave imaging diagnostic technique has been developed for measurements of density and temperature profiles and their fluctuation components in magnetically confined plasmas [1,2]. This technique uses a single set of optics and multichannel detector array instead of a multichannel optical path with a single detector for each chord.

We have developed a millimeter-wave two-dimensional imaging system for the application to the GAMMA 10 tandem mirror at the University of Tsukuba. It consists of a quasi-optical transmission line with parabolic and ellipsoidal mirrors and a heterodyne receiver with frequency of 70 GHz. The detector is 16 elements of beam-lead GaAs Schottky barrier diodes bonded to bow-tie antennas, which is called as a hybrid-type detector. Imaging system is also constructed in order to apply to the ECE measurement on Large Helical Device (LHD) at the National Institute for Fusion Science (NIFS). The frequency of the second-harmonic ECE on LHD ranges from 120 GHz to 180 GHz in phase II, and from 190 GHz to 260 GHz in the final phase, respectively. In order to cover above frequency range, monolithic-type detectors are designed and fabricated. The characteristics of the monolithic-type detector and the results of the experimental evaluation of the optics are reported in this paper.

2. EXPERIMENTAL APPARATUS

2.1. 2D imaging system on GAMMA 10

Schematic of the 2D imaging system on GAMMA 10 is shown in Fig 1. It is installed in the west-plug cell (z=971 cm), where z is the axial distance from the central-cell midplane. The optical system of the probe beam is designed using Gaussian-beam propagation theory. A scalar-feed horn produces symmetric radiation pattern with low sidelobes, which is well fit by Gaussian distribution. Probe beam is expanded by an off-axis parabolic mirror installed inside the vacuum vessel to cover upper-half of the plasma. The cross section of the probe beam is 200 mm x 200 mm at the plasma center. The receiving optics, an ellipsoidal

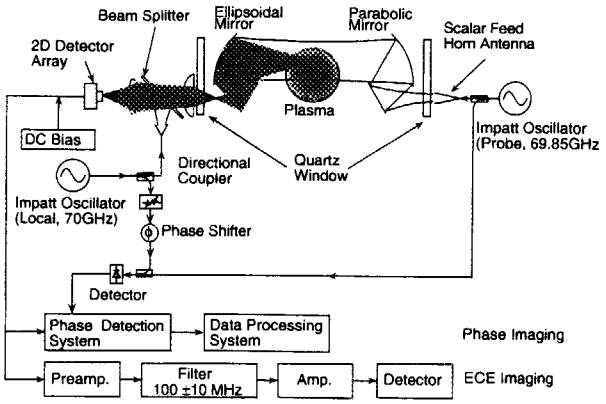

Fig. 1 Millimeter-wave imaging system installed in the GAMMA 10 tandem mirror.

mirror, a flat mirror, and polyethylene lenses, are designed by using a ray-tracing method to focus radiation signals onto a detector array. The diameter of the mirrors and lenses are determined in order to obtain desired resolution calculated using diffraction theory. The magnification of the optical system is designed to be 0.33.

The detector array consists of beam-lead GaAs Schottky barrier diodes bonded to 4 x 4 bow-tie antennas. It is installed inside an aluminum box for electrical shielding, and a 2D pyramidal horn antenna array in TE_{10} mode is attached to the input of the detector. A dichroic plate, made of 10 mm thick aluminum with 4.0 mm diameter hole and 4.5 mm spacing, is also attached to the vacuum window of the receiver side. Circular holes act as highpass filters to prevent the mixture of electron cyclotron resonance heating (ECRH) power with frequency of 28 GHz.

The imaging system is configured as a heterodyne interferometer as well as a heterodyne radiometer. The quadrature-type detection system provides the phase difference between two IF signals that is proportional to line density of the plasma. The second-harmonic ECE signals in the ordinary mode are mixed with local oscillator (LO) power on the detector array. The intermediate frequency (IF) signals amplified by 85 dB are fed to the band pass filter with passband of (100 ± 10) MHz, and are square-detected. Thus, the phase imaging and the ECE imaging in the O-mode can be obtained simultaneously.

2.2. ECE imaging system on LHD

The optics for ECE imaging on LHD are designed by using the similar method as shown in 2.1. An ellipsoidal mirror and a plane mirror located inside the vacuum vessel converges the ECE signals to pass a fused-quartz vacuum window with 192 mm in diameter. An object plane located at the plasma center is 3.0 m in front of the ellipsoidal mirror. The magnification of the optics is 0.68.

New monolithic-type detectors have been fabricated for the purpose of high frequency ECE on LHD plasmas. The details of the fabrication and mask pattern are shown in elsewhere [3]. It consists of the integration of a bow-tie antenna, down-converting mixer using a Schottky barrier diode, and hetero-junction bipolar transistor (HBT) amplifiers on a GaAs substrate. The HBT works as an IF amplifier with 10 dB voltage gain. The GaAs chip with 4.0 mm x 2.0 mm x 0.625 mm is mounted on the case made of gold-plated brass together with alumina substrate for dc bias of the SBD and HBT amplifiers. A coplanar waveguide on the other substrate is used for the connection of an IF output to a SMA connector.

3. EXPERIMENTAL RESULTS AND DISCUSSIONS

3.1. GAMMA 10 results

The detailed descriptions of the GAMMA 10 device are shown in elsewhere [4]. In each plug/barrier cell, two separate 28 GHz gyrotrons are used. Fundamental ECRH in the plug

region (ECRH-P) and second-harmonic ECRH in the barrier region (ECRH-B) produce warm and hot electrons that are necessary for effective formation of thermal barrier and confining (plug) potentials. When the ECRH power is applied at t=90 ms, the plug potential is created near the position of z=962 cm where the magnetic field strength equals to 1 T. At the region of z=971 cm where the imaging system is installed, the loss particles decrease due to the formation of the plug potential. The changes of the density profiles due to the application of the ECRH are clear as shown in Fig. 2. When the ECRH is turned off, the confining potential disappears, and a short burst appears in the line-density signal corresponding to the axial drain of the plasmas. The variation of the profile in the axial direction is caused by the change of the magnetic field. It is noted that the density profile in the core region decreases during the injection of the ECRH power. This region corresponds to that of the effective confining potential which coincides to the radial profile of the plug-ECRH power deposition. The phase resolution is estimated to be less than 1/200 fringe, where 1 fringe equals to the line density of 5.1×10^{13} cm^2 at 70 GHz.

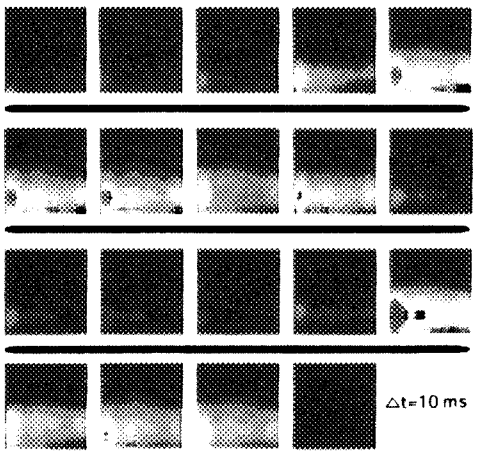

Fig. 2 Time evolution of radial and axial line-density profiles. The ECRH power is applied during t=90-140 ms. The vertical scale is 70 mm and the horizontal scale is 60 mm.

The imaging system is applied to the measurement of ECE. In the present experiment, the optical thickness of the second-harmonic O-mode is estimated to be less than 1 in the plug-cell plasma. The ECE signal starts to increase when the ECRH power is injected at t=90 ms and continues to be observed after the bulk plasma disappears at t=150 ms. This means that the ECE signal is mainly attributed by the mirror-trapped hot electrons. The hot electrons with energy up to 60 keV are produced by a combination of the ECRH-P and ECRH-B powers, which is useful for the formation of thermal barrier potentials in a tandem mirror plasma. It is shown that the ECE intensity for the simultaneous injection of the ECRH-P and ECRH-B is much larger than the sum of the intensity for the individual injection of each ECRH. This is due to the heating efficiency of the ECRH.

3.2. Performance test of LHD imaging system

The Airy pattern of a point source is measured in order to confirm the performance of the optical system. A 140 GHz source is located at the position corresponding to the plasma center. The source is imaged onto the detector array. The Airy patterns in the horizontal plane are shown in Fig. 3. The magnification of the optical system is also investigated experimentally, which agrees well with the designed value of 0.68.

The heterodyne characteristics of the MMIC detector are measured in a test stand using two oscillators in the frequency range of 70-140 GHz. One oscillator is used as an LO signal and the other as a radio frequency (RF) signal. Two signals are combined by a directional coupler, and radiated to the detector through a waveguide antenna. The heterodyne IF signal is fed to a spectrum analyzer. Figure 4 shows the heterodyne signal intensity as a function of IF measured with a spectrum analyzer. It is noted that rather flat response from 0.2 GHz to 9 GHz is obtained in contrast to a hybrid detector using a beam-lead SBD, which is probably

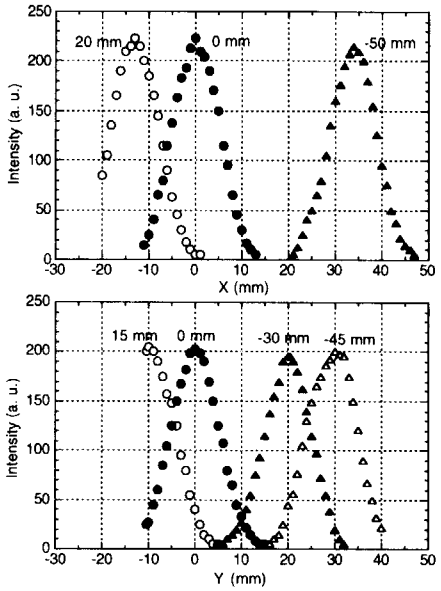

Fig. 3 Airy pattern of LHD optical system in the horizontal plane (top), and the vertical plane (bottom).

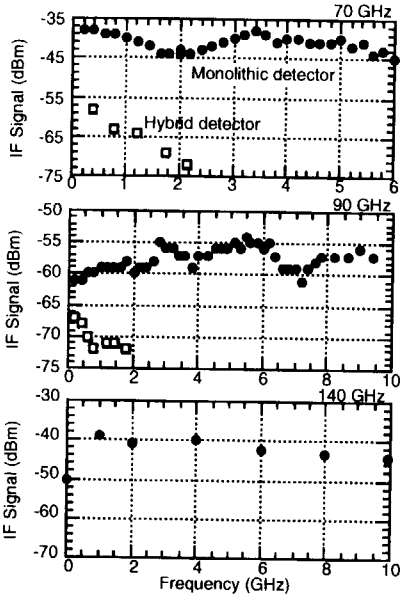

Fig. 4 Heterodyne characteristics of two tupes of detectors as a function of IF at 70, 90, and 140 GHz (from top to bottom).

due to the method of housing of the semiconductor chip as well as due to the small inductance of the signal line and the performance of the SBD. The present IF bandwidth, however, is limited to 9-10 GHz. This is mainly caused by the bandwidth of the HBT amplifiers. The IF bandwidth larger than 10 GHz is observed without HBT amplifiers. The heterodyne conversion loss of the detector, determined by scanning the LO power is estimated to be 8-12 dB at IF=3 GHz and LO frequency of 70 GHz.

4. SUMMARY

In summary, a millimeter-wave 2D imaging array has been applied to the GAMMA 10 tandem mirror. The optical system consisting of a parabolic mirror and an ellipsoidal mirror installed inside the vacuum vessel is effective to ease the restriction of the view by the vacuum windows. The imaging array successfully measures the time evolution of the second-harmonic ECE profiles as well as the 3D line-density profiles.

The optics for ECE imaging on LHD are designed by using the similar method as the GAMMA 10 system. The Airy pattern of a point source and the magnification factor at 140 GHz are in good agreement with the designed values. A novel detector using MMIC technology has been fabricated in order to apply the high frequency ECE measurements. The heterodyne characteristics of the detector are evaluated for various values of intermediate frequency. The response up to 8-10 GHz is confirmed and the low LO power requirement is identified. These are attractive to the measurement of ECE in large plasma devices.

ACKNOWLEDGMENTS

This work was supported in part by a Grant-in-Aid for Scientific Research from the Ministry of Education, Science, Sports and Culture, and also performed under the collaborating research program at the National Institute for Fusion Science.

REFERENCES

[1] B. H. Deng *et al.*, Rev. Sci. Instrum. 70 (1999) 998.
[2] N. Oyama *et al.*, Rev. Sci. Instrum. 70 (1999) 1003.
[3] H. Matsuura *et al.*, Electronics Lett. 33 (1997) 1800.
[4] K. Yatsu *et al.*, Proc. IAEA Fusion Energy Conference, Yokohama, Oct.19-24 (1998). (to be published in Nucl. Fusion)

2-2 Electron Cyclotron Emission measurements by means of a Grating Polychromator on the Large Helical Device

P.C. de Vries, K. Kawahata, Y. Nagayama, S. Inagaki, H. Sasao and Y Ito

National Institute for Fusion Science, 322-6 Oroshi-cho, Toki-shi, 509-5292 Japan

The electron cyclotron emission (ECE) spectrum at the Large Helical Device (LHD) is measured by a 14-channel grating polychromator. During standard operation the polychromator monitors 2nd harmonic frequencies (100 - 150 GHz) with a spectral resolution of 1.5 GHz. At sufficient high density the 2nd harmonic X-mode polarisation is optically thick and can be used to determine the temperature profile. However, the large magnetic field shear in LHD affects the ECE polarisation. This effect has been studied numerically. The wave polarisation was found to rotate in the laboratory frame. Experiments have been carried out by means of a polarisation rotator in the diagnostic waveguide system, which confirmed the calculations. By a proper setting of the polarisation rotator, the rotation can be corrected and pure X-mode is detected. Temperature profiles have been measured successfully by the polychromator.

Keywords: ECE Diagnostics, Mode Conversion, Large Helical Device

1. Introduction

The electron cyclotron emission (ECE) spectra from magnetised plasmas, in particular tokamaks, have been used for many years to determine the electron temperature profile. The analysis is straightforward. Different spectral components are emitted from a different position in the plasma, depending on the magnetic field. Two polarisation modes exists for ECE waves: X-mode with the electric field vector perpendicular to the magnetic field and O-mode with a parallel electric field vector. The two polarisation modes have different refractive indices and, hence, propagate differently through the plasma towards the diagnostic antenna. A specific harmonic and polarisation mode of the spectrum is monitored, which is optically thick, such that its intensity is proportional to the temperature.

However, the situation is more complex in the Large helical Device (LHD: R_{ax}=*3.75* m, *a=0.6-0.9* m B_{ax}=*1.5-3* T). The magnetic field configuration of a helical system, like LHD, differs from that of a tokamak. The field strength is a non-monotonic function of the radius, hence one frequency can be emitted at various positions in the plasma. Furthermore, the magnetic field is highly sheared. This large shear causes the propagation of the two polarisation modes to be coupled, with as a result mode conversion and polarisation rotation. The polarisation effects of the LHD plasma have been studied numerically [1]. A brief overview of the results will be given in this paper.

Beside a heterodyne radiometer [2,3,4] and Michelson interferometer [2,4], a grating polychromator is used to measure the ECE spectrum. The details of the diagnostic apparatus will be described in section 2. Experiments have been carried out in order to determine the polarisation of the ECE spectrum. In section 3 the results will be discussed and compared with the theoretical calculations. In section 4 it will be shown that electron temperature profiles can be resolved using the ECE spectra from LHD.

2. The grating polychromator at LHD

The advantages of a grating polychromator (GPC) are the high temporal resolution and the possibility to utilise the system over a broad wavelength range: $(\lambda_{max} - \lambda_{max})/\lambda_{centre} = 0.4$. The grating polychromator at LHD is set-up in a Czerny-Turner mount in order to avoid a large stray-light level. Grating polychromators have been applied to diagnose ECE radiation on various devices. A 14-channel system is presently operated at LHD that will be described below.

2.1 The waveguide system

The microwaves are received via the ECE diagnostic antenna and is *60m* circular oversized waveguide system [2]. The antenna views the plasma in the equatorial plane. A polarisation rotator and a polarisation splitter directs the appropriate polarisation mode towards the GPC. It was measured that a linear polarised wave rotates its polarisation over *33°* while being transmitted through the waveguide. As will be discussed later, the LHD plasma itself may also cause a polarisation rotation. The polarisation rotator can be used to correct for these effects. Before the entrance to the polychromator two low-pass-filters prevent higher order mode radiation (The cut-off frequencies are: $f^{co} = 248$ *GHz* and $f^{co} = 168$ *GHz*). In order to prevent damage by high power ECH sources, a notch filter was installed in the waveguide system [2].

2.2 The grating polychromator

Fig 1. shows the set-up of the grating polychromator. The circular waveguide is tapered to rectangular WR284. The electric field vector of the wave is directed horizontally. The microwaves enter via slit of *12 × 34.85 mm* and two small mirrors (*M1/M2*). Via a collimating mirror (*M3: 300 × 300 mm*) the microwave beam is focused on the grating (*G: 300 × 300 mm*). The grating consist of vertical grooves with a blaze angle of: $\theta_{blaze} = 20°$. It has an efficiency of *0.7 - 0.9* in the wavelength range: $\lambda/d = 0.5 - 1.2$, i.e. ($d = 3$ mm) $f = 200 - 83$ GHz. Gratings with a groove constant of $d = 2.3$, *3* and *5 mm* can be applied. The angle of the grating can be adjusted mechanically. The blazed grating scatters its refraction pattern on a large focusing mirror (*M4: 600 × 300 mm*) with a focus point of $R = 1500$ *mm*.

2.2 Detectors and data acquisition

The mirror (*M4*) directs the different wavelengths into 14 detector entrance slits of: *10.2 × 50 mm* (E-band waveguides), which are connected to the detectors. Each channel has a spectral resolution of $\Delta f^{FWHM} = 2.5$ GHz. The 14 liquid He-cooled detectors InSb diodes are mounted in a cryostat.

Low-noise pre-amplifiers, with a tuneable gain of *40* or *60* dB, are directly mounted on the cryostat. The signals are fed to the main amplifier/filter bank with gain settings of *1, 3, 10* × and filter settings of *10, 100* kHz and *1* MHz. The output can be digitised with a sampling rate of *250* kHz for *2* s. For long pulse operation additional data is stored with a sampling rate *10* kHz.

3. The polarisation of electron cyclotron emission spectrum

The plasma is a refractive medium for microwaves. While the ECE waves travel from the resonance, where they are emitted, towards the antenna, they can be refracted, re-absorbed or

reflected. Because X and O-mode have different refractive indices, their propagation differs too.

LHD has a specific magnetic field configuration (see Fig. 2). It has a maximum in the centre and a large shear (B^{pol}/B^{tor} is of order unity at $r=a$). Thus, each frequency, emitted at a different position, will have its X-mode polarisation under a different angel in the laboratory frame. Furthermore, the shear causes the propagation of the two polarisation modes to be coupled [5].

3.1 Coupled propagation in LHD

If $E_{//}$ and $E_{\perp}$ are the local electric fields of O and X-mode wave, the coupled wave equations of both modes can be written as [5]:

$$\frac{d^2E_{//}}{dr^2}+(\frac{\omega^2}{c^2}N_X^2-\phi^2)E_{//}=+2\phi\frac{dE_{\perp}}{dr}+E_{\perp}\frac{d\phi}{dr},$$

$$\frac{d^2E_{\perp}}{dr^2}+(\frac{\omega^2}{c^2}N_O^2-\phi^2)E_{\perp}=-2\phi\frac{dE_{//}}{dr}-E_{//}\frac{d\phi}{dr},$$

where, N_x and N_o, are the refractive indices for X and O-mode, respectively and ϕ is the gradient of the magnetic shear (see Fig. 2). In tokamak plasmas, were the shear is negligible, one finds the wave equations to be uncoupled. The coupled wave equations were solved for typical ECE frequencies, along their path towards the antenna. At the resonance, absorption and emission were determined according to the proper absorption and emission constants [6].

It was found that strong mode conversion occurred in low-density plasmas ($n_e < 0.25\ 10^{19}$ m^{-3}). However, at higher densities the orientation of the waves electric field vector rotated with the sheared magnetic field in the laboratory frame. In the case of X-mode it remained perpendicular to the field and mode conversion was negligible. In Fig. 3 the angle of the polarisation at the plasma edge for all 2nd harmonic frequencies is given for different densities. At low densities all frequencies exit the plasma under different angles, but at higher densities they undergo polarisation rotation, and exit under approximately the same angle, $\alpha=35°$. Polarisation rotation becomes stronger if the refractive indices of X and O-mode differ, and hence depends indirectly on the density.

Polarisation rotation is profitable, because, X and O-mode can de separated in LHD. Calculations showed that due to the large optical thickness of 2nd harmonic X-mode, wall reflections and emission from the second resonance are re-absorbed before they reach the antenna [1,7].

3.3 Experiments on polarisation

Experiments have been performed in order to verify the polarisation the ECE spectrum. During long pulse operation, the polarisation rotator was turned. The setting of the polarisation rotator was monitored by the data acquisition system. The plasma was sustained by Neutral Beam Injection (NBI) for *6* s. A magnetic field of $B_{ax}=2.75$ T was used. The results are plotted Fig. 4. The central density increased from $n_{e0}=1.5$ to $1.8\cdot10^{19}$ m^{-3}, yielding a decrease of the central temperature. The angle of the polarisation rotator is changed between *0* and *120°*. One of the Grating Polychromator channels (f = *150* GHz, R_{res} = *3.7* m) is plotted. The optical depth of O-mode is always smaller than, $\tau < 0.03$ but the X-mode emission is optical thick ($\tau > 5$). Thus the intensity for this frequency, usually matches the central electron temperature. However, the rotation of the polarisation causes a large oscillation.

In Fig. 5 the ratio between the radiation temperature and electron temperature is plotted versus the angle. This is the real angle of rotation in the LHD laboratory frame, i.e. the

polarisation rotator angle corrected by the offset rotation (see 2.1) in the total waveguide system. An oscillation is observed with a maximum at, $\alpha = \theta(a) \approx 35°$, when $T^{rad} = T^{x} = T_{eo}$. While a minimum is found if pure O-mode is detected. The O-mode intensity is about *70%* of that of X-mode. This high level can be explained by wall X-mode waves that are converted to O-mode upon reflection at the wall, which can propagate without re-absorption through the plasma [1,7]. At intermediate angles a mixture of X and O-mode is measured. The radiation temperature as a function of the polarisation rotator angle, α, for a given spectral component ω, can be given by,

$$T(\alpha) = T^{X} \cos^2(\alpha - \theta(a)) + T^{O} \sin^2(\alpha - \theta(a)),$$

where it is assumed that the wave undergoes perfect polarisation rotation up to the edge of the plasma. If the X-mode is optically thick and the intensity and the O-mode is *70%* of that of X-mode (calculated with an arbitrary reflection coefficient of the LHD wall of $\rho=0.95$ and a mode conversion fraction of $\pi=0.1$ caused by the reflection [1,7]), the above equation can be plotted in Fig. 5. A nice match between the measured and calculated curve is found.

4. Temperature profiles

During standard operation the polarisation rotator is set, such that it corrects for the rotation caused by the plasma, and hence, X-mode is fed to the GPC. Small variations in the polarisation angle, caused by changes in the magnetic field configuration, the position of the plasma edge, or non-perfect polarisation rotation are found to be negligible during normal operation.

Temperature profiles have been measured successfully by the grating polychromator during the last experimental campaigns of LHD. The first measurements will be discussed in this section. Discharges with $B_{ax}=2.75$ T have been analysed using a grating constant of $d = 3$ mm (incident angle of *-4.4* °) covering the frequency range of, *150 - 100* GHz. A radial coverage of, $r/a = 0 - 0.89$ was achieved. Because the magnetic field is a non-monotonous function of the radius in LHD (see Fig. 2) only information of the outside ECE resonance, and thus, half of the temperature profile can be obtained by the GPC. A second antenna, viewing from the opposite side, is required to reveal the inside profile [4].

4.1 Cross-calibration and comparison with Thomson scattering

The GPC is cross-calibrated against temperature profiles measured by the Thomson scattering diagnostic. For this purpose high density discharges ($n_e > 2 \cdot 10^{19}$ m^{-3}) are used, heated by neutral beam injection (NBI) with central electron temperatures of *2* keV.

The temperature profiles measured by Thomson scattering and the GPC matched over a large parameter range: $n_e > 1.0 \cdot 10^{19}$ m^{-3} and $T_e = 1 - 3.5$ keV. A comparison is shown in Fig. 6, where the temperatures of 3 GPC channels (ch. 13: $r/a = 0.08$, ch 8: $r/a=0.49$, ch4: $r/a=0.74$) compared with that given by Thomson scattering. The temperatures of the 2 discharges which are plotted decreased in time.

4.2 Measurements during ECH

The use of electron cyclotron heating (ECH) highly disturbed the grating polychromator signals. The plasma is initially ionised by ECH ($f=83$ GHz). In this initial low-density phase, extreme radiation temperatures up to *8* keV were detected, due to ECH generated non-thermal electrons.

During simultaneous heating of high density plasmas ($n_e > 1.5 \cdot 10^{19}$ m^{-3}) by NBI and ECH non-thermal electrons did not affect the measurement. Nevertheless, it was found that ECH also disturbed the GPC signals directly by an increased stray-light level. It caused a sudden jump in signal when ECH was switched on or off. Fluctuations in the stray-light level enhanced the noise. Although the monitored frequencies are far from the ECH frequency still several *10* eVs of stray-light were detected, despites of the notch filter in the waveguide. The averaged stray light level increased for lower frequencies, closer to the ECH frequency. At higher densities, when more ECH power is absorbed in the plasma, the stray-light decreased.

4.3. Temperature profiles during NBI

Temperature profiles have been measured during neutral beam injection. During NBI heating the density is generally higher than ($n_e > 1.0 \cdot 10^{19}$ m^{-3}) thus the outer resonance is sufficient optically thick.

Typical density profiles in LHD are flat, or slightly hollow, yielding quite peaked temperature profiles. Over a wide range of densities and temperatures, the temperature profile shape is very rigid. A characteristic LHD temperature profile with the almost triangular shape: $T(r/a) = T_0(1-(r/a)^{1.36})$ was found by fitting to the profile data.

Changes in the profile shape have been observed during central heating by ICH and after pellet injection. In the last case, cooling of the plasma edge by radiation and extreme hollow density profiles yielded a peaking of the temperature profile.

In Fig. 7 an example is shown of the temporal behaviour of the temperature profile. In this discharge (#8733) *5* pellets were injected, yielding an increase in density and a subsequent decrease in temperature. The plasma energy reached *754* kJ at the end of the NBI phase. After each pellet, a hollow density profile caused a fast peaking of the temperature profile. The change in profiles can be clearly seen in Fig. 8a and b. The profiles are shown at $t=0.81$ s, just after the before the pellet and at $t=0.82$ s. The hollow density profile results in a peaking of the temperature profile.

5. Conclusions

The large shear of the magnetic field in LHD might cause problems for the analysis of ECE spectra. The effect of the polarisation due to this large shear has been studied numerically as well as experimentally, by means of a polarisation rotator and a 14-channel grating polychromator.

At high enough density, mode conversion was found to be negligible. Calculations showed that in this case the polarisation of the ECE waves rotate in the laboratory frame. This rotation has been confirmed experimentally. If this rotation is not taken into account, a mixture of X and O-mode will be detected. A polarisation rotator is set in the waveguide system to correct for this effect.

Hence, 2nd harmonic X-mode spectra can be monitored. Temperature profiles have been successfully measured by the LHD grating polychromator.

Acknowledgements

The work presented in this paper has been performed with financial support of the Japan Society of Promotion of Science and the National Institute for Fusion Science.

References

[1] P.C. de Vries, et al, in the Proc. of the 26th Conf. on Plasma Phys. and Contr. Fusion, Maastricht (1999) Part II, p 25.
[2] Y. Nagayama, et al., Rev. Sci. Instrum. 70 (1999) 1034.
[3] S. Inagaki, et al., in the Proc. of the 26th Conf. on Plasma Phys. and Contr. Fusion, Maastricht (1999) Part III, p 105.
[4] Y Nagayama, et al., Overview of ECE diagnostics on LHD, in this proceedings.
[5] I. Fidone and G. Granata, Nucl. Fusion 11 (1971) 133.
[6] M. Bornatici, et al., Nucl. Fusion 23 (1983) 1153.
[7] P.C. de Vries, et al, submitted to Phys. Plasmas (1999).

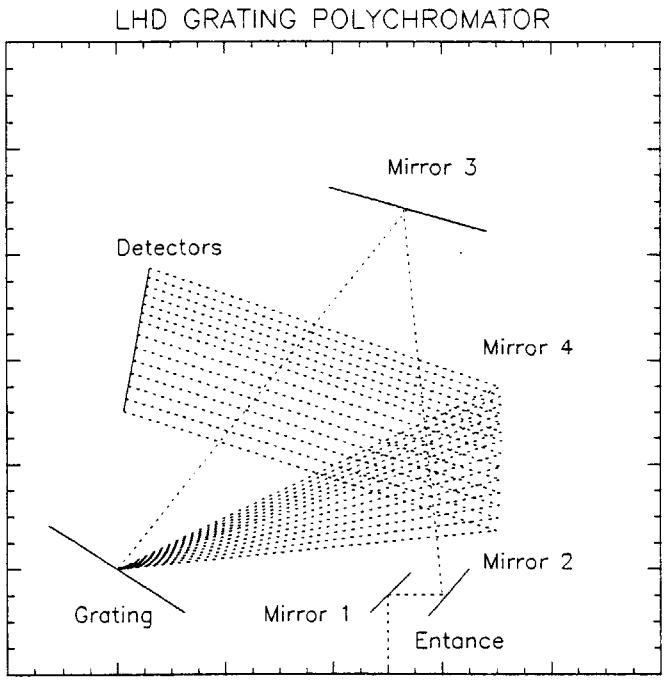

Fig. 1: Schematic drawing of the LHD grating polychromator

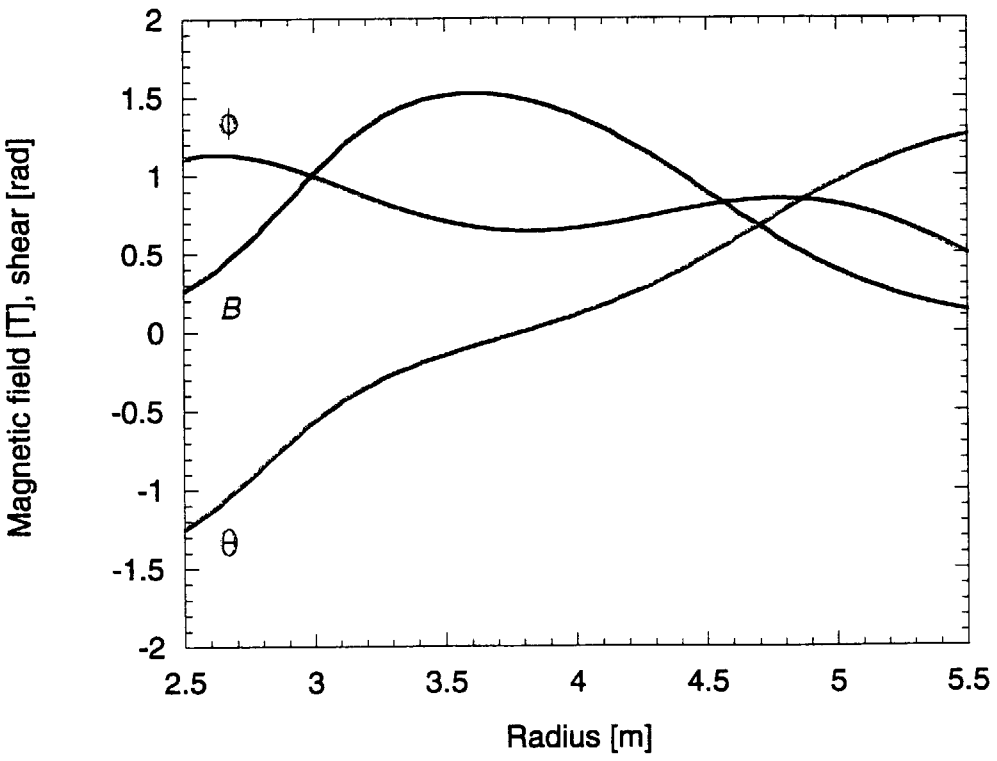

Fig. 2: The magnetic field configuration in the line-of-sight of the diagnostic antenna. The magnetic field amplitude, the shear, $\theta \equiv atan(B^{pol}/B^{tor})$, and its derivative, ϕ, are plotted.

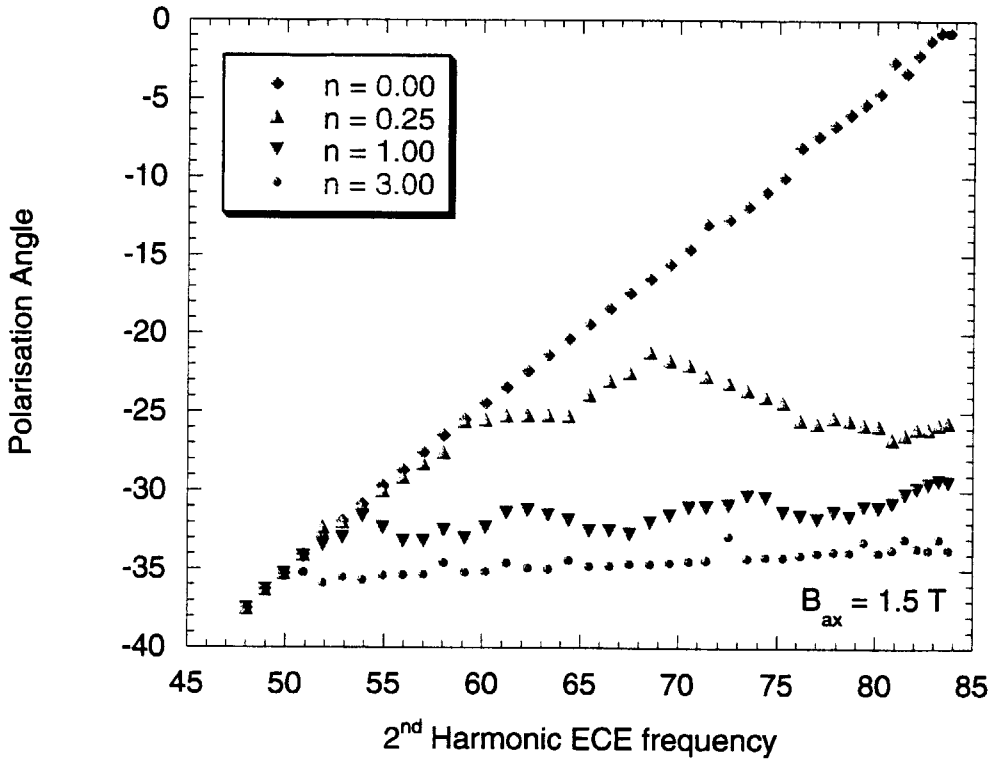

Fig. 3: The polarisation angle (angle of an X-mode waves electric field vector) at $r=a$ calculated for each spectral component using different plasma densities.

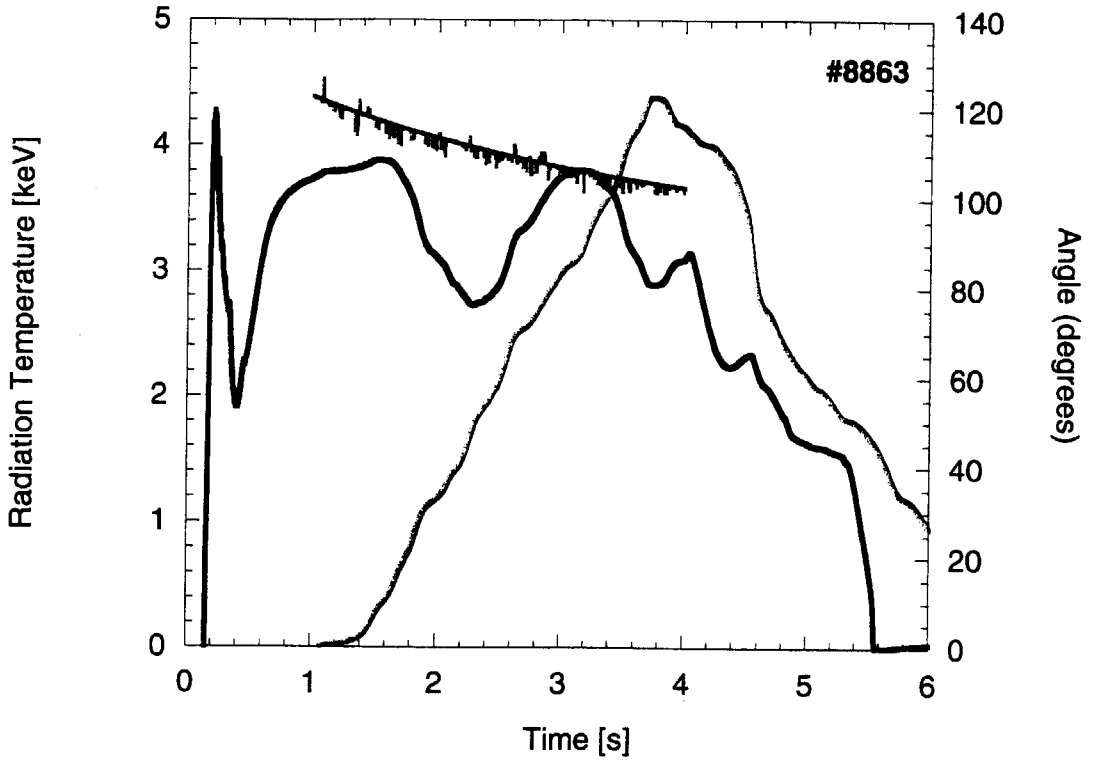

Fig. 4: The radiation temperature of the central CPC channel (#13) (blue curve), the central temperature and the polarisation rotator angle (red curve) are shown for discharge #8863.

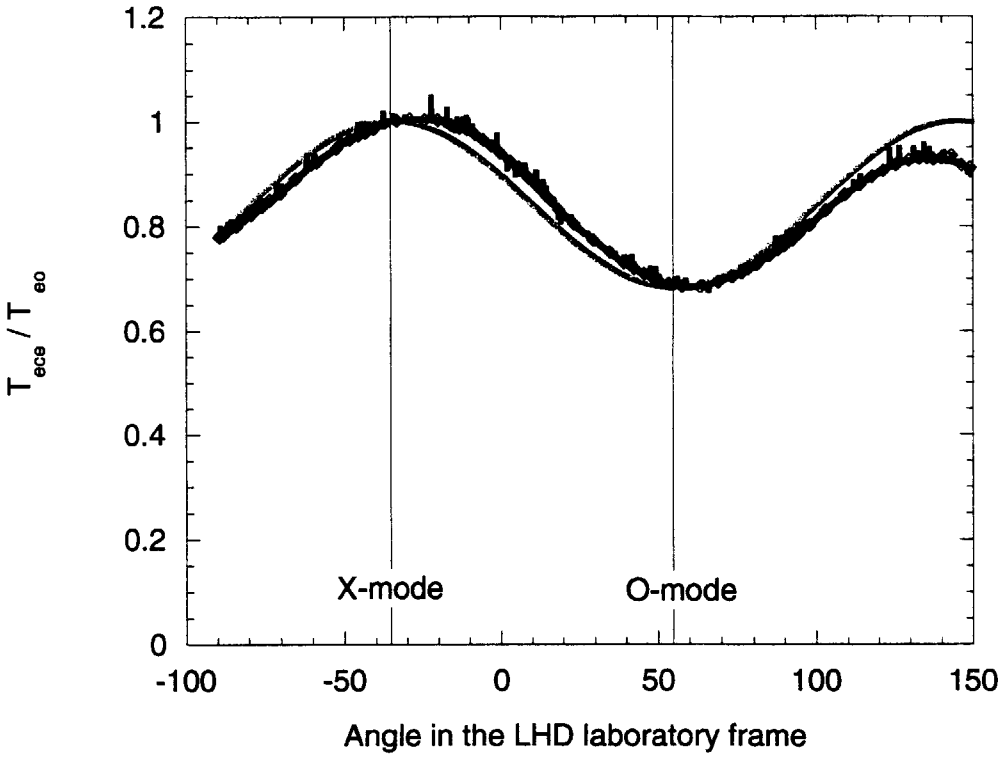

Fig. 5: The ratio between the ECE radiation temperature and the electron temperature, as a function of the polarisation angle in the LHD laboratory frame, together with the calculated curve are plotted.

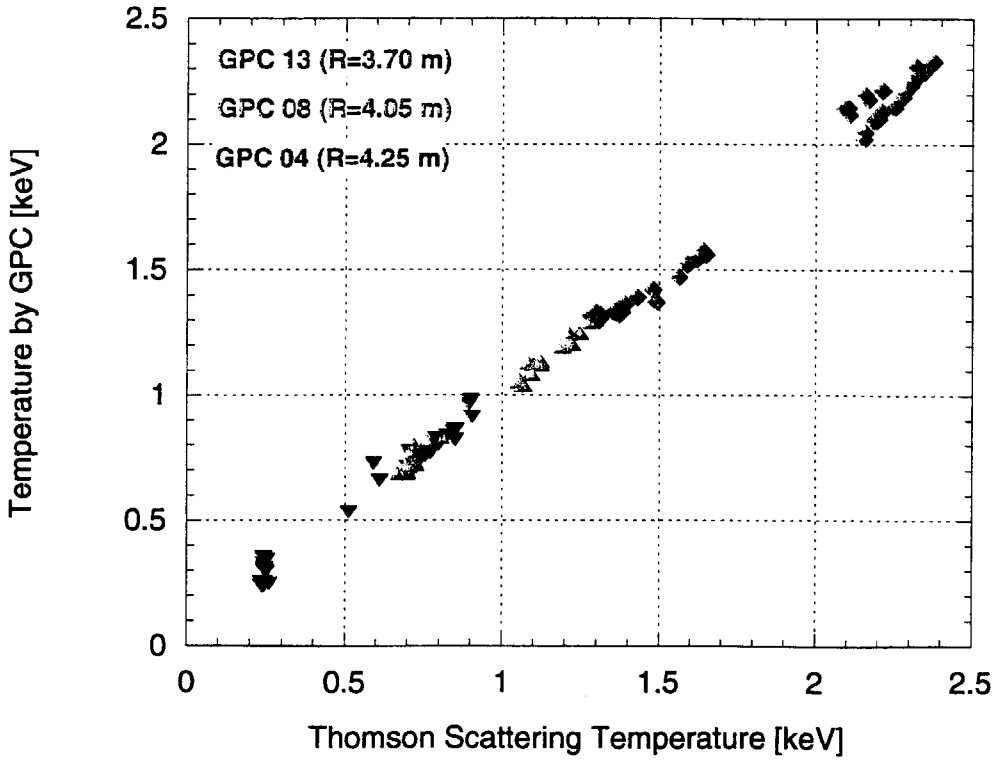

Fig. 6: Comparison of Thomson scattering and temperatures measured by the GPC for three different channels.

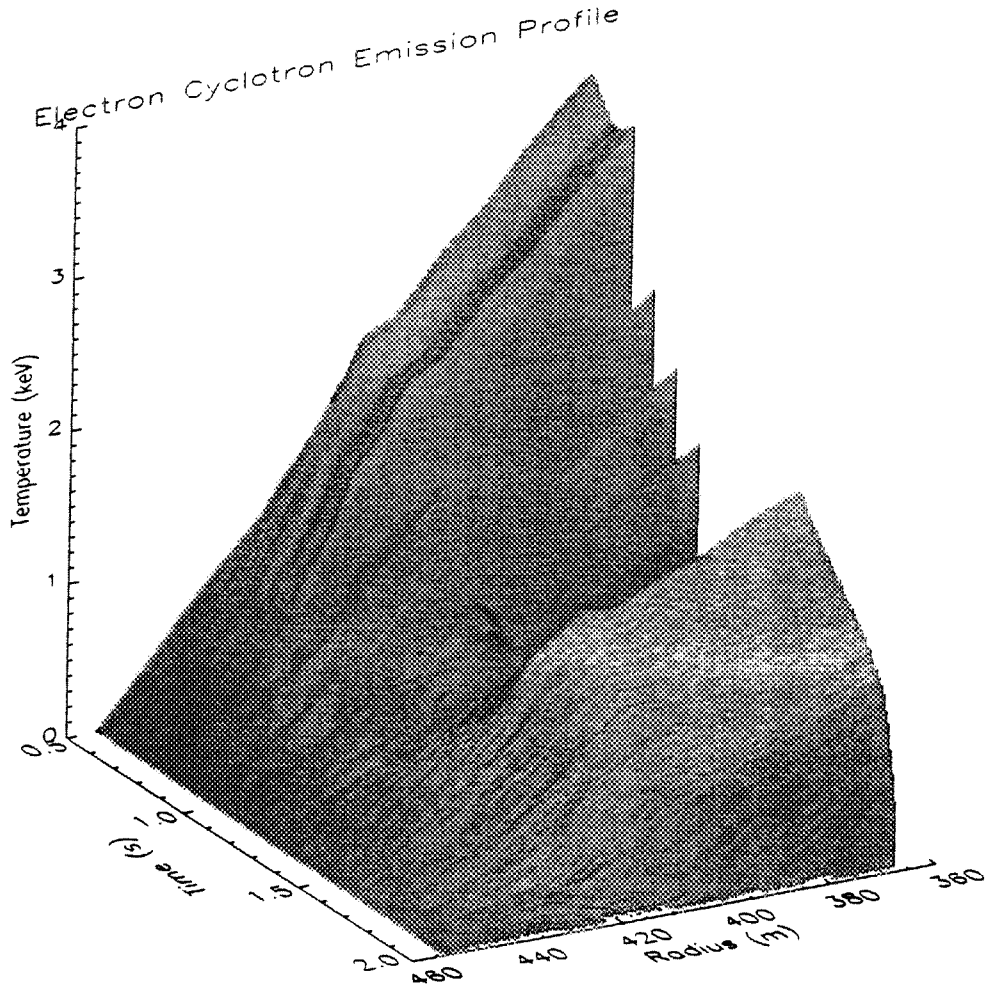

Fig. 7: The temporal behaviour of the electron temperature of discharge #8377. The initial ECH phase is omitted in this plot. Injection of pellets results in a collapse of the temperature.

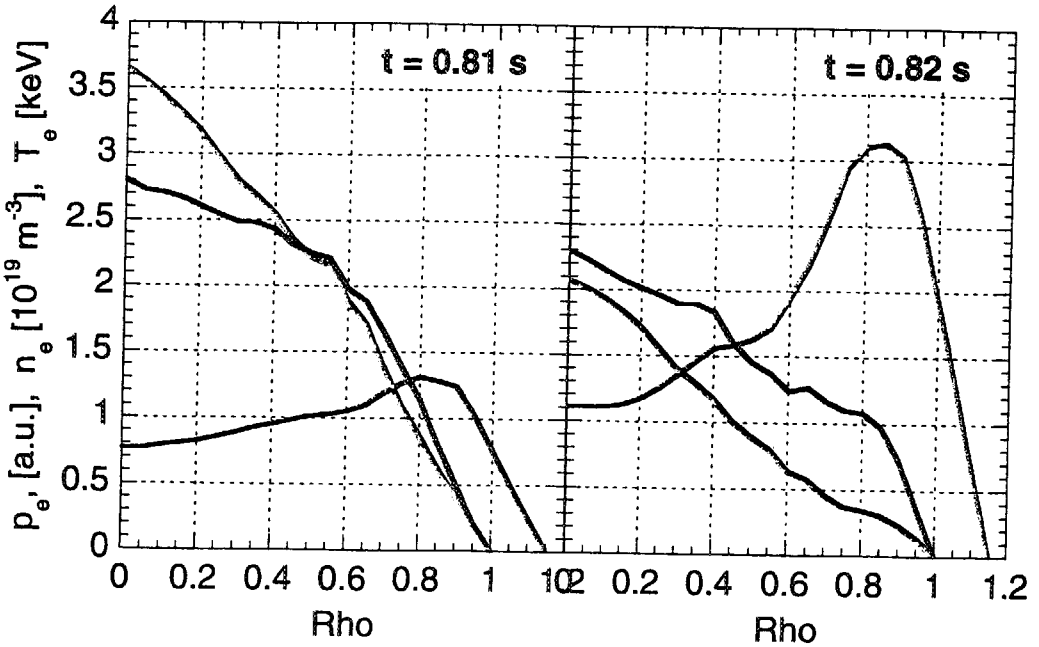

Fig. 8: Temperature (red), density (blue) and pressure (green) profiles of discharge #8733, at *t=0.81* s and *0.82* s

2-3 Electron Cyclotron Emission Diagnostic Systems for Electron Temperature Perturbation Measurement in JT-60U

A. Isayama, N. Isei, S. Ishida, M. Sato and JT-60U team
Japan Atomic Energy Research Institute, Naka Fusion Research Establishment

1. Introduction

In JT-60U, there are three electron cyclotron emission (ECE) diagnostic systems [1], which are the Fourier transform spectrometer system [2], the 20-channel grating polychromator system [3] and the 24-channel heterodyne radiometer system [4]. The Fourier transform spectrometer system is absolutely calibrated using liquid nitrogen, and its result is used for relative calibration of the grating polychromator system and the heterodyne radiometer system. The grating polychromator system and the heterodyne radiometer system, whose temporal resolution is 20 μs, are used for the measurement of electron temperature perturbations. In this paper, recent development and results of these ECE diagnostic systems are described.

2. The Heterodyne Radiometer System

A heterodyne radiometer is advantageous in that electron temperature perturbations can be measured with high signal-to-noise ratio. In JT-60U, the heterodyne radiometer system is mainly used for measurement of structure of electron temperature perturbations. In 1999, the number of channels was doubled to 24 by adding a new heterodyne radiometer. By using this system, ECE ranging from 176 to 200 GHz can be measured. Schematic diagram of the new heterodyne radiometer is shown in Fig. 1. It is composed of two components: 'front end' which converts the high frequency ECE to intermediate frequency (IF) and 'back-end' which ditect, divide and filter the IF signal. A Gunn oscillator with 91 GHz and a doubler is used for the local oscillator. Inputted ECE signal is firstly filtered to reject the heterodyne image band ranging from 164 GHz to 176 GHz. After then, the ECE signal is mixed with the signal from the local oscillator and converted to intermediate frequency (6-18GHz). At the back-end, the IF signal is divided into the 12 channels. Each channel contains a bandpass filter and a video detector. Band width of the filter is $f_0 \pm 0.25$ GHz. Here, f_0 is the center frequency of the bandpass filter which ranges from 6.5 to 17.5 GHz at 1 GHz intervals. The system noise of the heterodyne radiometer is 12 dB, and the noise temperature is about 4300 K. Linearity of the output is kept within ±5% in the range from -50 dBm to -20 dBm. After the detection, the signal of each channel is sent to isolation amplifier and analog-to-digital converter, and it is finally sent to the data acquisition computer through optical fibers.

After the upgrade of the heterodyne radiometer system, measurement range is extended as follows: R=3.7 - 4.2m for B_t=4.0 T, R=3.3 - 3.7 m for B_t=3.5 T and R=2.8 - 3.2 m for B_t=3.0 T. The range is shown in Fig. 2. By using the upgraded heterodyne radiometer, the whole structure of various MHD modes, such as tearing mode in the steady state high β_p mode discharges [5, 6] and the barrier localized mode, which is a kind of magnetohydrodynamic instability localized near the internal transport barrier, in the reversed shear discharges [7] can be measured.

One of the disadvantages of the heterodyne radiometer is that the measurement points can not be chosen freely but uniquely determined by the value of the toroidal field. Thus, if

the heterodyne radiometer for JT-60U is used in low field discharges such as B_t=2.1T, the measurement points locates outside the plasma. Furthermore, in the low field region, the grating polychromator is not available because of low signal-to-noise ratio. In order to measure the electron temperature in the low field region, the heterodyne radiometer for JFT-2M is installed. Since the design of the IF component is similar in both radiometers, only the RF component is replaced. The schematic diagram of the radiometer for JFT-2M is shown in Fig. 2. The radiometer contains a 96 GHz and a 34 GHz Gunn oscillators, and can measure ECE ranging from 100 GHz to 124 GHz at interval of 1 GHz. The measurement range, which is shown in Fig. 3, is as follows: R=2.8 - 3.4 m for B_t=1.9 T, R=3.2 - 3.8 m for B_t=2.1 T and R=3.7 - 4.4 m for B_t=2.4 T. An example is shown in Fig. 4, where toroidal field is 2.1 T. Sawtooth oscillations are clearly observed in this figure. The inversion radius can be also determined using this radiometer. The information is also important for the measurement of safety factor using the MSE (Motional Stark Effect) polarimeter.

In 1999, electron cyclotron wave injection system was installed aiming at the local heating and current drive. The frequency of the electron cyclotron wave is 110 GHz, and the maximum power is 1 MW at the gyrotron output. Power deposition can be controlled by a steerable mirror. Toroidal injection angle is fixed at about 15°. In 1999, tearing mode stabilization experiment was carried out using the EC injection system. Typical waveform of the discharge, where m/n=3/2 mode is destabilized, is shown in Fig. 5. Profiles of amplitude and phase of electron temperature perturbations in this discharge measured by the heterodyne radiometer is shown in Fig. 6. The amplitude is normalized by DC component of the electron temperature. The amplitude becomes small, and the phase is inverted across R≈3.62 m, which suggests that the center of a magnetic island locates at this position. The optimum injection angle was determined from the measurement of the heterodyne radiometer so that the EC wave can pass the center of the island. After the EC wave injection, magnetic fluctuations with n=2 measured by saddle coils were slightly decreased. Electron temperature perturbations near the center of the magnetic island were also decreased. However, so far, disappearance of the magnetic fluctuations and electron temperature perturbations, which suggests complete stabilization of the tearing mode, is not observed in a sequence of the discharges. The tearing mode stabilization experiment is planned after the increase of the injection power (up to 3 MW) in 2000.

3. The Grating Polychromator System

The grating polychromator system is advantageous in that the measurement points can be freely changed by changing the grating mirror angle. In JT-60U, the grating polychromator system is mainly used for measurement of electron temperature perturbation spreading to wider spatial region. Schematic diagram of the grating polychromator is shown in Fig. 7. ECE is firstly led to the polychromator which contains a grating mirror. The channel separation can be changed by replacing the grating mirror. Usually the grating mirror whose pitch is 1.6 mm is used. In this case, the channel separation is typically 6 cm in major radius. The frequency-resolved ECE is led to the InSb detectors through 20 waveguides. The detectors are cooled at 4.2K by a refrigerator. Since the refrigerator makes mechanical noise, three of the detectors are used for measurement of the noise. The noise is mainly composed of 2 Hz and 50 Hz components. The former is removed at the preamplifier by using a canceling circuit. The latter is removed by a numerical filter. After the preamplifier, the signals are led to the filter

amplifiers, and then to analog-to-digital converters. Finally they are sent to the data acquisition computer through optical fibers. It was found that EC wave from the ECH/ECCD system can reach the detectors as stray light even when the measurement frequency region does not overlap with the EC wave frequency. In order to reject the EC wave, a high pass filter, which has –60dB attenuation, was installed. Time evolution of ECE signal measured by GPS before and after the installation of the highpass filter is shown in Fig. 8. As is shown in this figure, the EC wave is completely rejected, and electron temperature during the EC wave injection can be measured.

By using the grating polychromator, electron temperature perturbations, such as sawtooth oscillations and disruption precursor, were observed. In a sequence of the reversed shear discharges, a collapse is often observed even in low beta region. In Fig. 9 (b), time evolution of stored energy measured by diamagnetic loops is shown, where a collapse occurs at t≈5.15 sec. Time evolution of electron temperature near the collapse is shown in Fig. 9 (c). At t=5.131 s, electron temperature is slightly increase near the edge and the first collapse occurs at t=5.133 s. By this collapse, electron temperature at the outer region ($r/a \geq 0.31$) suddenly decreases. On the other hand, electron temperature at r/a=0.23 slowly decreases, and that at r/a=0.17 does not decrease so much at the collapse. At t=5.1382 s, the second collapse occurs, and electron temperature at r/a=0.23 suddenly decreases, and that at r/a=0.17 slowly decreases after the collapse. At the third collapse at t=5.1504 s, sudden decrease in electron temperature is observed at r/a=0.17. Phase inversion of the electron temperature perturbations, which suggests the formation of magnetic islands, is also observed before the third collapse. From this process, it is thought that this collapse is caused by an external-kink mode. In a sequence of the reversed shear discharges, many kinds of precursor are observed. However, the cause of the collapses are not completely understood. Further analysis is being done.

When the steep ITB is formed in electron temperature, there is one (sometimes no) GPS channel which measure the change of the electron temperature. In those discharges, the wide channel separation of the grating polychromator becomes serious. In order to narrow the channel separation, a new detector system will be installed in early 2000. Since twenty waveguides are inserted between the existing waveguides, the channel separation becomes a half. The twenty detectors are cooled by liquid helium held by a cryostat whose diameter is about 50 cm. We chose the cryostat instead of a refrigerator in order to reduce noise. It is expected that the mechanical noise which is observed in the existing system is not observed at all in the new system. The measurement will be started in April.

4. Summary

ECE diagnostic systems for electron temperature perturbation measurement are described. In the tearing mode stabilization experiment, the location of the magnetic island was determined by using the upgraded heterodyne radiometer system. The optimum injection angle for the EC wave was determined from this measurement. Electron temperature perturbations in low field region were measured by installing the heterodyne radiometer for JFT-2M. The results on the sawtooth inversion radius were also informative for calibration of the MSE polarimeter. Disruption precursor in the reversed shear discharge was measured by the grating polychromator. In one of the discharges, mini-collapses were occurred from the edge region, which suggests that one of the candidates for the collapse is an external kink mode.

Acknowledgements

The authors wish thank Dr. A. Funahashi, Dr. H. Ninomiya, Dr. R. Yoshino and Dr. H. Kimura for their continuing support.

References

[1] M. Sato, S. Ishida, N. Isei, A. Isayama, H. Shirai, T. Oyevaar, M. Teranishi, N. Iwama and K. Uchino, Fusion Engineering and Design **34–35** (1997) 477.

[2] M. Sato, N. Isei and S. Ishida, JAERI-M 93-057, "Development of Fourier Transform Spectrometer System", (1993) 359.

[3] S. Ishida, A. Nagashima, M. Sato, N. Isei and T. Matoba : Rev. Sci. Instrum. , **61** (1990) 2834.

[4] N. Isei, M. Sato, S. Ishida, K. Uchino, A. Nagashima, T. Matoba and T. Oyevaar, Rev. Sci. Instrum. **66** (1995) 413.

[5] Y. Kamada, A. Isayama, T. Oikawa, Y. Sakamoto, N. Hosogane, H. Takenaga, Y. Kusama, T. Fujita, S. Takeji, T. Ozeki, Y. Ishii, S. Tokuda, K. Ushigusa, O, Naito, S. Ishida, Y. Koide, T. Fukuda, T. Takizuka, H. Shirai, T. Hatae and the JT-60U team, Proc. 17th IAEA Fusion Energy Conf., Yokohama 1998, IAEA-CN-69/CD2/EX9/2.

[6] A. Isayama, Y. Kamada, T. Ozeki and N. Isei, Plasma Phys. Control. Fusion **41** (1999) 35.

[7] J. Manickam, T. Fujita, N. Gorelenkov, A. Isayama, Y. Kamada, M. Okabayashi, M. Bell, R. Bell, R. Budny, E. Fredrickson, S. Ishida, Y. Ishii, F. Levinton, T. Ozeki, H. Shirai, S. Takeji and M. Zarnstorff, Proc. 17th IAEA Fusion Energy Conf., Yokohama 1998, IAEA-CN-69/CD2/EX8/4.

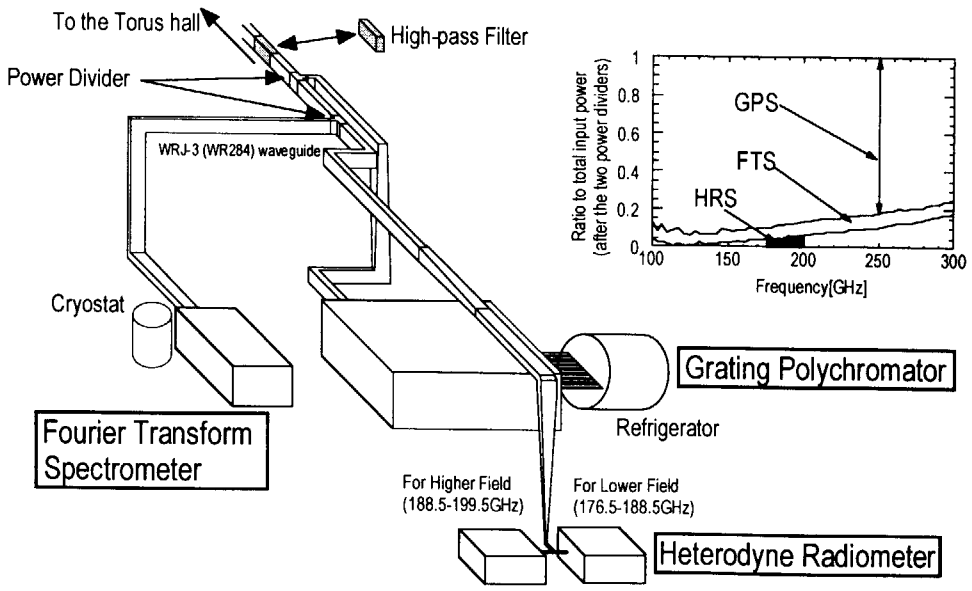

Fig.1: Schematic view of ECE diagnostic systems.

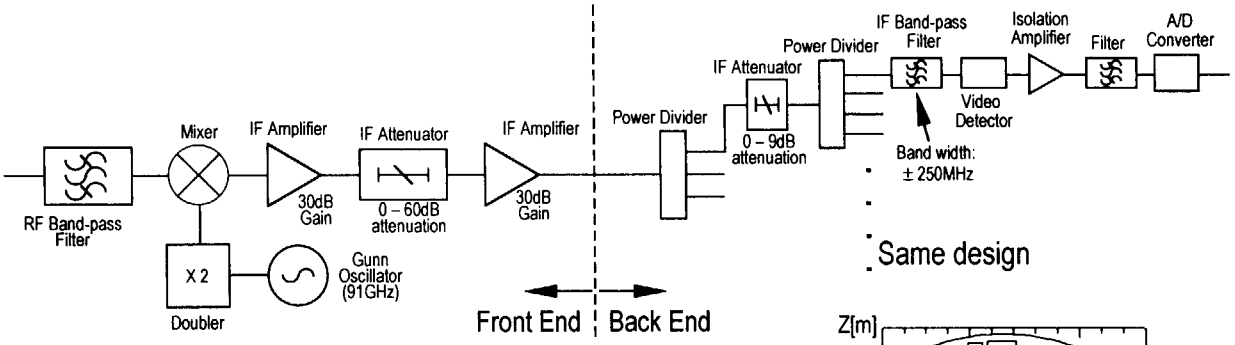

Fig. 1: Schematic diagram of the new radiometer

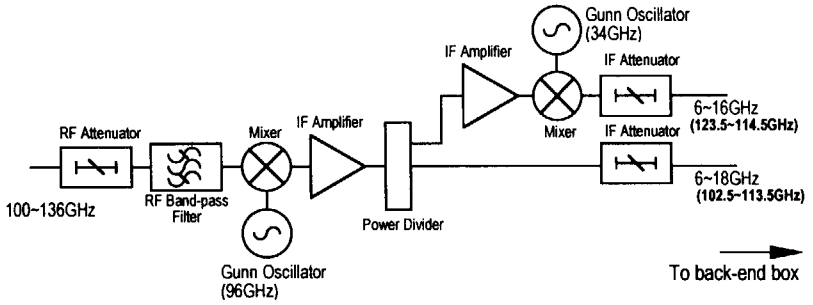

Fig. 2: Schematic diagram of the front-end of the radiometer for JFT-2M.

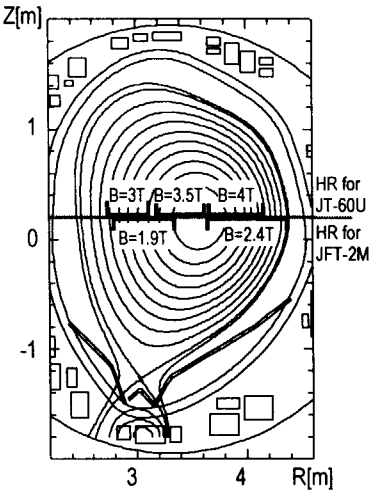

Fig. 3: Measurement range of the heterodyne radiometer system at various magnetic field.

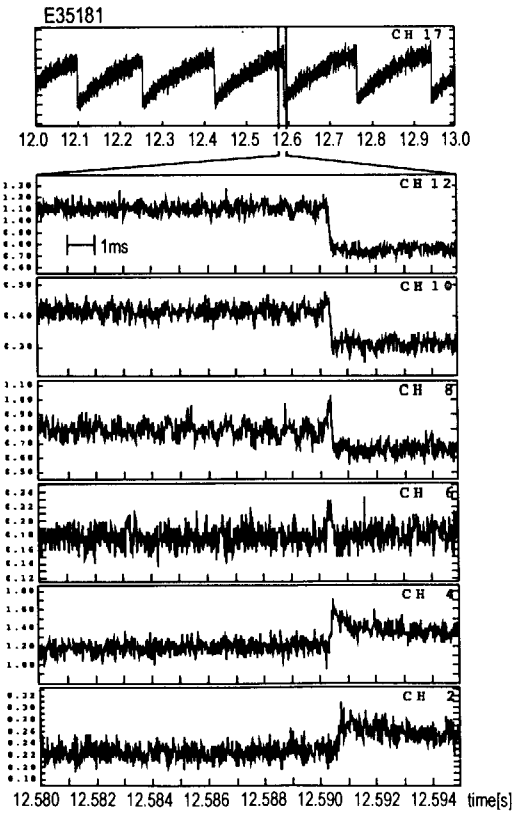

Fig. 4: Typical waveform of sawtooth crash measured by the radiometer for JFT-2M.

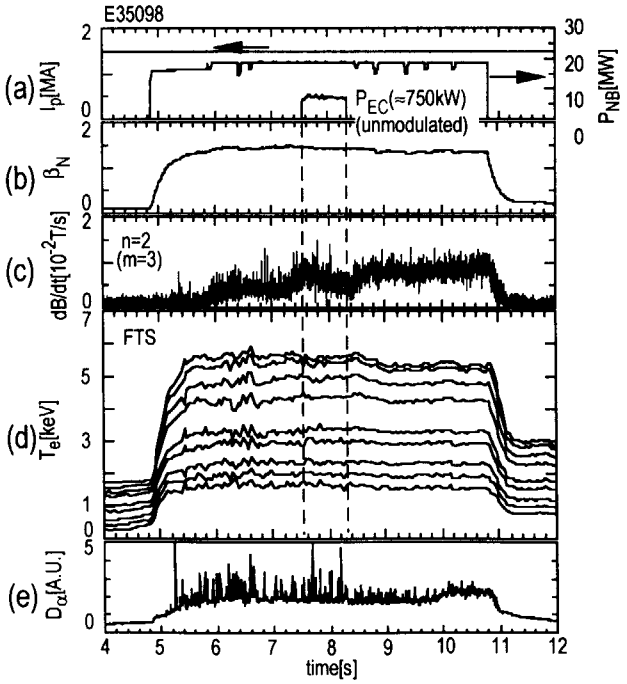

Fig. 5: Typical waveform of (a) Plasma current, NB and ECH power, (b) normalized beta, (c) amplitude of magnetic fluctuation with n=2, (d) electron temperature, (e) Dα signal in an tearing mode stabilization experiment.

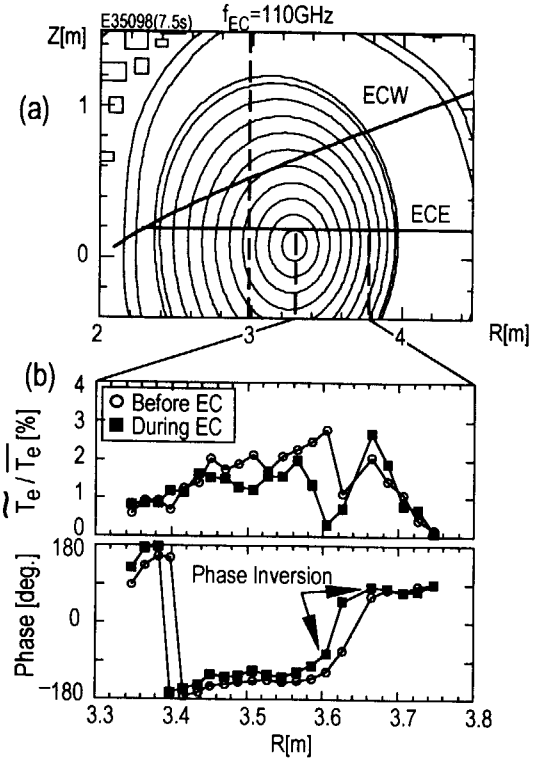

Fig. 6: (a) Plasma shape and ray of the injected EC wave, (b) amplitude and phase of electron temperature perturbation.

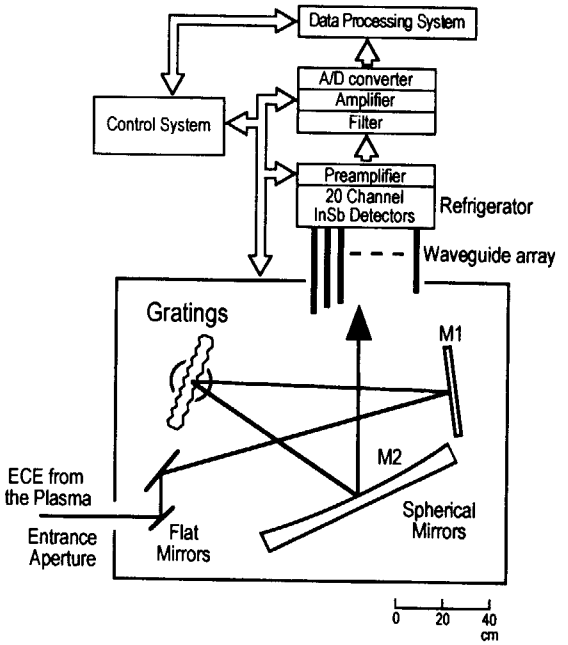

Fig. 7: Schematic diagram of the grating polychromator.

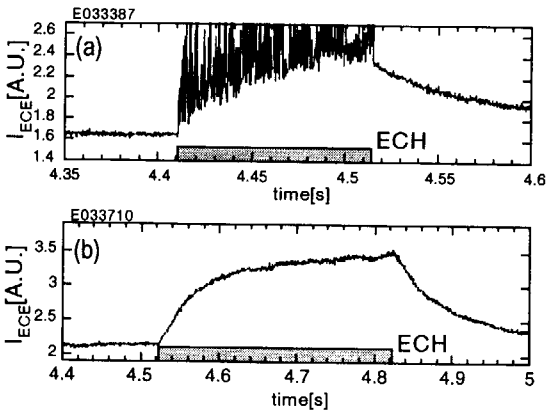

Fig. 8: (a) Time evolution of electron temperature measured by GPS without power divider. (b) Time evolution of electron temperature measured by GPS with power divider

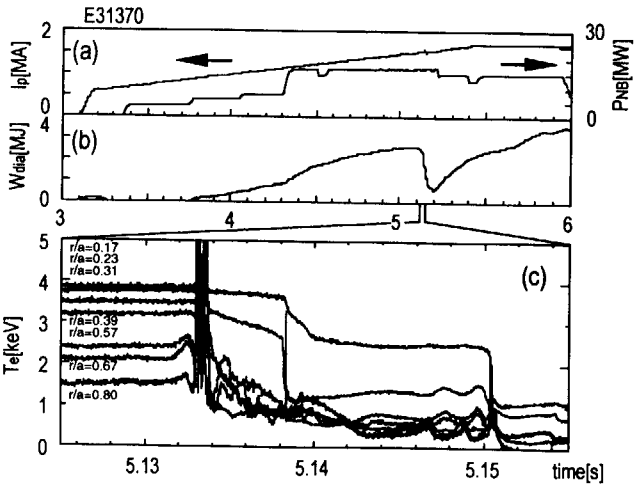

Fig. 9: Typical waveform of (a) plasma current and NBI power, (b) stored energy measured by diamagnetic loops and (c) electron temperature measured by the grating polychromator.

JAERI－Conf 2000－007

Fifth Australia-Japan Workshop on Plasma Diagnostics, December 15-17, 1999, JAERI, Japan

2-4 Reflectometric Measurements on LHD

T. Tokuzawa, K. Kawahata, R. O. Pavlichenko, K. Tanaka, A. Ejiri*

National Institute for Fusion Science, Toki 509-5292, Japan
**Graduate School of Frontier Sciences, Univ. Tokyo, Tokyo 113-0033, Japan*

Abstract

Pulsed radar reflectometer is the suitable reflectometric technique, in order to study the effect of the strong magnetic shear on polarization of microwave in the Large Helical Device (LHD). Because pulsed radar reflectometry is measured the delay time of the reflected wave, it can be distinguished between X-mode and O-mode polarized wave. At X-mode operation it is found the position of the ergodic edge layer is steady in spite of the increased density in the core region during neutral beam is injected. If the electron density is not reached to the critical cutoff one, the pulsed radar system could be used as a delayometer. The measured delayometer signal is almost in agreement with the numerical calculation using the assumption which the polarization of the propagated wave into the plasma is decided at the edge region, nevertheless the angle of the magnetic field line to the magnetic axis is changed in the propagated direction of the launched wave.

Introduction

It is very important to know the edge density profile and fluctuation information for the magnetic confined devices. In order to measure these plasma parameters with high temporal and spatial resolution, we try to apply microwave reflectometer on LHD. Reflectometer is a compact system and needs a small access to the device and also has a higher resolution than conventional diagnostic methods. In the world there are several types of reflectometers such as; FM-CW reflectometer, AM reflectometer, pulsed radar reflectometer, ultra-short pulse reflectometer, homodyne

reflectometer, heterodyne reflectometer, correlation reflectometer, etc. On LHD, we have been applied three types of reflectometer system. One is three-channel homodyne reflectometer for NBI interlock[1]. Second is pulsed radar reflectometer for density fluctuation measurement. Third is FM reflectometer for density profile measurement.

In this paper we are concerned with especially pulsed radar reflectometer. Because LHD is complex structure of the magnetic field configuration and also has a large magnetic shear, the launched microwave may become complicated behavior[2]. In order to study this effect of the strong magnetic shear on polarization of microwave, we think the pulse radar reflectometer is the suitable reflectometric technique. Because pulsed radar reflectometry is measured the delay time of the reflected wave not to be measured the phase, it can be distinguished between X-mode and O-mode polarized wave even if the mode conversion and/or polarization rotation is occurred.

Pulsed radar reflectometry

The schematic of U-band pulse radar reflectometer system is shown in Fig. 1. A 51GHz Gunn oscillator is used as a source. The output power is 50 mW. PIN switch is used as a pulse modulator. The separate, transmitter and receiver horns are used in order to avoid the mixture of spurious reflecting components in the waveguides, vacuum window, etc. The antenna is a conical horn with teflon lens for focusing the microwave beam and can be moved horizontally using a remote controller. The reflected wave picked up by the receiver horn is mixed with reference a 39 GHz microwave in a mixer. The IF signal is filtered by band-pass-filter and then detected of the envelope of the reflected wave. The detected pulses are fed to diagnostics room using electro-optical converter. And then time-of-flight (TOF) measurement is carried and the data is acquired by CAMAC (Aurora 14 with a 1Mword memory) and windows NT based personal computer. The launched pulse is measured just after PIN switch to avoid the jitter of the pulse generator and PIN switch, and we measure the time difference between the launched pulse and the reflected one. The pulse width is around 2ns. The repetition rate is 250 kHz in the standard condition because the TOF measurement system is required the condition that the repetition rate is less than 400 kHz.

Figure 2 shows the characteristic frequencies in the condition that the magnetic field strength is 2.75T and the magnetic axis position is 3.6m in the standard operational

mode in the LHD 3rd cycle. When we use the X-mode right-hand cutoff, we can measure in the range where R=4.5-4.55m for 51GHz and R=4.2-4.55m for 60GHz.

Experimental results

LHD plasma is usually ignited by ECH and then neutral beam is injected. It is found that the ergodic region and the edge surface layer are constructed steadily in Fig. 3(a). The reflected position is changed about 5 cm during the time is changed from at (1) to at (2), so that the delay time is changed about 7 ns. Figure 3(b) shows the power spectrum density at these two times. Fluctuation level of the ergodic region is 20 times larger than the inner plasma region. A coherent mode is sometimes appeared and its frequency is about 1-3kHz.

We also applied E-band (60 GHz) pulse reflectometer system. It is found the reflected position is inner than the case of 51GHz. When the edge density is grown up, the cutoff position is close to outer edge surface layer. So, it is found that if we construct multi channel reflectometer system, the density profile can be measured.

When we launch both X/O-mode microwave pulse simultaneously, two reflected pulses can be measured. The time evolution of the delay time is shown in Fig. 4. During t=2.0-3.5 s the launched wave is reflected from two plasma layers by X-mode cutoff. We think that it is caused by the reflection from the divertor legs. At t=3.8 s the wave is penetrated and reflected from inner wall by O-mode propagation. It is found the both polarized microwaves can be propagated. Especially, O-mode wave is propagated through plasma as it is. So if we modify the TOF system, it is found that the system can be measured both reflected signal and compared the behavior of density and magnetic fluctuation.

If the electron density is not reached to the critical cutoff density, the pulsed radar system could be used as a delayometer. The interferometer is measure the phase difference caused by the plasma, on the other hand the delayometer is measure the time delay by plasma. The merit of the delayometer is not to be arisen any phase jump. In Fig. 5 the solid line is the numerical calculation using the millimeter wave interferometer data and the assumption that the polarization of the propagated wave into the plasma is X-mode. The delayometer signal is almost in agreement with the numerical result, nevertheless the angle of the magnetic field line to the magnetic axis is changed in the propagated direction of the launched wave.

Summary

For the density fluctuation measurement, the pulsed radar reflectometer system has been applied on LHD. It can be recognized the polarized waves and measured the edge ergodic plasma fluctuation. Initial experiment of delayometric measurement is carried and its signal is almost agreement with numerical calculation using the assumption which the polarization is decided at the edge region.

Multi channel pulsed radar reflectometer system is planed to measure the correlation and profile measurement. For the detailed study of the effect of the magnetic shear to the wave propagation, the waveguide rotator is planning to be added.

References

1. A. Ejiri, *et al.*, in this workshop.
2. K. Nagasaki, *et al.*, Phys. Plasmas **6** (1999) 556.

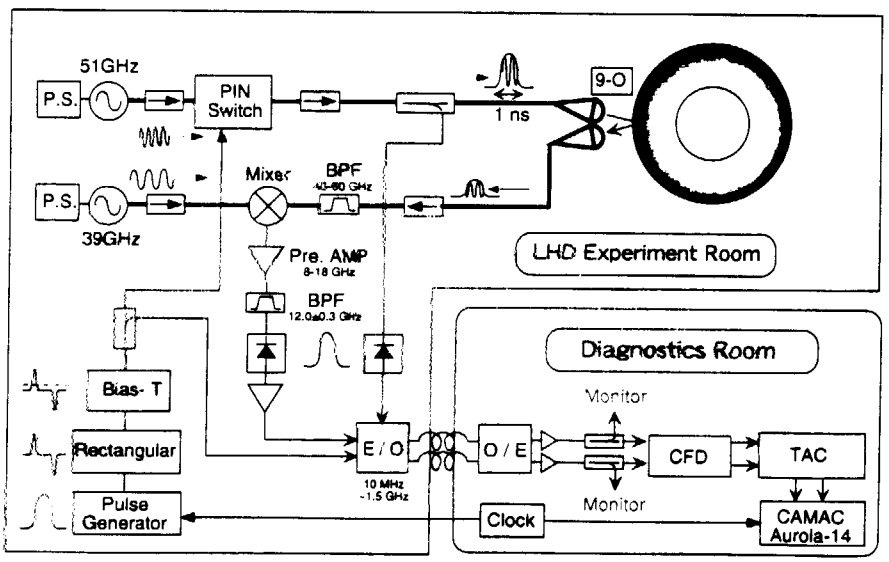

Fig. 1 Schematic of U-band pulse radar reflectometer system

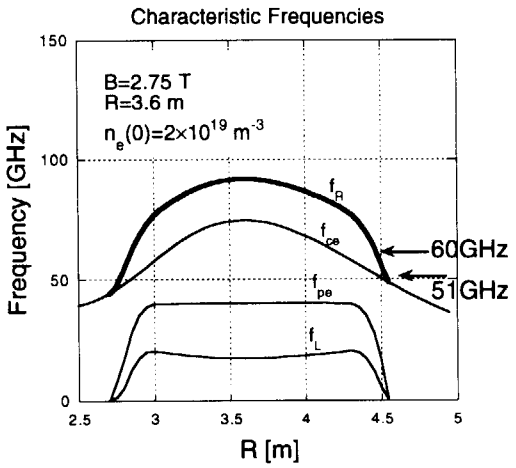

Fig. 2 Radial profile of the characteristic frequencies in the condition that B=2.75 T, R_{axis}=3.60m.

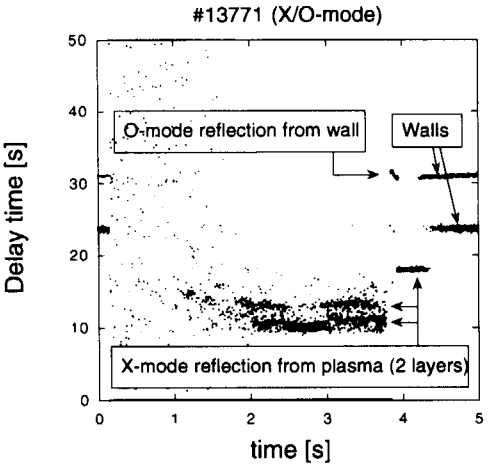

Fig. 4 Time evolution of the delay time, when both X/O-mode polarized wave is launched.

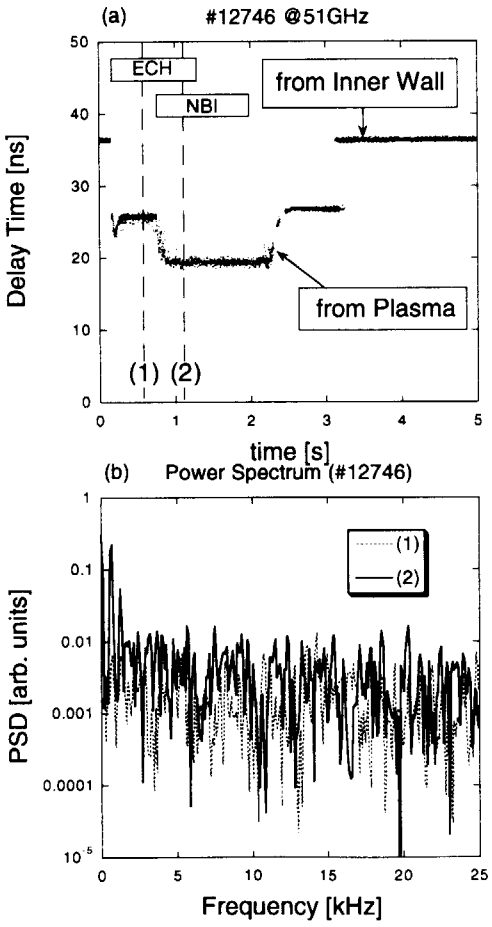

Fig. 3 (a)Time evolution of the delay time. (b) Power spectrum densities of the signal.

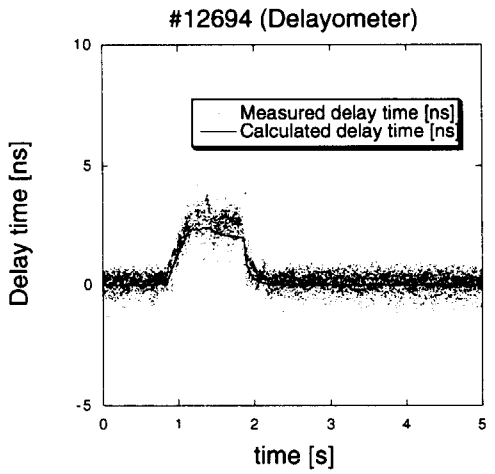

Fig. 5 Time evolution of the delayometer signal (dots) and numerical calculated delay time (solid line).

2-5 Millimeter Wave Imaging Diagnostics of Plasma Turbulence

B.H. Deng, C.W. Domier, N.C. Luhmann, Jr.
Department of Applied Science, University of California at Davis, Davis, CA 95616, USA
A.J.H. Donné
FOM Institute for Plasma Physics 'Rijnhuizen', P.O. Box 1207, 3430 BE, Nieuweigen, The Netherlands
E. Mazzucato, H. Park
Princeton Plasma Physics Laboratory, Princeton University

Abstract Novel millimeter wave imaging diagnostic techniques for the study of plasma turbulence, i.e., the Electron Cyclotron Emission Imaging (ECEI) of plasma electron temperature fluctuations, and the Microwave Imaging Reflectometry (MIR) for plasma density fluctuation measurements, are discussed. Illustrative experimental results of ECEI are presented.

1. Introduction

Anomalous plasma transport remains an outstanding issue in magnetic fusion studies. One of the main reasons limiting the understanding of this important phenomenon is the difficulty in acquiring detailed fluctuation data, especially in the high temperature plasma core region [1,2]. It was not until 1993 that plasma core electron temperature fluctuations ($\tilde{T}_e$) were measured by applying the intensity interferometric technique to Electron Cyclotron Emission (ECE) diagnostics [3]. However, it was soon realized that relatively poor spatial resolution (compared to that required by fluctuation studies) and the one-dimensional nature of conventional ECE radiometers have limited the available information of $\tilde{T}_e$ [2,4]. This has led to the appearance of a novel ECE diagnostic, Electron Cyclotron Emission Imaging (ECEI), which utilizes compact millimeter wave imaging arrays as the heterodyne receivers [2,5,6]. This unique two-dimensional diagnostic has excellent spatial resolution, and has been successfully applied to fluctuation studies in the TEXT-U and RTP tokamaks [2, 5,6]. New information such as poloidal wavenumbers and 2-D structures of the fluctuations have been obtained [2,7].

In a separate development path, microwave reflectometry has been utilized to study plasma density fluctuations ($\tilde{n}_e$) for more than two decades [8]. However, this radar-like method retrieves the target information from the group delay of the reflected microwave signal along the sight line. This inevitably is modulated by the plasma fluctuations transverse to the sightline, so that quantitative interpretation of the data is very difficult [8]. Recently, it has been proposed that the imaging approach can solve the ambiguity in reflectometric measurements of plasma density fluctuations [8,9].

In Sec. 2, the main aspects of the implemented ECEI diagnostic systems are described, along with representative experimental results. New developments in imaging diagnostics, which includes microwave imaging reflectometry (MIR), and the combined three-dimensional ECE and reflectometric imaging diagnostic, are discussed in Secs. 3 and 4, respectively.

2. ECE Imaging of Plasma Electron Temperature Fluctuations

2.1ECE Imaging Diagnostic

Electron cyclotron emission (ECE) radiometers have been standard diagnostics for measuring plasma electron temperature profiles in tokamaks since 1974 [10]; and recently, the have been utilized to study the electron temperature fluctuations in the plasma core [3,4,11]. Conventional ECE diagnostics measure electron temperature profiles by using a single antenna/receiver aligned along a horizontal chord in the direction of the major radius. Therefore, 2-D measurements are impossible with this single sight line arrangement. The spatial resolution of such a system in the transverse direction of the sight line is limited by the divergence of the Gaussian beam pattern of the antenna, typically about 2 to 5 cm for small to medium size tokamaks [12]. As the sample volumes of conventional ECE radiometers are aligned radially, it is impossible to measure the poloidal wavenumbers of the turbulence, which is essential for understanding the relation between drift wave turbulence and anomalous transport of tokamak plasmas [2,11]. Thus, it is desirable to construct diagnostics with poloidally separated sample volumes. It is expected that drift wave fluctuations have peak power at poloidal wavenumbers of about $k_\theta \sim 2cm^{-1}$ [13]. Therefore, it is important to improve the spatial resolution of the ECE diagnostics to ≤ 1 cm, so that the systems are sensitive to fluctuations of $k_\theta \leq 3cm^{-1}$.

To meet the above requirements, a novel ECE radiometer, the ECE Imaging diagnostic, has been developed and applied to the TEXT-U and RTP tokamaks [2,5,6]. The principle of the diagnostic is illustrated in Fig. 1. Instead of a single receiver located in the tokamak midplane as in conventional ECE radiometers, the ECEI systems utilized the hybrid millimeter wave imaging arrays as the receiver/mixers. Shown in Fig.2 is the mask layout of the ECEI arrays. In the system, the elements of the arrays are aligned vertically, and measure at the same frequency, so that the sample volumes of the imaging systems are vertically aligned in the plasma. The horizontal position of the sample volumes are determined by the magnetic field strength and the ECE frequency, or the LO frequency of the diagnostic systems. By varying the magnetic field strength or the LO frequency, the sample volumes can be scanned through the plasma cross section to achieve two-dimensional measurements. As all the sample volumes are positioned at the focal plane of the imaging optics, i.e., the Gaussian beam waist location, excellent spatial resolution of about 1 cm is achieved.

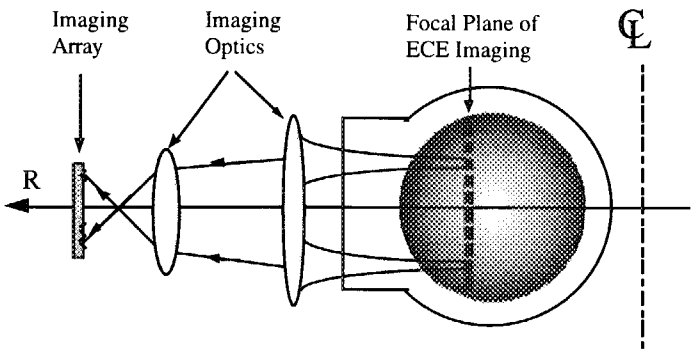

Fig.1 Schematic of the ECEI diagnostic, showing the imaging array and the imaging lenses. The sample volumes can be scanned horizontally (see text).

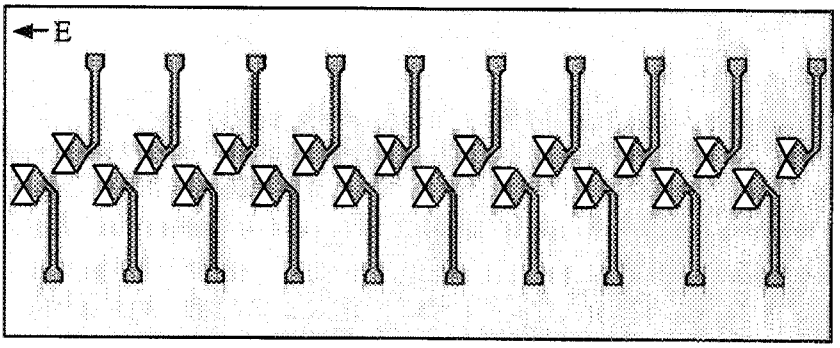

Fig. 2 Mask layout of the RTP ECE Imaging array.

Shown in Fig. 3 is the schematic of the RTP ECEI system. The motorized frames can be translated horizontally to maintain good spatial resolution, when the sample volumes are scanned across the plasma cross-section. From laboratory tests, it is found that for both the TEXT-U and RTP systems, the interchannel spacing is about 1.3 cm. The beam waist (diameter at 1/e intensity) is about 1 cm for the middle channels. This value increases to about 1.5 cm for the edge channels due to spherical aberrations and edge diffraction, mainly due to limited port size.

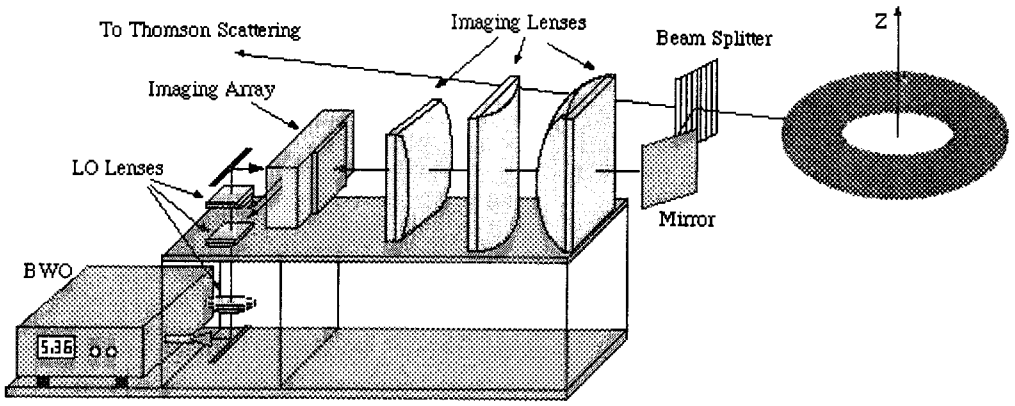

Fig. 3 ECE Imaging diagnostic system implemented on the RTP tokamak. The beam splitter allows the ECEI system and the Thomson scattering system to measure along the same vertical chord of the plasma.

2.2Examples of Experimental Results

Shown in Fig. 4 are the cross power spectral density and cross phases of T_e fluctuations measured by the ECEI system in TEXT-U [2]. Two sets of data are obtained from identical plasma conditions, except that in one set of the discharges, the ECEI system is translated horizontally so that the sample volumes are increased from 1 cm to 2.7 cm (defocused). It is seen that, with degraded spatial resolution, the measured cross power spectral density and cross phases are attenuated due to the sample volume effects [14]. This illustrates the advantage of high spatial resolution ECEI system in plasma fluctuation diagnostics. More results are presented elsewhere [2,7].

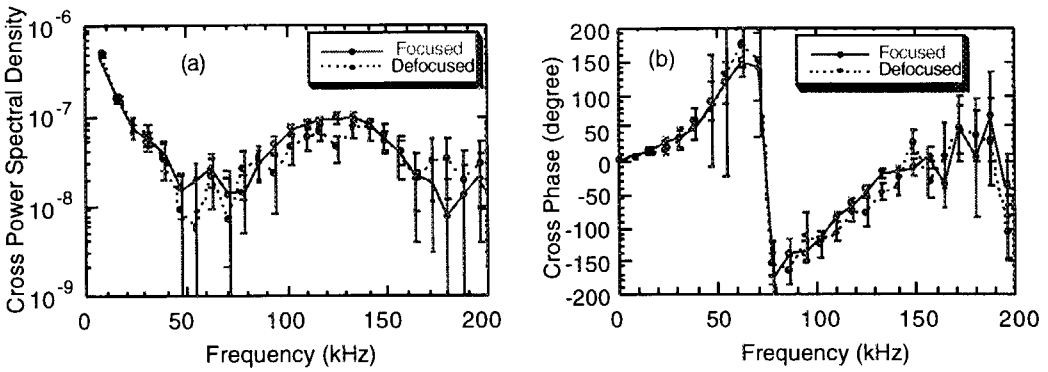

Fig. 4 Sample volume effects in the measurement of drift wave fluctuations (70-170 kHz). The measured cross power spectral density (a) of T_e fluctuations is decreased by ~30%, while the cross phases (b) are decreased by ~10% when the sample volumes are increased from 1 cm to 2.7 cm.

3. Microwave Imaging Reflectometry of Plasma Density Fluctuations

As conventional radar-type reflectometers measure the reflected wave at a single point far away from the plasma cutoff layer, it is impossible to resolve the complicated interference pattern originating from complicated plasma fluctuations [8,9]. Therefore, accurate interpretation of the data is impossible. In view of this difficulty, Mazzucato has recently proposed the concept of imaging reflectometry [9], in which the plasma reflection layer is imaged onto the detector array. Equivalently, an array of detectors simultaneously measure at the plasma cutoff layer, so that the fluctuation structures can be resolved. Shown in Fig. 5 is a schematic of a microwave imaging reflectometer (MIR) being designed for the TEXTOR tokamak. It differs from the ECEI system [Fig.(1)] in that optics is required for illumination of the plasma cutoff layer, and that the imaging optics needs to be designed to match the curvature of the cutoff layer, which may vary with plasma conditions as well as the frequency of measurement.

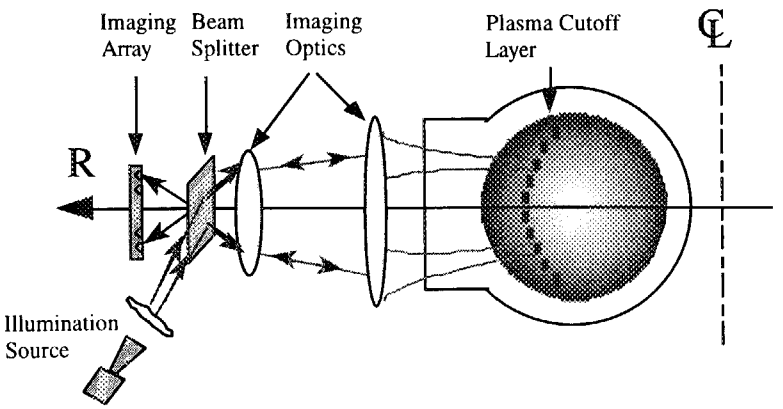

Fig. 5 Schematic of Microwave Imaging Reflectometry.

4. 3-D ECE and Reflectometric Imaging of Plasma Turbulence

As a next step of the millimeter wave imaging diagnostic development, two dimensional imaging arrays will be developed and will be utilized to construct 3-D microwave imaging diagnostic systems, as shown in Fig. 6 [2,9,15]. These systems will combine the ECE imaging diagnostic and the reflectometric imaging diagnostic, so that both the electron temperature and density fluctuations as well as the correlation between these fluctuation quantities can be measured simultaneously. It is expected that new information obtained in this fashion will further advance the understanding of plasma microturbulence and related anomalous transport phenomena [2,9,15].

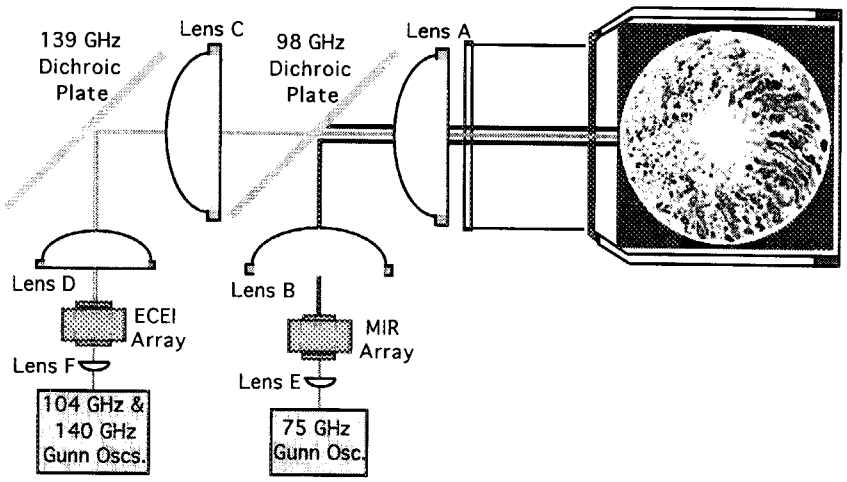

Fig. 6 Schematic of 3-D ECE and Reflectometric Imaging Diagnostic

Acknowledgments

This work is supported by the U.S. Department of Energy under contracts No. DE-FG03-95ER-54295 and W-7405-ENG-48, and by NWO and EURATOM.

References

[1]. N. Bretz, Rev. Sci. Instrum., 68, 2927 (1997).

[2]. B.H. Deng, Two Dimensional Electron Cyclotron Emission Imaging Study of Electron Temperature Profiles and Fluctuations in Tokamak Plasmas, Ph.D. dissertation, UC Davis, (1999).

[3]. H.J. Hartfuss, et al., Proc. Tenth Joint Workshop on Electron Cyclotron Emission and Electron Cyclotron Heating, Ameland, the Netherlands (1997) p.119.

[4]. G. Cima, C. Watts, and R.F. Gandy, Rev. Sci. Instrum., **66**, 798 (1995).

[5]. R.P. Hsia, B.H. Deng, W.R. Geck, C. Liang, C.W. Domier, N.C. Luhmann, Jr., D.L. Brower, and G. Cima, Rev. Sci. Instrum. **68**, (1997) 488-491.

[6]. B.H. Deng, et al., Rev. Sci. Instrum. **70** (1999) 998-1001.

[7]. B.H. Deng, *et al.*, Phys. Plasmas, **5**, 4117 (1998).

[8]. E. Mazzucato, Rev. Sci. Instrum., **69**, 2201 (1998).

[9]. E. Mazzucato, Proc. 24th International Conference on Infrared and Millimeter Waves, September 6-10, 1999, Monterey, CA.

[10]. A.E. Costley, R.J. Hastie, J.W.M. Paul and J. Chamberlain, Phys. Rev. Lett. **33** (1974) 758-761.

[11]. G. Cima, et al., Phys. Plasma, **2** (1995) 720-726.

[12]. H.J. Hartfuss, T. Geist and M. Hirsch, Plasma Phys. Control. Fusion **39** (1997) 1693-1769.

[13]. P.C. Liewer, Nucl. Fusion **25** (1985) 543-621.

[14]. R.V. Bravenec, A.J. Wootton, Rev. Sci. Instrum. **66**, 802 (1995).

[15]. C.W. Domier, et al., Proceeding of the 9th International Symposium on Laser Aided Plasma Diagnostics, Lake Tahoe, California, USA, 1999.

2-6 Development of O-mode reflectometer for density fluctuation measurement on JT-60U

N. Oyama and K. Shinohara

Naka Fusion Research Establishment, Japan Atomic Energy Research Institute, Naka-machi, Naka-gun, Ibaraki 311-0193, Japan

Abstract

The study of relation between turbulence and transport is very important to understand characteristics of the internal/edge transport barrier (ITB/ETB). Recently, core correlation reflectometer using X-mode propagation has been installed on JT-60U tokamak. In order to complement the reflectometer system as to the dependence of measured point on toroidal magnetic field, we have been designed 3ch O-mode reflectometer system.

The 34 GHz fixed frequency reflectometer has been measured density fluctuations in the O-mode reflectometer system as a start. Clear change of the fluctuation spectra in low-frequency region, f < 40 kHz, at the *H-L* back transition and abrupt increase of density fluctuation in high-frequency region, f > 100 kHz, at starting X-point MARFE activity are observed.

I. Introduction

JT-60U has achieved high performance plasma up to Q_{DT} = 1.25 in the reversed magnetic shear (RS) plasma[1]. Then, to realize the steady-state operation as well as high performance is the next step to the fusion reactor. In such plasma, the internal transport barrier (ITB) is the key to improve plasma confinement. Therefore, the ITB physics such as formation conditions, controllability by changing plasma rotation and so on are under investigation. The relation between transport and turbulence is also important to understand the physics related to the transport barrier. A reflectometer is one candidate to measure the fluctuations in such a high energy plasma. Therefore, the X-mode core correlation reflectometer has been applied to the fluctuation measurement in ITB region.

The X-mode core correlation reflectometer, which has been developed in collaboration with Princeton Plasma Physics Laboratory, successfully measured the decay length of density fluctuations as shown in Ref. [2-3]. The frequency range of the system is optimized for toroidal magnetic field, B_T, from 3.3 to 4.0 T in a consideration of typical density profile. Therefore, the system can not measure in lower B_T discharges due to the disappearance of cut-off layer. In typical density case, there is no cut-off layer in a discharge of B_T < 3.0 T.

On the other hand, using O-mode propagation, the cut-off layer depends only on the electron density. In order to measure various case of plasma configurations, 3ch O-mode reflectometer has been designed for density fluctuation measurement to complement X-mode system.

II. Instruments

The targets of O-mode reflectometer is the change of fluctuation during formation of the transport barrier, *H-L* and *L-H* transition, ELM and MARFE activity and so on. These targets are varying from edge to core plasma region. To cover these region, we chose 3 frequencies, 34GHz fixed, 34 to 40GHz selectable and 50GHz fixed, which correspond to the cut-off density of 1.43, 1.43-1.98 and 3.10 $\times 10^{19}$ m^{-3}, respectively. Examples of target plasma are shown in Figure 1.

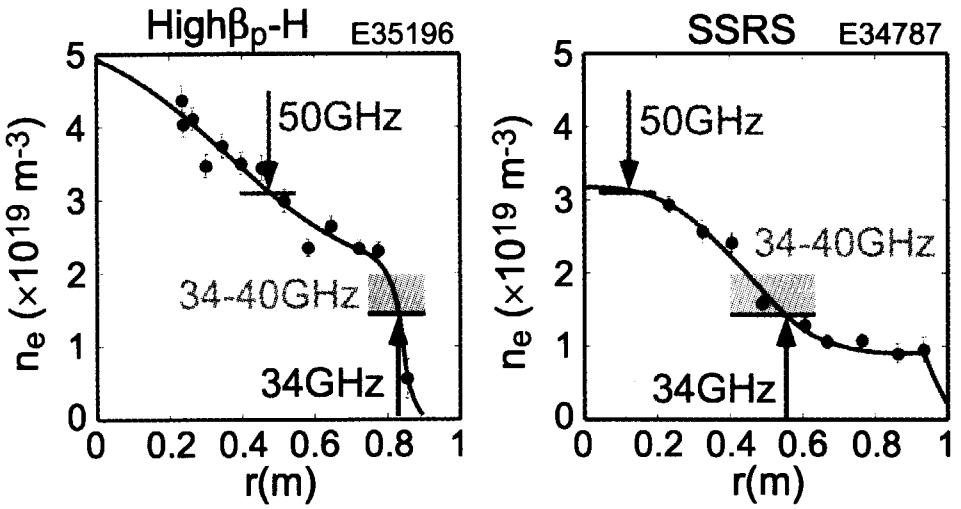

Fig. 1 Typical density profile measured with the YAG Thomson scattering system [4] together with the cut-off position of each frequency. Left figure is high β_p-*H* mode plasma in relatively high density case and right one is steady-state reversed magnetic shear plasma with *L* mode edge.

The transmission line which consists of corrugated waveguide was shared between X-mode and O-mode system to measure the same location of a plasma and to avoid the limitation of diagnostics port. Two separate lines for the incident wave and the received wave are used to reduce the cross talk and each line has focusing antenna with steering system which can control poroidal and toroidal mirror angle independently. The transition from rectangular waveguide in Q-band to corrugated waveguide for O-mode system using horn with lens is directly connected to the wire-grid beam splitter which acts as the polarization separator.

Figure 2 shows the schematic of millimeter-wave section of the O-mode reflectometer. There is some difference among each channel, but basically each channel is configured as a heterodyne system having two separate sources. They produce two intermediate frequency (IF) signals, one comes from the plasma, IF_{SIG}, and the other is used as a reference, IF_{REF}, with the frequency of 140 MHz. The optical fiber link system, which can transfer the signal in the frequency range from 10 MHz to 1.5 GHz, carries these IF signals from Torus Hall to Diagnostic Hall. The quadrature-type phase detection system provides sin- and cosine-components, $E_r \sin\theta$ and $E_r \cos\theta$, in each channels. The outputs are acquired by PC-based 12 bit digitizer with 4 MW memory and then stored on the magneto optical (MO) jukebox via network file system (NFS) as shown in Fig. 3.

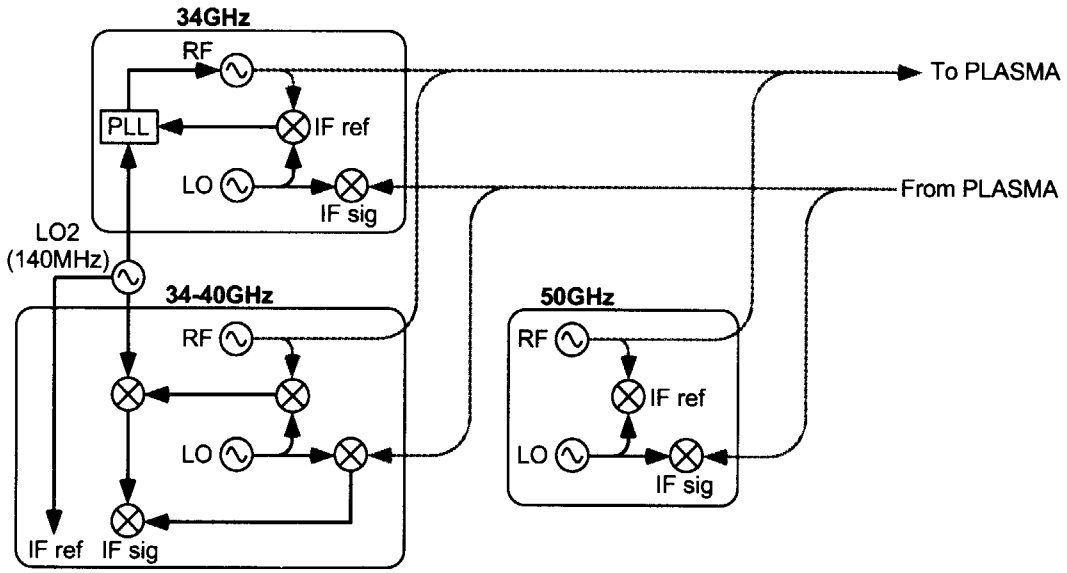

Fig. 2 Schematic of millimeter-wave section of the O-mode reflectometer.

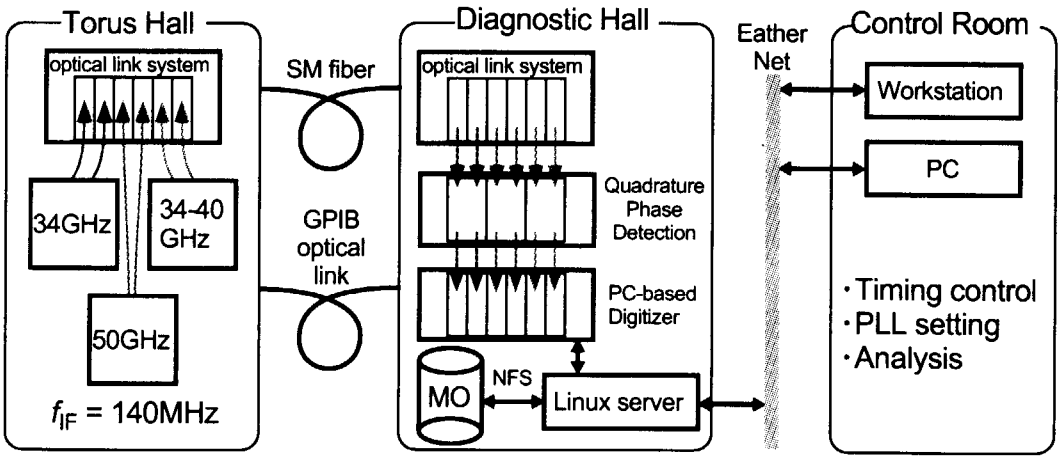

Fig. 3 Schematic of the IF section and data acquisition system.

III. Experimental results

The 34 GHz fixed frequency O-mode reflectometer has been started to measure the density fluctuation in JT-60U routinely. The response of the reflectometer system was checked by reconstruction of the plasma motion from the phase variation of the reflected signal, since phase variation corresponds to the movement of cut-off layer directly assuming the density profile unchanged. The movement of cut-off layer calculated using reflectometer signal is in good agreement with that of plasma center as shown in Fig. 4. In lower density case that there is no cut-off layer, we also confirmed that the system acts as a interferometer. Then, the reflectometer system has been applied to the edge fluctuation measurement.

Figure 5 shows the time evolution of D_α signal measured at divertor region and spectrogram of the complex amplitude of reflectometer signal in degradation phase of high β_p-*H* mode plasma. Increase of the fluctuation with the frequency lower than 40 kHz is clearly observed during *L*-mode phase. One feature of time slice of the spectrum is the reduction of zero frequency component, but total reflected power in low frequency region is same in both case. After *L-H* transition at t = 8.52 s, the fluctuation level decreased same as before *H-L* transition. Unfortunately, the exact position of cut-off layer is unknown, since we didn't have all Thomson scattering data in this shot. But we supposed that the cut-off position didn't move so much, because the line averaged density was almost constant at both transition,

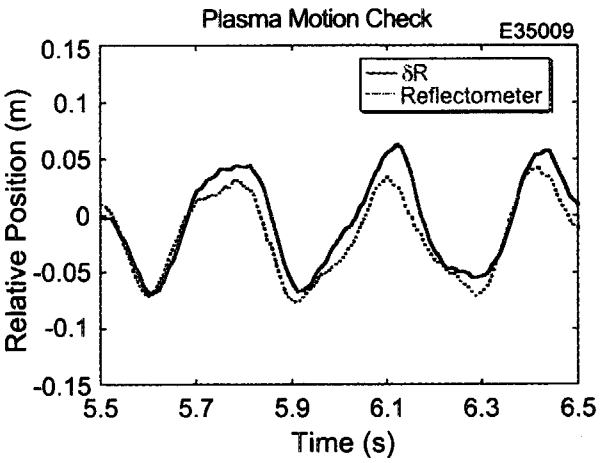

Fig. 4. Reconstruction of the plasma motion (dotted line) together with the motion of the plasma center (solid line). The plasma position was swung radially in 3 Hz with keeping plasma shape.

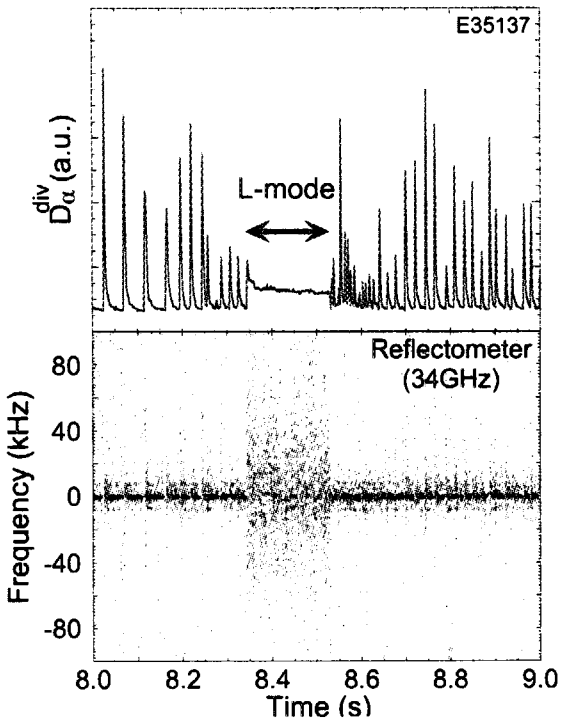

Fig. 5. Time evolution of D_α signal at divertor region and spectrogram of the reflectometer signal. *H-L* back-transition occurred at t = 8.35 s.

H-L and *L-H* transitions in this shot.

In JT-60U, there is some real-time feedback system to control plasma such as density feedback, stored energy feedback, temperature gradient feedback and so on. We also try to control divertor plasma using neutral pressure ratio feedback system, which control the injection of gas puffing using a pressure ratio between inner and outer divertor region, to sustain a detached divertor. To obtain the behavior of neutral pressure in a high recycling divertor plasma for optimization of parameters in a feedback system, pressure response of inner and outer divertor region has been studied under various case of gas puffing configuration so far.

Figure 6 shows the electron density profile and the spectrogram of the reflectometer signal in high recycling divertor plasma. In this shot, neutral beam power and gas puffing from divertor were applied from t = 5.0 s and then radiation in the divertor region gradually increased toward an X_p-MARFE occurred at t = 8.4 s. At starting X_p-MARFE, abrupt increase of the high frequency fluctuation in the range of larger than 100 kHz is observed as shown in Fig. 6(b). Although the density in the core region was gradually increase during X_p-MARFE, the location of cut-off layer is almost same at measured time as shown in Fig. 6(a). This increase of the fluctuation was finished in a few millisecond, which is much faster than saturation time of radiation from the divertor and changing time of density and temperature.

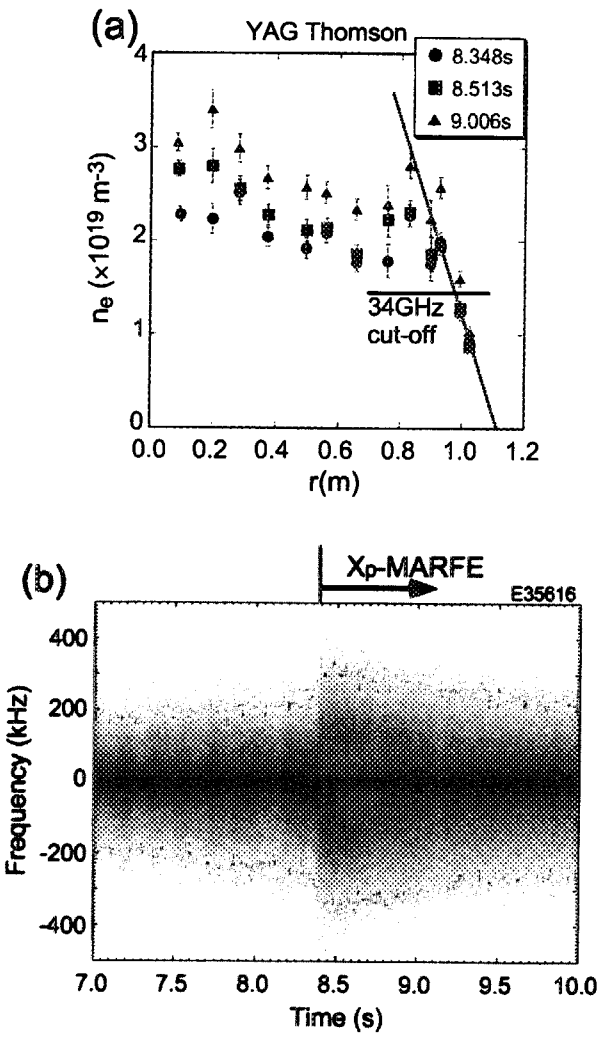

Fig. 6. Electron density profile (a) measured with the YAG Thomson scattering system before X_p-MARFE, t = 8.348 s, and during X_p-MARFE, t = 8.513 and 9.006 s, and the spectrogram of the reflectometer signal (b).

The response of the spectrum change at starting X_p-MARFE is curious in its dependence of gas-puff location. Figure 7 shows the integrated signal in the frequency range of larger than 100 kHz in divertor and main puff case. Although abrupt increase of the

fluctuation was observed at starting Xp-MARFE using divertor gas puffing, using main gas puffing located at top of the plasma, the fluctuation signal starts to decrease at starting Xp-MARFE as shown in Fig. 7. The starting time of the Xp-MARFE is different in these case. But there is no clear difference at that time in major parameter around measured point such as density, temperature and plasma rotation among two cases. Therfore, we need further experiments for detailed discussion to find the answer.

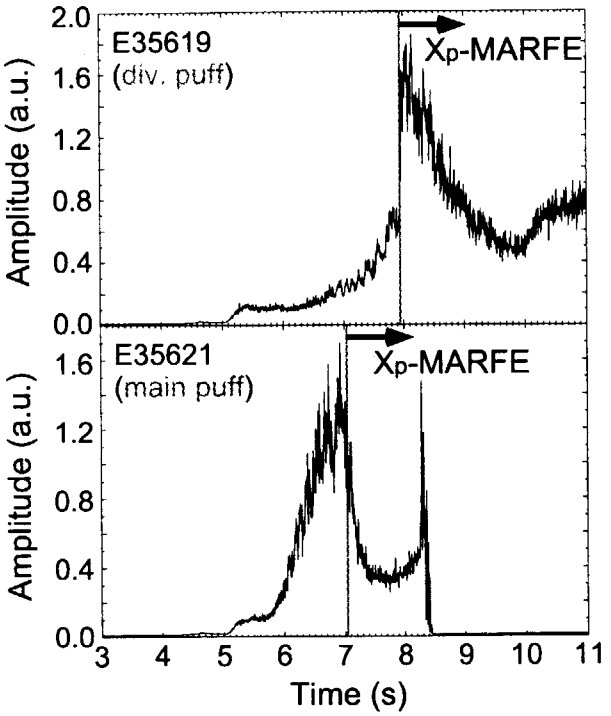

Fig. 7. Integrated signal in high frequency region, $f > 100$ kHz, in divertor (upper) and main puff (lower) case.

Acknowledgement

The authors would like to thank Dr. R. Yoshino for his continuing support and encouragement and acknowledge the members of the Japan Atomic Energy Research Institute who have contributed to the JT-60U projects.

Reference

[1] T. Fujita *et al.*, Nucl. Fusion **38**, 207 (1998).

[2] K. Shinohara *et al.*, Rev. Sci. Instrum. **70**, 4246 (1999).

[3] R. Nazikian *et al.*, "Core density fluctuations in reverse magnetic shear plasmas with internal transport barrier in JT-60U", in *Plasma Physics and Controlled Nuclear Fusion Research* (Proc. 17th Int. Conf. Yokohama), Post Deadline, Vienna, 1998, IAEA.

[4] T. Hatae *et al.*, Rev. Sci. Instrum. **70**, 772 (1999).

2-7 Polarization Spectroscopy Using Optical Coherence-based Techniques

J. Howard
Plasma Research Laboratory,
Australian National University. Canberra ACT 0200

Abstract

We demonstrate the utility of coherence techniques for the measurement of Zeeman and Motional Stark Effect spectral multiplets. A spherical quadrature polarimeter constructed of birefringent plates mutually oriented at 45° and followed by a polarizer is used to modulate the intensity of the π and σ components. This effects a modulation of the centre frequency and/or spectral width of the light which can be measured by the MOSS spectrometer. Apart from the simplicity and photon-economy of the new approach, we show that coherence methods naturally yield both the magnitude and orientation of the magnetic field that gives rise to the polarization alignment.

1 Introduction

The use of coherence methods for Doppler spectroscopy has been discussed by Howard *et al* (these proceedings). It is often the case that spectral lines are also split by magnetic or electric fields (possibly induced). The amount of splitting and the polarization orientation of the multiplet components convey information about the vector fields $\boldsymbol{B}$ or $\boldsymbol{E}$. By modulating the polarization state of the multiplet, it is possible to vary the spectral content of the light. The change in the spectral shift or width is then sensed by the MOSS spectrometer as a variation of the interferogram phase or envelope. The phase and amplitude of these modulations give information about the orientation and magnitude of the originating field (electric or magnetic).

In the first part of this paper we describe a spherical quadrature polarimeter based on two birefringent plates and an analyzer that enables simultaneous determination of the three Stokes parameters. The applicability of the combined polarimeter and MOSS spectrometer for MSE measurements has been described elsewhere [1]. The primary advantages are higher light throughput and the elimination of narrowband interference filters for isolating the central σ cluster of lines. In this paper we give an overview of the MSE application and look at the utility of coherence methods for estimating the plasma magnetic field using Zeeman effect splitting.

2 Polarimeter

The polarimeter uses two birefringent phase plates (delays δ_1 and δ_2) having their fast axes mutually oriented at 45°. The plates are followed by an analyzer oriented to transmit light polarized parallel to the fast axis of the first phase plate (the x direction) (see Fig. 1).

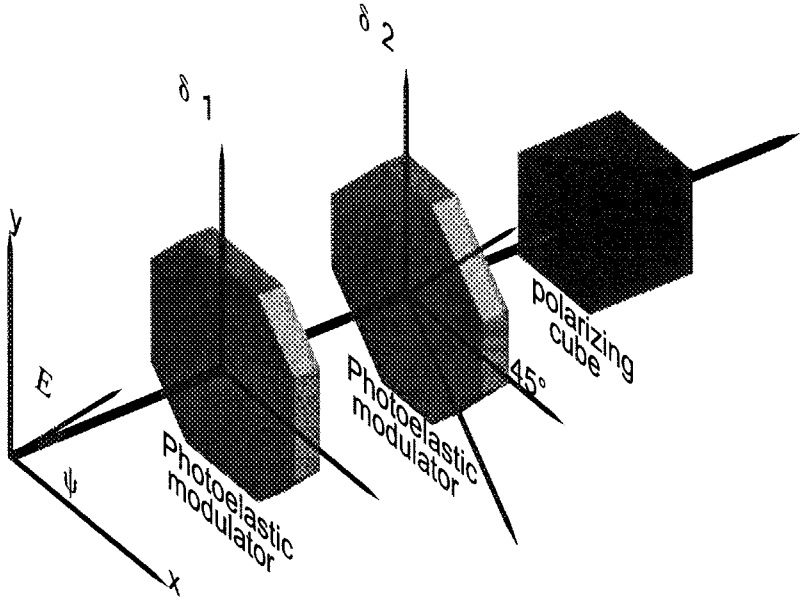

Figure 1: Optical layout for the spherical quadrature polarimeter.

The intensity of the light transmitted (or reflected) by the analyzer is related to the Stokes vector of the input radiation by [2]

$$P = \frac{\mathcal{I}}{2}(1 \pm \boldsymbol{s}.\boldsymbol{p}) \quad (1)$$

$$\boldsymbol{s} = (\cos 2\psi \cos 2\chi,\ \sin 2\psi \sin 2\chi,\ \cos 2\chi) \quad (2)$$

$$\boldsymbol{p} = (\cos \delta_2,\ \sin \delta_2 \sin \delta_1,\ \sin \delta_2 \cos \delta_1) \quad (3)$$

where $\boldsymbol{s}$ is the Stokes vector, ψ is the tilt angle of the vibrational ellipse and χ the ellipticity. Equation (3) defines an optical phase shift vector analogous to the Stokes vector. If the phase plates are replaced by photoelastic modulators operating at frequencies Ω_1 and Ω_2 it is possible, using appropriate delay amplitudes and synchronous detection techniques to measure simultaneously all the components of $\boldsymbol{s}$.

3 Motional Stark Effect

Motional Stark effect (MSE) polarimetry is now a standard diagnostic for estimating magnetic field pitch angle in tokamaks using high power heating beams [3, 4, 5, 6]. The MSE technique relies on the splitting of the high energy neutral beam Balmer α light into orthogonally polarized σ and π components as a result of the motion-induced strong electric field $\boldsymbol{E} = \boldsymbol{v} \times \boldsymbol{B}$ experienced in the rest frame of the neutral atoms. When viewed in a direction perpendicular to $\boldsymbol{E}$ the Stark split σ and π components are polarized respectively perpendicular and parallel to the direction of $\boldsymbol{E}$. When viewed along $\boldsymbol{E}$ the σ components are unpolarized and the π components have no intensity. The magnetic field pitch angle is usually estimated by isolating and measuring the polarization direction of the central cluster of σ lines.

The polarimeter proposed here requires a quarter wave plate and a single photoelastic modulator. To show this, we note that the electric field vectors for the σ and π components are linearly polarized and orthogonal so that $\chi = 0$ with ψ taken as the orientation of the σ components. Fixing the first phase plate delay $\delta_1 = \pi/2$ (quarter wave plate) and sinusoidally modulating the second phase plate delay $\delta_2 = \delta \sin \Omega_P t$ with modulation amplitude $\delta = \pi/2$ we obtain for the output intensity at the two polarimeter ports

$$2P_{\pm}(\nu) = \mathcal{I}(\nu)\,[1 \pm \zeta_P(\nu) \cos(2\psi - \delta \sin \Omega_P t)] \tag{4}$$

where $\mathcal{I} = \mathcal{I}_\sigma + \mathcal{I}_\pi$ is the total intensity and $\zeta_P = (\mathcal{I}_\sigma - \mathcal{I}_\pi)/(\mathcal{I}_\sigma + \mathcal{I}_\pi)$ is the nett polarization "contrast". Provided the difference $\mathcal{I}_\sigma - \mathcal{I}_\pi$ in component intensities is sufficiently great, the polarimeter signals will give the quadrature components $\sin(2\psi)$ and $\cos(2\psi)$ at Ω_P and $2\Omega_P$ respectively.

Since the integrated intensities for the σ and π components are comparable [7], some spectral discrimination is required to increase the polarization contrast. The standard approach is to isolate the σ components using a narrowband interference filter. This is satisfactory provided the Stark splitting $\Delta\nu_S$ is sufficiently large for the π components to fall substantially outside the filter passband. It is also necessary that the splitting be large or comparable to the spectral broadening of the line due to the neutral beam divergence or range of viewing angles. Tilt-tuned narrowband interference filters are required for each observing position. The filters are lossy and make no use of the available π light. All these issues bear on the achievable signal to noise ratio which in turn limits the range of beam energies and magnetic field strengths for which MSE is useful.

As we have seen, the polarimeter transmits alternately the π and σ manifolds using polarization modulation techniques at frequency Ω_P. Since the spectral bandwidth of the π manifold is greater than for the central σ components, the MOSS spectrometer can enhance the signal modulation depth given an appropriate choice of time delay τ (see paper by Howard *et al.* - these proceedings). The

MOSS is essentially a fixed delay Fourier transform spectrometer whose output signal is given by

$$S = I_0[1 \pm \zeta \cos(\phi_0 + \phi_1 \sin \Omega t)] \tag{5}$$

where I_0 is the spectrally integrated incident light intensity, $\phi_0 = 2\pi\nu_0\tau$ depends on the spectral line centre frequency ν_0, ζ is the fringe contrast (depends on spectral line width) and $\phi_1 \sin \Omega t$ is an externally imposed modulation with $\phi_1 = \pi/2$. In practice, the polarimeter and MOSS spectrometer would be combined, thereby eliminating the need for the polarimeter analyzing cube. The combined system is shown in Fig. 2.

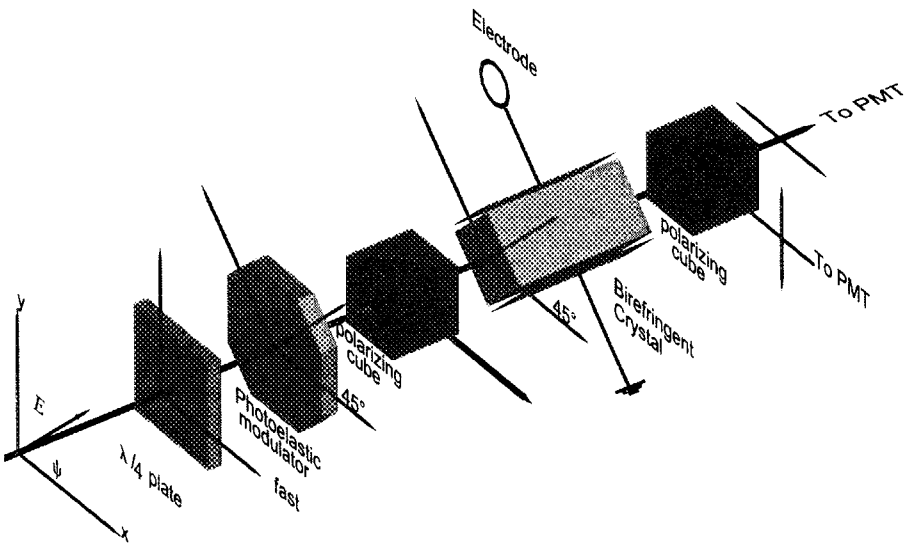

Figure 2: Layout for the combined spherical quadrature polarimeter/MOSS spectrometer.

Because of its wide field of view (see Michael and Howard - these proceedings), a combined polarimeter/MOSS camera can be located close to the viewing port and the signals relayed by optical fibre to one or more detector arrays. Since the full multiplet is observed, only a relatively wideband interference filter is required to isolate the full energy emission spectrum. In practice, such a wideband filter could be used for a number of viewing channels simultaneously, thereby eliminating the need for an array of tilt-tuned narrowband interference filters.

For the combined system, the light intensity at the final transmit polarizer port is given by

$$S = I_0/2[1 + (\zeta_\sigma \cos^2 \Psi + \zeta_\pi \sin^2 \Psi) \cos \Phi] \tag{6}$$

$$\begin{aligned} \Psi &= 2\psi + \delta_2 \sin \Omega_P t \\ \Phi &= \phi_0 + (\pi/2) \sin \Omega_M t \end{aligned} \tag{7}$$

where Ω_P and Ω_M are the modulation frequencies for the polarimeter plate and the MOSS birefringent plate respectively. Taking $\Omega_P < \Omega_M$, it is apparent that the ellipse orientation ψ is carried by the phase of the amplitude modulation (at frequency Ω_P) impressed on the MOSS interferometer carier signal (at Ω_M). The depth of this amplitude modulation $\zeta_\sigma - \zeta_\pi$ yields the magnetic field strength $\mid \boldsymbol{B} \mid$. The difference in contrast between the central σ and wing π clusters can be maximized through appropriate choice of the dc phase offset ϕ_0 introduced by the birefringent plate. Variations in beam energy will be registered as changes in the offset phase ϕ_0. For simplicity (though not necessity) the above analysis has assumed that the total intensities of the σ and π manifolds are comparable [7].

4 Zeeman Effect

The measurement of the poloidal magnetic field in a tokamak from the Zeeman splitting and polarization of the magnetic dipole radiation from heavy ions was suggested by Feldman [8]. While first results were promising [9], the accuracy of the method was limited by signal to noise ratio problems. More recently, however, accurate measurements of the poloidal field profile in the outer region of JIPP T-IIU discharges during current ramping experiments have been obtained by measuring the Zeeman splitting of HeII (468.8 nm) [10].

The upper and lower electronic levels of an atom or ion in a weak magnetic field are split into $2J + 1$ sublevels with energy shifts given by

$$\Delta E_{JM} = g_{\alpha JM} M \mu B \tag{8}$$

where, for $L - S$ coupling, $g_{\alpha JM}$ is the Landé splitting factor, μ is the Bohr magneton and α denotes quantum numbers other than the total angular momentum J and magnetic quantum number $\mid M \mid \leq J$. Because of these shifts, the spectral line is split into a number of components whose relative intensities and polarizations depend on the corresponding changes in J and M [8, 11]. Viewed along $\boldsymbol{B}$, the intensity is zero for the $\Delta M = 0$ lines and is circularly polarized clockwise for $\Delta M = +1$ and counterclockwise for $\Delta M = -1$. Viewed in the direction perpendicular to $\boldsymbol{B}$, the emission is linearly polarized perpendicular to B for $\Delta M = 0$ and parallel to $\boldsymbol{B}$ for $\Delta M = \pm 1$. For tokamaks, this splitting is often small compared to the Doppler broadening. The polarization tagging of the frequency shifted Zeeman components is thus essential for their discrimination against the unshifted component.

We consider a coordinate system where γ is the angle between the helical field lines and the line of sight (taken in the x direction) and ξ is the projection of $\boldsymbol{B}$ onto the orthogonal $y - z$ plane as shown in Fig. 3. The local radiant intensity

for the nth spectrally shifted circular component is $\mathcal{I}_n^{(\Delta M)}(\nu_0 \pm \Delta\nu_n^{(\Delta M)})$ where $\Delta\nu_n^{(\Delta M)}$ the frequency shift of the nth line of the group exhibiting the change in magnetic quantum number ΔM. The resulting spectrum and polarization state of the emergent radiation is the integral over the line-of-sight of the contributions from all components of the Zeeman multiplet.

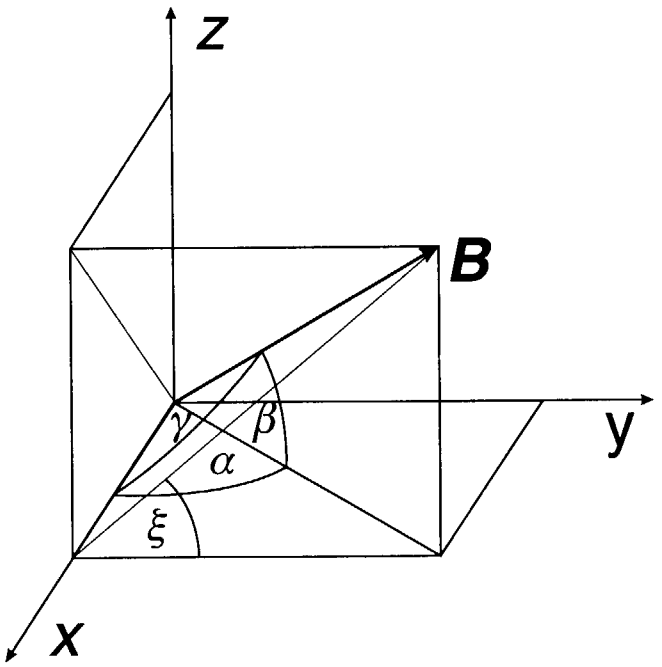

Figure 3: Geometry for analysis of Zeeman effect. The viewing line is along the x axis.

For simplicity, let us ignore the line integration and assume a simple Zeeman triplet. The Stokes vectors for the central and shifted components are given respectively by

$$\begin{aligned} \boldsymbol{s}_0 &= (-s_1, s_2, 0) \\ \boldsymbol{s}_\pm &= (s_1, -s_2, \mp s_3)/2 \\ (s_1, s_2, s_3) &= (\sin^2\gamma\cos 2\xi, \sin^2\gamma\sin 2\xi, 2\cos\gamma). \end{aligned} \tag{9}$$

Taking $\boldsymbol{p} = (0, 0, 1)$ (i.e. $\delta_1 = 0$, $\delta_2 = \pi/2$), Eq. (3) gives the polarimeter output

$$4P = (1 - s_3)\mathcal{I}(\nu_0 + \Delta\nu) + (1 + s_3)\mathcal{I}(\nu_0 - \Delta\nu) \tag{10}$$

where $\mathcal{I} = \mathcal{I}_+ = \mathcal{I}_-$ and $\Delta\nu$ is the Zeeman frequency shift. Following the Fourier transforming action of the MOSS spectrometer, the signal is proportional to

$$S = I_0 \pm I_0\Gamma(\phi)\cos[\phi_0(1 - 2\cos\gamma\Delta\nu/\nu_0) + \phi_1\sin\Omega t] \tag{11}$$

where ϕ_0 is the spectrometer phase delay and $\Gamma(\phi_0)$ is the Fourier transform of the spectral line shape $\mathcal{I}(\nu)$. The phase of the interferogram is modulated

by the component of the magnetic field strength in the direction of the viewing line. This is due to the switching between the left and right handed polarizations brought about by the polarimeter, and the resulting shift in the centre frequency of the emission line that is detected by the MOSS spectrometer. Note that the phase modulation is independent of the overall line-shape details of the Zeeman multiplet. On the other hand, methods that rely on fitting the nett circular polarization spectral profile must normally allow for the multiplet structure [9].

By simultaneously modulating δ_1, the polarimeter also switches transmission between the perpendicular and parallel components of the multiplet (in the same way as for MSE). This modulates the specral line width (or coherence length) which the MOSS registers as a modulation of the total fringe visibility. In this way it is possible to also measure the perpendicular component of $\boldsymbol{B}$ (angle ξ).

Acknowledgements

It is a pleasure to acknowledge useful discussions with Mr. C. Michael.

References

[1] J. HOWARD, Rev. Sci. Instrum. **70**, 368 (1999).

[2] J. HOWARD, Rev. Sci. Instrum. **66**, 383 (1995).

[3] F. M. LEVINTON *et al.*, Phys. Rev. Lett. **63**, 2060 (1989).

[4] F. M. LEVINTON *et al.*, Rev. Sci. Instrum. **61**, 2914 (1990).

[5] D. WROBLEWSKI *et al.*, Rev. Sci. Instrum. **61**, 3552 (1990).

[6] D. WROBLEWSKI and L. L. LAO, Rev. Sci. Instrum. **63**, 5140 (1992).

[7] J. XU *et al.*, Fus. Eng. and Design **34-35**, 293 (1997).

[8] U. FELDMAN *et al.*, J. Appl. Phys. **56**, 2512 (1984).

[9] D. WROBLEWSKI, L. K. HUANG, and H. W. MOOS, Rev. Sci. Instrum. **59**, 2341 (1988).

[10] H. KURAMOTO *et al.*, Fusion Eng. And Design **34-35**, 285 (1997).

[11] C. CANDLER, *Atomic Spectra* (Hilger and Watts, London, 1964).

2-8 LIF diagnostics for low temperature and fusion plasmas

B.W. James, I.S. Falconer, H.J. Kim[1], B.C. Zhang[2], M. Ibrahim, M.J. Wouters[3] and G. Roupillard[4]

School of Physics
University of Sydney
NSW Australia 2006

Laser induced fluorescence (LIF) techniques allow the measurement of many plasma properties with a high degree of spatial and temporal resolution. The LIF process involves laser excitation of a transition from the ground or a metastable level of an atom, ion or molecule and observation of the subsequent fluorescence from a transition which may be directly or indirectly connected to the excited level. The radiation source is usually a tunable dye laser; cw dye lasers provide very high spectral resolution while pulsed dye lasers achieve high temporal resolution with lesser spectral resolution. The plasma parameters which can be measured using LIF include relative species density, species velocity and electric field. This talk will present results of recent LIF measurements of hydrogen atom temperature in a microwave discharge, ion velocity in a presheath, and electric field in a sheath. The proposed use of LIF to measure electric fields in the H-1 Heliac is also be discussed.

Introduction

Laser induced fluorescence (LIF) is a plasma diagnostic technique in which a laser is tuned to a transition from a sufficiently populated level of an atom, ion or molecule, usually a ground or metastable level. The subsequent fluorescence when the atom, ion or molecule undergoes a transition to a lower level is observed. As shown in Figure 1(a), the lower level of the fluorescent transition is generally different from the original level. Indeed this is the preferred situation as it allows a high rejection of stray laser light from the detection system. One of the features of LIF diagnostics is the high degree of spatial resolution, as shown in Figure 1(b).

Many plasma parameters can be measured using LIF diagnostic techniques, particularly in the case of low temperature plasmas where species with bound electrons are abundant. LIF can be used to identify the presence of species, their densities, and their velocity distributions. Electric and magnetic fields can also be measured from their effect on the quantum states involved, and hence the corresponding effect on the transition probabilities and spectral distributions of the transitions between the states.

This paper describes and presents results of measurements of the atomic temperature in a high pressure hydrogen microwave discharge similar to those used for diamond thin film

[1] present address: Kyushu University, Kasuga, Fukuoka 816-8580, Japan
[2] present address: Thin Film Group, Chartered Semiconductor Manufacturing Ltd, Singapore738406
[3] present address: CSIRO Division of Telecommunications and Industrial Physics, Australia 2070
[4] present address: ESPEO, Université d'Orléans, 45067-ORLEANS cedex 2, France

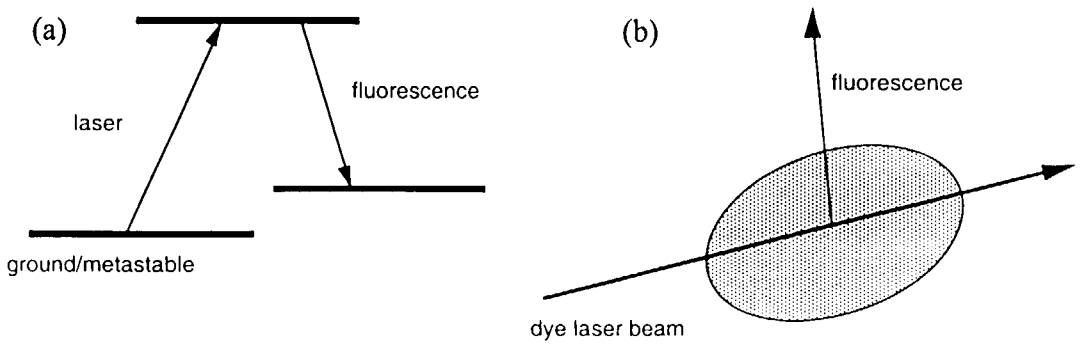

Figure 1 (a) Typical LIF energy level scheme (b) Typical geometry of a LIF measurement

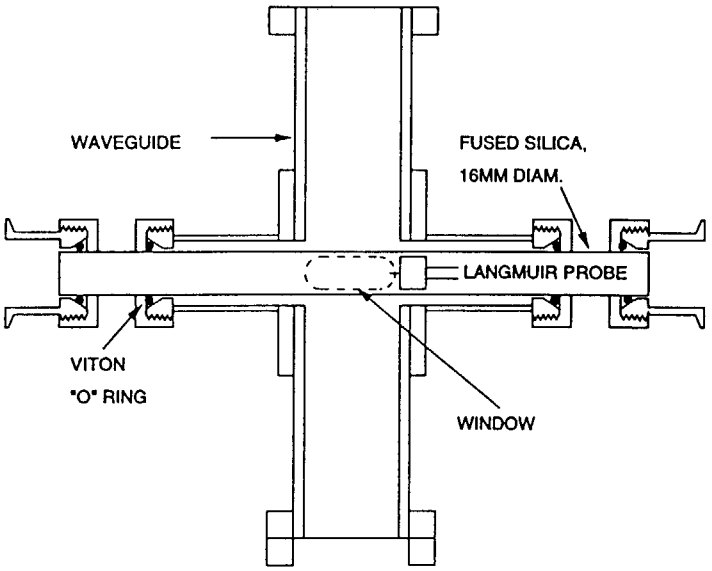

Figure 2 Microwave discharge used to measure hydrogen atom temperature

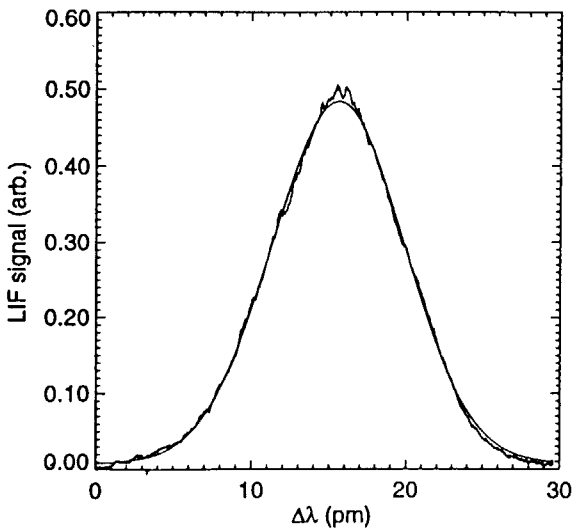

Figure 3 Fluorescence (Ha) profile as the laser is tuned through the two-photon excitation transition from $n = 1$ to $n = 3$.

deposition, ion drift velocity in the presheath of an rf plasma sheath in a helicon wave plasma source, and the electric field in the sheath of a dc hollow cathode discharge.

Hydrogen temperature in a microwave discharge

The experimental set up, shown in Figure 2, used a microwave discharge in a silica tube passing through a rectangular microwave waveguide. Radiation at 205 nm from the frequency doubled output of an excimer pumped, pulsed dye laser operating at 410 nm was used to excite hydrogen atoms from their ground state to the $n = 3$ level, with fluorescence of the Hα transition observed. The spectral profile of the fluorescence, recorded as the laser was tuned through the excitation transition, is shown in Figure 3. The profile is well fitted by a Gaussian profile, confirming that the hydrogen atoms are thermalised at a temperature of around 1200 K. Atomic hydrogen in such discharges is important as it plays a crucial role in the surface processes which are involved in the deposition of diamond films in which case the discharge is doped with ~ 1% CH_4 [1]. Further details of this measurement are available elsewhere [2].

Drift velocity in a plasma presheath

This measurement was made in a helicon wave plasma source used for thin film deposition [3]. This device used rf bias applied to the substrate holder in order to accelerate ions into depositing thin films, such as boron nitride [4]. The ion velocity in the presheath, which links the rf sheath to the bulk plasma, was measured using the experimental arrangement shown in Figure 4. This experiment used argon; the argon ion LIF scheme is shown in Figure 5. Because of the Doppler shift associated with the ion motion towards the biased electrode, fluorescence was observed when the laser was tuned above and below the excitation transition by equal amounts. The drift velocity of the ions, determined for the difference in laser wavelength required to produce fluorescence, is shown in Figure 6. These results show that the velocity profile in the presheath is not affected by the application of rf bias, suggesting that the effect of rf bias is localised to the sheath itself. The ion temperature could also be determined by fitting Gaussian profiles to the LIF spectra.

LIF measurement of electric field

LIF techniques for measuring electric fields in plasmas are based on the Stark effect which leads to shifting and splitting of transitions and the enhancement of the transition probabilities of forbidden transitions due to wavefunction mixing. The measurement reported here uses a technique due to Oda and coworkers [5] which uses a forbidden transition from the 2^1S metastable state of helium. Stark mixing between the levels shown in Figure 7 causes the forbidden transition to be a function of the perturbing electric field. With increase in the principal quantum number of the upper levels the technique becomes sensitive to lower values of electric field. As the quadratic Stark effect is applicable, for a sufficiently strong field the electric field is given by

$$I_f / I_a = a + bE^2$$

where a and b are constants, and I_f and I_a are the fluorescent signals resulting from excitation respectively of the forbidden transition and the adjacent allowed transition (see Figure 7).

Results of measurements on a hollow cathode discharge in helium at 0.7 torr are shown in Figure 8. Calibration was achieved by requiring that the potential difference between the

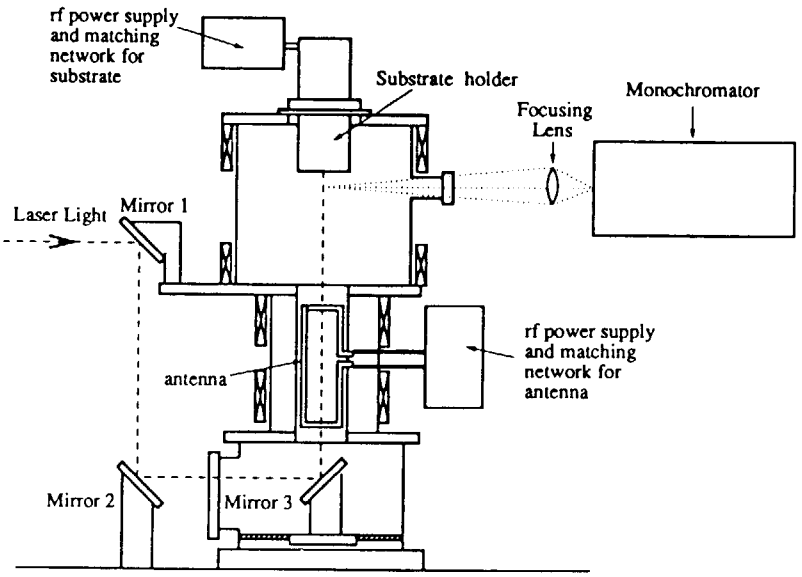

Figure 4　The helicon wave plasma source and LIF set up.

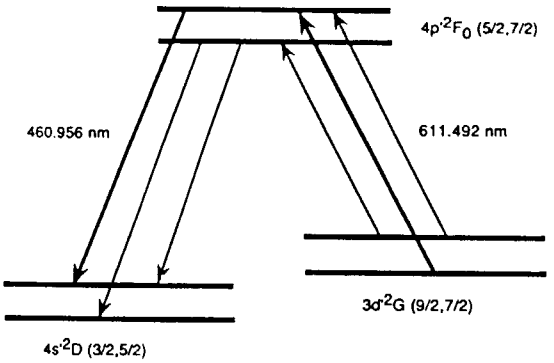

Figure 5　Argon ion LIF scheme

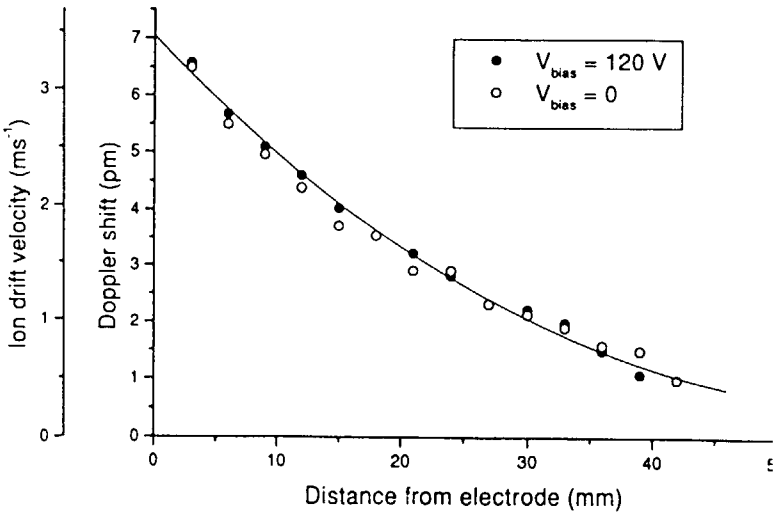

Figure 6　Ion velocity in plasma presheath for rf bais of 120 V, and in the absence of rf bias.

cathode and the mid point is equal to the total potential difference across the discharge. This measurement confirms similar measurements made by Oda and coworkers [5]. A variation on this technique which uses polarisation of the fluorescence to determine the field [6] does not require calibration.

Measurement of Electric Field in H-1 Heliac

In common with other magnetically confined plasmas, the H-1 Heliac [7] can operate in a high confinement mode which is characterised by an enhanced radial electric field. Direct measurement of this field is important for understanding this mode of operation. It is planned to use the LIF technique described above to measure the radial field in H-1. There are however a number of issues which require attention to ensure the success of such a measurement. These are the generation of a helium beam with a sufficiently high metastable density, calibration of the technique in the absence of electrodes, and the effect of the confinement magnetic field on the fluorescence polarisation.

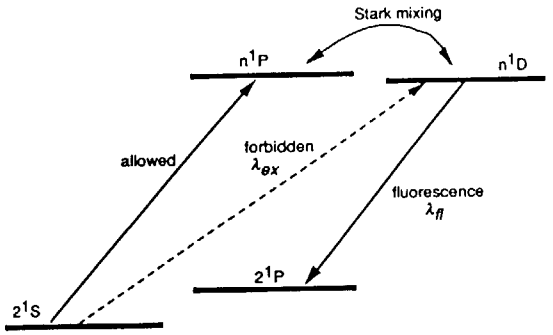

Figure 7 Helium LIF scheme for measuring electric fields

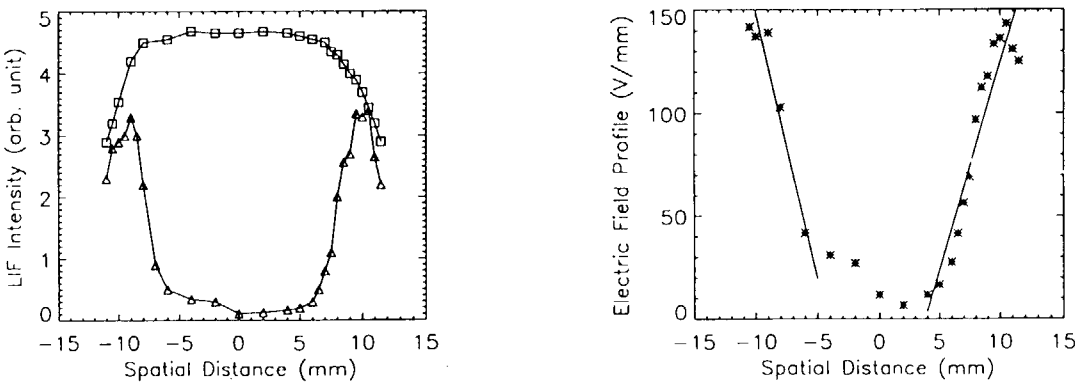

(a) (b)

Figure 8 (a) Fluorescence and (b) electric field as a function position in a parallel electrode hollow cathode discharge.

Conclusions

LIF techniques allow the measurement of many plasma parameters with high spatial and temporal resolution and minimal perturbation. LIF measurements of atom temperature in a microwave discharge, ion drift velocity in a helicon wave plasma, and electric field in a hollow cathode discharge have been described. The last technique is proposed for measuring radial electric fields in the H-1 Heliac.

Acknowledgements

The authors acknowledge assistance from the Australian Research Council, the Australian Institute of Nuclear Science and Engineering, and the Science Foundation for Physics within the University of Sydney.

References

1. J. Khachan, J.R. Pigott, G.F. Brand, I.S. Falconer and B.W. James, *Rev. Sci. Instrum.*, **64** 2971 (1993)

2. M.J. Wouters, J. Khachan, I.S. Falconer and B.W. James, *J. Phys. D: Applied Physics*, **31** 2004 (1998).

3. D.R. McKenzie, W.D. McFall, H. Smith, B. Higgins, R.W. Boswell, A. Durandet, B.W. James and I.S. Falconer, *Nucl. Instr. Meth. Phys. Res. B*, **106** 90 (1995).

4. D.R. McKenzie, W.D. McFall, S. Reich, B.W. James, I.S. Falconer, R.W. Boswell, H. Persing, A.J. Perry and A. Durandet, *Surface & Coating Technology*, **78** 255 (1996).

5. H. Sakai, K. Takiyama, M. Kimura, M. Yamasaki, T. Oda and K. Kawaski, *J. Nucl. Mater.*, **196-198**, 1135 (1992).

6. M. Watanabe, K. Takiyama and T. Oda, *Rev. Sci. Instrum.*, **70**, 903 (1999).

7. M.G. Shats, D.L. Rudakov, B.D. Blackwell, G.G. Borg, R.L. Dewar, S.M. Hamberger, J. Howard and L.E. Sharpe, *Phys. Rev. Lett.*, **77** 4190 (1996).

2-9 Measurement of Electric field distribution in Ar plasma

H. J. Kim, V. P. Gavrilenko, T. Ikutake, M.D. Bowden and K. Muraoka
Interdisciplinary Graduated School of Engineering Sciences,
Kyushu University, Kasuga Fukuoka 816-8580, Japan

Electric field distribution in the sheath region of the discharge is important because it govern the behavior of the charged particles which directly influence the characteristics of the deposited thin film and etching properties in processing plasma. In particular the electric field in Ar has practical importance because the Ar is most commonly used gas species in the processing plasma.

In this paper we present the results of the measurement of the electric field distributions in Ar discharge. The strength of the electric field was determined by comparing the set of numerically calculated spectra corresponding to the transitions from the lower metastable level $4s[3/2]_2$ to Rydberg levels of Ar atoms and experimentally obtained LOG (Laser Optogavanic) spectra. The effect of laser polarization on the LOG spectra was considered to determine the direction of electric field vector. The effect of the electric field gradient within the spatial width of the laser beam was taken into account.

The population of the lower metastable level $4s[3/2]_2$ was transferred by laser radiation (~ 300-320 nm) to the Rydberg states, nf (n = 6,7,...14), of Ar atoms. The Stark splitting of Rydberg levels of argon atoms was observed using LOG spectroscopy. When the electric field is strong enough the linear Stark effects of the forbidden lines which appear due to Stark mixing of wave functions were used as a measure of electric field strength. When the electric field is weak the separation between forbidden lines is not resolved and the magnitude of the electric field was measured using the quadratic shifts of allowed lines corresponding to the transition $4s[3/2]_2$ – nf [5/2].

The LOG spectra were obtained for 3 different laser polarization, parallel to electric field vector, orthogonal to electric field vector and at the angle of 45 degrees to electric field vector. The experimental spectra give a good agreement with theoretically calculated spectra.

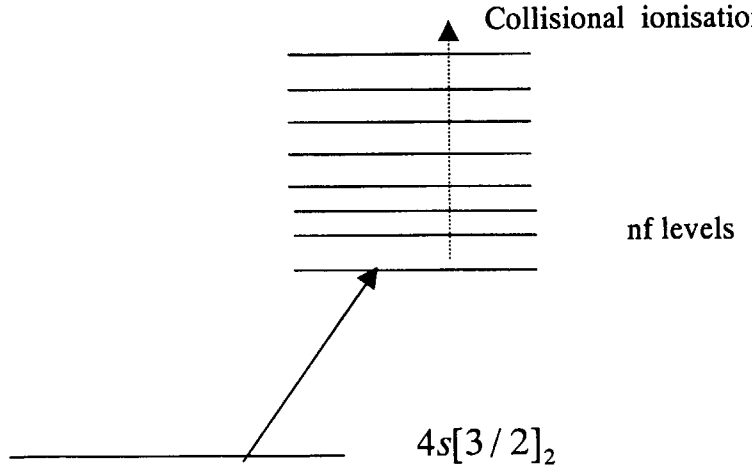

Fig. 1 Spectroscopic energy scheme used for the LOG expeiment

We use the laser excitation from the lower metastable level $4s[3/2]_2$ in order to populate Rydberg levels of argon atoms (see Fig. 1). The laser source used was a tunable dye laser pumped by a xenon chloride excimer laser. The laser was operated at $\lambda \sim 640\,nm$ and the laser output was frequency doubled to generate the radiation at $\lambda \sim 320\,nm$ which was needed for the experiment. The output of the dye laser had a pulse duration of $25\,ns$ and a spectral width of $0.2\,cm^{-1}$. The beam was directed through the plasma parallel to the electrode surfaces. For the measurement of the Stark splitting of Rydberg levels of argon atoms we use the method of laser optogalvanic (LOG) spectroscopy. The experimental apparatus were shown in Fig.2

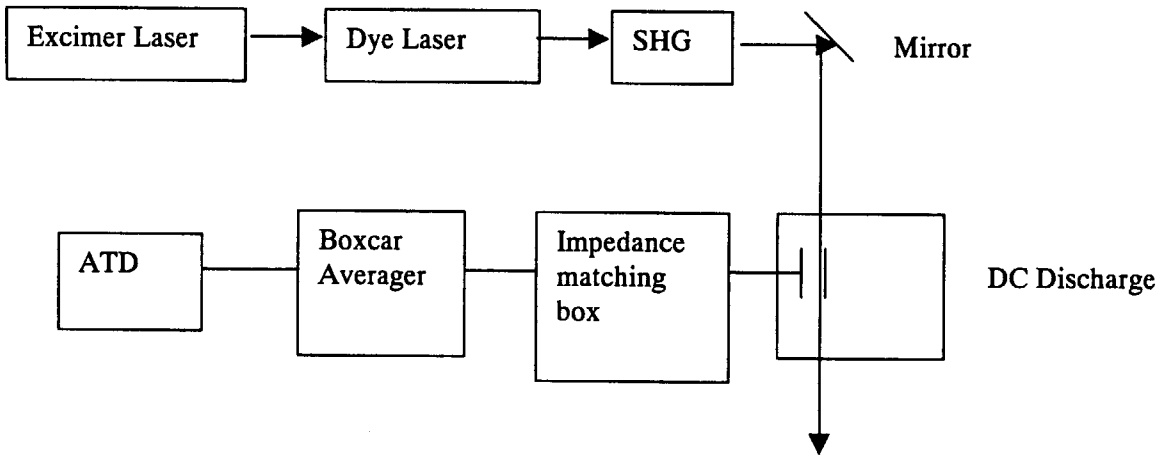

Fig2. Experiment set-up for the LOG experiment

Stark effect of Rydberg levels of an argon atom

To calculate the Stark effects of nf levels of argon atoms, we solve numerically the following Schrödinger equation for the Rydberg energy levels of argon atoms in the electric field F

$$H\psi = \varepsilon\psi,\ H = H_0 + ezF. \qquad (1)$$

Here H_0 is the unperturbed Hamiltonian of an argon atom, and ezF is the operator of dipole interaction of the argon atom with the electric field F. We used the basis wave functions of energy levels of argon atoms in the form $\varphi = |nl[K]_J\rangle$ where n is the principal quantum number of the Rydberg electron, l is orbital momentum of the Rydberg electron , j_C is the ion-core total angular momentum, $K = j_C + l$ is the angular momentum, and $J = K + s$ is the total angular momentum of the whole argon atom.

It is assumed that the axis z is chosen parallel to the direction of the vector F. The matrix H_0 is diagonal, its elements being unperturbed energies of argon levels. The detailed expression for z are derscribed in Ref. [1]

Since the initial state $4s[3/2]_2$ has a small admixture of the state $3d[3/2]_2$, laser excitation can populate nf Rydberg states of argon atoms. It follows that within nf Rydberg levels

having the same n, only two fine-structure doublets $nf[3/2]_{1,2}$ and $nf[5/2]_{2,3}$ can be populated by laser radiation in the absence of an electric field F. When $F \neq 0$, the wave functions of the levels $nl[K]_J$ having the same n are intermixed. This leads to the appearance of a large number of Stark components in the LOG spectrum of argon atoms in an electric field.

The intensity of the Stark components in the LOG spectrum for the fixed magnitude of the electric field F is obatained by calculating the transition probabilities between lower level $3d[3/2]_2$ and upper nf level. It is assumed in (4) that the Zeeman states $|3d[3/2]_2, M\rangle$ $(M = 0,\pm1,\pm2)$ of the lower level are equally populated. The position of Stark components in the LOG spectrum are determined by the values ε which obtained by solving the equation (1).

Results and discussion.

The figure 3 shows the experimental LOG spectra obtained from a plasma at 4.2 ± 0.5 Torr and the theoretical spectra obtained for the various magnitudes of the mean electric field F_0. These spectra correspond to the transitions from the lower level $4s[3/2]_2$ to the upper levels of principal quantum number 7 and 10 respectively. When the laser beam is far from the cathode, the spectra show only two main peaks corresponding to the transitions 4s[3/2]2 – nf $[5/2]_{2,3}$ and 4s[3/2]2 – nf $[3/2]_{2,3}$ where n = 7 and 10 respectively. When the laser beam is closer to the cathode, many peaks are observed due to Stark mixing.

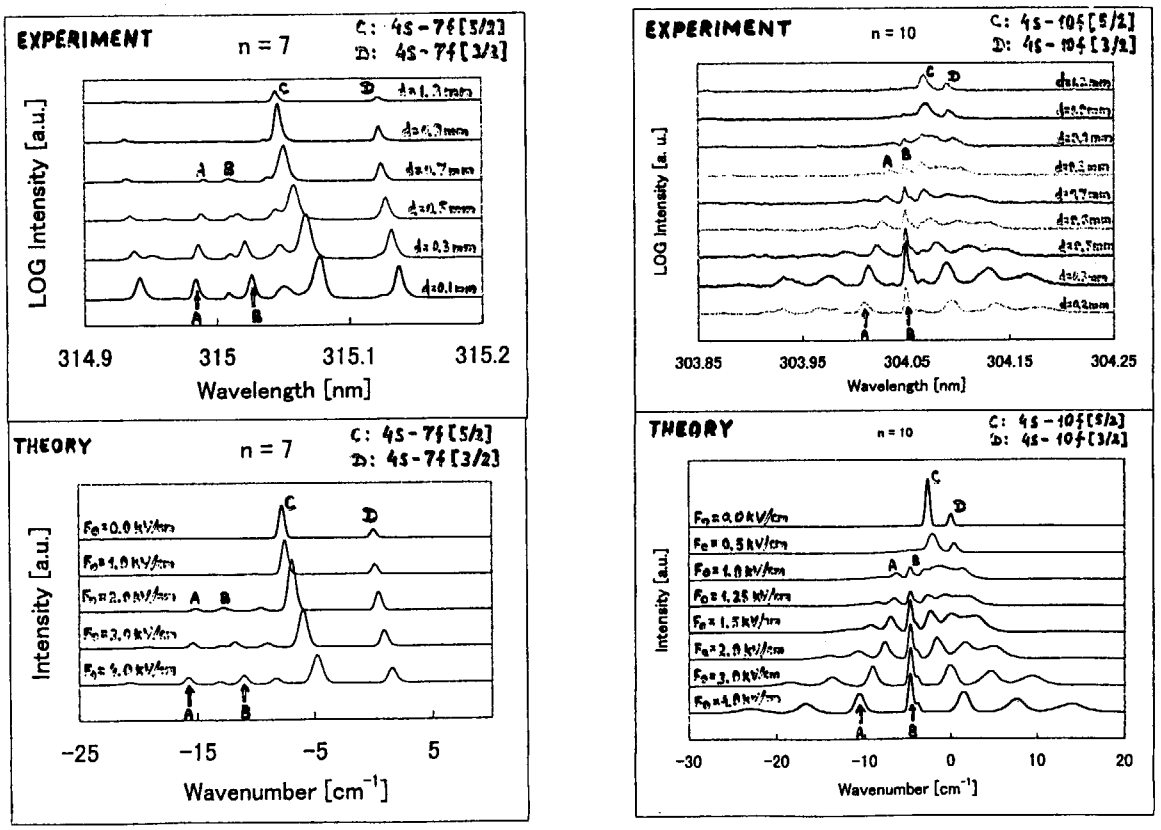

Fig.3 Experimental LOG spectra and theoretical spectra for n = 7 and 10.

The magnitude of electric field

When the electric field is very weak, and the separation between forbidden spectral lines is not resolved, the magnitude of the electric field can be measured using the small Stark shift of the allowed spectral lines corresponding to the transitions $4s[3/2]_2$ – nf [K] where $K = 3/2$ and $5/2$. When the electric field is sufficiently strong, there are many possibilities to measure this field by comparing experimental and theoretical Stark spectra. This is due to the fact that the positions of most peaks in the Stark spectrum are sensitive functions of electric field. One of the best possibilities to measure rather weak electric fields is to use the dependence of the separation between two closely spaced spectral lines indicated in Fig. 3 by letters A and B on the magnitude of the electric field.

Figure 4 demonstrates the spatial distribution of the electric field in the cathode region of the discharge. The magnitude of the electric field F_0, indicated by points in Fig. 4, was deduced from the dependence of the separation between lines A and B on F_0. The voltage drop across the cathode sheath can be calculated by integrating the field space distribution shown in Fig. 4. In particular, the magnitude of such an integrated voltage across the gap from 0.0 mm to 1.4 mm (the distance is counted from the cathode) constitutes about 96% of the voltage of 255 ± 5 V which was applied across the whole discharge.

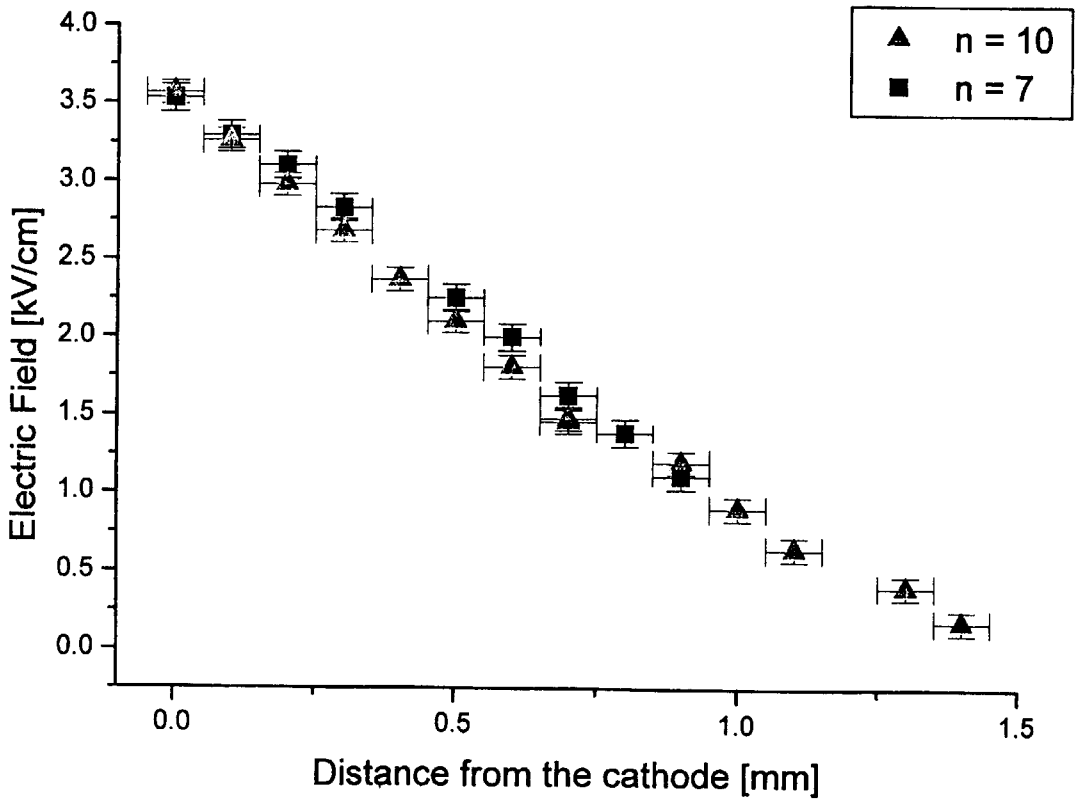

Fig 4. Electric field distribution in the vicinity of the cathode in DC glow discharge.

The effect of the electric field gradient

The important feature of the experimental LOG spectra, observed in the vicinity of the cathode, is that the profiles of the outer spectral components are broader as compared to those of the central components. This feature indicates that the electric fields are inhomogeneous within the cross-section of the laser beam because of the electric field gradient. The reason, why the outer spectral components are broader than the central ones, can be explained by the combination of two factors. Firstly, for the inhomogeneous electric fields, the different argon atoms within the cross-section of the laser beam see different magnitudes of the electric field. Secondly, for argon atoms, when the magnitude of the electric field F is being varied, the corresponding variation of the positions of the outer spectral components is greater than the variation of the positions of the central components.

The effect of laser polarization

Figure 5(a) shows the theoretical spectra, for n = 9, obtained for three different laser polarization, parallel to electric field vector, orthogonal to electric field vector and at the angle of 45 degrees to electric field vector. It can be seen that the experimental spectra, presented in Fig. 5(b), are well described by the theoretical spectra given in Fig. 5(a). It shows the possibility of determining the direction of electric field in Ar plasma.

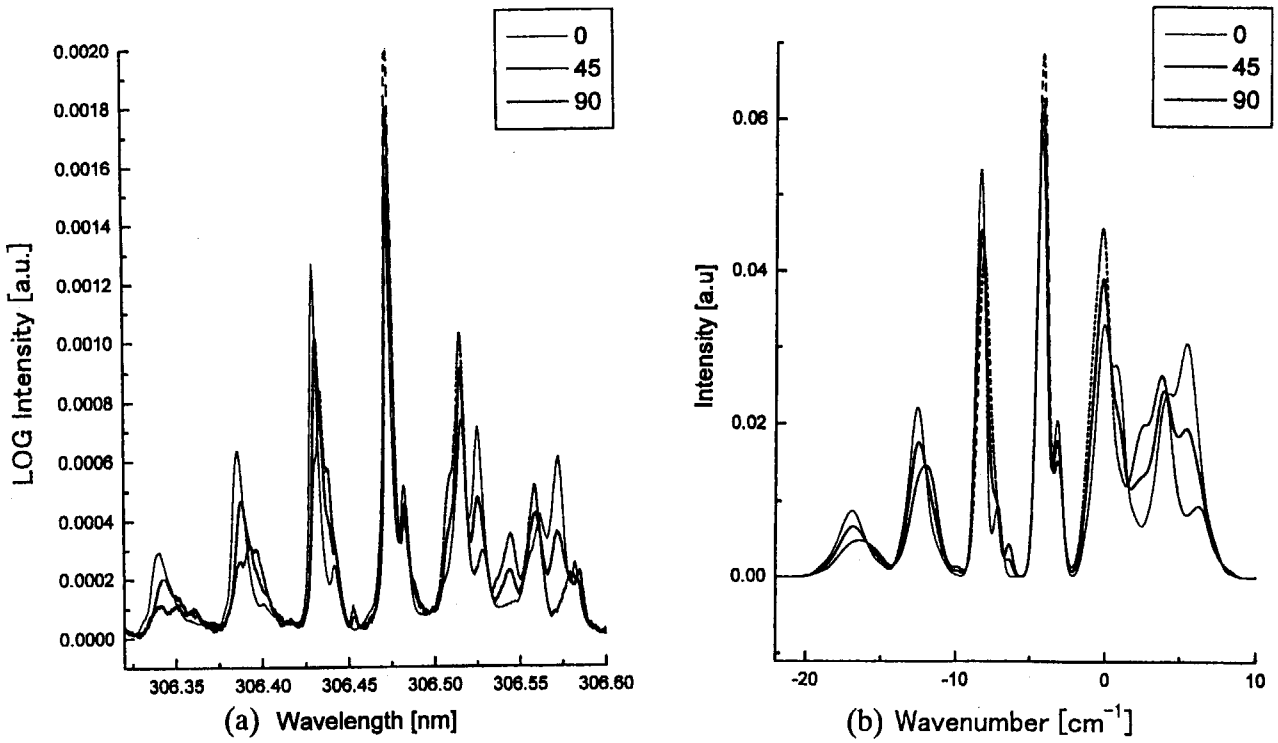

Fig 5. Effects of laser polarization. 0, 45 90 indicate the laser polarization, parallel to electric field vector, orthogonal to electric field vector and at the angle of 45 degrees to electric field vector respectively.

References

1. M. D Bowden, V. P. Gavrilenko, T. Ikutake, J. B. Kim, H. J. Kim and K. Muraoka, Measurements of electric fields in a discharge plasma using laser optogalvanic detection of the Stark effect of argon atoms, Contribution to Plasma Physics, submitted

2-10 Laser Spectroscopic Measurement of Electric Field Structure Induced in Plasma-Edges in Magnetic Field

T.ODA*, K.TAKIYAMA and M.WATANABE
Department of Applied Physics and Chemistry, Faculty of Engineering, Hiroshima University, Higashi-Hiroshima 739-8527, Japan
**Faculty of Engineering, Hiroshima Kokusai Gakuin University, Nakano, Aki-ku, Hiroshima 739-0321, Japan*

A new laser-induced fluorescence (LIF)technique was developed to directly measure the electric field distribution with high spatial resolution in plasma edges under magnetic field. As a model-type experiment, sheath electric field distribution was measured in front of a biased metal plate inserted into an ECR helium plasma flow under magnetic field. Good agreement was obtained between the potential difference over the sheath determined from the measured distribution and the applied bias voltage. Applicability of our LIF technique to the case of strong magnetic field was discussed. Detectable range of the electric field is estimated.

1. Introduction

The direct measurement with high spatial resolution of electric field distribution in the plasma-edges is highly desired today because the electric field is well recognized to play important roles in the plasmas.

We have proposed a sensitive method for measurement of the sheath electric field structure in discharge plasmas which utilizes polarized laser-induced fluorescence (LIF) spectroscopy.[1,2] In this method, we observe only the polarization degree of the subsequent allowed fluorescence following the forbidden-line excitation from the singlet helium metastable (2^1S) atom, which is due to the Stark effect and the electric quadrupole (QDP) transition. Because strong magnetic field is applied in fusion devices, further improvement is required for our LIF spectroscopy.[3]

In this paper, we report a model-type experiment to measure the sheath electric field distribution in front of a metal plate inserted in an ECR plasma flow in a magnetic field when the negative bias is applied to the plate by using our improved LIF technique. The bias voltage dependence of the sheath thickness is discussed. This will make a usefull contribution to diagnostics in the biased divertor experiments.

Applicability of our LIF technique is described to the case of strong magnetic field in showing excitation spectra of the Stark and QDP components observed in the Zeeman split sublevels in a hollow cathode discharge plasma.

Detectable range of the electric field by our method is also discussed.

2. Forbidden-line excitation of He I 2^1S atom for electric field measurement in magnetic field

A partial energy level diagram of HeI and the relevant transitions among the magnetic sublevels are shown in Fig. 1, where the polarization direction of the excitation laser e_z is taken as the z-axis and is parallel to the magnetic field B and the electric field E directions. Note that selection rule for the Stark

transition is different from that for the QDP transition. The Stark absorption coefficient B^S is expressed by a function of E while the QDP coefficient B^Q is independent of E. Consequently, both transitions produce the anisotropic population called "alignment" between the magnetic sublevels of the upper level (4^1D) by laser excitation. Then the LIF signal is polarized as a result of

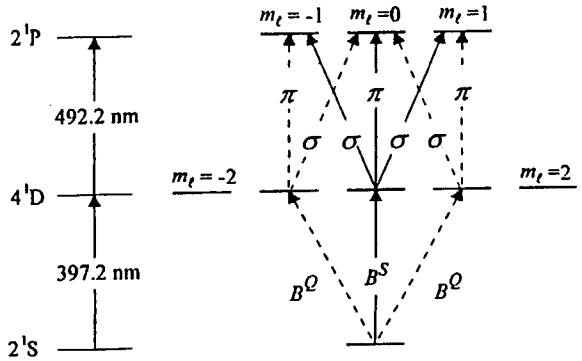

Fig. 1. Partial energy diagram of HeI and relevant transitionsamong the magnetic sublevels in $E//B$ configuration.

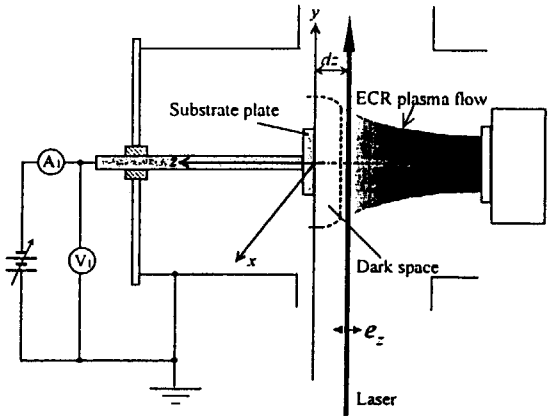

Fig. 2. The geometry of LIF observation. Bias voltage (-10 ~ -80V) is applied to the metal plate.

the alignment of the upper level. We denote the sum of the π components of LIF (492.2nm line) as shown in Fig. 1 by I_z and that of the σ components by I_y. Both I_z and I_y are observed as a function of time because of excitation by a short-pulse laser.

It is essential to characterize the polarization of LIF using longitudinal alignment $\alpha(t)$ defined by,[4]

$$\alpha(t)=\frac{I_z(t)-I_y(t)}{I_z(t)+2I_y(t)}. \qquad (1)$$

Because of the collisions by the plasma particles, $\alpha(t)$ decays exponentially with a characteristic time constant τ_{da}. This decay process is called "disalignment". Then the initial value α_0 of $\alpha(t)$ can be determined from $\alpha(t)$ at the onset time of the laser pulse. In the case of low pressure discharge plasma such as ECR plasmas, τ_{da} is much longer than the instrumental response time τ. In this case, α_0 can be easily determined from LIF signals.

Using the similar procedure to those described in ref. 3, the longitudinal alignment α_0 in the case of our excitation scheme is expressed by

$$\alpha_0=\frac{2B_R+1}{4B_R+4}, \qquad (2)$$

where $B^R=B^S(E)/B^Q=I^S/I^Q$. When the quadratic Stark effect is valid, B^S is proportional to the square of E. Then we obtain $B^R=E^2/C^2$ where the constant C means the electric field strength for $B^S(E)=B^Q$; e.g. C=240 V/cm for n=4. Then, E is expressed by,

$$E=C\sqrt{\frac{4\alpha_0-1}{2-4\alpha_0}}. \qquad (3)$$

We can directly determine E when α_0 is obtained from the LIF observation. From eq.(3), α_0=1/4 at E=0, while α_0 approaches to 1/2 when E becomes infinity.

3. Bias effect of electric field distribution in front of a metal disk in a plasma flow

The geometry of our LIF experiment is shown in Fig. 2. The ECR He plasma is produced by an NTT type ECR plasma source (AFTEX PS-501). The discharge conditions are: He gas pressure of 3.3×10^{-2} Torr, microwave frequency of 2.45 GHz and power of 260 W. A brass plate with diameter of 25 mm and thickness of 5 mm is inserted perpendicularly to the z-axis. The DC bias voltage from -10 V to -80 V with respect to the ground is applied to control the sheath potential. The excitation laser light pulse (pulse width of 5 ns and repetition of 10 Hz) with wavelength of 397.2 nm and line width of 1 pm is introduced into along the y-axis. The LIF signal, is detected by using a polarizer and a 25cm monochromator. The signal is averaged over 1500 shots using a digitizing oscilloscope (Tektronix TDS620, 2Gs/s). Spatially resolved measurement of LIF is carried out by moving the optical system along the z-axis with a spatial resolution of 0.2 mm. Distance from the plate is denoted by dz(mm). By using a probe, T_e and n_e measured at dz = 8.5mm are ~2 eV and ~1×10^{10} cm^{-3}, respectively, which is almost constant for all the bias voltages applied. On the other hand, the plasma potential Φ_p is ~6V to ~3V.

Fig. 3 shows the temporal variation of the LIF polarization components and $\alpha(t)$ observed at dz=0.4mm in the sheath region. The plate is biased with -80V. The initial longitudinal alignment α_0 is determined from extrapolating the fitted line to the time of laser onset. We obtain τ_{da} = 300 ns and α_0 = 0.44, from which the value of E is determined to be 420 V/cm.

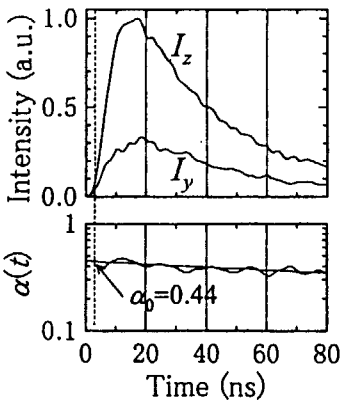

Fig. 3. Temporal variation of each polarization components I_z and I_y, and of longitudinal alignment of 492.2 nm LIF observed at dz=0.4mm in the sheath region. The bias voltage is -80V.

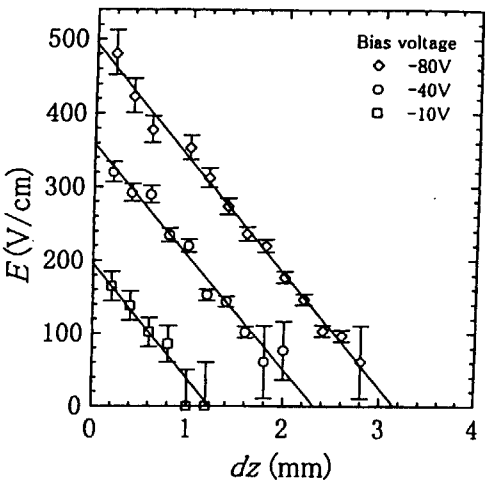

Fig. 4. Spatial distributions of measured electric field along the z-axis for three different bias voltages.

Figure 4 shows the spatial distribution of the electric field obtained for various bias voltages. It is noted that each distribution is linear against the distance from the substrate surface (dz=0). This means that the net positive charge density is constant in the sheath. The potential difference V_{LIF} between the sheath determined from the electric field distribution agrees well with the applied bias voltage V_0. This indicates that our LIF measurement is reliable for the electric field distribution in plasmas such as in the sheath.

As shown in Fig. 4, the sheath thickness increases as the negative bias increases. Figure 5 shows the bias voltage V_0 dependence of the sheath thickness

s. The thickness is proportional to the square root of V_0. For such a sheath having linear electric field distribution, it is well known that s is proportional to $V_0^{1/2}$.[5] This sheath model explains well our experimental results.

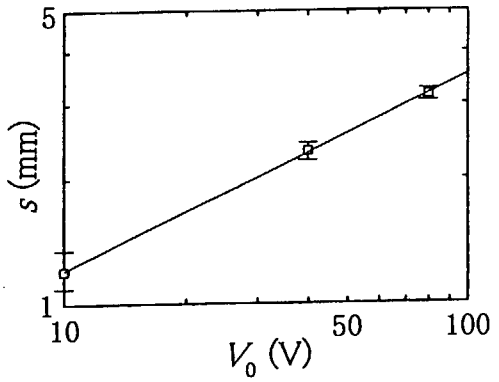

Fig. 5. Measured sheath thickness s versus bias voltage V_0.

4. Laser-induced fluorescence in the case of strong magnetic field

To show applicability of our LIF technique described above to the case of strong magnetic field in fusion devices, we discuss results obtained in another experiment which is carried out in a hollow cathode discharge plasma under magnetic field of 2.5 kG. The He plasma is produced in a plane-parallel hollow cathode consisting of a pair of disk electrodes with a diameter of 40 mm and a separation of 11 mm as shown in Fig.6. The LIF observation is made in the similar way as in the ECR plasma, except that the 2^1S atoms are excited up to the 3^1D level. The spatial distribution of sheath electric field is also determined from measured polarization P in this case. The cathode-fall potential obtained from the electric field distibution agreed well with the measured value by a probe. The detail has been reported in ref. 3.

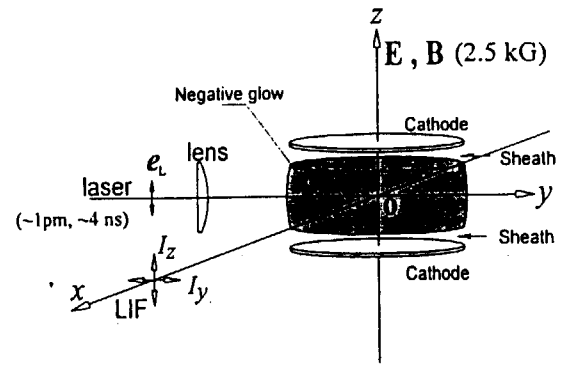

Fig. 6. Observation geometry for laser-induced fluorescence in the hollow cathode discharge plasma under strong manetic field.

In the strong magnetic field, the Stark and QDP excitations shown in Fig. 1 can be separately made because of the Zeeman splitting between the magnetic sublevels. To demonstrate this situation, excitation spectra were observed of the LIF by scanning the laser wavelength covering the Zeeman splitting of 3^1D. Figure 7 shows the observed excitation spectra (a) in the negative glow where negligible electric field exists and (b) in the dark space where the sheath electric field is induced. The fitted spectrum shown in Fig. (a) has two peaks due to the QDP excitations to $m_l = \pm 1$ of 3^1D because of negligibly weak electric field. Then the fitted curve is resolved into two Gaussian components. By using this result, another fitted spectrum shown in Fig. (b) is resolved into three components, the central one corresponding the Stark excitaion to $m_l = 0$, which is caused by the

sheath electric field. The two side components are also due to the QDP. The stark component is found to be almost the same in height with the QDP ones, from which the value of E is estimated to be 1.2 kV/cm.

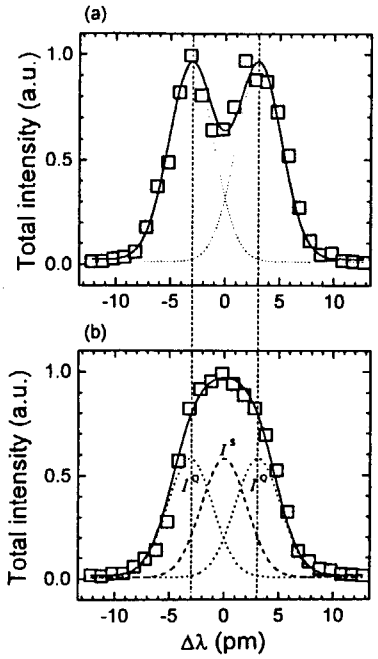

Fig. 7. Excitaion spectra of the LIF observed by scanning the laser wavelength covering the Zeeman splitting under B = 2.5 kG, (a)in the negative glow and (b) in the dark space.

The Zeeman splitting becomes larger with increasing magnetic field strength. Figure 8 shows calculated excitation spectra under B = 2 T and E = 0.85 kV/cm. In such a case as in fusion devices, the 2^1S atoms have to be separately but simultaneously excited to both Stark and QDP sublevels to determine the electric field. This can be made by an adequate laser system.

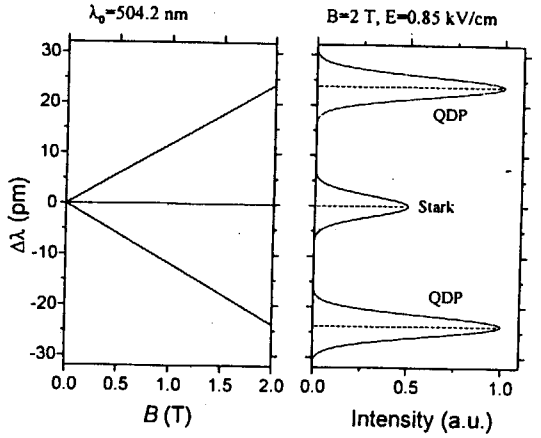

Fig. 8. Calculated excitation spectra under B = 2 T and E = 0.85 kV/cm.

4. Concluding remarks

The present polarized LIF spectroscopic technique was successfully applied to direct measurement of localized electric field structure in front of the metal plate inserted in ECR plasma flow in magnetic field. The bias effect of the plate on the electric field structure was also revealed. It was also demonstrated that this technique was applicable to measurement in strong magnetic field such as in fusion devices.

To increase the sensitivity of electric field measurement, we can use the n=5 scheme (2^1S-5^1D). Detectable range of the electric field is estimated in Fig. 9.

For n = 5, the detectable range extends from ~10 V/cm to ~120 V/cm while the corresponding range is from ~80 V/cm to ~900 V/cm for n = 4.

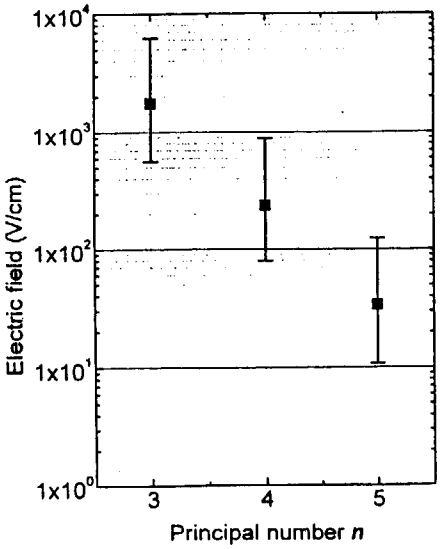

Fig. 9. Estimated detectable range of electric field versus principal quamtum number n.

References

1) T. Oda and K. Takiyama: *Proc. 7th Int. Symp. Laser-Aided Plasma Diagnostics*, 1995, p.227.
2) H. Sakai, K. Takiyama, M. Kimura, M. Yamasaki, T. Oda and K. Kawasaki: J. Nucl. Mater. 196-198 (1992) 1135.
3) M. Watanabe, K. Takiyama and T. Oda: Rev. Sci. Instrum. **70** (1999) 903.
4) T. Fujimoto, C. Goto, Y. Uetani and K. Fukuda: Jpn. J. Appl. Phys. **24** (1985) 875.
5) M. A. Lieberman and A. J. Lichtenberg: *Principles of plasma discharges and materials processing* (Wiley-Interscience, New York, 1994) p.164.

2-11 A Spectroscopic Study of Ion Channels in a Prototype Inertial Electrostatic Confinement Reactor

S. Collis and J. Khachan
School of Physics, Sydney University
NSW 2006, Australia

Inertial Electrostatic Confinement (IEC) involves using a semi-transparent and negatively biased grid to accelerate light nuclei towards a common centre for the purpose of generating neutrons through fusion reactions.

This project investigated the plasma properties in a small prototype IEC device that was operated using a relatively low grid bias in a discharge of hydrogen. Electrostatic lenses, which are the product of the geometry of the grid, create ion channels. Doppler shift spectroscopy was performed on the emission produced by charge exchange reactions in these channels.

Using the spectra we obtained, we were able to determine energies, ratios of hydrogen species (H^+:H_2^+:H_3^+) and thermal properties of ions present in these channels.

A discussion of results will be presented with particular emphasis on the implications of our findings to the construction of a portable neutron production device.

1.Introduction

Although Tokamaks have long been thought to be the best option as a fusion reactor, they lack the simplicity and portability that would be desired of a small-scale neutron production facility.

This report is about an investigation into an alternate method for initiating fusion reactions to produce neutrons: Inertial Electrostatic Confinement (IEC). The primary aim of this project was an investigation of fundamental plasma properties in an IEC device, with a particular focus on ion beams generated in such a device.

In the short term it is envisaged that IEC devices will be used as small portable sources of neutrons for applications such as elemental analysis of materials and medical treatments.

2.Grid Configurations

The three ring grid (figure 2.1a) was made by spot welding three stainless steel rings together. Stainless steel was chosen because it is non-magnetic. The outer grid (figure 2.1b) was constructed from a brass mesh which was welded onto a stainless steel supporting structure.

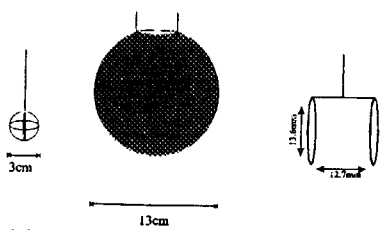

Figure 2.1
IEC grid configurations

Our experiments were focused on the ion channels. A three ring grid (figure 2.1a) can be thought of as eight closed loops which creates four opposing loop pairs. Ion channels were observed (figure 2.2) to form in the centres of these loops.

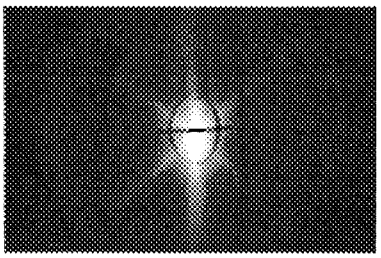

figure 2.2
Ion Channels in an IEC reactor

Many of the measurements were carried out on one channel since all channels were identical. To achieve this, we used a grid (figure 2.1c) which was made from two rings with a diameter of 13.6 mm. These are designed to form electrostatic lenses similar to those formed by two opposing triangles of the three ring grid.

3.Plasma Generation

Hirsch used an oxide coated outer grid as a source of electrons to generate a plasma when the inner grid potential was turned on, resulting in a DC discharge. In our experiment, we decided to look at an IEC system that has a separate plasma generating system. To maintain spherical symmetry, the plasma produced must be relatively uniform around the outer grid and the signal used to generate the plasma must not interfere with the plasma dynamics inside the outer grid.

Our system consists of a lower chamber (which was not used in our experiments), a glass tube (G) with a single loop antenna (H) and an upper processing chamber:

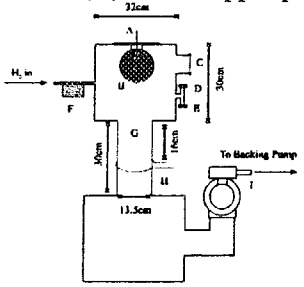

Figure 3.1
Experimental setup

A	High voltage feed through
B	IEC inner and outer grids
C	Quartz window
D	Capacitance Manometer
E	Ion gauge Manometer
F	Mass flow controller
G	Glass discharge tube
H	Single loop antenna connected to matching network
I	Turbo molecular pump

In its normal mode of operation, a 13.56 MHz radio frequency generator connected to the antenna (H) excites (primarily) the m = 0 mode of a helicon wave, but for our purposes the

antenna was used to inductively generate a plasma. When the rf generator (connected to the single loop antenna / matching network) is operated at 10W it produced a low density (~10^{10} cm^{-3}) low temperature plasma (T_e~1eV, T_i~0.03eV).

4.Potential Calculations

To find the potential between a biased inner grid and the earthed outer grid Poisson's equation must be solved. In a vacuum this reduces to Laplace's equation:

$$\nabla^2 V(x,y,z) = 0 \tag{4.1}$$

The geometry of the grids used in our experiments impose boundary conditions which lack the simplifying symmetries regularly used to solve equation (4.1). So instead, we assume that the potential is due to rings of charge (in the shape of the grid). If we have a distribution of point charges at x_n, y_n, z_n with charges q_n, the potential at an arbitrary point x, y, z is:

$$V(x,y,z) = \frac{1}{4\pi\varepsilon_0}\sum_n q_n\left((x_n - x)^2 + (y_n - y)^2 + (z_n - z)^2\right)^{-1/2} \tag{4.2}$$

After running the simulation, the validity of the model was checked by plotting an equi-potential surface (or iso-surface), using the visualisation and data processing package AVS, at the grid potential:

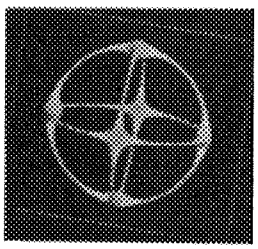

Figure 4.1
Equipotential surface at the grid potential

As shown in figure 4.1, the model produces a "virtual wire". This is a grid which is an exact solution to the model we used. The virtual grid closely resembles the real grid except for where the approximation breaks down at the wire joins. This is due to our charges having a fixed position which does not allow them to redistribute themselves to maintain a uniform charge density at a join (the charge density around any one given ring is uniform, but at a join the two rings come into contact and the density increases).

One plane of potentials that is of particular interest is that which contains the centres of the two triangles, that is, in the plane of an ion channel. Figure 4.3b shows contours (equi-potential lines) of the potential well. Each contour has a thickness of $0.2V/V_{grid}$, where V_{grid} is the potential of the grid. Figure 4.3a shows the plane in which the contours of figure 4.3b were taken:

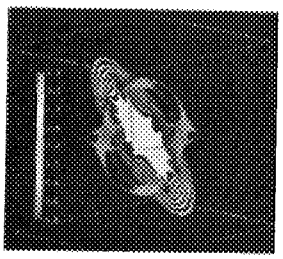

(a)

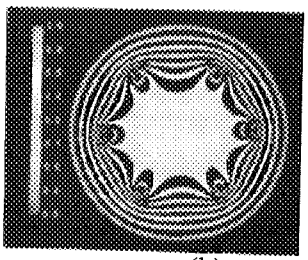

(b)

Figure 4.3
Threshold contour plots of potential well structures

As previously stated, our approximation only breaksdown near the welding joints, so this plot is perfectly valid since it is far enough away from the joints.

5.Optical Setup

Light from the discharge exited the vacuum chamber through port (C) (in figure 3.1) where it was focused by a lens with a focal length of 15 centimetres.

For the spectra taken in this experiment we used an Optical Multi-channel Analyser (OMA). The OMA has two components: A 500mm monochromator with a 2400 lines per mm grating and a intensified CCD array detector (see figure 5.5).

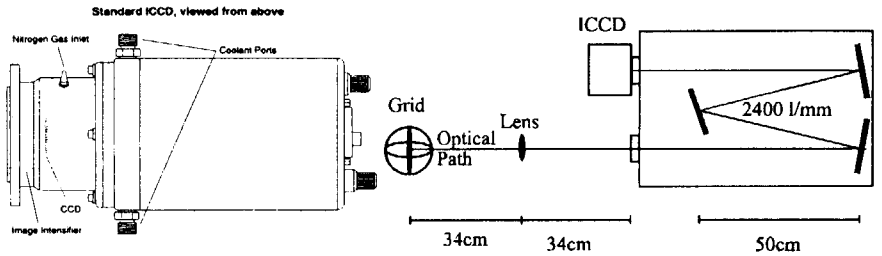

Figure 5.5
Optical setup

To further reduce thermal noise, the entire intensifier-CCD assembly was cooled to -30°C by a Peltier cooler and dry nitrogen flowed over the array to stop water vapour freezing onto the chip and causing it to crack.

6. Charge Exchange

The following charge exchange reactions between hydrogen ions and atomic hydrogen can occur[1], where the underlined species have approximately the same velocity:

$$\begin{aligned} \underline{H^+} + H &\longrightarrow \underline{H^*} + H^+ \\ \underline{H_2^+} + H &\longrightarrow \underline{H^*} + \underline{H} + H^+ \\ \underline{H_3^+} + H &\longrightarrow \underline{H^*} + \underline{H_2} + H^+ \end{aligned} \qquad (6.1)$$

where the superscript * refers to an excited state.

If the neutral species is molecular hydrogen, the following reactions occur:

$$\begin{aligned} \underline{H^+} + H_2 &\longrightarrow \underline{H^*} + H_2^+ \\ \underline{H_2^+} + H_2 &\longrightarrow \underline{H^*} + \underline{H} + H_2^+ \\ \underline{H_3^+} + H_2 &\longrightarrow \underline{H^*} + \underline{H_2} + H_2^+ \end{aligned} \qquad (6.2)$$

Because the atom is initially neutral, the sum of the energies of the resulting neutrals is close to the energy of the ion that caused the event. McClure[2] experimentally determined the charge exchange differential cross-section for a variety of incident ion energies. The differential cross-section for charge exchange reactions between H_2 molecules and 10keV H^+ ions is shown in figure 6.1 below.

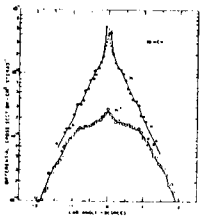

Figure 6.1
Differential cross-section for a charge exchange reaction between H^+ and H_2^+ at 10keV

Figure 6.1 shows that the number of particles that will be scattered into angles greater than 2 degrees is very small. From this we can conclude that charge exchange products do not deviate significantly from the path of the incoming ion.

7.Two Ring Spectral Profile

Below is a spectrum taken from the two ring grid. The spectrum is a line of emission integral. The intensity is greatest in the centre of the grid, which contains very weak (negligible) electric fields.

There are a few important facts to note: The emitters (from the reactions in equation 6.2) are all neutral hydrogen atoms so there are no metastable states or molecular transitions. Also, according to Volger[3] the resulting hydrogen fragments (in equation 6.2) resulting from an H_2^+ or H_3^+ impact event have approximately the same velocity (The difference in energy is approximately 0.5eV).

The spectrum below (figure 7.1a) contains a total of ten peaks. This was not completely obvious until a detailed analysis of the system was done.

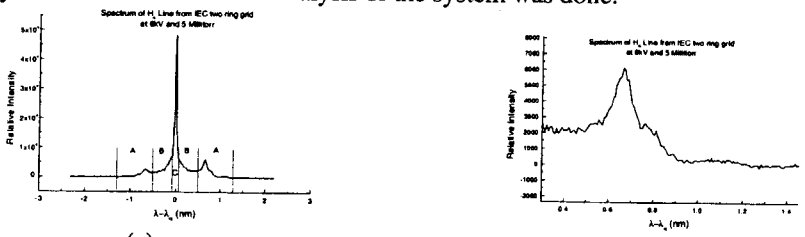

(a) (b)

Figure 7.1
Components of the Hα spectrum

Region A (in figure 7.1a, also enlarged in figure 7.1b) is due to the incoming and outgoing ion beams. This region contains six (three incoming and three outgoing) beams due to three different species of hydrogen ions.

Region B is due to a thermal background. It is the emission due to three Maxwellian velocity distributions for the three different masses of the ions. It is envisaged that this background is formed by ion scattering due to columbic collisions with the other oncoming beam and possibly becoming thermalised.

Region C (in figure 7.1a) is due to dissociative excitation of the neutral hydrogen, which is stationary in the lab frame. Charged species gain energy from the electric field produced by the grid. Energy is transferred between ions through columbic collisions. However, the cross section for collisions between neutral and ionic hydrogen is much smaller than the coulomb collision cross-section. As a result, the temperature of the gas was near room temperature (~300 K). This will yield a half width of 0.005 Angstroms. Since this value is sufficiently small we used the width of this line to determine the instrumental broadening.

8.Three Ring Profile

The spectra presented in this section was recorded by Kristie Foulkes[4]. Spectra were recorded for voltages ranging from 1 kV (B) to 12 kV (M). The pressure was kept at ~5 millitorr.

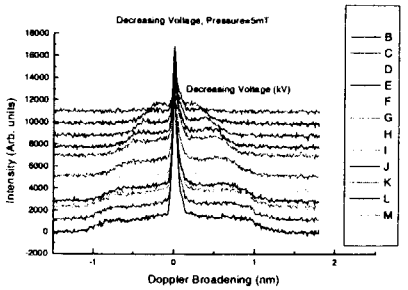

Figure 8.1
Varation of the H_α line with grid potential
Adopted from [4]

Spectra shown in figure 8.1 contain the same features as the spectra for the two ring grid but have four peaks due to charge exchange (one for each ion beam). From the wavelength at which our signal drops below the noise level we found that the maximum energy that an ion reaches was 27% of the vacuum well depth.

9.Quantities Obtained from the Two Ring Grid Spectra

By fitting Gaussians to each of the peaks present in the three ring grid we were able to observe changes in beam energy, ion temperate and relative density (by doing rate equation modeling), with respect to the grid potential.

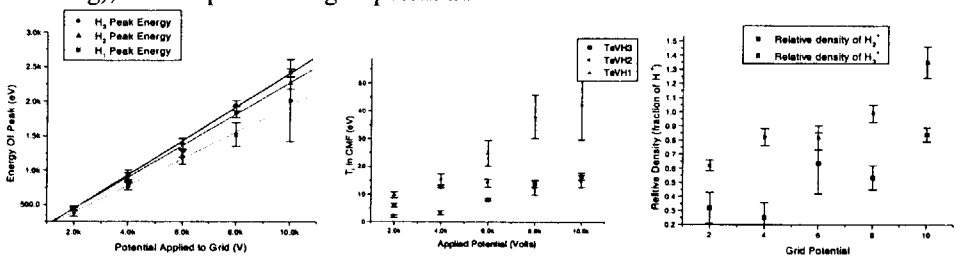

Figure 9.1
Variation of plasma properties with grid potential

The energies of the three species are equal, however due to their different mobilities the are collisionally heated (due to collisions with the background gas) differentially.

10.Conclusion

We have shown that when a three ring grid is immersed in a plasma ion channels are formed due to electrostatic lenses formed by the grid wires. The ion beams formed consist of H^+, H_2^+ and H_3^+ and have an energy equal to 27% of the vacuum electrostatic potential well depth. We have also shown that, due to increased collisions with background gasses, the beams are heated when the potential is increased (which results in an increased beam flux).

References

[1] C Barbeau J Jolly *J. Phys. D: Appl. Phys.* **23**, 1168 (1990)
[2] G McClure *Phys. Rev 3A* **140**, 769 (1965)
[3] M Volger, *Z. Physik A* **7-10**, 288 (1978)
[4] Kristie Foulkes, Physics III project

2-12 Plasma Polarization Spectroscopy

Atsushi Iwamae, Takeru Inoue, Akihiro Tanaka, Kazuki Kawakami and Takashi Fujimoto

Department of Engineering Physics and Mechanics, Graduate School of Engineering,

Kyoto University, Kyoto 606-8501, Japan

Polarization of radiation emitted from plasma reflects the anisotropic properties of the plasma, especially the angular anisotropic distribution of electron velocities. Polarization has been observed on impurity ion lines from the WT-3 tokamak and GAMMA 10 tandem mirror device.

1. Introduction

In the case that an electron travelling from z-direction on the z-axis collide with a classical atom located at the origin and the energy of the electron is just enough to excite the atom, the electron gives all of its momentum and energy to the atom. The atomic electron begins to oscillate back and forth on the z-axis. This atom is a classical oscillating electric dipole, emitting radiation, which is polarized in the z-direction, the π-light. When the energy of the incident electron is very high, and it passes near the atom, the atom is exerted a pulsed electric field, the direction of which is, roughly speaking in the x-y plane. The atom is excited in this direction, and emits the σ-light. The situation with actual quantum atoms is more complicated but the fact that angular anisotropic excitation produces polarized radiation is still valid.

When the velocity distribution of electrons in plasma is anisotropic, e.g., Maxwellian distribution is accompanied by a beam component, the emitted radiation should be polarized. This reasoning suggests that, from the observed polarization characteristics of emitted radiation, we should be able to investigate the anisotropic velocity distribution of electrons. The first observation of polarization from a tokamak plasma was reported [1].

2. WT-3 tokamak

An image reducing (1/8) optics focussed the image of the plasma on the entrance slit (10 mm in height) of the monochromator. Behind the slit, a calcite plate is placed, which displaced horizontally the extraordinary ray (the π-light which is polarized in the toroidal direction) from the ordinary ray (the s-light polarized in the poloidal direction) by about 0.5 mm. These rays were dispersed and focussed on the CCD detector. We thus obtained a polarization resolved and space resolved spectrum. Beryllium-like oxygen triplet lines (OV 2s3s 3S1 – 2s3p 3P0,1,2) and helium-like carbon line (CV 2s 3S1 – 2p 3P0,1,2) were observed. In the former case, the weakest line, J=1-J=0, which is never polarized, was used for the

purpose of calibrating the relative sensitivities of our detection system for the two linearly polarized components. It was found that, for the Joule heating mode, the 1-1 and 1-2 lines had stronger s-components than the p- components. Figure 1 shows the longitudinal alignment $A_L = (I\pi - I\sigma)/(I\pi + 2I\sigma)$ at a certain time (the signal accumulation was over 0.1 ms) against the distance from the central chord.

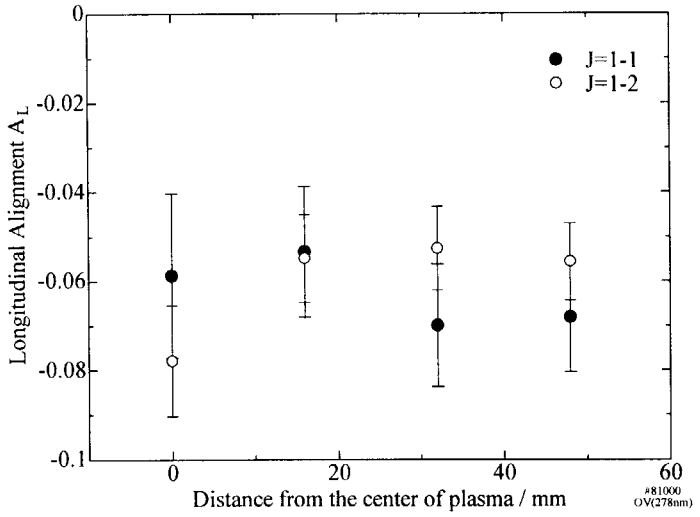

Figure 1

We have constructed the atomic kinetic mode for the purpose interpreting our experimental data, the population-alignment collisional-radiative model. In this model, to each ionic level two quantities are assigned, i.e., the population and alignment. The former quantity gives the intensity of the emitted line and the latter gives the polarization of the line. A set of rate equations is constructed for the populations and another for the alignments, and they are solved in the quasi-steady-state approximation. We tentatively assume that the electron velocity distribution is expressed by different *temperatures* for the toroidal direction and poloidal direction. The negative longitudinal alignments in Fig. 1 suggest that the poloidal temperature is higher than the toroidal one: the pancake-shaped distribution, but we are still unable to interpret quantitively the result yet.

2. GAMMA 10 tandem mirror

The image of the plasma in the central part of the mirror machine was focused on the vertical slit, and the image of the slit was polarization resolved by a calcite plate located just behind it and focussed by a lens on the entrance surface of the optical fibers aligned in two columns. Each of the five pairs of the optical fibers accepted the p – and s- components of the radiation emitted from the same line of sight through the plasma. The other ends of the fibers are aligned in a line to fit the entrance slit of the

monochromator. We thus obtained the polarization resolved spectrum for five locations of the plasma, each 7.5 mm apart. Figure 2 shows an example of the spectra for one location. The broad line in the

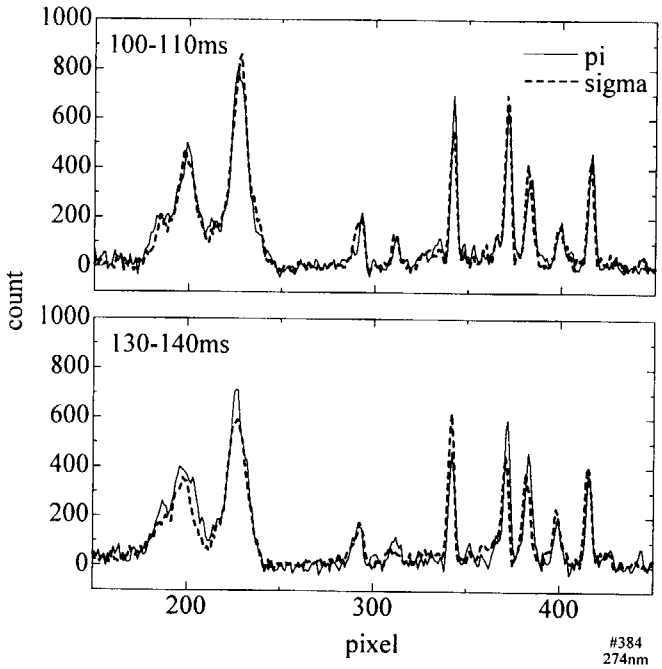

Figure 2

shorter wavelength side are the beryllium-like oxygen lines, which are the same as those presented in Fig.1. The sharp lines in the longer wavelength region are those of singly ionized iron ion. The upper traces shows no polarization with the former lines in this time interval, but one of the iron lines shows substantial polarization.. These lines are emitted from the different parts of the plasma; the oxygen lines from the central part and the iron line from the peripheral part. It is suggested that, while the central part has an isotropic velocity distribution of electrons, the outer part has an anisotropic distribution, "shape" of which changes with time.

References

1. T. Fujimoto *et al.* Phys. Rev. E 54, R2240 (1996).

2. T. Fujimoto and S. A. Kazantsev, Plasma Phys. Control. Fusion 39, 1268 (1997).

3. S. Grabbe and G. Csanak (private communication).

2-13 Drive Circuitry for the MOSS Spectrometer

Andrew Cheetham†, Clive Michael and John Howard

Plasma Research Laboratory,
Research School of Physical Sciences and Engineering,
Australian National University, Canberra ACT 0200 Australia

The Modulated Optical Solid State (MOSS) spectrometer developed at the H1-National Facility [1] is now used to monitor and measure the ion temperature and flow in a plasma discharge with time resolution good enough to study temperature and flow fluctuations by inexpensive, non invasive, optical means.

The operation of the MOSS spectrometer has been described in some detail elsewhere in this conference (J Howard, *Doppler Coherence Spectroscopy on H-1NF*). To summarise, a birefringent crystal is used to impose a phase delay between the two polarisations of a light beam collected from a chord through the plasma. These two waves are then recombined to produce an interference pattern. The amount of phase delay can be modulated by imposing a voltage across the crystal. If this modulation is of sufficient amplitude then the resulting signal registers the local coherence envelope and phase at the mean phase delay. These quantities relate directly to line integrals of intensity weighted temperature and flow speed via the Doppler effect.

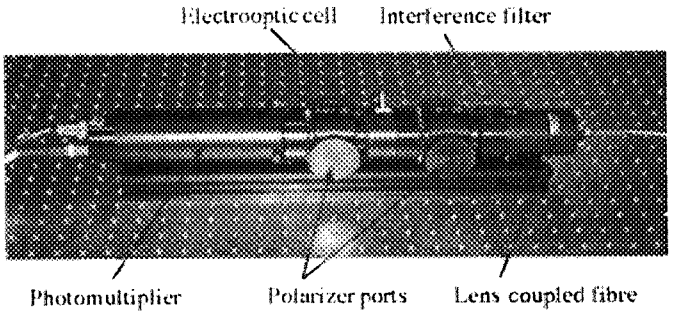

Figure 1: A photograph of the MOSS Spectrometer showing the light from the plasma being fibre coupled in from the right. Then passing through an interference filter to isolate the line to be examined, a polariser the birefringent crystal, a second polariser and finally the detector.

It is easy to show that for a plasma that assumes a Maxwellian ion energy distribution, the signal from the detector will be of the form:

$$S = I_0\left[1+\zeta\cos\{\phi_0(1+\beta)+\phi_1\}\right] \qquad \ldots 1$$

Where:

S = Intensity detected　　I_0 = Incident light intensity

ϕ_0 = Phase delay due to birefringence　　ϕ_1 = small perturbation to ϕ_0

$\beta = \frac{v_D}{c}$ = Normalised ion drift velocity　　ζ = Fringe Contrast Function $= e^{-\frac{T_s}{T_c}}$

The phase delays within the crystal are functions of the crystal parameters and the voltage applied to the crystal. The static phase delay due to the birefringence is given by:

$$\phi_0 = \frac{2\pi BL}{\lambda}$$

† Permanent address: Plasma Instrumentation Laboratory, University of Canberra, ACT 2601, Australia.

Where, B is the birefringence, L is the path length in the crystal and λ is the wavelength of the light. For a typical crystal in use on H-1NF (L=250mm) the static phase delay is approximately 5000 wavelengths.

The delay is modulated using the electro-optical properties of the crystal, such that:

$$\phi_1 = \frac{\pi L \delta}{\lambda d} V$$

where, δ is the electro-optical coefficient of the crystal, d is the distance across the crystal (between the electrodes) and V is the applied voltage. If the applied voltage oscillates at angular frequency Ω then the phase perturbation will oscillate about the value ϕ_0 by an amount.

$$\phi_1 = \frac{\pi L \delta}{\lambda d} V \sin(\Omega t).$$

Simple accurate operation of a MOSS spectrometer requires some care in the provision of the modulation voltage that is applied to the birefringent crystal. The crystal is driven such that the optical path length difference between the two polarisations oscillates, generating a oscillating phase difference with an amplitude of $\pi/2$. Though this value is not critical, the algebra involved to extract the data from the signal is much simpler for a $\pi/2$ phase sweep. This modulation requires an applied voltage of between 1000 and 3000V_{pp}, depending on the thickness of the crystal and the wavelength of the light. The modulation frequency is chosen to ensure sufficient bandwidth to carry the plasma information (typically 100Hz to 100kHz)

The analysis technique used to reduce the data involves quadrature sampling of the signal. Using this technique harmonic components higher than 2Ω are aliased down to the first two harmonics, such that the contrast (ζ), phase (ϕ_0) and intensity (I_0) can be calculated as a function of time, requiring only four point per cycle. Clearly, since this scheme relies on harmonic analysis, to be reliable the drive signal to the crystal must be harmonically clean. The MOSS operation has been simulated using a *Labview* program. Using this program and injecting varying amounts of harmonic content into the drive signal it has been possible to estimate contaminating effect of higher harmonics on the inferred parameters. Second harmonic content affects only the calculation of the phase and not that of the temperature, which is obtained from the fringe contrast (see equation 1). The presence of third harmonic distortion on the drive voltage affects both the phase and the contrast.

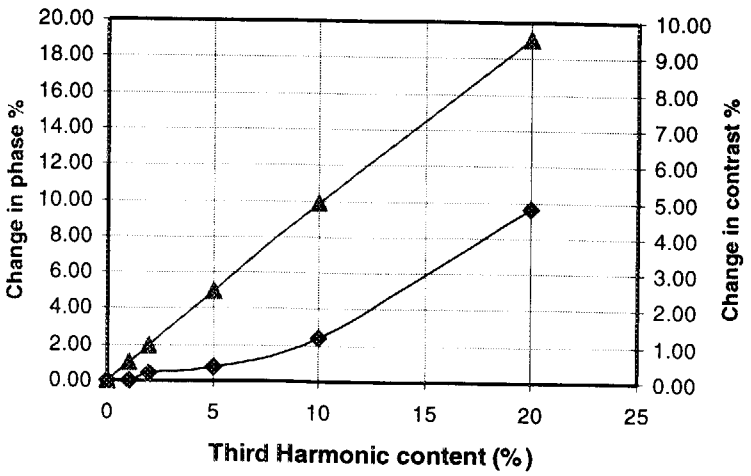

Figure 2: This graph shows the effect of 3rd harmonic distortion of the crystal drive signal on the calculation of the phase and the fringe contrast. The effect on the fringe contrast is not so severe with only 0.5% error induced by a 5% 3rd harmonic component.

The drive system used at H-1NF comprises a synthesized signal source which drives a high power (300W) audio amplifier. This signal is then fed into a 1:100 transformer to obtain the required voltage across the crystal. The system can be driven entirely from a PC using a DAQ card to provide the signals and to carry out the data acquisition.

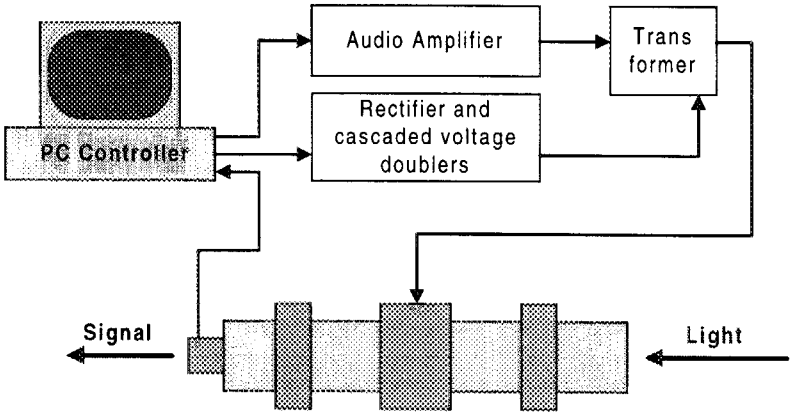

Figure 3: Shows a block diagram of the operation of a typical MOSS spectrometer. The DC bias to the crystal using the circuit shown has not yet been implemented.

This circuit works very well, however, the combination of the inductive transformer, the capacitive load and the piezo-mechanical properties of the crystal leads to some interesting resonances in the circuit. The main problems that had to be overcome include the resonance between the load is capacitive and the transformer inductance; the avoidance of both series and parallel resonance problems; operation off resonance where the primary currents can be very large. A transformer can be modelled using an equivalent circuit such that the input impedance (to the transformer) seen by the power supply (or amplifier) can be calculated as a function of frequency. Such a transformer model must include:

Ideal reflection of the load into the primary,
Imperfect coupling between primary and secondary,
Transformer core losses, and
Resistance and capacitance of the windings.

The implementation of such a model leads to an equivalent circuit of the form:

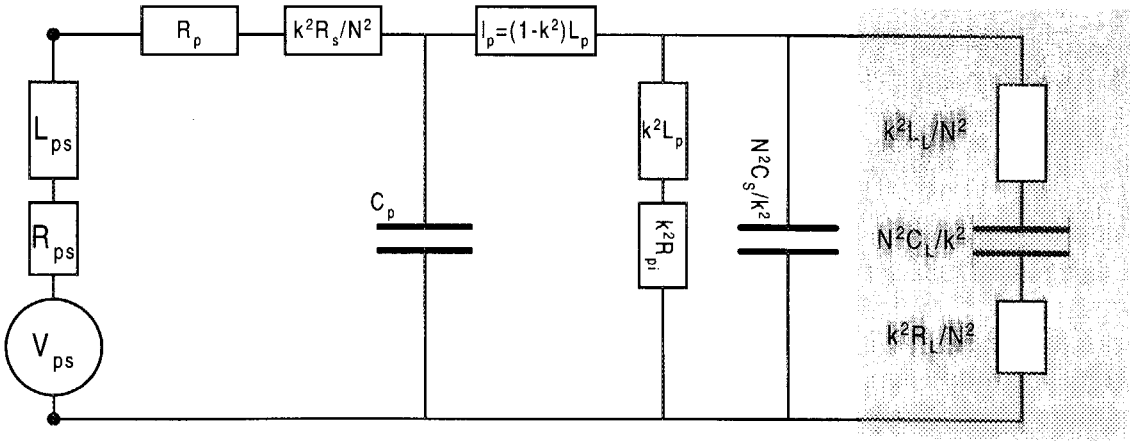

Where: Lp is the primary inductance — Cp is the parasitic capacitance of the primary
R_p is the resistance of the primary
R_s is the resistance of the secondary — C_s is the capacitance of the secondary
l_p is the leakage inductance — k is the coupling factor
1:N is the turns ratio (primary to secondary)
C_L is the load capacitance — R_L is the load (to simulate crystal)
L_L is the load inductance
R_{ps} is the power supply resistance — L_{ps} is the inductance on the power supply

For the transformer currently in use the parameters have been measured and calculated using this model to fit the measured response under test conditions: 50Ω source impedance, low voltage. The transformer was then connected to the MOSS circuit and the measured and predicted responses were compared.

Figure 4: shows the frequency response of the voltage and current in the transformer primary for a crystal voltage of ±1000V at 11kHz.

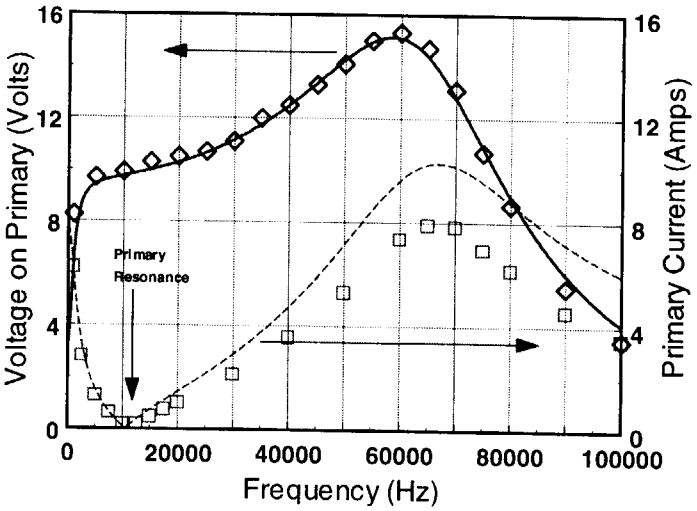

The data from the model and from the measurement are in good agreement for frequencies less than 50kHz. Above that the amplifier response, which is not included in the model, reduces. It shows clearly the effect of the resonances in the circuit, in particular that the primary current can become very large if used away from the optimum frequency, 11kHz in this case. When used at the primary resonance, indicated in figure 4, the primary current and hence power demands are low, the harmonic distortion of the signal of the signal applied to the crystal is very low. A typical example is shown in Figure 5

Figure 5: compares the spectrum of the original signal and the drive voltage applied to the crystal. Although there are some harmonics generated in the circuit, both the second and third harmonics are less than 50dB, equivalent to about 0.3% content.

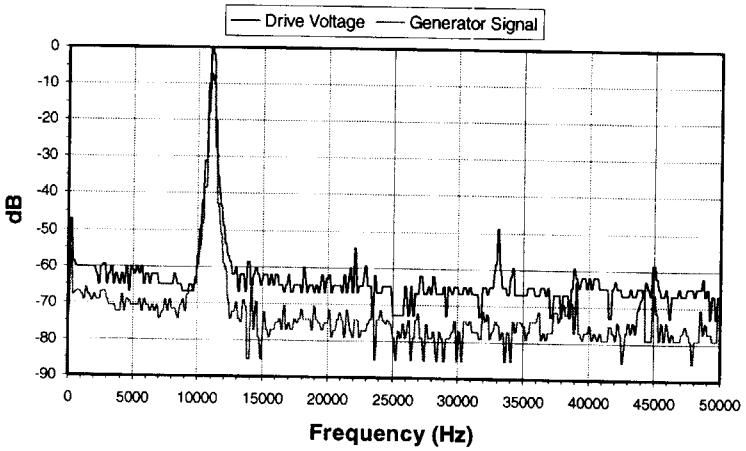

In summary, we have realised an inexpensive circuit using an audio amplifier and transformer that can provide an oscillating ±2kV voltage that is fully compatible with PC control. A dc bias can also be provided, using PC control, to adjust the static phase delay. We have successfully modeled the transformer circuit allowing optimisation of the crystal drive and have successfully operated the MOSS at modulation frequencies between 1 and 100kHz using 3 separate transformers. Work is continuing to design circuits that can handle several crystals and that can achieve voltages up to ±10kV for multi crystal applications.

The standard high frequency design of the MOSS that is employed on H-1NF was modified using this modelling technique in order to design a low frequency system that would be suitable for installation on LHD where time scales are much longer. This system was successfully installed and operated on LHD in December 1999.

[1] John Howard, Rev. Sci. Instrum. **70** (1999) 368-371

3-1 Optical Fibre Sensing of Plasmas

G.A. Woolsey and G.B. Scelsi

School of Physical Sciences and Engineering,
University of New England, Armidale, NSW 2351, Australia

§1. Introduction

A consequence of the development of optical fibre technology for communications has been the application of optical fibres to the sensing of a wide range of physical and chemical parameters. Any of the properties of fibres that are important for communications are significant for sensing: these include their small dimensions, their insulating nature and their immunity to high voltage and electromagnetic noise. These attributes make them particularly attractive for diagnostics of plasmas and electrical discharges. As insulators, optical fibres create none of the electrical disturbance or breakdown problems often associated with metal probes, and their small dimensions mean that distortion of plasma or discharge structure is minimised. With many plasmas and discharges occurring in environments that are electromagnetically noisy and which involve high voltages, signal transfer and processing through optical fibres provides significant benefits. The small dimensions of optical fibres provide good spatial resolution, and their facility for remote sensing can be particularly useful when working with large-scale systems.

Many of the wide range of physical parameters for which optical fibre sensors have been developed are relevant for plasma diagnostics, and these include temperature, pressure, gas flow, electric field and electric current. Furthermore, some of the optical fibre approaches to chemical sensing are capable of application to plasmas. Optical fibre sensors essentially come in two forms, intrinsic and extrinsic. In the former, the fibre itself is the sensing element, and in the latter, fibres are used to transmit light to and from a separate sensing element.

§2. Basic principles of optical fibre sensing

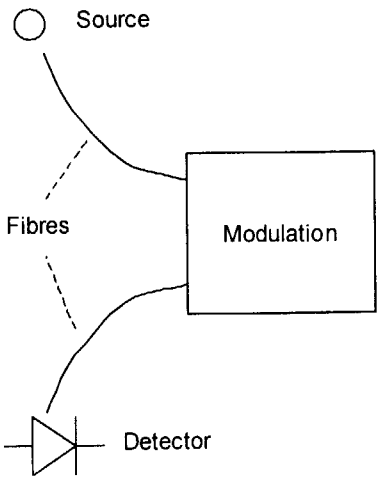

Fig 1 Basic arrangement of an optical fibre sensor

The basic principle of an optical fibre sensor is depicted in Fig 1. A source of light – it might be a white light source, an LED, or a laser– launches light into a fibre. The light passes through a region where it is modulated by the quantity to be measured. The modulated light is transmitted through a fibre to the detector. In an extrinsic sensor, the light leaves the input fibre to be modulated before being collected by a second output fibre. In an intrinsic sensor, a single fibre transmits the light from the source to the detector, and the light is modulated while it is in the fibre. Characteristics of the light that can be modulated are intensity, phase, polarisation and wavelength. Most extrinsic sensors are essentially optical fibre modifications of established optical diagnostic techniques. For example, plasma densities have been measured using optical interferometry with the light coupled directly to an optical fibre and split into reference and scene beams with a bidirectional coupler [1]. This paper emphasises intrinsic all-fibre sensors where the light is retained within the fibre system throughout. These sensors have most potential for diagnostics of plasmas since they are relatively easy to assemble, have few alignment problems, are immune from electromagnetic interference and can offer good spatial resolution.

§3. Modulation techniques

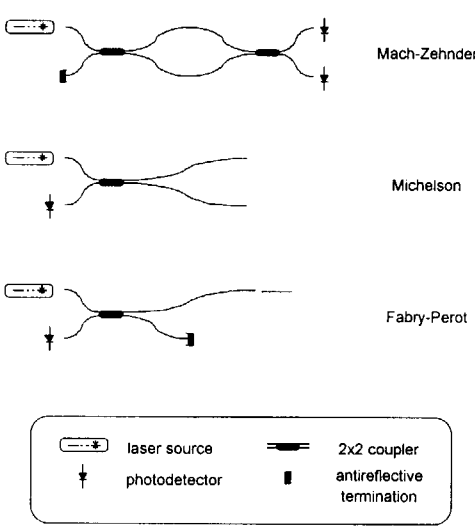

Fig. 2 Three optical fibre interferometers.

3.1 Phase modulation

In optical fibre sensors that rely on the modulation of the phase of the light propagating through the fibre, the phase modulation is measured interferometrically. Single-mode optical fibres carry monochromatic light without altering its coherence characteristics and can therefore be used to assemble optical interferometers. Fig. 2 shows the schematic arrangements of three commonly used optical fibre interferometers. The similarity to unbound-beam interferometers is apparent given that the 2 x 2 directional coupler is the optical fibre equivalent of a conventional 50% beam splitter. The Michelson interferometer relies on the Fresnel reflection at the cleaved ends of the two fibre arms, generated by the refractive index discontinuity between silica and air. In the Fabry-Perot case, the resonant cavity consists of a section of single-mode fibre that has been carefully cleaved at the two ends to provide optically flat and smooth surfaces. A review of optical fibre interferometers and a discussion of their application to precision measurement are given by Jackson [2]. As an illustration, we shall examine a Mach-Zehnder interferometer fibre sensor for measuring temperature. One of the fibres between the bidirectional couplers is isolated from external changes in temperature and pressure, while the second fibre is the sensor arm. A short length of the second fibre is exposed to the environment where the temperature is to be measured. A change in temperature T changes the optical path length by changing both the refractive index n of the fibre material and the length L of the fibre. The sensitivity of the sensor to temperature is given by

$$\frac{1}{L}\frac{d\phi}{dT} = \frac{2\pi}{\lambda}\left[\frac{n}{L}\frac{dL}{dT} + \frac{dn}{dT}\right]$$

where $\frac{1}{L}\frac{dL}{dT}$ is the temperature coefficient of linear expansion, and $\frac{dn}{dT}$ is the temperature coefficient of refractive index. For fused silica, the values of these coefficients are 5 x 10^{-7}/°C for expansion and 10 x 10^{-6}/°C for refractive index. That is, the variation of refractive index with temperature is substantially greater than the variation of fibre length with temperature. Putting in these values together with the refractive index n value of 1.456 and the wavelength of the red line of the helium-neon laser 632.8 nm gives

$$\frac{1}{L}\frac{d\phi}{dT} = 107 \ rad\,°C^{-1}\,m^{-1} = 17 \ fringes\,°C^{-1}\,m^{-1}$$

The arrangement can be used to measure any quantity that will cause a change in optical path along one arm. Such parameters include temperature, pressure, strain, magnetic field and electric field.

3.2 Polarisation modulation

Early work on the application of optical fibres to plasmas concentrated on current measurement. The concept of the optical fibre current sensor is shown in Fig 3. A length of single-mode fibre is coiled several times around the plasma and linearly-polarised light from a laser diode is launched into the fibre coil. The current in the plasma produces a magnetic field with cylindrical field lines that are parallel to the fibre wrapped around the bar. This means that the linearly-polarised light propagating through the fibre is acted upon by a longitudinal magnetic field. The light therefore experiences the Faraday magneto-optic effect where the direction of polarisation of the light in the fibre is rotated by an amount proportional to the magnetic field, and to the length of path exposed to the magnetic field.

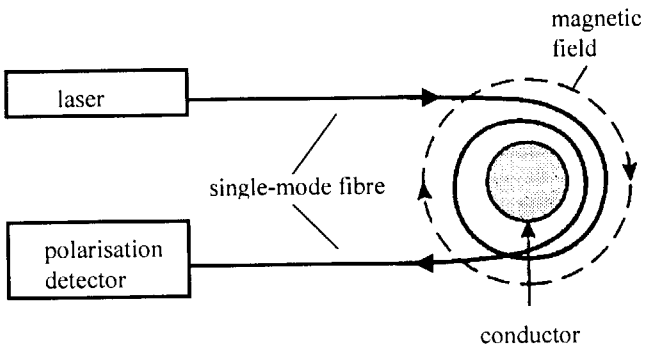

Fig 3 The principle of the optical fibre current sensor

The total angle of rotation ρ of the direction of polarisation is proportional to the line integral of the magnetic field around the loop, that is, $\rho = NV\oint \mathbf{H} \cdot d\mathbf{l}$ where N is the number of turns of the coil, H is the magnetic field, L is the length of a fibre loop and V is the Verdet constant, which for fused silica is 1.6° $m^{-1}T^{-1}$. Using Ampere's circuital theorem, we can write the line integral of the magnetic field around a current-carrying conductor equal to the current. Hence $\rho = NVI$ where I is the current measured.

3.3 Fibre Bragg gratings and wavelength modulation

When a silica fibre is exposed to the radiation from a holographic interferometer illuminated with a coherent ultraviolet source in the wavelength region 244-248 nm, a permanent periodic modulation of the refractive index of the germanium-doped core is produced to form a set of partially reflecting planes [3]. When light from a broadband source is transmitted along this fibre, a set of beams is reflected from the planes and these beams interfere with each other. The interference is destructive unless each beam is in phase with the others. The wavelength at which the reflected beams are in phase is given by Bragg's law: $\lambda_B = 2n\Lambda$, where n is the core index of refraction and Λ is the period of the index modulation. The set of planes, normally of length between 1 and 20 mm, is referred to as an in-fibre Bragg grating. Perturbation of the grating, for example by a change of temperature, strain or pressure, results in a shift in the Bragg wavelength. A change of Bragg wavelength with temperature arises from both a refractive index change and thermal expansion of the fibre. For silica fibre, the wavelength-temperature sensitivity is a few pm per degree [4,5]. Whereas optical fibre interferometric sensors are illuminated by highly coherent lasers, fibre Bragg grating sensors generally require a broadband light source and a high-resolution wavelength-shift detection system. Fibre Bragg grating sensors have been used to measure strain, temperature, pressure and dynamic magnetic field, although their application to plasmas has been confined to temperature measurement. A review of fibre Bragg gratings has been published by Rao [6].

3.4 The evanescent field and intensity modulation

Light travelling through an optical fibre is not confined completely to the core of the fibre. The evanescent field surrounding the core results in some transmission in the fibre cladding or in the medium surrounding a naked fibre core. The depth of penetration outside the core is of the order of one wavelength. The evanescent field of a naked-core fibre can be exploited for sensing. Numerous chemical, environmental, biochemical and medical sensors have been developed, some of which involve absorption of the evanescent field and some of which incorporate a dye or fluorescent material coated onto the fibre core. Evanescent-field sensors have been used to measure gas densities, levels of solid deposition and pH values [7,8]. Plasma applications of evanescent-wave sensing have been confined to absorption techniques.

§4. Temperature sensing in plasmas

Intrinsic optical fibre sensing of temperature in plasma environments has been confined to the discharge and plasma work of our group at the University of New England, and some solid surface measurements in plasma processing systems at other laboratories. We have exploited interferometric sensing of temperature in glow discharges, in a planar-coil inductively-coupled RF plasma and in the Heliac H-1 magnetically confined plasma at the Australian National University.

The glow measurements were made in a DC argon discharge. A glow is a weakly ionised plasma so that fibre heating is by neutrals, and the fibre reaches equilibrium with the neutral gas so that the gas temperature is measured. A Fabry-Perot interferometer was chosen for these measurements. An integrated approach was used, and for any cross-sectional plane of the discharge, the sensing fibre could be scanned across the discharge. In each measurement the optical fibre sensor measures the integral of the temperature distribution along a straight-line path within the heated volume of gas. After collecting a set of such integral measurements for different chords, it is then possible to recover the entire temperature distribution by means of a deconvolution method. The results of a set of measurements are displayed in Fig. 4 alongside a diagram of the argon glow structure.

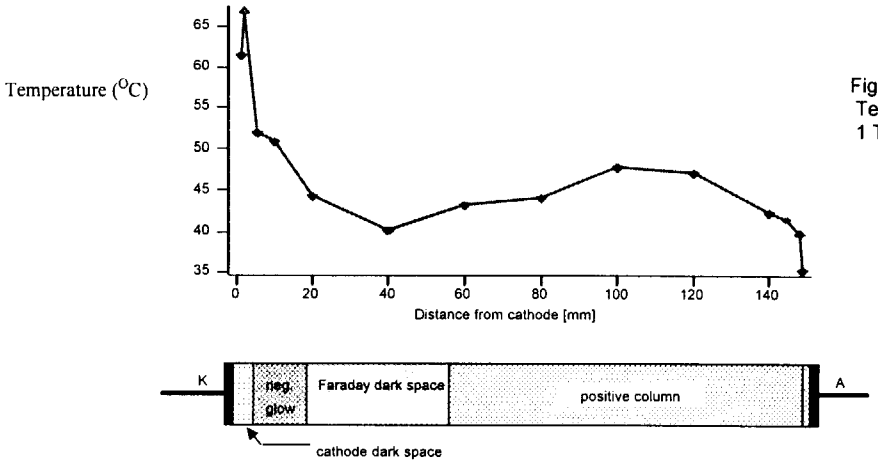

Fig 4
Temperature distribution in a 1 Torr, 4 mA, argon discharge

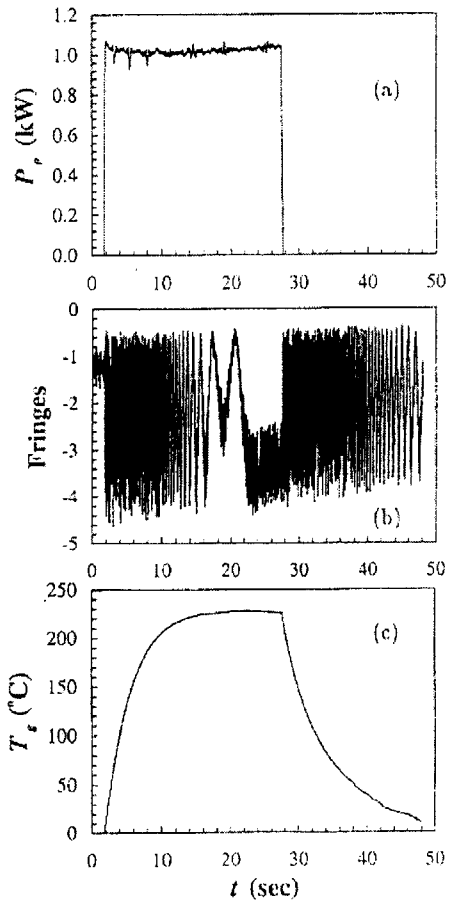

Fig 5 Response of gas temperature in plasma to RF pulse: (a) Power (b) Fringes (c) Temperature

A Fabry–Perot temperature sensor with a 17 mm fibre arm, representing essentially a point sensor, has been installed in a planar coil, inductively-coupled RF plasma [9]. Like the glow discharge, the dominant particles in the plasma are neutrals and these are responsible for heating the fibre. The primary aim of this work was to demonstrate the efficacy of optical fibre sensing in an RF plasma, free of RF interference. The results of two simple experiments were reported. Firstly, the reactor chamber was filled with argon to a pressure of 30 mTorr and the RF power switched on for a short period (26 s) to produce a high electron density H-mode discharge. The power dissipated in the plasma (Fig 5a) and the signal from the temperature sensor (Fig 5b) were recorded. The sensor signal displays the interferometer fringe shift as a series of 2π fringes, and these are analysed to provide a temperature–time distribution (Fig 5c). The gas temperature was then examined during an E- to H-mode discharge transition. The temperature was found to rise from close to ambient in the E-mode to 250°C above ambient in the H-mode, and the time between the transition and attainment of the equilibrium H-mode temperature was measured to be 20 s.

A similar point sensor has also been used to probe a Heliac helical-axis stellarator – the H-1 Australian National Facility at the Australian National University in Canberra [10]. In this plasma, it is ions

that heat the fibre probe, and calculations of fibre temperature based on a knowledge of ion energy and density and the thermal properties of the fibre agree closely with the temperature values of a few tens of degrees above ambient measured with the optical fibre probe. The probe has been used to obtain spatial distributions of ion flux within the plasma, and a screened probe has verified that positive ions are the major species responsible for heating the fibre. The fibre probes were found to be robust, with one probe surviving a thousand plasma shots with no noticeable deterioration of response, although some etching of the cladding surface did occur.

Other plasma applications of optical fibre interferometric sensing of temperature in fusion plasma systems includes the work of Forman *et al* [11] in which they developed a 3-element fibre Bragg grating sensor arrangement for measuring the temperature of the carbon tiles on the Los Alamos CPRF/ZTH plasma. The three sensors had Bragg wavelengths of 830.1 nm, 833.0 nm and 836.0 nm, using as a light source a broadband superradiant diode centred on 833 nm. Wavelength shifts were measured using a grating spectrograph. Wavelength shifts were found to increase linearly with temperature over the temperature range 25 to 95 °C. This work demonstrates the potential of fibre Bragg grating sensors for distributed sensing where the variation of a parameter over a wide area can be monitored using a continuous length of fibre and a single light source and monitoring station.

Another area of plasma physics which is utilising optical fibre temperature sensing is that of RF plasma sputtering. Here again the small dimensions of fibre sensors and their immunity to electromagnetic interference provides substantial advantages over more conventional measuring devices such as thermocouples. Both Fabry-Perot interferometer [12] and fibre Bragg grating [13] sensors have been used in RF plasma sputtering systems to monitor the substrate temperature.

§5 Current and magnetic field sensing

Chandler and his co-workers at Los Alamos were the first to use the Faraday magneto-optic effect in an optical fibre to measure plasma current [14,15]. Their measurements were made by looping a single-mode fibre around the aluminium shell of ZT-40, a reversed-field-pinch that produced toroidal plasma currents in the range 80 to 400 kA. Around the same time, Lassing et al [16] made optical fibre sensor measurements of the toroidal plasma current in the high-beta tokamak SPICA II at the FOM Institute for Plasma Physics in the Netherlands. Both groups reported good agreement between current measurements made with a Rogowski coil and those made with the optical fibre sensor, and each found that the fibre sensor displayed much less noise and higher frequency response.

It is significant however that optical fibre sensing of plasma current has not been exploited to any extent since this pioneer work of the 1980s. This is due to problems associated with birefringence in single-mode optical fibres. These fibres allow the propagation of two degenerate modes with orthogonal polarisations. In an ideal fibre with perfect circular symmetry along the fibre length, the two states are degenerate and the state of polarisation of the guided wave propagates along the fibre unchanged. In practice, however, perfect circular symmetry along the fibre length does not exist due to intrinsic and extrinsic birefringence. Intrinsic birefringence is introduced during manufacture in the form of anisotropy of the refractive index of the core and asymmetry of the core geometry. Extrinsic birefringence arises when the fibre is perturbed externally by temperature variations or as a result of being bent, squeezed or stretched. Hence the fibre behaves as a birefringent medium due to a difference in the effective refractive indices of the two degenerate modes, and the state of polarisation is maintained over lengths of only a few metres. In the work described above, the birefringence problem was reduced, but not eliminated, by using fibres that were twisted or spun during manufacture. This has the effect of creating a high degree of circular birefringence which tends to average out the linear birefringence to produce a low birefringence fibre. Because of this problem of fibre birefringence, the development of optical current sensors has concentrated on devices that use bulk optic materials with high Verdet constant and no birefringence. These are finding commercial application in the electric power industry but they are not suitable for use on plasmas. However, now that methods of manufacturing fibres with low inherent birefringence have become available, along with the development of techniques for removing both inherent and bend-induced birefringence, it is possible that optical fibre sensing of plasma current will yet prove its worth [17].

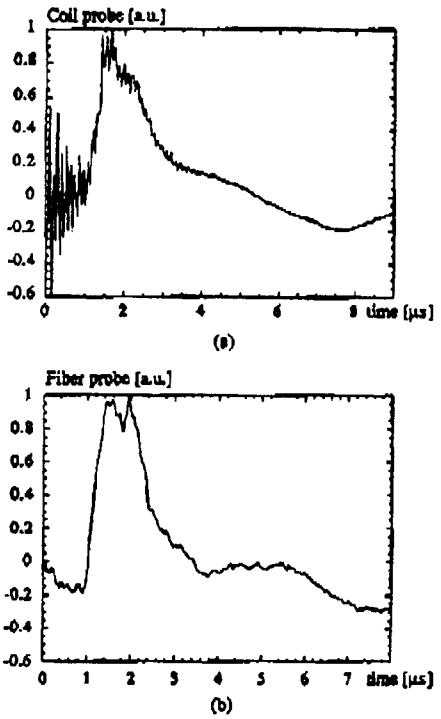

Fig 6 Magnetic field as a function of time in a helium plasma (15 kV, 1 mbar) (a) magnetic coil (b) optical fibre

A more recent application of optical current sensing based on the Faraday effect is the measurement of magnetic field in a z-pinch discharge [18]. Here the fibre loop was placed within the plasma chamber and set to different radii (20-70 mm) for successive pulses in order to map the magnetic field through the plasma. Birefringence effects were minimised by using an ultra-low birefringence fibre (no details given) and a single loop only. The noise difference between the magnetic and optical measurements is seen in Fig 6. Once again, the fibre suffered little damage following hundreds of discharges.

§6. Chemical sensing

Chemical sensing in plasmas using evanescent-field processes has been confined to the measurement of deposition rates in etching systems and to the monitoring of molecular dissociation in SF_6 glows and coronas. In an SF_6 discharge, dissociation of SF_6 molecules leads to the production of gaseous and solid by-products and hence a reduction in SF_6 content. This means that in any high-voltage system that uses high-pressure SF_6 gas as an insulating medium, insidious coronas or switching arcs will lead to a reduction in insulation efficiency.

One consequence of dissociation in an SF_6 glow discharge is the production of sulphur and its deposition on the discharge chamber wall. A measurement of this deposition could thus be used to monitor the degradation of the insulation. Such a measurement has been made in our laboratory by examining transmission through a 0.6 mm-diameter silica fibre immersed in an SF_6 glow discharge, maintained at a pressure of 1 Torr and a current of 10 mA over a period of seven hours [19]. Measurements were made with both white-light and He-Ne laser (633 nm) sources. A total fall in fibre output intensity of around 20% was found to occur over the period of the 7-hr glow discharge. An electron-microscope analysis of the coated fibre revealed that the deposited material was indeed sulphur and indicated that the thickness of the sulphur coating after 7 hr was around 600 nm. The results suggest that optical fibre sensing of sulphur production could be an appropriate technique for insulation monitoring in SF_6-insulated high-voltage systems.

A similar approach has been taken to monitor deposition rates and layer thicknesses on the walls of integrated-circuit plasma-etching chambers [20] and to monitor the deposition of polypyrrole thin films by AC plasma polymerisation [21]. Monitoring an etching chamber is useful for developing efficient cleaning schedules and for reducing down time. The ideal sensor should indicate optimum conditioning times following clean up, and warn of impending particulate formation so as to prevent film flakes from the chamber wall depositing on the substrate. Quick *et al* [20] found that transmission through unclad multimode quartz fibres inserted into etching plasmas (CHF_3 and O_2) decreased with time. This was interpreted as being due to polymer build up on the fibre, causing scattering of the light impinging on the fibre/plasma boundary, plus irreversible surface roughening of the fibre. Jose *et al* [21] also measured rates of transmission loss and hence of thin-film deposition, and interpreted the transmission loss as being due to evanescent-wave interaction.

§7. Conclusion

Although the use of optical fibre sensing for measurements in plasmas and electrical discharges has been limited, the results that have been obtained have been promising, and in some cases the results have been unavailable from other plasma diagnostic techniques. The versatility of optical fibre sensors, which allows such a wide range of physical and chemical parameters to be measured, does provide many opportunities for the development of appropriate plasma fibre probes. Clearly, the early work of the late 1980s on current sensing of plasmas with optical fibres was not as successful as had been hoped, mainly because of birefringence problems, and this experience may have sent a negative message on optical fibre sensing to the plasma community. But developments since that time in optical fibre design, fibre sensing techniques and optoelectronic components have greatly extended the possibilities for plasma application. It is hoped that the work described in this paper will generate new interest in the optical fibre sensing of plasmas, in areas such as gas temperature monitoring, particle and radiation flux measurement and plasma processing of surfaces. The advantages of optical fibre probes for plasma study – small size, insulating, immunity to electromagnetic noise, remote sensing – are well proven.

References

1. B.J.Warthen and J.S.Shlachter, *Proc.IEEE Int.Conf. on Plasma Science*, Madison, 220, 1995
2. D.A.Jackson, *J.Phys.E*, 18, 981-1001, 1985
3. G.Meltz, W.W.Morey and W.H.Glenn, *Opt.Lett.*14, 823-825, 1989
4. W.W.Morey, G.Meltz and W.H.Glenn, *Proc.SPIE*, 98-107, 1989
5. Y-J.Rao, A.B.L.Ribeiro, D.A.Jackson, L.Zhang and I.Bennion, Opt.Lett.20, 2149-2151, 1995
6. Y-J.Rao, *Meas.Sci.Technol.* 8, 355-375, 1997
7. O.S.Wolfbeis, in *Optical Fiber Sensors*, B.Culshaw and J.Dakin (eds.), Artech House, Boston-London (1997), vol. IV, chap. 8, pp. 53-107.
8. B.D. MacCraith, M.McDonagh, G.O'Keefe, E.T.Keyes, J.G.Vos, B.O'Kelly and J.F.McGilp, *Analyst*, 118, 385, 1993
9. V.A.Everett, I.M.El-Fayoumi, I.R.Jones and G.A.Woolsey, *Proc.12th Int.Conf.Gas Discharges and Applications*, Greifswald, 358-361, 1997
10. V.A.Everett and J.N.Howard, *22nd AINSE Plasma Sci.& Tech.Conf*, Canberra, 69, 1999
11. P.R.Forman, F.C.Jahoda and E.R.Aksay, *Rev.Sci.Instrum.* 61, 2970-2972, 1990
12. Y.Yunhae, C.E.Lee, R.A.Atkins, W.N.Gibler and H.F.Taylor, *J.Vac.Sci.Technol.* A 8, 3247-3250, 1990
13. N.K.Zayer , P.J.Henderson, A.J.C.Grellier and C.N.Pannell, *J.Vac.Sci.Technol.* A 17, 871-876, 1999
14. G.I.Chandler and F.C.Jahoda, *Rev.Sci.Instrum.*, 56, 852-854, 1985
15. G.I.Chandler, P.R.Forman, F.C.Jahoda and K.A.Klare, *Appl.Opt.* 25, 1770-1774,1986
16. H.S.Lassing, W.J.Mastop, A.F.G.van der Meer & A.A.M.Oomens, *Appl Opt*, 26, 2456-2460, 1987
17. G.W.Day, K.B.Rochford and A.H.Rose, *Proc.11th Int.Conf. Optical Fiber Sensors*, Sapporo, 124-129, 1996
18. G.Breglio, D.Cautiello, M.de Magistris, L.de Menna, E.Miano and C.Visone, *IEEE Trans.Plasma Science*, 23, 381-387, 1995
19. G.A.Woolsey, D.Vukovic and G.B.Scelsi, *Proc.11th Int.Conf. Optical Fiber Sensors*, Sapporo, 474-477, 1996
20. A.K.Quick, N.Hershkowitz and M.Sarfaty, *Proc.IEEE Int.Conf. on Plasma Science*, Boston, 281, 1996
21. D.Jose, M.S.John, P.Radhakrishnan, V.P.N.Nampoori and C.P.G.Vallabhan, *Thin Solid Films*, 325, 264-267, 1998

3-2 Results from the new JT-60U neutron time-of-flight spectrometer.

M. Hoek, T. Nishitani and Y. Shibata

Department of Fusion Plasma Research
Naka Fusion Research Institute
Japan Atomic Energy Research Institute
Naka-machi, Naka-gun, Ibaraki-ken

Abstract

In this paper, the first results from measurements with the new 2.45 MeV neutron time-of-flight spectrometer at JT-60U are described. The spectrometer was installed August 1999 and neutrons from NBI-heated deuterium plasmas were measured for a time-period of 1-month (Sep 1999). These measurements showed that neutron energy distributions can be obtained when the neutron yields from the plasma are below 10^{15} neutrons/s. With higher neutron yields, only random coincidences were detected. Improvements of the spectrometer involves a smaller first scattering detector with an active voltage divider. An improved calibration procedure for the second detector has also been suggested and will be implemented.

Introduction

At JT-60U, neutron diagnostics of fusion plasmas have been emphasized on measuring total neutron yields utilizing fission chambers [1]. However, although the neutrons from a fusion plasma are commonly regarded as mono-energetic (2.45 MeV or 14.1 MeV depending on the reacting species of the fusion reactions), the energy spectrum of the neutrons is also of interest. There have been attempts to measure the neutron energy distribution with He-3 chambers [2] but the maximum allowed count-rate is limited and it has been necessary to add up several shots to get a neutron energy distribution.

A 2.45 MeV neutron spectrometer based on neutron time-of-flight coincidence measurement between two fast plastic scintillators [3] has been installed at the JT-60U Tokamak. According to Monte Carlo simulations of the neutron transport in the spectrometer, the efficiency and resolution was calculated as $2.8 \cdot 10^{-2}$ cm^2 and 105 keV, respectively [4]. The accuracy of the Monte Carlo code was confirmed by measurements utilizing 14.1 MeV neutrons [5].

The spectrometer is located ~9 m below the plasma center and will measure the emitted neutrons in a vertical line-of-sight. For an assumed efficiency as calculated by Monte Carlo and for a total neutron yield of 10^{16} n/s the count-rate from true coincidences is estimated to 6 kHz.

In this paper, the first results from the spectrometer are descried. The data were collected during one month of deuterium (D) plasma operation with Neutral Beam Injection (NBI).

Principle of the spectrometer

The neutron spectrometer is based on the principle of measurement of the time-of-flight, TOF, between two fast (~ns) plastic scintillators. The source neutrons, which enter through a collimator (70 cm length, 0.4·0.8 cm^2), interact with the first scintillator (D0) located in the neutron beam. The amplitude of the generated signal depends on the scattering angle of the neutron, which implies that an energy discriminator window can be utilized. Some of the scattered neutrons are detected by a second large scintillator (D1) and a second coincidental time signal is generated. To reduce the random coincidences, the start-stop sequence is reversed.

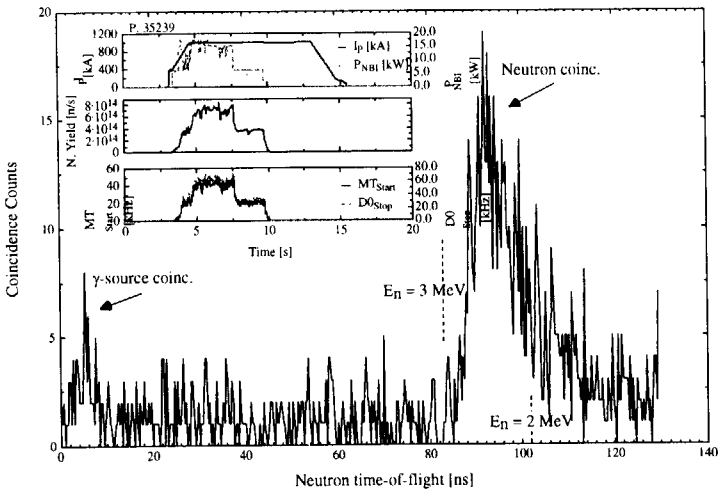

Fig. 1. Neutron TOF spectrum measured by the spectrometer. The peak positioned at 92 ns are the coincidences from 2.45 MeV source neutrons. The time scale is adjusted to the position of the coincidences from a γ-calibration source at 5.5 ns.

To keep the time resolution as good as possible, the detectors are positioned on a "constant TOF sphere". It can be shown that for mono-energetic neutrons that scatter with protons in the lower pole of the sphere (in the central point of the D0-detector (5·10 cm^2, 2 cm thickness), the TOF to another point on the spherical shell is independent of the scattering angle. Therefore, to achieve a constant TOF for mono-energetic source neutrons and to accomplish a high efficiency, a big D1-detector has been chosen (30·60 cm^2, 2 cm thickness) that is bent in such a way that it follows the constant TOF sphere. The major limiting factor of the scintillator size is the attenuation and timing deterioration of the generated light during its way to the photo-cathode of the PM-tube. Therefore, two PM-tubes are connected via adiabatic light guides to the 30·2 cm^2 edges of the D1 scintillator and the distance between the scintillator edges has been limited to 60 cm. The time signals from these two photo-multiplier, PM, tubes are then averaged, utilizing a mean-timer, MT, module, to minimize the deterioration of the D1 time signal.

Monte Carlo calculations have shown [4] that the resolution is optimal for a neutron scattering angle (in the D0 detector) of 25°. However, to reduce the amount of stray neutrons to the D1 detector, a neutron scattering angle of 35° was chosen.

The concept of a constant TOF sphere has been taken one step further by introducing a second constant TOF sphere (see fig. 1 in [4]). For this sphere, the neutron TOF is constant

for those monoenergetic neutrons that scatter along the 2nd spherical shell in the direction of the center of the D1 detector. The D0 detector is therefore tilted –70° to approximately follow the 2nd spherical shell while the central point of the D1-detector is positioned on the sphere. According to Monte Carlo calculations, the resolution increased by 30% by such a configuration.

Measurements and results

In Fig. 1 a neutron TOF spectrum measured by the spectrometer is shown. For this pulse the neutron yield is relatively low ($3.2 \cdot 10^{15}$ neutrons). In this experiment, a Co-60 γ-calibration source was positioned on the D0 detector. The position of the γ-peak gives us an absolute time scale reference. The distance between the D0- and the D1-detector is 163.8 cm, which means that the γ-peak should be located at 5.5 ns. The absolute time scale was accordingly adjusted. With this time calibration, the peak of the neutron TOF spectrum was located at 92 ns which is in agreement with the flight time of 2.45 MeV source neutrons, scattered 35°.

The plasma current and the power of the NBI is also shown in the figure. Typical start- and stop- count-rates from the MT and the D0 detector are 40-50 kHz and 60-70 kHz, respectively.

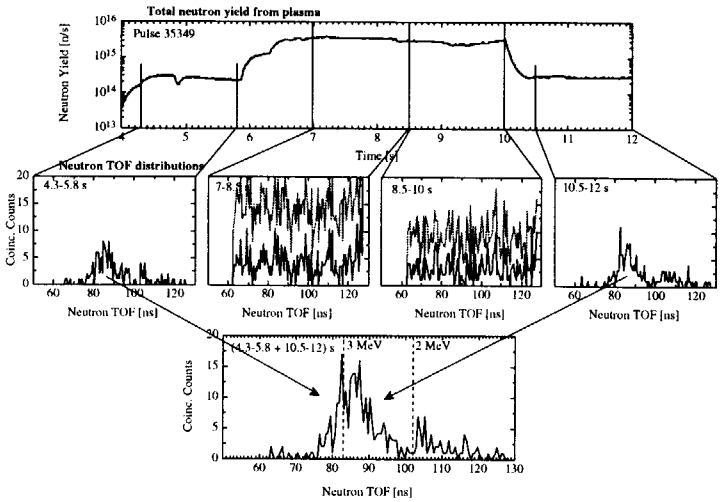

Fig. 2. Measured neutron TOF spectra for 4 time intervals. For high neutron yields ($>10^{15}$ n/s), only random background is registered. For lower neutron yields (~$2\text{-}3 \cdot 10^{14}$ n/s) coincidence spectra can be measured. The figure also shows the sum of two time intervals where a coincidence peak is registered. The neutron energy interval 2-3 MeV as derived from the neutron flight-time, is also indicated.

In Fig. 2 a neutron TOF measurement of a pulse with a high total neutron yield is shown. For lower neutron yields (<$2\text{-}3 \cdot 10^{14}$ n/s) we get coincidental counts corresponding to 2.45 MeV neutrons. The count-rates of the detectors in these cases (4.3-5.8 s and 10.5-12 s in the figure) are 15-20 kHz from the MT (starts) and 30-40 kHz from the D0 detector (stops). As the neutron rate increases by a factor of 10, the count-rate of the MT increases with the same amount. However, the D0 detector (located in a direct line-of-sight to the plasma) increases only with a factor of 5. The gray curves are coincidences uncorrected for random

coincidences. The black curves are corrected for random background, utilizing the count-rates of the starts and the stops.

Also shown is the integrated measured neutron TOF spectrum where the integration was done during the low neutron yields (4.3-5.8 s and 10.5-12 s). The positions of the neutron flight-times corresponding to 2- and 3 MeV are indicated. 2.45 MeV neutrons should peak at 92.5 ns but is weighted towards shorter flight-times (higher neutron energies). The reason for this is the uncertainty in the time calibration. For this pulse, the maximum time between start and stop, registered by the TAC, is 100 ns. This means that it is difficult to make a time calibration using a γ-source. The time calibration was therefore based on an earlier calibration with a maximum time range of 200 ns.

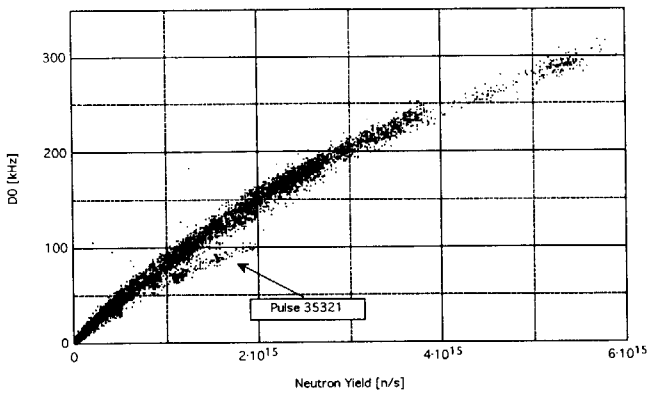

Fig. 3. D0 detector count-rate versus the total neutron yield. The count-rate is non-linear most likely because of the passive circuit of the voltage divider for the PM-tube.

The D0 detector is located in the direct line-of-sight and can therefore be exposed for a very high neutron flux (~$2.5 \cdot 10^5$ n/cm^2·s [3]). The D0 detector also registers γ-radiation which is estimated as 10% of the neutron flux [6]. The present design of the voltage divider for the D0 detector is of passive type. This means that for high enough count-rates, the voltages between the dynodes of the PM-tube drops and the signal level drops as well. The discriminator levels of the D0 detector are well calibrated using γ-calibration sources [5]. However, if the amplitude of the signal drops, then the interesting range of amplitudes will not coincide with the discriminator amplitude window and the relevant coincidences are lost. Fig. 3 shows the count-rate of the D0 detector plotted versus the neutron yield as measured by a fission chamber. The count-rate is clearly non-linear which could mean that the measured coincidences at higher count-rates (< $2 \cdot 10^{15}$ n/s) are purely false coincidences.

To investigate the fraction of background events in the D1 detector, we removed the D0 detector from the line-of-sight for a series of pulses. In Fig. 4, the count-rate from the MT is plotted versus the total neutron yield from the plasma. Only those pulses that gave a neutron peak in the PHA spectra are included in the plot for the case when the D0 detector was present.

The count-rate from the mean-timer (with and without the D0 detector) is linear with the neutron yield. From best linear fits we could estimate the background as more than 90% of the interesting events. Unfortunately, this is a severe problem of the present design. To register more true coincidences and to measure neutron energy distributions at higher total neutron yields, we need to reduce this background substantially. Irrelevant events from the D1

detector give irrelevant starts to the TAC, which is likely to be stopped by an event from the D0 detector. The D0 detector sits in the line-of-sight of the plasma and the random coincidence background therefore dominates.

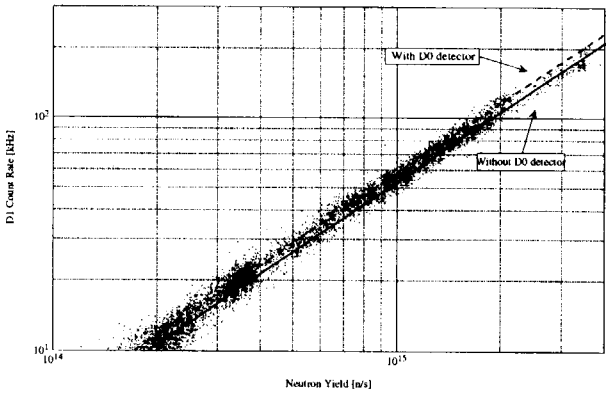

Fig. 4. Count-rates of the MT with and without the D0 detector in the neutron beam. From best linear fits of the count-rates, it is estimated that more than 90% of the count-rate comes from background events.

Summary

It is clear that the performance of the spectrometer deteriorates as the total neutron yield increases. For a count-rate of the D0 detector exceeding ~80 kHz (corresponding to a total neutron yield of 10^{15} n/s), the count-rate becomes non-linear with the neutron yield. We expect that the passive voltage divider of the PM-tube leads to signal attenuation for higher count-rates. To solve this we therefore need to modify the voltage divider and reduce the size of the scintillator of the D0 detector.

From the experiments where the D0 detector was removed from the line-of-sight, we could estimate that the fraction of relevant events in the D1 detector was merely 10%. This can be an effect from improper settings of the discriminator levels (too low). The output signals from the D1 detector has been energy calibrated but the results from that calibration were uncertain. Improvements of the calibration procedure have been suggested and will be implemented.

To increase the fraction of relevant events in the D1 detector we also need to improve the shielding around the D1 detector. However, the shielding is already substantial and it is not trivial to increase it further. Monte Carlo calculations of the effects from different shielding geometries are in progress.

Acknowledgements

One of us (M. Hoek) would like to express his gratitude for the granted JAERI fellowship at JT-60U Tokamak in Naka, Japan.

We are in great debt to Dr. Kramer at the JT-60U laboratory and Dr. G. Grosshög at Dept. of Reactor Physics, Chalmers University of Technology in Sweden for their valuable comments on the detectors, electronics and neutron energy measurement techniques.

References

[1] T. Nishitani, H. Takeuchi, T. Kondoh, T. Itoh, M. Kuriyama, Y. Ikeda, T. Iguchi, and Cris W. Barnes, Rev. Sci. Instrum., 63 (11) 5270-5278, 1992.

[2] T. Nishitani and J. D. Strachan. Japanese Journal of Applied Physics, 29 (3) 591-596, 1990.

[3] T. Elevant, M. Hoek and T. Nishitani, "Design study of a time-of-flight neutron spectrometer for JT-60U", Japan Atomic Energy Research Institute Report JAERI-M 93-123 (1993)

[4] M. Hoek, T. Nishitani, H. Takahashi, M. Nakazawa and T. Elevant, Fusion Engineering and Design 45 (1999) 437-453.

[5] M. Hoek, T. Nishitani, H. Takahashi, M. Nakazawa and T. Elevant. "The JT-60U 2.45 MeV Neutron Time-of-Flight Spectrometer". Submitted to Fusion Engineering and Design, Sep. 1999.

[6] N. Miya, Naka Fusion Research Establishment, Japan Atomic Energy Research Institute, Japan, Private communication

3-3 Fusion gamma-ray diagnostics for D-^{3}He experiments in JT-60U

T. Nishitani, Y. Shibata*, K. Tobita and Y. Kusama

Naka Fusion Research Establishment, Japan Atomic Energy Research Institute,
Naka-machi, Naka-gun, Ibaraki-ken 311-01, Japan
* Department of Nuclear Engineering, Nagoya University, Nagoya, 464-8603, Japan

ABSTRACT

The preliminary D-^{3}He experiments was done on JT-60U with the negative-ion-based-NBI(N-NBI) in reversed shear plasmas. Gas of ^{3}He was puffed in the plasma initiation and just before the N-NB injection of 3.5 MW with 360 keV. The D-^{3}He reaction produce s 3.6 MeV alpha and 14.7 MeV proton, however, has a small branch of 2.5×10^{-5} which provides ^{5}Li and 16.7 MeV gamma-ray. The total D-^{3}He reaction rate was evaluated by the gamma-ray measurement using BGO ($Bi_4Ge_3O_{12}$) scintillator of ϕ3" × 3" located 17 m below the plasma center. The pulse hight analysis of the gamma-rays provides the D-^{3}He fusion power of 110±30 kW during N-NB injection.

1. INTRODUCTION

The D-^{3}He reaction is attractive for the alternative fusion reactor, because it does not produce neutrons, and for the estimation of alpha particle behaviors in D-T plasma because the D-^{3}He reaction produces almost same energy alphas as D-T reaction. The reaction cross-section has strong dependence on the incident energy of D or ^{3}He. In JET, 140 kW of the D-^{3}He fusion power was generated with ^{3}He minority heating by ICRF[1]. The negative ion-base neutral beam injector (N-NBI) [2] with 500 keV is suitable for the D-^{3}He experiment because the D-^{3}He reaction cross-section is maximized at D energy of ~500 keV, and has a potential to produce ~ 1MW of theD-^{3}He fusion power in 10 MW injection [3].

Reaction equations of D-^{3}He are shown in Eq.(1) and (2). Almost all of the D-^{3}He reaction s produce protons and alphas which are confined in the plasma, so the direct measurement of the D-^{3}He reaction rate is very difficult. However, D-^{3}He reaction has a small branch to produce ^{5}Li and 16.7 MeV gamma-ray as shown in Eq.(2). We can evaluate the D-^{3}He reaction rate with the 16.7 MeV gamma-ray measurement.

$$D + {}^3He \rightarrow p\,(14.7\ MeV) + \alpha\,(3.6\ MeV) \quad [100\%] \qquad (1)$$

$$D + {}^3He \rightarrow {}^5Li + \gamma\,(16.7\ MeV) \quad [0.0025\%] \qquad (2)$$

2. DIAGNOSTIC SET-UP

In the energy range higher then 10 MeV, gamma-ray are measured with elecron and positron pear creation process. The cross-section of the pear creation increases with Z^2 where Z is the charge number of the detection material. So the high Z material is suitable for the detection of 16.7 MeV gamma-rays. We employed the BGO ($Bi_4Ge_3O_{12}$) scintillator, whose density is

7.13 g/cm^3, with a size of ϕ3" × 3".

Figure 1 shows the arrangement of the gamma-ray detector on JT-60U. The detector is located 15 m below the plasma center and measures the emitted gamma-rays in a vertical line-of sight. The floor penetration with 4 × 8 cm^2 is used as a pre-collimator. The detector is mounted inside the heavy collimator which used be for the NE213 neutron spectrometer. The collimator is made with polyethylene as a fast neutron moderator, borated polyethylene as a thermal neutron absorber, and lead as a gamma-ray shield.

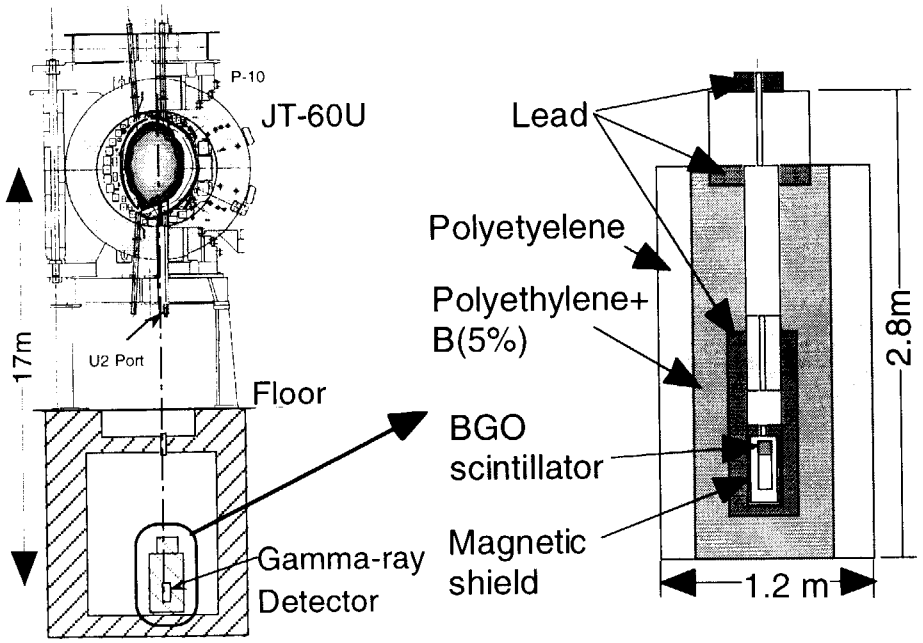

Fig.1. Arrangement of the gamma-ray detector on JT-60U.

Generally, energy and efficiency calibrations of gamma-ray detectors are done with radio-isotope (RI) gamma-ray sources. However, RI sources with the gamma-ray energy higher then 3 MeV are not available. The energy output of the BGO detector was calibrated preliminary with ^{137}Cs (0.667 MeV) and ^{60}Co (1.17 and 1.33 MeV). Extrapolation from those energy to 16.7 MeV may give large uncertainty. We calibrated the detector in the high energy region using neutron capture gamma-rays from structural materials in DD discharges. Figure 2 shows the gamma-ray spectrum measured in DD discharges, where H(n,γ)D[2.22 MeV], ^{16}O(n,γ)^{17}O[4.14 MeV], ^{52}Cr(n,γ)^{53}Cr[7.94 MeV], and ^{58}Ni(n,γ)^{59}Ni[9.00 MeV]are identified.

Detection efficiency calibration is much difficult for 16.7 MeV gamma-rays. We calculated the efficiency with the Monte Carlo code MCNP-4B[4] with 3-dimentional modeling of the BGO detector, where the incident gamma-ray beam with 50 mm diameter is well collimated onto the detector head. Figure 3 shows the detection efficiency of the full energy peak and single photon escaped peak as a function of the gamma-ray energy. Single photon escaped peak which corresponds to escape of the photon of the positron annihilation from the detector is almost comparable for 16.7 MeV gamma-rays. Because the energy resolution of the BGO detector is about 14 %, we could not distinguish the full energy peak and single photon escaped peak which is 0.511 MeV lower than full energy peak. Here we adopted 40 % of the total efficiency including

single photon escaped peak.

Count rate of the BGO detector for gamma-rays higher than 15 MeV is measured with 10 ms time duration during whole discharges (15 s). Pulse high spectrum is measured with 300 ms time duration and 500 channels of the conversion gain in the CAMAC ADC.

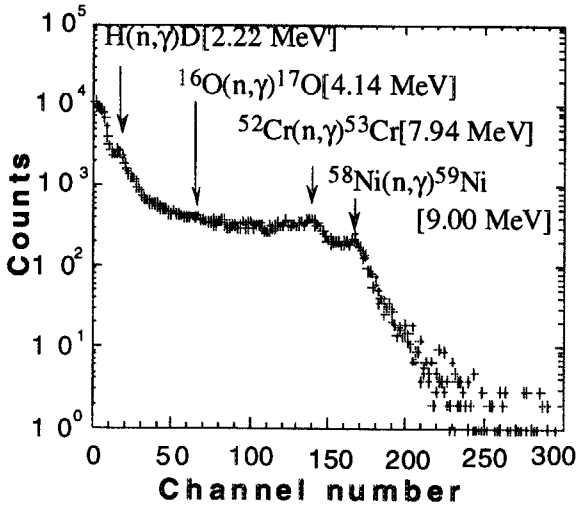

Fig.2. Gamma-ray spectrum during DD discharges.

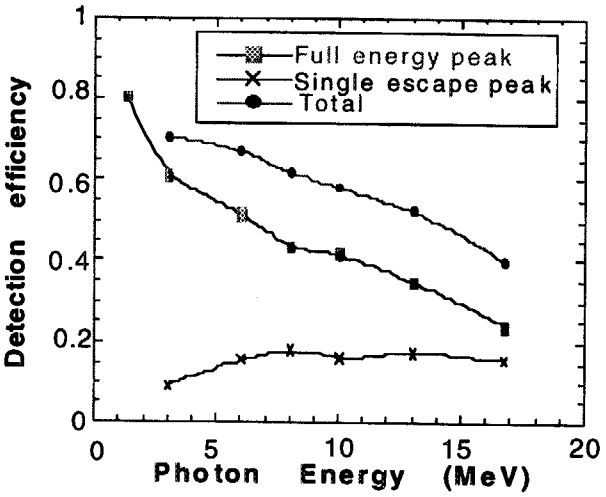

Fig.3. Detection efficiency of BGO detector calculated with MCNP-4B.

3. EXPERIMENTS

We tried the preliminary D-^{3}He experiments with N-NBI in reversed shear(RS) plasmas [5]. The RS plasma has rather high electron temperature in wide region, which is preferable to increase the fast ion density due to longer showing down time. Figure 4 shows the waveforms of the D-^{3}He experiment in JT-60U.

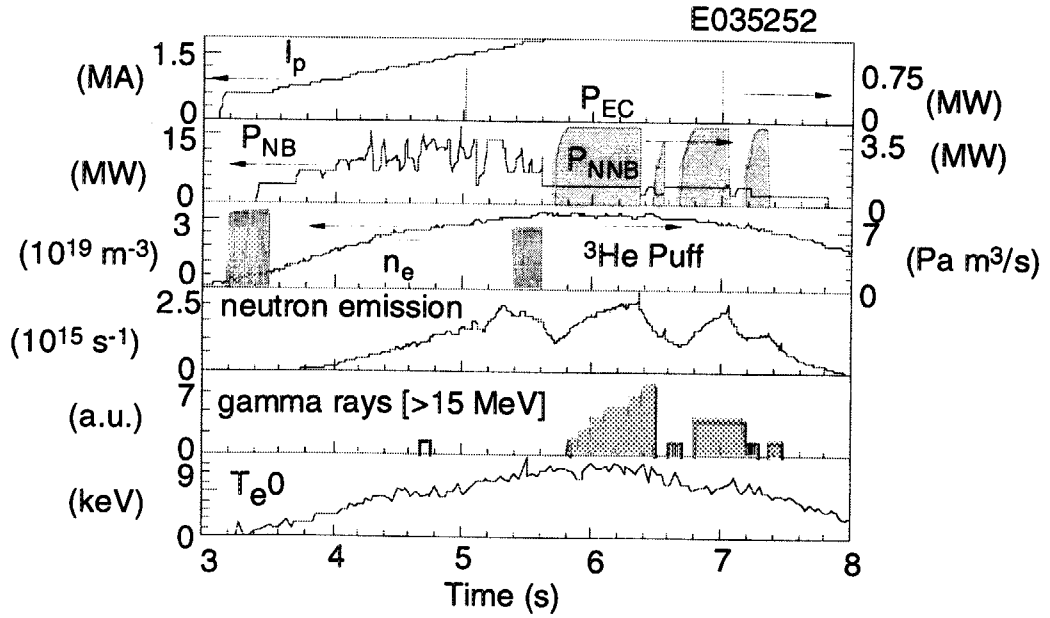

Fig. 4. Waveforms of the D-^{3}He discharged with N-NB injection in JT-60U.

Gas of ^{3}He was puffed in the plasma initiation and just before the N-NB injection of 3.5 MW with 360 keV. Positive ion NBs of deuterium were used to create the RS configuration and increase the electron temperature. The real time feedback control of the stored energy was used in the current rump-up phase, therefore the positive NB power was modulated. ECRF of 0.4 MW(plasma input power) was injected into core region to boost the electron temperature. The count rate of the gamma-ray s increases during the N-NB injection.

Figure 5(a) shows the gamma-ray spectrum during N-NB injection in the D-^{3}He experiment compared with that of DD discharge with almost same neutron emission. Two broad peaks around 16 MeV and 14 MeV are identified in the D-^{3}He discharge, which corresponds to γ_0 and γ_1 shown in Fig.5(b). The D-^{3}He fusion power is evaluated to be 110±30 kW from the counts of γ_0 whose fraction is 0.0025% for the total D-^{3}He reaction rate.

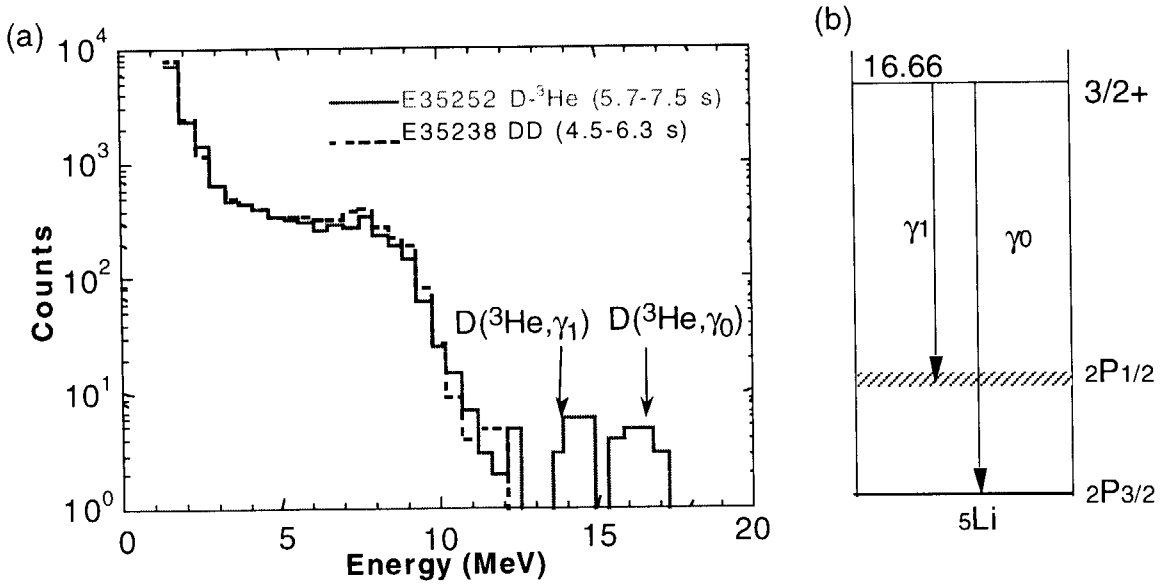

Fig. 5. (a) Gamma-ray spectrum during N-NB injection in the D-^{3}He discharge compared with that of DD discharge with same neutron emission rate, and (b) level scheme of ^{5}Li.

4. SUMMARY

In JT-60U, the preliminary D-^{3}He experiments was done with N-NBI in RS plasmas. We adopted the BGO scintillator for the D-^{3}He fusion power measurements. The BGO scintillator of ϕ3" × 3" is mounted in the collimator located 17 m below the plasma center. The energy calibration of the detector was done by neutron capture gamma-rays from the structural material in DD discharges. The detection efficiency is calculated with Monte Carlo code. From the measured gamma-ray spectrum, the D-^{3}He fusion power is evaluated to be 110±30 kW during N-NB injection n the D-^{3}He experiment.

In 2000, we will try to demonstrate the ~1 MW of D-^{3}He fusion power production with the increase in the NNB power to ~10 MW and with 2 or 3 of ^{3}He beams in the positive NBs. The fusion gamma-ray detector will be replaced with a new BGO scintillator of ϕ4" × 4" in order to increase the detection efficiency.

AKNOWLEDGEMENT

The authors would like to thank Dr. F. Maekawa for his support with the BGO detector usage.

REFERENCEES

[1] G. Sadler, J.P. Christiansen, G.A. Cottrel, et al., in Proc. 18th European Physical Society Conference on Controlled Fusion and Plasma Physics, Berline, 1991, Vol. 15c, Part I (1991), 29.

[2] M. Kuriyama, N. Akiba, T. Aoyagi, et al., Fusion Eng. Des. **39-40** (1998) 115.

[3] M. Yamagiwa, Plasma Phys. Controlled Fusion **34** (1992) 715.

[4] J.F. Briesmeister (Ed.), Los Alamos National Laboratory Report, LA-12625-M, Los Alamos National Laboratory, (1993).

[5] T. Fujita, S. Ide, H. Shirai, et al., Phys. Rev. Lett. **78** (1997) 2377.

3-4 Collective Thomson Scattering Based on Pulsed CO_2 Laser in JT-60U

T. Kondoh, S. Lee, Y. Tsukahara

Naka Fusion Research Establishment, Japan Atomic Energy Research Institute

Naka-machi, Naka-gun, Ibaraki-ken, 311-0193, Japan

In JT-60U, a collective Thomson scattering system (CTS system) based on a pulsed CO_2 laser (10.6 μm, 10J, 1μs) have been developed to measure ion temperature and fast-ion velocity distribution and also to demonstrate feasibility of measurements of confined alpha particles and ion temperature in ITER. In this paper, we describe the present status of the JT-60U CTS system.

1. Introduction

Measurement of energy distributions of DT produced confined alpha particles will be essential in diagnosing a fusion reactor since the energy transferred to the plasma from the slowing down of alpha particles is required to maintain ignition. Studies of alpha particle confinement will be an important physics program also for ITER experiments. Several methods for the measurement of alpha particle velocity distribution have been studied, including CO_2 laser Thomson scattering [1, 2, 3]. Recently, Bindslev et al. reported detection of scattering from plasma fluctuations driven by fast ion population using 140 GHz gyrotrons [4]. The advantages of using CO_2 laser are as follows: (1) there is practically no plasma emission near 10μm to interfere with the detection on any tokamak, (2) the calculation of the alpha effect on the cross section is straightforward by avoiding $\mathbf{k}\cdot\mathbf{B}=0$, (3) Faraday rotation and refraction are unimportant, (4) good absorption notch filters (hot CO_2 gas cell) exist to eliminate the stray laser line from the scattered signal and (5) the CO_2 laser diagnostic does not require any major source or detector development.

In JT-60U, in order to demonstrate a measurement of the velocity distribution of D-T produced alpha particles, the collective Thomson scattering system with a pulsed CO_2 laser has been developed. The construction of the optical system in the torus hall (including remote control mirrors) has been completed in the year 1999. Measurement in the JT-60U plasma will start in the year 2000.

2. CTS System in JT-60U

Both tangential and vertical access was considered on JT-60U; the tangential view is preferred because of better spatial resolution (polidal spatial resolution ΔR ~ 2 cm). For vertical access, the profile is averaged over the scattering length (spatial resolution ~ 46 cm),

however, we chose vertical access because of difficulties of tangential access. The laser beam passes vertically through the plasma using top and bottom vertical ports about 20 cm in diameter. Since no return route for the scattered light was found for vertical access, the scattered light returns to the injection port.

Schematic of the CTS system on JT-60U is shown in Fig.1. The laser design chosen for the CTS diagnostic is a transversely excited atmospheric (TEA) pressure laser with energy of greater than 10 joules per pulse. We control both the pulse shape and wavelength by injecting a beam from a small cw CO_2 laser into the TEA laser cavity. The beam diameter confirmed with thermal paper burn pattern is fixed at about 4 cm by the output optics and apertures on the laser tube flanges. Waveform of an output monitor indicates a nominal pulse width of 1 μs at FWHM.

Input and output windows of JT-60U vacuum vessel are ZnSe coated with PVAR to withstand over 20 J/pulse power. All mirrors are made of Molybdenum and the nearest mirrors to the tokamak are remotely controlled. CCD cameras monitor the He-Ne laser for calibration of optical alignment. The beam lines is enclosed for safety and purged with dry nitrogen to insure good transmission.

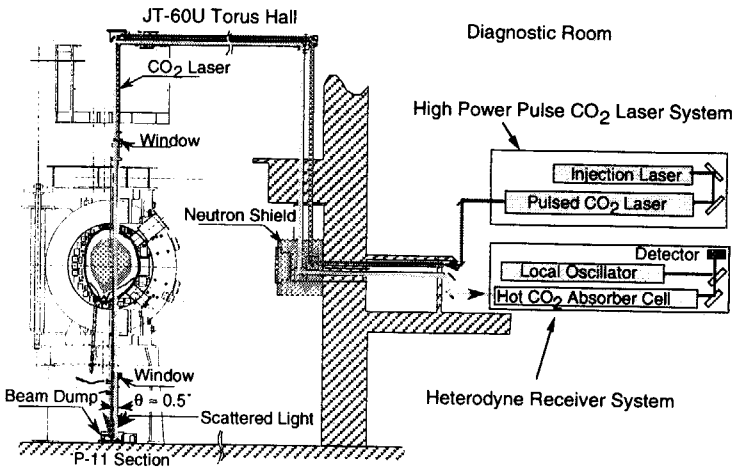

Fig. 1 Schematic view of the Collective Thomson Scattering System in JT-60U. The distance from the CO_2 laser to the JT-60U plasma is about 70m.

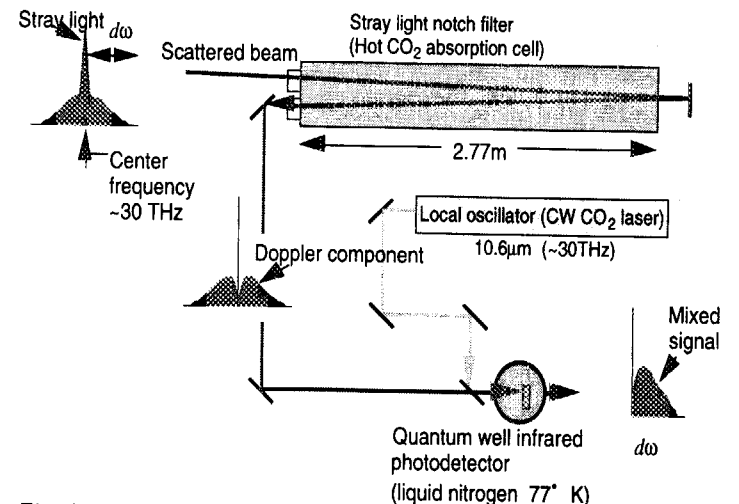

Fig. 2 Schematic of the heterodyne receiver system with stray light notch filter in JT-60U.

Figure 2 shows schematic view of a heterodyne receiver system. A notch filter with hot CO_2 gas reduces stray light from the scattered signal. The filter provides absorption of about 50000 at a bandwidth of less than 500. To obtain a good S/N value in JT-60U, a quantum-well

infrared photodetector (QWIP) are used. QWIP detectors are manufactured by the growth of alternating layers of GaAs and GaAlAs. A local oscillator laser for the receiver is a DC-excited CW CO_2 laser. The laser incorporates a feedback stabilization system to maintain operation on line center of the 10P20, 10.6 μm transition. The basic requirements for the receiver are a noise-equivalent-power (NEP) of less than 9 x 10^{-19} W/Hz and a bandwidth of 3 GHz. The NEP could be actually determined by using a blackbody with a known temperature at diagnostic room. The NEP is below the specified level of 6~9 x 10^{-19} W/Hz up to a frequency of 3 GHz, the specified bandwidth.

Figure 3 shows a 6-channel filter bank for the spectrum analysis of the scattered light in the frequency range from 0.4 GHz to 4.5 GHz. Scattered signal is evaluated by ch1- ch4 detectors for T_i<15keV plasmas and Ch5 will be used for high temperature plasmas (T_i >15keV). Channel 6 detector will be used for fast ion diagnostics. Figure 4 shows expected scattered spectra and detected power for each channel.

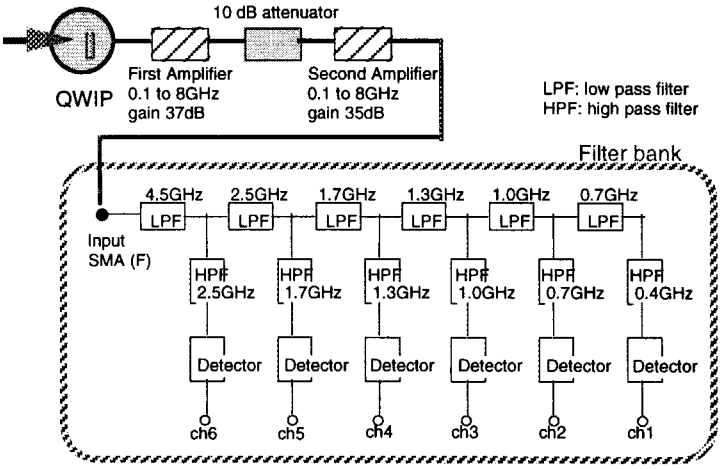

Fig. 3 Six-channel filter bank for spectrum analysis of the scattered light.

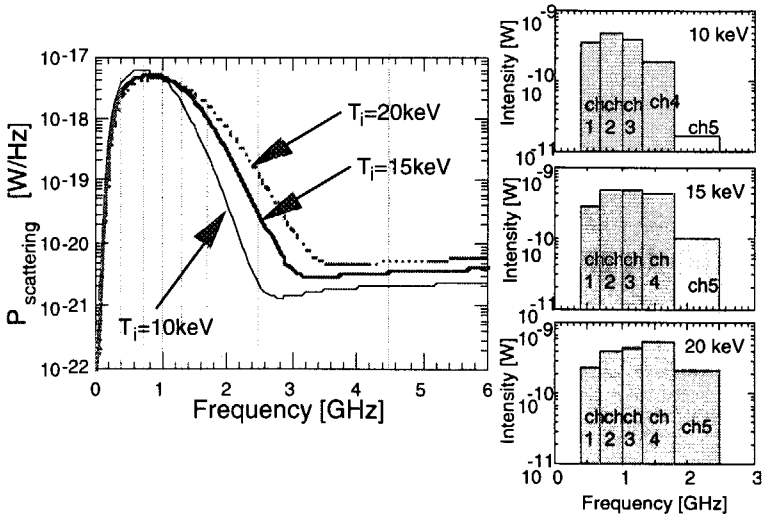

Fig. 4 Expected scattered power as a function of frequency shift from the injection laser and detected power for each channel. Plasma parameters are $n_e=n_D=1\times10^{20}m^{-3}$, ion temperature of T_i=10, 15 and 20 keV.

3. Fast ion Diagnostic

In order to prove the possibility of fast ion diagnostic, the negative ion based neutral beam (NNB) heating experiments will be studied in JT-60U. Figure 5 shows the calculated scattered spectrum for slowing down distribution of injected beam ions of E_{beam} = *400 keV*, n_{beam} = 2×10^{18} m^{-3}. Good S/N ratio for ion tail is not expected by use of the same bandwidth (B=0.5 GHz) as ion temperature measurement. Therefore the bandpass filter with a

bandwidth of B = 2GHz will be used in order to measure fast ions. Wide band filter will improve the S/N ratio, because S/N ratio is proportional to square root of the bandwidth. Observation of scattered spectrum by the fast ions can be expected in negative ion based neutral beam (NNB) heated plasma using present laser and detection system.

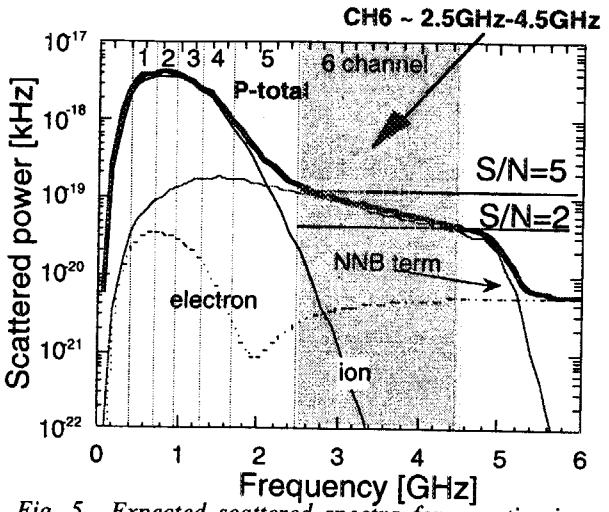

Fig. 5 Expected scattered spectra for negative-ion based neutral beam heated plasma. Individual contributions to the scattered power due to electrons, bulk-ions and NNB-ions are indicated. Plasma parameters are $n_e=n_D=8\times10^{19}m^{-3}$, $T_e=8keV$, $T_i=15keV$, $E_{beam}=400\ keV$, $n_{beam}=2\times10^{18}\ m^{-3}$.

4. Summary

The analysis performed in this article shows that the CO_2 laser and the heterodyne receiver systems can measure fast ion tail and ion temperature of D-T burning plasma in RC-ITER. Measurement of fast ions in NNB heated plasma is also possible by use of wide band filter and detectors. A calculation was also performed to evaluate the possibility of high-energy alpha particle measurement of D-3He plasma in JT-60U. Although the experiment is expected to be the first measurement of confined alpha particles in a burning plasma, it seems difficult with the present plasma parameters. The tangential view is preferred because several spatial resolutions are available and a long path is beneficial to the discrimination of scattered power from incident laser beam. Collective Thomson scattering will be constructed in JT-60U for a proof-of-principle. The development of this ion tail diagnostic for JT-60U could contribute a great deal to alpha particle and ion temperature measurement for ITER.

Acknowledgments

We would like to thank Dr. D. P. Hutchinson, Dr. R. K. Richards, and Dr. C. A. Bennett in Oak Ridge National Laboratory for producing the laser and detector system and for helpful discussion.

References

[1] D. P. Hutchinson *et al.*, Rev. Sci. Instrum. **56**, 1075 (1985)

[2] R. K. Richards, D. P. Hutchinson, C. A. Bennett, H. T. Hunter, and C. H. Ma, Appl. Phys. Lett. **62**(1), 28 (1993)

[3] R. K. Richards, D. P. Hutchinson, and C. H. Ma, Rev. Sci. Instrum. **66**, 497 (1995)

[4] H. Bindslev et al., Phys. Rev. Lett. **83** , 3206 (1999)

List of Participants

1	Andrew Cheetham	University of Canberra (Visiting Fellow: Australian National University)	adc112@rsphysse.anu.edu.au
2	Scott Collis	University of Sydney	
3	Peter deVries	National Institute for Fusion Science	deVries@nifs.ac.jp
4	Akira Ejiri	University of Tokyo	ejiri@plasma.phys.s.u-tokyo.ac.jp
5	Takashi Fujimoto	Kyoto University	a53080@sakura.kudpc.kyoto-u.ac.jp
6	Akimasa Funahashi	Japan Atomic Energy Research Institute	funahasa@fusion.naka.jaeri.go.jp
7	Kouki Hatae	Japan Atomic Energy Research Institute	hatae@naka.jaeri.go.jp
8	Magnus Hoek	Japan Atomic Energy Research Institute	magnush@fusion.naka.jaeri.go.jp
9	John Howard	Australian National University	John.Howard@anu.edu.au
10	Shunsuke Ide	Japan Atomic Energy Research Institute	ide@naka.jaeri.go.jp
11	Toshitaka Idehara	Fukui University	idehara@maxwell.apphy.fukui-u.ac.jp
12	Akihiko Isayama	Japan Atomic Energy Research Institute	isayama@naka.jaeri.go.jp
13	Atsushi Iwamae	Kyoto University	iwamae@jasmine.kues.kyoto-u.ac.jp
14	Brian James	University of Sydney	B.James@Physics.usyd.edu.au
15	Kazuo Kawahata	National Institute for Fusion Science	kawahata@ms.nifs.ac.jp
16	Yasunori Kawano	Japan Atomic Energy Research Institute	kawano@naka.jaeri.go.jp
17	Heejae Kim	Kyushu University	hjkim@asem.kyushu-u.ac.jp
18	Takashi Kondoh	Japan Atomic Energy Research Institute	kondoh@naka.jaeri.go.jp
19	Yoshinori Kusama	Japan Atomic Energy Research Institute	kusama@naka.jaeri.go.jp
20	Seishu Lee	Japan Atomic Energy Research Institute	leesei@fusion.naka.jaeri.go.jp
21	Neville Luhmann, Jr	University of California	ncluhmann@ucdavis.edu
22	Atsushi Mase	Kyushu University	mase@astec.kyushu-u.ac.jp
23	Clive Michael	Australian National University	cam112@rsphysse.anu.edu.au
24	Tomohide Nakano	Japan Atomic Energy Research Institute	nakanot@fusion.naka.jaeri.go.jp
25	Masahiro Nemoto	Japan Atomic Energy Research Institute	nemoto@naka.jaeri.go.jp
26	Takeo Nishitani	Japan Atomic Energy Research Institute	nisitani@naka.jaeri.go.jp
27	Toshiatsu Oda	Hiroshima Kokusai Gakuin University	oda@g.hkg.ac.jp
28	Isamu Ogawa	Fukui University	ogawa@maxwell.apphy.fukui-u.ac.jp
29	Shigeki Okajima	Chubu University	sokajima@kalen.isc.chubu.ac.jp
30	Naoyuki Oyama	Japan Atomic Energy Research Institute	oyaman@fusion.naka.jaeri.go.jp
31	Hyeon Park	PPPL, Princeton University	hpark@pppl.gov
32	William Payne	University of Sydney	
33	Kouji Shinohara	Japan Atomic Energy Research Institute	shinohak@fusion.naka.jaeri.go.jp
34	Tatsuo Sugie	Japan Atomic Energy Research Institute	sugie@naka.jaeri.go.jp
35	Tokihiko Tokuzawa	National Institute for Fusion Science	tokuzawa@nifs.ac.jp
36	Gerry Woolsey	University of New England	gwoolsey@metz.une.edu.au
37	Ryuji Yoshino	Japan Atomic Energy Research Institute	yoshinor@fusion.naka.jaeri.go.jp

Organizer:

Akimasa Funahashi (Japan Atomic Enerugy Research Institute)
Kazuo Kawahata (National Institute for Fusion Science)
John Howard (Australia National University)
Ryuji Yoshino (Japan Atomic Enerugy Research Institute)

Scientific secretary (Japan Atomic Enerugy Research Institute):

Tatsuo Sugie
Tomohide Nakano

Secretary (Japan Atomic Enerugy Research Institute):

Shuji Yoshinari
Junko Takahashi
Takako Shirato

Participants of the Fifth Australia-Japan Workshop on Plasma Diagnostics
at the front of JT-60 Control Building (16 December, 1999).

This is a blank page.

国際単位系(SI)と換算表

表1　SI基本単位および補助単位

量	名称	記号
長さ	メートル	m
質量	キログラム	kg
時間	秒	s
電流	アンペア	A
熱力学温度	ケルビン	K
物質量	モル	mol
光度	カンデラ	cd
平面角	ラジアン	rad
立体角	ステラジアン	sr

表2　SIと併用される単位

名称	記号
分，時，日	min，h，d
度，分，秒	°，′，″
リットル	l，L
トン	t
電子ボルト	eV
原子質量単位	u

1 eV = 1.60218 × 10^{-19} J

1 u = 1.66054 × 10^{-27} kg

表3　固有の名称をもつSI組立単位

量	名称	記号	他のSI単位による表現
周波数	ヘルツ	Hz	s^{-1}
力	ニュートン	N	$m\cdot kg/s^2$
圧力，応力	パスカル	Pa	N/m^2
エネルギー，仕事，熱量	ジュール	J	N·m
工率，放射束	ワット	W	J/s
電気量，電荷	クーロン	C	A·s
電位，電圧，起電力	ボルト	V	W/A
静電容量	ファラド	F	C/V
電気抵抗	オーム	Ω	V/A
コンダクタンス	ジーメンス	S	A/V
磁束	ウェーバ	Wb	V·s
磁束密度	テスラ	T	Wb/m^2
インダクタンス	ヘンリー	H	Wb/A
セルシウス温度	セルシウス度	℃	
光束	ルーメン	lm	cd·sr
照度	ルクス	lx	lm/m^2
放射能	ベクレル	Bq	s^{-1}
吸収線量	グレイ	Gy	J/kg
線量当量	シーベルト	Sv	J/kg

表4　SIと共に暫定的に維持される単位

名称	記号
オングストローム	Å
バーン	b
バール	bar
ガル	Gal
キュリー	Ci
レントゲン	R
ラド	rad
レム	rem

1 Å = 0.1 nm = 10^{-10} m

1 b = 100 fm^2 = 10^{-28} m^2

1 bar = 0.1 MPa = 10^5 Pa

1 Gal = 1 cm/s^2 = 10^{-2} m/s^2

1 Ci = 3.7 × 10^{10} Bq

1 R = 2.58 × 10^{-4} C/kg

1 rad = 1 cGy = 10^{-2} Gy

1 rem = 1 cSv = 10^{-2} Sv

表5　SI接頭語

倍数	接頭語	記号
10^{18}	エクサ	E
10^{15}	ペタ	P
10^{12}	テラ	T
10^{9}	ギガ	G
10^{6}	メガ	M
10^{3}	キロ	k
10^{2}	ヘクト	h
10^{1}	デカ	da
10^{-1}	デシ	d
10^{-2}	センチ	c
10^{-3}	ミリ	m
10^{-6}	マイクロ	μ
10^{-9}	ナノ	n
10^{-12}	ピコ	p
10^{-15}	フェムト	f
10^{-18}	アト	a

（注）

1. 表1－5は「国際単位系」第5版，国際度量衡局 1985年刊行による。ただし，1 eVおよび1 uの値はCODATAの1986年推奨値によった。
2. 表4には海里，ノット，アール，ヘクタールも含まれているが日常の単位なのでここでは省略した。
3. barは，JISでは流体の圧力を表わす場合に限り表2のカテゴリーに分類されている。
4. EC閣僚理事会指令ではbar，barnおよび「血圧の単位」mmHgを表2のカテゴリーに入れている。

換算表

力

N(=10^5 dyn)	kgf	lbf
1	0.101972	0.224809
9.80665	1	2.20462
4.44822	0.453592	1

粘度　1 Pa·s(N·s/m^2) = 10 P(ポアズ)(g/(cm·s))

動粘度　1 m^2/s = 10^4 St(ストークス)(cm^2/s)

圧力

MPa(=10 bar)	kgf/cm^2	atm	mmHg(Torr)	lbf/in^2(psi)
1	10.1972	9.86923	7.50062 × 10^3	145.038
0.0980665	1	0.967841	735.559	14.2233
0.101325	1.03323	1	760	14.6959
1.33322 × 10^{-4}	1.35951 × 10^{-3}	1.31579 × 10^{-3}	1	1.93368 × 10^{-2}
6.89476 × 10^{-3}	7.03070 × 10^{-2}	6.80460 × 10^{-2}	51.7149	1

エネルギー・仕事・熱量

J(=10^7 erg)	kgf·m	kW·h	cal(計量法)	Btu	ft·lbf	eV
1	0.101972	2.77778 × 10^{-7}	0.238889	9.47813 × 10^{-4}	0.737562	6.24150 × 10^{18}
9.80665	1	2.72407 × 10^{-6}	2.34270	9.29487 × 10^{-3}	7.23301	6.12082 × 10^{19}
3.6 × 10^6	3.67098 × 10^5	1	8.59999 × 10^5	3412.13	2.65522 × 10^6	2.24694 × 10^{25}
4.18605	0.426858	1.16279 × 10^{-6}	1	3.96759 × 10^{-3}	3.08747	2.61272 × 10^{19}
1055.06	107.586	2.93072 × 10^{-4}	252.042	1	778.172	6.58515 × 10^{21}
1.35582	0.138255	3.76616 × 10^{-7}	0.323890	1.28506 × 10^{-3}	1	8.46233 × 10^{18}
1.60218 × 10^{-19}	1.63377 × 10^{-20}	4.45050 × 10^{-26}	3.82743 × 10^{-20}	1.51857 × 10^{-22}	1.18171 × 10^{-19}	1

1 cal = 4.18605 J(計量法)

= 4.184 J　(熱化学)

= 4.1855 J　(15 °C)

= 4.1868 J(国際蒸気表)

仕事率　1 PS(仏馬力)

= 75 kgf·m/s

= 735.499 W

放射能

Bq	Ci
1	2.70270 × 10^{-11}
3.7 × 10^{10}	1

吸収線量

Gy	rad
1	100
0.01	1

照射線量

C/kg	R
1	3876
2.58 × 10^{-4}	1

線量当量

Sv	rem
1	100
0.01	1

（86年12月26日現在）